Phononic Metamaterials Based on Complex Geometries

"A New Kind of Metamaterial"

Sisi (Sophie) Ni

B.Eng. Materials Science and Engineering

Nanyang Technological University, Singapore

Submitted to the Department of Materials Science and Engineering in

Partial Fulfillment of the

Requirements for the Degree of

Doctor of Philosophy in Materials Science and Engineering

at the

Massachusetts Institute of Technology

May 2014

[June 2014]

Signature redacted

Signature of Author.....
Sisi (Sophie) Ni
Department of Materials Science and Engineering

Signature redacted

Certified by .....
Edwin L. Thomas
Dean of Engineering
Professor of Materials Science and NanoEngineering
Thesis Supervisor

Signature redacted

Accepted by .....
Gerbrand Ceder
R. P. Simmons Professor of Materials Science and Engineering
Chair, Departmental Committee on Graduate Students

Wir müssen wissen.
Wir werden wissen.

- David Hilbert

PhoXonic Metamaterials Based on Complex Geometries

"A New Kind of Metamaterial"

By Sisi (Sophie) Ni

Submitted to the Department of Materials Science and Engineering

in Partial Fulfillment of the Requirements for

the Degree of Doctor of Philosophy in Materials Science and Engineering

at the Massachusetts Institute of Technology May 2014

Abstract

Facing the growing challenges of energy, environment, security and disease treatment, the demand for novel materials are growing. While the material centric approach have resulted in development of new materials for advanced applications, we introduce a geometric approach as a complementary point of view for further innovation in this ever expanding and growing field. Inspired by the ubiquitous fractals-like geometry of in natures, the scale transformation (i.e. dilation or contraction) is included in the framework since fractal geometries shows structures at all scales (usually discrete and finite in physical world). We developed our framework using metamaterials since it enable us to design "atoms" or "molecules" and their relative arrangement with greater freedom (i.e. not limited by the chemical bond or ionic bond in classical materials system).

We studied metamaterials using prefractals from both exact-self similar fractal and random fractal samples. For exact-self similar fractals, we choose H tree based prefractals and Hilbert Curve prefractals bounded system given their unique geometric properties and wide applications. Guided by the framework, we investigated several key parameters (e.g. level of iteration, geometric anisotropy, impedance contrast, arrangement of subunit, resolution) that would dictate the dispersion behavior of the system. It was found that for exact-self similar prefractals, multiple spectrum bandgaps (i.e. broadband response) can be achieved with increased level of iterations where translation symmetry is imposed through boundary condition. Furthermore, the transition from scale dependence and independent described by the general framework has been observed for all the samples we studied. Furthermore, for single prefractal resonator, subwavelength ($\sim 1/75\lambda$) behavior has been observed and explained using a simple analytical model. For metamaterials based on fractional Brownian motion, the Hurst constant is found to be a good indicator of phononic behavior of the system, besides other parameters studied.

Our findings does not only expand the repertoire for novel materials by introducing the ubiquitous yet unconventional geometry to metamaterials; but also have interdisciplinary applications in biology, seismology, arts, hence shine lights on our understanding of nature.

Thesis Supervisor: Edwin L. Thomas

Title: William and Stephanie Sick Dean of the George R. Brown School of Engineering Professor of Materials Science and NanoEngineering

Table of Contents

Acknowledgement

Words are never enough to describe my gratitude for my experience here at MIT, but I shall endeavor. My colorful journey at MIT is filled with challenges, excitement, joy and a list too long to finish. The research itself constantly push me out of my conform zone and explore the opportunities in the landscape of advanced materials. I did not only gained in-depth knowledge and experimental skills about my research area, but I also gained problem solving skills that would benefit me for the rest of my life. Besides my research, I also benefit greatly from the innovative culture of MIT and the great minds at MIT inspired me to make a difference using my knowledge and skills.

First and foremost, I would like to thank my advisor, Prof Edwin (Ned) Thomas for his guidance over the past few years. He gives me the freedom to pursue the subjects I am passionate about regardless how unconventional it might seems. Without him, I would not have the opportunity to discover the wonderful world fractal, which did not only change my view on advanced materials, but completely changed my view about the world around us. He also patiently guide me through the research process by sharing his insights, creativity and passion about science. At times of frustration and struggles, his enthusiasm about science would inspire me to cope with them with courage and strength. I always feel refreshed and energetic after our discussion about the problems and progress, since he would always come out with ideas and penetrating suggestions that would steer the research back to track or new direction. His way of thinking is highly intuitive and accessible to audience with different background, which influenced me deeply on how to effectively communicate my research. Besides research, he also shared wisdom about life that guided me through tough times. He is always kind and supportive for me to pursue my interest besides research, which allows me to discover myself further. I could never hope for a better mentor than him and feel so fortunate to be his students. I only hope my work can repay his guidance, kindness and wisdom. I could not have been where I am today without him.

I thank Prof Geoffrey Beach and Prof Jeffrey Grossman for being on my committee and for their constant support by including me in their group meetings. Their encouragement and support helped me greatly through the difficult times. Their critical comments and suggestions for my thesis and presentations helped me greatly both professionally and personally.

I would also like to thank some of my group members that I have been lucky enough to work with. Dr. Koh Henry is a true scholar with the highest standard for research and his intellectual vision always amazed me. His passion for fundamental understanding between physics and metamaterials inspired me deeply. I learned a great deal from our discussion on this topic and I am impressed by his broad and in-depth knowledge on the field. His constant support and guidance also helped me through the ups and downs of research and I can only hope my work would reply his help to certain extend. Dr Markus has always a great mentor, his pragmatism ground me and his humor is a constant source of joy. His help on experimental setups can never be overstated. I would also like to thank Dr Joe Walsh, Dr Lin Jia, Dr Fan Yin, Charlotte, and Dr John Singer for all the memories we shared.

I would also like to thank group members from Prof Geoffrey Beach's group for including me and treat me like a group member. The limited knowledge about magnetism and the time I spend together with Saturo, Liz, Uwe, Seong Hoon, et al. are priceless.

I would also like to thank Prof Nick Fang and his group member, Dr Xu, Ma Chu for help me with experimental setup and introduce me to the world acoustic from a different view point.

I would also like to express my gratitude towards the professors that I had the fortune to interact with from DMSE. Their knowledge and word of wisdom pave the way for my intellectual endeavor. I also want to thank all the aspiring material scientist and engineers I get to know over the past few years at DMSE, no symmetry element could be sufficient to describe them all.

I also want to thank all the friends I had as a member of graduate student council and other student groups! Your friendship is a constant source of happiness and inspiration for my journey at MIT and I will treasure it for life. Your determinations, creativity and passion push me to reach for the sky and even higher!

I also want to thank Angelita, Elissa for constant help and guide me through the journey with their kindness and support.

I also want to thank Prof Ma, who see the potential in me and help me to pursue my dream despite the obstacles. His attitude towards research and work had a huge impact in me. Although you are not with us anymore, I hope my work can repay your support and belief in me.

To my parents, who have the insight to name me $NiSi_2$ and the most wonderful individuals in my life, word can never express my gratitude towards you, thank you for always supporting me and believing in me no matter how selfish I am for being so far away to pursue this request. I can only hope my work would at least make up the sufferings you have to endure. I dedicate this thesis to you.

List of Figures and Tables

1. Introduction: A Blueprint for Innovation

As material scientists and engineers, we continue to design materials with improved/unique properties for new applications. There are two general approaches taken in developing new designer materials. One is the "materials centric" approach, which focuses on developing new materials possessing properties that address specific applications; the other "geometry centric" approach focuses on engineering structure or geometry/architecture of conventional materials to achieve novel properties through fabrication of systems of materials (device-like materials, e.g. a Si/Air photonic crystal). While both approaches take different perspectives, they can be complementary in materials engineering. Advancements in nanotechnology expand the range of feature size (with respect to shape of the artificial atom) achievable, hence open up platform for exploring the novel configurations/structures that can cover a wide range of length scale and include a wide variety of materials.

With the traditional material science tetrahedron emphasizing the relationship between the structure, processing and properties and performance, the material centric approach usually starts from the building blocks, such as atoms, molecules and connect them in new and often complex ways though new and better processing techniques. This approach allows endless possibilities since so many different parameters can be varied and yields new high performance materials in various categories, with a growing atomistic understanding of the original properties of the materials. Meanwhile, the proposal of "artificial atoms" to create metamaterials is another highly innovative approach to design new material systems. The expansion of building blocks beyond atoms and molecules and new ways to arrange/bond them greatly expand the horizon for material scientists and engineers. Since the artificial atoms are not limited by the elementary units (i.e. ions, electrons, molecules), their shapes and sizes can have unlimited choice. This defines the foundation for a geometric approach for designing new materials. Furthermore, the bonding between unites can expand beyond the traditional choice (i.e. ionic, covalent, or Van der Waals etc.) and be visualized as versatile links with geometric characteristics, e.g. one can employ magnetic forces to assemble units. While the "artificial atoms" provide many exciting opportunities to expand the designer material repertoire, it also presents a formidable challenge given so many choices.

To address this challenge, we endeavor to develop a general intuitive framework, that would provide a systematic way not only consistent with the set of metamaterials so far discovered, but also able to provide a blueprint for innovation. Hence, a general framework to shine light on material design and also needs to be formulated from a practical point of view. Koh(C. Y. Koh, 2011) proposed a governing framework to guide the design of phononic metamaterials utilizing a combination of global symmetry principles with conservation principles and the concept of broken symmetry. This theoretical approach would be a powerful tool for designing materials for wide range of advanced applications; moreover, the general framework is applicable for a wide range of wave/particle interactions with structures given the minimal assumption require.

1.1 Phononic metamaterials

To implement and verify the theory, a phononic metamaterial system was chosen, where both theoretical knowledge and experimental technologies have undergone progress over the past few years. Here the phononic metamaterial refers to artificial materials that possess exotic phononic properties that are not present in nature, i.e. spectral bandgap, negative refraction(C. Y. Koh, 2011)(Feng, 2009)(Genet & Ebbesen, 2007)(X. Xiao et al., 2011). Their unique properties are usually derived from new materials components and/or novel architecture/structures. This make them attractive for a wide range of applications, for example, a superlens, negative bulk modulus, negative density etc.

Photonic crystals and photonic metamaterials have seen significant growth in the past few years due to technological development for various applications(S. Zhang, 2010) (H.-H. Huang, 2009). The temptation to draw an analogy between photons and phonons leads to similar applications for phononic metamaterials. Although the analog seems to be natural, given the similar form of equation governing the propagation of electromagnetic waves and elastic waves in periodic structures, phonons behave differently than photons. Two polarization degrees of freedom can be supported in structures made of non-conducting materials due to the transverse nature of electromagnetic wave propagation. In contrast, three polarization degrees of freedom can be supported for phonons propagating in solids. Although the added degree of freedom gives more flexibility and control for designing materials' properties, it also adds complexity in understanding the behavior.

Despite the challenges and limitations, significant progress has been made for phononic crystal/metamaterials(Guenneau et al., 2005)(I, Mihail Sigal et. al, 2005)(Y. Pennec, 2010)(S. Yang, 2002)(S. Zhang, 2010)(Feng, 2009). While the flourishing field of photonics provides a wide variety of choice for optimize performance of phononic metamaterials for tailored applications(H. Chen, 2010)(Chin, R., 2009) (F. Liu, 2009), a general guidelines that could unify most of the hypothesis would be desirable from a practical point of view. The framework proposed by Koh (C. Koh, 2011) could potentially shine light on this extremely diverse field by pointing out the fundamental principles and developing physical intuition.

By utilizing the concept of the global symmetry principle with the conservation principle, the framework developed by Koh leads to a physical understanding behind the relations between the physical geometry of topography and wave propagation behavior in phononic metamaterials. To verify the framework, it is natural to apply it to design experiments and compare prediction with experimental observables.

A local resonant sonic system has attracted a great deal of attention in the literature after the pioneering work by Liu et al. (Z. Liu, 2000). While conventional Bragg scattering requires the periodic structure to be comparable to the wavelength of the acoustic wave, on the contrary, a "local resonator" can be up to two orders of magnitude smaller in size than the wavelength in the matrix. This feature is attractive for allowing highly compact structures for various applications, i.e. sound shielding, superlens (Ho, 2003; P. Sheng, 2003)(G. Wan, 2004; H.Gang, 2006; Milton, 2006; P. Sheng, 2007).

Aiu et al. obtained a subwavelength spectral gap by using 3D matrix-rubber-scattering system fabricated by Liu etc. They also obtained transmission dips with rubber coated lead particles randomly distributed in the matrix, which leads to the conclusion that local resonator is essential for the formation of the subwavelength spectral [Liu, Z. (2000).] while the periodic lattice is not necessary. They therefore claimed they discovered a new paradigm for the band gap opening mechanism (different from Bragg Scattering mechanism), which could be described by "negative bulk modulus" near the resonance. Their system can been modeled by a mass spring model, with the lead as internal mass connected to the matrix through the rubber shell acting as a spring. The dispersion ω (k) appears as Figure 1.1D, where k is the wave vector for the periodic structure in reciprocal space, and ω is the eigenfrequency corresponds to the wave vector. The built in

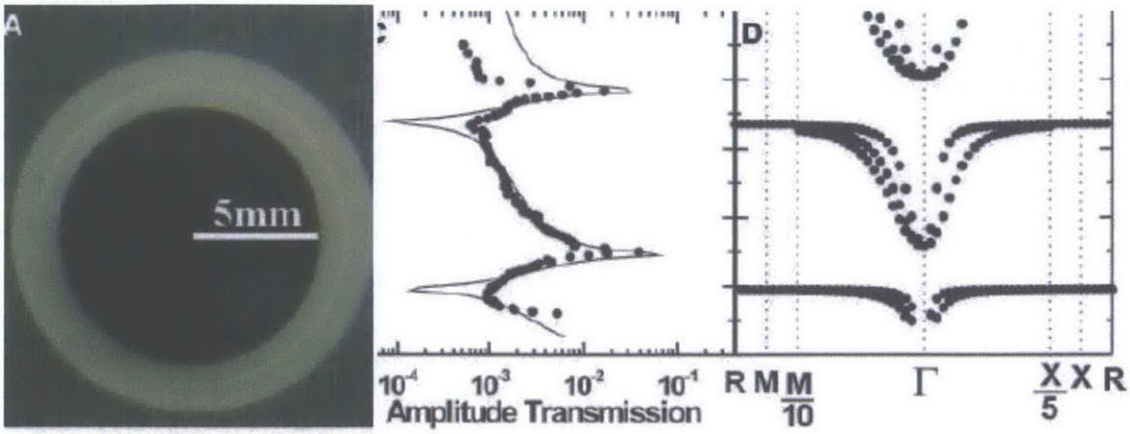

Figure 1.1: Cross section of a rubber coated lead sphere that forms the basic structure unit (B) for an 8X8X8 sonic crystal. (C) Calculated (solid line) and measured (circles) amplitude transmission coefficient along the [100] direction are plotted as a function of frequency. The calculation is for a four-layer slab of simple cubic arrangement of coated spheres, periodic parallel to the slab. The observed transmission characteristics correspond well with the calculated band structure (D), from 200 to 2000 Hz, of a simple cubic structure of coated spheres. Three modes (two transverse and one longitudinal) are distinguishable in the [110] direction, to the left of the Γ point. The two transverse modes are degenerate along the [100] direction, to the right of the Γ point. Note the expanded scale near the Γ point. Image obtained from (Z. Liu, 2000) .

resonance generates flat bands that interact with the linearly dispersed elastic wave and open the subwavelength spectral gap. Hence, the position of the gap is primarily determined by the material properties of the resonator, under the mass-spring model.

The researchers later attributed the negative dynamic mass to the relative out of phase motion between the scatterer and the matrix allowed by the soft rubber using a simulation with multiple scattering methods(Sheng, 2003). They also developed an analytical model using the generalized effective medium theory to predict the double negative (i.e. both effective density and effective bulk modulus) behavior with rubber sphere arranged in fcc lattice in water(J. Li & C. Chan, 2004). The same structure generates both monopolar and bipolar resonance that are responsible for the negative bulk modulus and density respectively.

Despite their claim of not requiring periodic microstructure, Sanchez et al. (S. Dehesa, 2003) conducted a theoretical study using a variational method and found that the subwavelength gaps produced by local states depended on symmetry of the lattice, similar as the Bragg gaps, due to the weak interaction between the localized states. Recently, Larabi et al. (Sheng et al., 2007) also investigated the multicoaxial cylinders in water. They find that the transmission properties and band structure can be significantly affected by the nature of the matrix, i.e. solid or fluid. Using

FDTD simulation, they demonstrate that the transmission dip can be tuned by varying the geometric parameters of the coaxial cylinders. A transmission dip has also been obtained with a 1D array of subwavelength Helmholtz resonators connected to a tube by Zhang et al (Zhang et al, 2008. The negative group delay time/velocity infers a negative effective dynamic modulus near the resonance frequency. They further demonstrated a 3D holey-structured metamaterial superlens that can image down to a feature size of $\lambda/50$(Zhu et al., 2010). The holey structured materials can couple strongly to the evanescent waves with Fabry-Perot resonance, which carry subwavelength information of the sample, and transmit these waves through the lens to obtain image that overcomes the diffraction limit. This demonstration promises potential for range of a wide advanced applications, such as high resolution non-destructive ultrasonic evaluation.

Since this metamaterial relies on the built-in resonance of the scatterers, the quasistatic limit, long wavelength assumption for an effective medium becomes problematic. Zhang et al. (Zhu et al., 2010) tried to introduce an effective theory by abandoning the quasistatic assumption and demonstrated that effective mass density, effective bulk modulus and effective shear modulus can all be negative in a 2D system.

The conventional distinction between a resonant metamaterial and a crystal lies in the position, i.e. frequency/wavelength, where the primary (the lowest ω) spectral gap forms. Moreover, the proposed mechanism for a local resonance sonic system does not require a periodic arrangement of the scatterers (Z. Liu, 2000)(P. Sheng, 2003). Although the proof for this is relatively weak, it is based on a far-field transmission calculation of a disordered system, which although it proves the scattering mechanism, does not prove anything definite about the origin of bandgap formation, because it also depends on other factors, i.e. the source excitation and matrix geometry, the interface where the interaction occurs etc.

This local approximation assumption may be misleading due to by the material choices in the particular system. Because of the large material impedance contrast between rubber and lead, the mechanical spring is only weakly coupled through the lattice. Therefore, the non-locality is weak in this system masked by the choice of the materials; the perceived local mechanism is not a distinct mechanism itself(C. Y. Koh, 2011). Furthermore, the fact that the avoided crossing happens at a small but finite wave vector, indicates non-locality of the interaction.

Our studies show that each eigenmode's polarization field has to conform to the little group of the respective wave vectors. *Avoided crossing* is the general mechanism to form spectral gap and it implies non-locality in the presence of a lattice. The choice of the constituent materials will only perturb the degree of non-locality; sometimes, depending on the degree of impedance contrast, making the system seemly behave in a local regime. This can be demonstrated by tuning the material parameters such that the "weakness" of the non-locality becomes clear (Appendix A).

1.2 Fractal geometry

Complex geometries, especially fractal (i.e. self-similar structure) geometries, are ubiquitous in nature(Mandelbrot, 1977, 1983, 1997, 1999, 2002, 2004a), e.g. a coastline, mountain skylines, trees, water falls, as shown in Figure 1.1. However, due to its "problematic" nature, e.g. such curves, surfaces are non-differentiable, they were shunned by mathematicians or even termed as

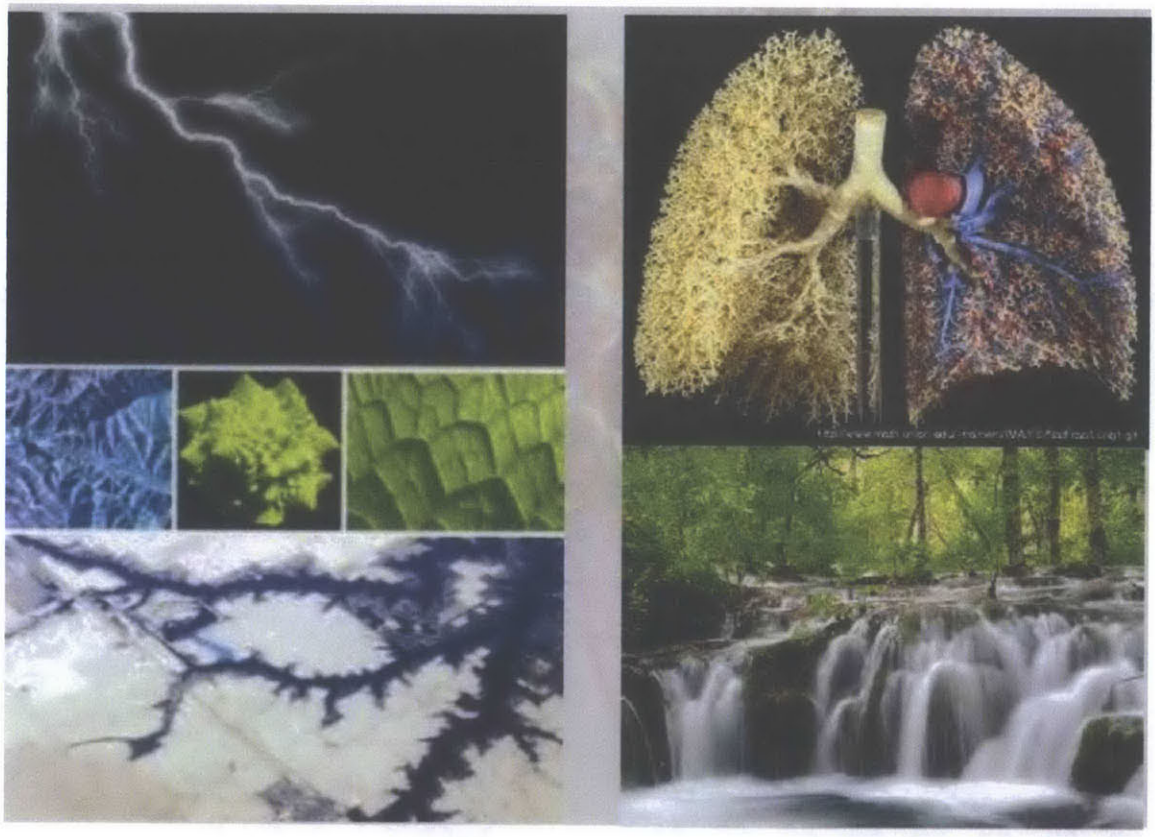

Figure 1.2: Fractal geometry observe in nature and biological system

"monster" curves. Then in the 1960s, mathematician Benoit Mandelbrot coined the term "fractal" from the Latin Adjective *fractus*.(Mandelbrot, 1983) to discuss a new geometry that embraces the roughness of nature. Fractal geometry is "a rough or fragmented [geometry] that can be split into parts", which is characterized by self-similarity, i.e. the degree of their irregularity and/or fragmentation is similar at all length scales. This soon captured the interests of many mathematicians with their "abnormal" properties that deviate from those associated with the smooth geometries.

Fractal geometry can be generated by several techniques; one of them is the Iterated Function System (IFS), whose algorithms can be deterministic or random. If we represent a linear transformation f as a matrix $A = \begin{pmatrix} rcos\theta & -ssin\phi \\ rsin\theta & -scos\phi \end{pmatrix}$, then an affine linear transformation can be defined as a map $F : \mathbb{R}^2 \to \mathbb{R}^2$ if $F\begin{pmatrix} x \\ y \end{pmatrix} = A\begin{pmatrix} x \\ y \end{pmatrix} + \begin{pmatrix} e \\ f \end{pmatrix}$.

Hence, we define a mapping $F : S \to : S$ as *contraction* if for some $0 < \alpha < 1$,

$||F(z_1) - F(z_2)|| \leq \alpha||z_1 - z_2||$, for all $z_1, z_2 \in S$.

Then *Iterated Function System (IFS)* is the system $\{S : F = \cup_{i=1}^{N} F_i\}$, where $F_1, F_2, \ldots, F_N$ are family of contractions mapping in the complete matrix space $\mathbb{R}^k$ and S is a close bounded subset of $\mathbb{R}^k$. Some common fractal geometries, such as Sierpinski Triangle and Koch Curve (as shown in Fig 1.3, can be generated using this method. Moreover, the Koch Curve was the first example for a curve that is not differentiable anywhere.

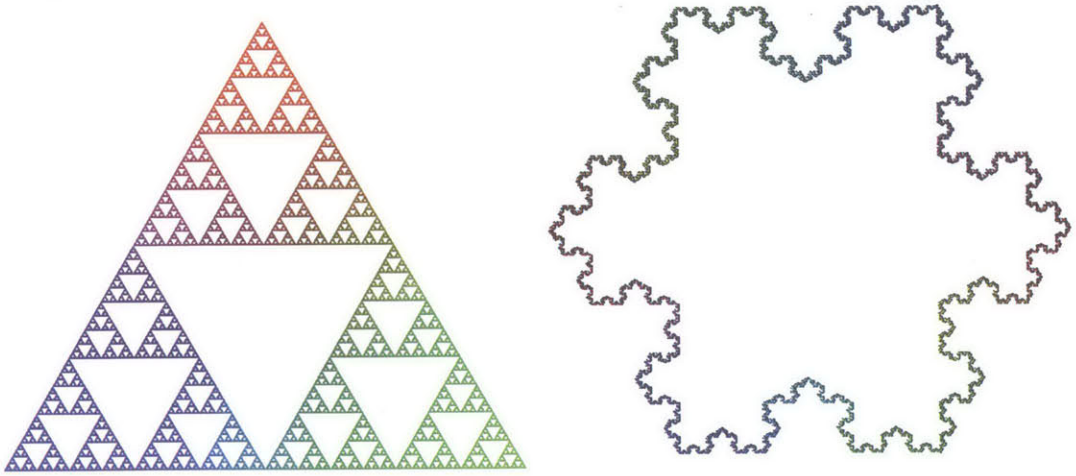

Figure 1.3 Fractal geometry observe in nature and biological system

To study the fractal geometry in a more rigorous way, various parameters and tools are used. Dimension is central to fractal geometry as it measures irregularities at different scales of size. Hence, it contains much information about the geometrical properties of a set. Starting from a cube with length 1, we subdivide it into many small cubes with side-length s = 1/k for any positive integer k. We obtain N(s) = k3 = s−3 little cubes, where the exponent 3 here is the dimension. Similarly, if a set X in $\mathbb{R}^n$ can be subdivided into some finite number N(s) of subsets, each a rescaled copy of X by a linear factor s, then we define the "self-similarity dimension" of X as the unique value d that satisfies N(s) = s−d, where d = log(N(s))/log(1/s). This dimension is usually applicable to exact linear self-similarity, i.e. each piece is a rescaled copy of the total set. However, for more general set, where the similarity is not exact, the Box-counting dimension (Figure 1.3) is introduced. Again for a bounded subset X in $\mathbb{R}^n$, a regular grid of cubes with side-length s is used to partition $\mathbb{R}^n$. If there are N(s) cubes intersecting X, then "box-counting dimension" of X is defined as lim→0 log(N(s))/log(1/s). This approach can be implemented by easily computer; however, it is not always well defined since the limit will not exist in many cases. If we further relax the requirement of same size cubes and replace them with circles, we can derive the more general Hausdorff dimension. The Hausdorff dimension has the advantages of being defined for any geometry, and is mathematically easy to manipulate. However, Hausdorff dimension is also difficult to calculate or estimate using computational methods.

Figure 1.1.4: Ways to estimate different fractal dimension for coastline of Great Britain, box counting dimension with different edge width value s (a) and Hausdorff dimension with different measuring circle diameter (b).

There is no simple agreed upon definition for fractals that can encompass all the objects in the physical world. However, mathematicians still try to define fractals such that they can be studied more rigorously using mathematical tools. Mandelbrot defined it as "a set for which the Hausdorff Besicovith dimension strictly exceeds the topological dimension". The topological dimension is our intuitive understanding of integer dimension in Euclidean space, e.g. a point is zero dimensional, a smooth curve is one-dimensional, a disc in the plane is two-dimensional etc.

Given fractals are not smooth and have divergent derivatives, the assumption of differentiability renders the traditional differential calculus insufficient. Hence to adequately study the behavior and properties of fractal geometries, fractional calculus was introduced. Although mathematical fractal themselves can be a fascinating subject in the abstract, and applications in physical systems make it even a more attractive system to investigate. Although there is no real fractal existing in nature (due to the infinity requirement), the exact ideal fractal can be used to study the approximate fractals found in nature. The concept of fractal can be extended in both the spatial and temporal sense. The self-similar behavior makes these objects attractive model to study system without the translational symmetry required in crystal solids. The fractional calculus can be a powerful tool to study complexity, when time scales of macroscopic and microscopic processes cannot be well separated. Since we cannot smooth out the microscopic fluctuations, the conventional Hamilton's equation of motion ceases to be adequate. Therefore, fractional calculus can be used to study several physical and biological systems, such as turbulent flow, viscoelastic materials (with memory) and phase transitions. When nonlinearity and randomness start to influence the system behavior, a new modeling strategy is necessary. Therefore, fractional time derivatives (with diverging initial values and long-time memory) and special fractal derivatives (with long-range interaction) have been used to modeling complex dynamic system and chaos (Mandelbrot, 1997)(Mandelbrot, 2004b).

1.3 Fractals in wave processes

Four groups of phenomena have been studied extensively using the fractal approach due to their inherent fractal characteristic in physics. They are 1) aggregation behavior, 2) random walks and diffusion, 3) percolation and 4) dynamical chaos. Fractal properties in wave processes have also

been studied in depth for the last few decades. The fractal nature in wave processes can exhibit themselves in different ways: 1) materials with fractal geometry serve as bulk medium for wave propagation; 2) emissions and scattering of emitters/scatterers with a fractal distribution; 3) fractal interface between a medium that interacting with waves; 4) fractal behavior arising from the nonlinearity of the wave interaction. For a bulk fractal medium, a transition from low frequency delocalized phonon states to a high frequency localized "fractons state" has been observed. The frequency spectrum of the fractons exhibits a power law distribution due to the scale invariance. This model has been used to explain the behavior of disordered media, such as amorphous polymers and resins. The peculiar fracton-phonon interaction can describe the thermal behavior of disordered media quite effectively.

Acoustic cavitation initiated the development of fractal analysis for random signals and fields. The sound emitted by the cavitation bubble in an intense sound field exhibits chaotic behavior due to its nonlinear dynamics. This concept finds further application in seismoacoustics to help predict earthquakes by studying the wave propagation behavior. A fractal drum has also captured attention when it was proposed and studied by B. Sapoval et al. By fixing a membrane to a fractal Koch Curve-like boundary made of steel, the fractal drum tried to address whether you can tell the shape of the drum by listening to its sound alone. It was found the fractal contour with Dirichlet boundary condition changes the special character of the wave field drastically. It imposes a strong spatial decay of the waveform inside fractal contour bounded cavities. Strong attenuation of vibration near the rigid edge was observed, which could be useful for damping applications. The density of states at lower frequencies was also found to be lowered, due to repulsion between states. Moreover, the localized waveform, named "fractinos" to distinguish them from fractons was found near the boundary. This fractal interface model is proposed to study binary amorphous glasses or composites where interfaces could have fractal dimension.

Several approaches have been taken to compute the eigenvalues and eigenvectors of fractal systems. For fractal drums (fractal interface), the vibration spectrum is computed using the analogy between the Helmholtz equation $\Delta\Psi = (\frac{1}{c^2})\frac{\partial^2\Psi}{\partial t^2}$ and the diffusion equation $\Delta\Psi = (\frac{1}{D})\frac{\partial\Psi}{\partial t}$. By defining the solution to be of the form $z(x,y,t) = \psi(x,y)\exp(-\frac{t}{\tau})$, the initial distribution (of

particles) $\psi_0(x,y)$ can be found with given boundary condition. Then, the next state can be found by $z_1(x,y,t=0) = z_0(x,y,t=0) - \psi_0(x,y)\int \psi_0(x,y) z_0(x,y,t=0)\mathrm{d}x\mathrm{d}y$. To study the eigenfunctions on Koch Snowflakes, Lehel mapped the unit disk to a polygon approximating the fractal conformally first and then solved a weighted eigenvalue problem on the unit disk by a spectral collection method. Most of the methods involve iteration, which make sense given the iterative nature of IFSs in generating the fractals.

Designer materials based on fractal geometry have also been investigated by several groups (Bader, 2005; Crnojevic-Bengin, 2008; Doyle, 2010; X. Huang 2010; Ito, 2010; Jacquin, 1994; Kubota, 2009; Lévy-Véhel 2010; Rammal, 1983; Schreiber, 1985; Shalaev, 2000a, 2000b, 2000c). Its irregularity and self-similarity leads to unique properties that are different from conventional periodic crystals or metamaterials, hence herald new opportunities for a range of applications.

Fractal geometry has also attracted interest in the antenna community since they allow for more compact design, with their lower resonant frequency compared to conventional antenna(Crnojevic, 2010; Potapov, 2008;) (Jacquin, 1994; Potapov & Matveev, 2010). Since fractal antennas possess self-similarity, the scaling law then indicates that they will exhibit multi-band character and high confinement of the EM field, hence high Q factors(Evelyne Lutton, 2005; X. Huang et al., 2009; Jacquin, 1994; Kubota et al., 2009; Seuront, 2010; F. Miyamaru et al., 2008; Palandoken, 2010). Studies also showed how the geometric factor and fractal order would influence the performance of the fractal resonators(Kubota 2009; Mejdoubi 2009; F. Miyamaru 2008). Besides fractal antennas, small particles fractal aggregates also demonstrate interesting behavior(Seuront, 2010; Potapov, 2010; V. Shalaev, 2000; V. M. Shalaev, 2000b, 2000c). Due to a lack of long range order yet high connectivity, the localized electric field on the fractal cluster leads to huge field enhancement, which hence leads to nonlinear optical phenomena, such as the Kerr effect, enhanced optical emission, etc.

Recently, fractal geometry (mostly H shaped units) has also been introduced in electric, magnetic and plasmonic metamaterials(X. Huang et al., 2009). With self-similarity, the structures possess multiband EM responses covering a broad frequency. By stacking fractal patterns, the structure exhibits a polarization and incidence angle-independent stop band. A fractal plasmonic metamaterials supports both TE and TM polarized Surface Plasmonic Polariton (SPP). It also possesses multiple resonances in both in-plane directions. All these unique properties present

opportunities for applications, i.e. superlens, light polarization manipulator, slow light(Ito, 2010; Jacquin, 1994; Potapov, 2010)(X. Huang et al., 2010).

There exist far fewer studies regarding phononic metamaterials with fractal geometry(Bader, 2005; Lévy-Véhel 2005). Although fractal structure has been used in architecture for acoustic purposes, more often it is for aesthetic reasons(Woloszyn, 2005). With a growing interest in phononic metamaterials with frequencies ranging from ultrasonic to heat, a general framework would be valuable to both understand the mechanisms and guide the designs. The design of framework proposed by Koh(C. Y. Koh, 2011), could be utilized to guide and unify the field.

1.4 Scale relativity

Significant progress has been made on the study of both abstract fractals, e.g. fractal groups and fractal sets, and physical and biological systems with inherent fractal properties. The question about the physical origin of fractal behavior still fascinates scientists and engineers. To address this question, we shall go back and start from the very foundation of modern physics by introducing the framework of scale relativity. Aiming to address how to reconcile the concept of quantum mechanics with the concept of general relativity, scale relativity tries to find the underlying fundamental principles for quantum mechanics' postulates and rules.

Starting from principle of relativity, i.e. "laws of physics should be of such a nature that they apply for any state of the reference system", which implies that physical quantities are defined relative to the state of a reference system. Although this principle is still philosophical at this stage, it can be implemented by three interconnecting principles in a physical system: 1) the principle of covariance, 2) the principle of equivalence and 3) the geodesic principle. It was found that if the principle of relativity itself is applied to *scales*, in addition to position, orientation and motion, the quantum mechanics can be derived/recovered from this foundation. Hence the introduction of scale variables, which represent dilation and contraction, the laws of physics could include both classical and quantum laws. This would shine light on the transition from the quantum to the classical regime.

To comply with the principle of relativity, a continuous space-time assumption is still retained. A clarification is needed here before we proceed further. "Continuity" and "differentiability" are two different concepts since a continuous curve (e.g. Koch Curve) can be nondifferentiable (in the traditional sense) anywhere. As mentioned before, by giving up the assumption of differentiability, a new generalization of the description of space-time is needed. This generalization can be considered the continuation of generalization from flat geometry to curved space-time geometry. It was found that the nondifferentiable and fractal geometry of space-time will lead to the essence of quantum physics. Besides the fractal geometry we observed in nature, the theory was also motived by another perspective from quantum mechanics itself. Feynman found that the typical quantum mechanics path (i.e. those that contribute to path integral) are nondifferentiable and fractal. The transition from quantum to classical regime was defined as the de Broglie scale $\lambda_{dB} = \hbar/p$, where p is the momentum of the particle.

Under the scale relativity framework, the generalized Heisenberg relation may be deduced from the conjectured fractal structure. By reformulating the wave function, the Schrödinger equation can be derived from this equation of motion. The general solution with a mathematical structure of Lorentz groups for both motion and scale (log-Lorentz form) is obtained for special relativity theory. An existence of a universal, unreachable lower scale in Nature is also been derived from the breaking of scale relativity symmetry at the de Broglie scale and the log-Lorentz form of scale transformation. Since this unreachable scale is invariant under dilation; it plays a similar role as vacuum light velocity for motion.

Therefore, this thesis endeavors to build on the design framework laid out by Koh using the conceptual framework from scale relativity. Starting from the geometric perspective, we strive to apply the framework on metamaterials with complex fractal geometry. In Chapter 2, we will briefly explain the original design framework and expand it further by borrowing the concepts from scale relativity. Then we will apply the framework on metamaterials based on exact self-similar like prefractal geometry in chapter 3. To deviate further from conventional well-defined symmetric structure, we studied metamaterials based on fractional Brownian motion in Chapter 4 (random fractals that are statistically similar). With the physical understanding of the framework in mind, we applied it to design mesoscopic surface acoustic devices, which can be potentially used for

"smart skin" device in chapter 5. The chaotic behavior of acoustic cavitation have also been Finally, future works would be proposed based on the unique properties of the fractal structures in Chapter 7. Finally, we conclude the thesis by highlighting the findings and a high level vision for the future of metamaterial based on for fractal geometries.

1.5 References

Bader, R. (2005). Turbulent k − model of flute-like musical instrument sound production. In L.-V. Jacques & L. Evelyne (Eds.), *Fractals in Engineering* (pp. 109–121). Springer.

Chen, H., & Chan, C. T. (2010). Acoustic cloaking and transformation acoustics. *Journal of Physics D: Applied Physics*, *43*(11), 113001.

Chin, J. Y., Liu, R., Cui, T. J., & Smith, D. R. (2009). Rapid Design for Metamaterials. In R. L. Tie Jun Cui, David R. Smith (Ed.), *Metamaterials: Theory, Design, and Applications* (pp. 61–89). Springer.

Crnojevic-Bengin, V., Radonic, V., & Jokanovic, B. (2008). Fractal Geometries of Complementary Split-Ring Resonators. *IEEE Transactions on Microwave Theory and Techniques*, *56*(10), 2312–2321.

Doyle, J. F. (2010). *Study of 1D multifunctional acoustic metamaterials. Policy*. Purdue University.

Evelyne Lutton, J. L.-V. (2005). *Fractals in Engineering:: new trends in theory and applications*. (J. Lévy-Véhel & E. Lutton, Eds.). © Springer-Verlag London Limited 2005.

Feng, Y. (2009). Compensated Anisotropic Metamaterials : Manipulating Sub-wavelength Images. In *Metamaterials: Theory, Design, and Applications* (pp. 155–181). Springer.

Gang Wang*, Xisen Wen, Jihong Wen, Lihui Shao, and Y. L. (2004). Two-Dimensional Locally Resonant Phononic Crystals with Binary Structures. *Phys. Rev. Lett.*, *93*(15), 4.

Genet, C., & Ebbesen, T. W. (2007). Light in tiny holes. *Nature*, *445*(7123), 39–46.

Goffaux, C., & Sánchez-Dehesa, J. (2003). Two-dimensional phononic crystals studied using a variational method: Application to lattices of locally resonant materials. *Physical Review B*, *67*(14).

Guenneau, S., & Ii, A. B. M. (2005). Elastic waves in arrays of elliptic inclusions. *Z. Kristallogr*, *220*, 906–911.

Ho, K. M., Cheng, C. K., Yang, Z., Zhang, X. X., & Sheng, P. (2003). Broadband locally resonant sonic shields. *Applied Physics Letters*, *83*(26), 5566.

Hong-Gang, Z., Yao-Zong, L., Ji-Hong, W., Dian-Long, Y., Gang, W., & Xi-Sen, W. (2006). Sound Absorption of Locally Resonant Sonic Materials. *Chinese Physics Letters*, *23*(8), 2132–2134.

Huang, H.-H. (2009). *Dynamic characteristics of an acoustic metamaterial with locally resonant microstructures*. Purdue University. Retrieved from

Huang, X., Xiao, S., Ye, D., Huangfu, J., Wang, Z., Ran, L., & Zhou, L. (2010). Fractal plasmonic metamaterials for subwavelength imaging. *Optics Express*, *18*(10), 10377.

Huang, X., Xiao, S., Zhou, L., Wen, W., Chan, C. T., & Sheng, P. (2009). Photonic Metamaterials Based on Fractal Geometry. In *Metamaterials: Theory, Design, and Applications* (pp. 215–245).

I, M. S., Ii, M. S. K., Iii, E. N. E., Iii, M. K., & Psarobas, I. E. (2005). Classical vibrational modes in phononic lattices : theory and experiment. *Z. Kristallogr*, *220*, 765–809.

Ito, S. (2010). *Fractal THz slow light metamaterial devices*. Oklahoma state university. Retrieved from

Jacquin, A. (1994). An introduction to fractals and their applications in electrical engineering. *Journal of the Franklin Institute*, *331*(6), 659–680.

Koh, C. Y. (Henry). (2011). *Generalized Phononic Networks: Of Length Scales, Symmetry Breaking and (Non) locality "Controlling Complexity through Simplicity."* Massachusetts Institute of Technology.

Kubota, S., Miyamaru, F., & Takeda, M. W. (2009). *Terahertz response of fractal metamaterials. 2009 34th International Conference on Infrared, Millimeter, and Terahertz Waves* (pp. 1–2). IEEE.

Li, J., & Chan, C. (2004). Double-negative acoustic metamaterial. *Physical Review E, 70*(5).

Liu, F., Cai, F., Peng, S., Hao, R., Ke, M., & Liu, Z. (2009). Parallel acoustic near-field microscope: A steel slab with a periodic array of slits. *Physical Review E, 80*(2), 026603.

Liu, Z. (2000). Locally Resonant Sonic Materials. *Science, 289*(5485), 1734–1736.

Mandelbrot, B. B. (1977). *Fractals : form, chance, and dimension* (p. 365). San Francisco : W. H. Freeman, c1977.

Mandelbrot, B. B. (1983). *The fractal geometry of nature* (p. 468). San Francisco : W.H. Freeman, c1983.

Mandelbrot, B. B. (1997). *Fractals and scaling in finance : discontinuity, concentration, risk : selecta volume E* (p. 541). New York : Springer, c1997.

Mandelbrot, B. B. (1999). *Multifractals and 1/f noise : wild self-affinity in physics (1963-1976) : selecta volume N* (p. 442). New York : Springer, c1999.

Mandelbrot, B. B. (2002). *No TitleGaussian self-affinity and fractals : globality, the earth, 1/f noise and R/S* (p. 654). New York : Springer, c2002.

Mandelbrot, B. B. (2004a). *Fractals and chaos : the Mandelbrot set and beyond : selecta volume C* (p. 308). New York: New York : Springer, c2004.

Mandelbrot, B. B. (2004b). *The (mis)behavior of markets : a fractal view of risk, ruin, and reward / Benoit B. Mandelbrot and Richard L. Hudson.* (p. 317). New York: New YOrk.

Mejdoubi, A., & Brosseau, C. (2009). Reflectance and absorbance of all-dielectric metamaterial composites with fractal boundaries: A numerical investigation. *Journal of Applied Physics, 105*(2), 024110.

Milton, G. W., & Nicorovici, N.-A. P. (2006). On the cloaking effects associated with anomalous localized resonance. *Proceedings of the Royal Society A: Mathematical, Physical and Engineering Sciences, 462*(2074), 3027–3059.

Miyamaru, F., Saito, Y., Takeda, M., Hou, B., Liu, L., Wen, W., & Sheng, P. (2008). Terahertz electric response of fractal metamaterial structures. *Physical Review B, 77*(4).

Palandoken, M., & Henke, H. (2010). Fractal negative-epsilon metamaterial. *2010 International Workshop on Antenna Technology (iWAT)*, (1), 1–4.

Pennec, Y., Vasseur, J. O., Djafari-Rouhani, B., Dobrzyński, L., & Deymier, P. a. (2010). Two-dimensional phononic crystals: Examples and applications. *Surface Science Reports, 65*(8), 229–291.

Potapov, a. a., Gil'mutdinov, a. K., & Ushakov, P. a. (2008). Systems concept and components of fractal radio electronics: Part I. Development stages and the state of the art. *Journal of Communications Technology and Electronics, 53*(9), 977–1020.

Potapov, a. a., & Matveev, E. N. (2010). Fractal electrodynamics. Scaling of the fractal antennas based on ring structures and multiscale frequency-selective 3D media and fractal sandwiches: Transition to fractal nanostructures. *Journal of Communications Technology and Electronics, 55*(10), 1083–1101.

Rammal, R. (1983). Nature of eigenstates on fractal structures. *Physical Review B, 28*(8), 4871–4874. doi:10.1103/PhysRevB.28.4871

Schreiber, M. (1985). Fractal character of eigenstates in weakly disordered three-dimensional systems. *Physical Review B, 31*(9), 6146–6149.

Seuront, L. (2010). Self-Similar Fractals. In *Fractals and Multifractals in Ecology and Aquatic Science* (pp. 25–98). CRC press Taylor & Francis Group.

Shalaev, V. (2000). Surface-Enhanced nonlinear optical phenomena. In V. M. Shalaev (Ed.), *Nonlinear optics of Random Media: Fractal composites and metal-Dielectric Films* (pp. 45–50). Springer.

Shalaev, V. M. (2000a). *Nonlinear optics of Random Media: Fractal composites and metal-Dielectric Films*. (V. M. Shalaev, Ed.) (volume 158., pp. 1–147). Springer.

Shalaev, V. M. (2000b). Random Metal -Dielectric films. In *Nonlinear optics of Random Media: Fractal composites and metal-Dielectric Films* (pp. 139–141).

Shalaev, V. M. (2000c). Small-Particle Fractal Aggregates. In *Nonlinear optics of Random Media: Fractal composites and metal-Dielectric Films* (pp. 21–73). Springer.

SHENG, P., MEI, J., LIU, Z., & WEN, W. (2007). Dynamic mass density and acoustic metamaterials. *Physica B: Condensed Matter*, *394*(2), 256–261.

Sheng, P., Zhang, X. X., Liu, Z., & Chan, C. T. (2003). Locally resonant sonic materials. *Physica B: Condensed Matter*, *338*(1-4), 201–205.

Woloszyn, P. (2005). Acoustic diffraction patterns from fractal to urban structures : applications to the Sierpinski triangle and to a neoclassical urban facade. In *FRACTALS IN ENGINEERING* (pp. 97–108). Springer-Verlag London.

Xiao, X., Wu, J., Miyamaru, F., Zhang, M., Li, S., Takeda, M. W., … Sheng, P. (2011). Fano effect of metamaterial resonance in terahertz extraordinary transmission. *Applied Physics Letters*, *98*(1), 011911. doi:10.1063/1.3541652

Yang, S., Page, J., Liu, Z., Cowan, M., Chan, C., & Sheng, P. (2002). Ultrasound Tunneling through 3D Phononic Crystals. *Physical Review Letters*, *88*(10), 1–4. doi:10.1103/PhysRevLett.88.104301

Zhang, S. (2010). *ACOUSTIC METAMATERIAL DESIGN AND APPLICATIONS*. University of Illinois at Urbana-Champaign. Retrieved from

Zhu, J., Christensen, J., Jung, J., Martin-Moreno, L., Yin, X., Fok, L., … Garcia-Vidal, F. J. (2010). A holey-structured metamaterial for acoustic deep-subwavelength imaging. *Nature Physics*, *7*(1), 52–55. doi:10.1038/nphys1804

2. The General Framework for Metamaterials

2.1 Design framework

Phonons are present in all media with a general frequency range that covers 12 orders of magnitude in scale and with up to 3 polarization degrees of freedom. The rich and complex behavior of phonons presents both challenges and opportunities to manipulate and control them. In this chapter, we set out the framework to address the question of how to optimize the phononic behavior of metamaterials with the same set of governing principles.

The framework builds upon the mathematical structure of group theory and concepts of symmetry breaking, which illuminate the phononic behavior in and across different media. By pointing out the importance of relevant length scale, the feasibility of using the continuum approximation in forming the guideline is established given that the classical limit still holds even at the 10-100nm length scale.

Starting from the conservation equations, i.e. continuity of mass and momentum flow, the general equations of classical waves can be developed. For some conserved quantity, M(t), in some region of space Ω, with a boundary $\partial\Omega$, and boundary gradient normal n, the conservation principle states as (C. Y. Koh, 2011)

$$\frac{dM(t)}{dt} = R(t) + S(t)$$

$$where M(t) = \int_{\Omega} \rho(\vec{r},t)dV, R(t) = \int_{\partial\Omega} \vec{F}(\vec{r},t) \bullet ndS, S(t) = \int_{\Omega} s(\vec{r},t)dV,$$

$$\frac{dM(t)}{dt} = R(t) + S(t)$$

where $M(t) = \int_{\Omega} \rho(\vec{r},t)dV$, $R(t) = \int_{\partial\Omega} \vec{F}(\vec{r},t) \cdot ndS$, $S(t) = \int_{\Omega} s(\vec{r},t)dV$,

F(r,t) and S (r, t) represent the corresponding flux of the quantity, and source (sink) in the region respectively. If the mass and linear momentum are substituted in the equation for elastic waves, the elastic wave equation can be recovered. Moreover, this approach provides additional insight through correct identification of the processes that lead to the development of the wave equation.

Since the polarization states of phonons pose a major challenge, understanding their physical origin is crucial. Phonons are a simple form of Goldstone modes, which result from breaking the

continuous symmetry of the medium. The atoms form a discrete array with translational symmetry such that moving along by lattice spacing leaves the properties invariant. Each such broken symmetry will give rise to a maximum of one new mode. It can be proven that the most general classification of polarization eigenstates is determined by the underlying symmetry of the medium. Therefore, when the inhomogeneities reach the length scale that can be sampled by the wave (i.e. breaking the apparent continuous/homogenous symmetry/medium), the phononic spatial dispersion behavior would change. Hence, the relevant length scale is determined by the inhomogeneity in the medium and the wavelength. Since there is no absolute relevant length scale, the distinction between artificial structure and bulk crystal become itself artificial and can be removed.

Group theory studies the linear algebraic structure of groups and has several applications in physics and chemistry since it can transform complex symmetry operation into simple linear algebra. By connecting symmetry operations to matrices and basis functions, the representation theory can shine light on properties of physical systems. Group theory dictates that the spatial symmetries of the particular phonon eigenmodes have to be an irreducible representation (irreps) of the isotropy group of the wave-vector of interest. While the global constraints delineate the possible phonon eigenmodes a material system might have, knowledge of the microscopic dynamics in the dispersion relation is necessary for designing in desirable functionality. The most common desirable property to explore is to find the condition that determines the formation of wide complete spectral gap. Bragg scattering at the Brillion Zone is a well-known mechanism to generate a bandgap in a periodic structure along a particular direction. Recently, local resonance of a material element has been also identified as a distinct gap opening mechanism. A closer study of the eigenmodes in particular structures reveals that both mechanisms are manifestation of a more general notion, that of *avoided crossing*. Avoided crossing can be defined as "detuned crossing" where the eigenvalues (of the Hamiltonian) remain different due to coupling between states). One typical example is the diatomic system, where the potential energy curves do not cross each other(Redding, 1973; Sun L. et al, 1992). An intuitive way to understand this can be achieved using the Schrodinger equation and its wave functions. If the two original states ψ_1 are ψ_2 independent of each other (i.e. exist in orthogonal subspace), they would cross each other and remain an exact solution of the Schrodinger equation without being perturbed. However, if the two states ψ_1 are ψ_2 are not independent of each other and have some common properties, the system

will find admix them in certain way (i.e. coupling might happen). And the common properties can be manifested in the symmetry of the state since it is the most general spatial properties, regardless of the electron state. No longer the exact solution of the Schrodinger equation, ϕ_1 and ϕ_2 - the diabatic solution- can be used to represent ψ_1 are ψ_2 – adiabatic solution. Since the coupling between ϕ_1 and ϕ_2 could perturb the system, the resultant adiabatic solution will not cross(Raoul B, et al, 2011). A similar principle also applies in the metamaterial system, avoided crossing happens between eigenmodes with the same irreps. Therefore, by identifying the symmetry of medium, avoided crossings can be predicted and controlled to form bandgaps.

Avoided crossing occurs at all length scales and depends on the relevant isotropy groups of the wave vector. The interaction strength between modes influences the extent of spatial dispersion (non-locality), i.e. a spatially localized wave usually has a flat dispersion curve. The extent of non-locality is influenced by geometry (e.g. the mechanics connectedness of a medium), and the relevant impedance contrast of the different constituents, which control the group velocity along the bands. To further illuminate the relation of the physical topology of a structure to its phononic properties, the concept of **"dynamical mechanical band"** is introduced to classify the nature of phononic behavior: *extended and tight-biding lattice classes*. This simplified concept is derived from the knowledge that dynamic impedance contrast is the key factor that determines phononic behavior at the interface between constituents.

In sum (Figure 2.1), this framework starts from conservation principle to drive the governing equations. It utilizes the mathematical construct of group theory to establish the global principles governing the possibilities of band dispersion. Using the concept of broken symmetry, the eigenmodes are classified according to representation theory of the groups. Avoided crossing is the fundamental mechanism for opening a spectral gap, and it can only happen between eigenmodes with the same symmetry group with respect to the relevant wave vector. Therefore, it shows that the generalized requirement for gap opening is i) choice of the correct plane or space groups symmetry for scattering motifs and their lattice; ii) controlling the set of avoided crossings. While the interaction strength for a particular avoided crossing depends on several characteristics, fortunately, they can be collected under one parameter, the so called "dynamic mechanical bond" to simplify the design principle, the Moreover, by taking a variational approach, this framework

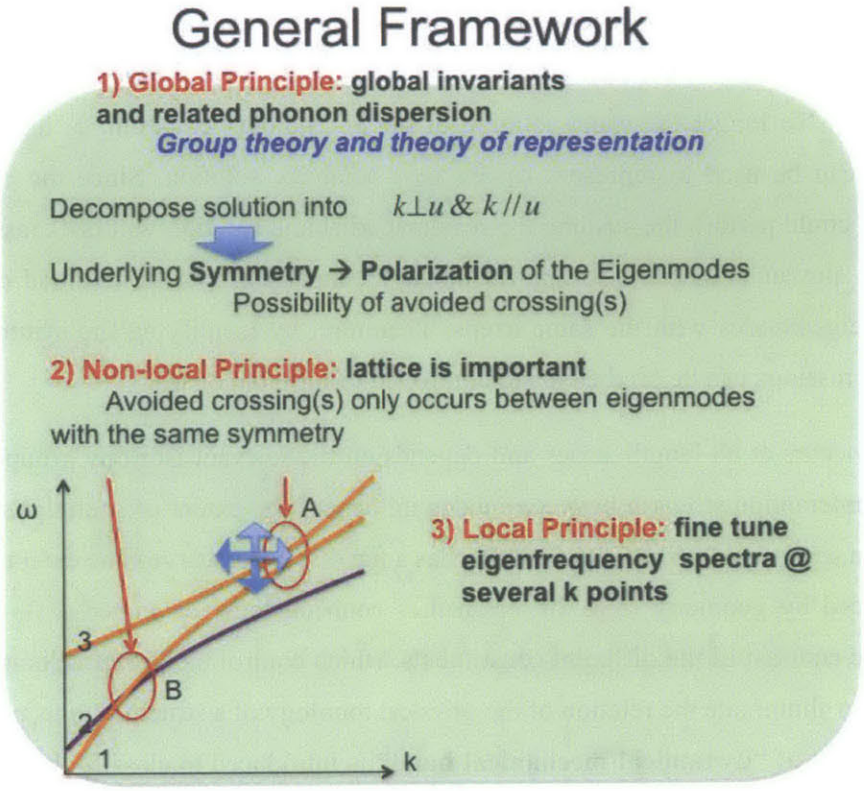

Figure 2.1 Schematic of the design framework with all the 3 main principles listed. The dispersion plot shows 3 bands, where Mode 1 and 3 have the same symmetry group with respect to k and an avoided crossing occurs at A. Band 1 and 2 can cross, as at B since they have different symmetry with respect to k.

proves to be a powerful tool to control and design the phononic medium to achieve desirable properties tailored towards specific applications. To verify our design framework, we next apply the framework to study conventional metamaterials systems detailed in Appendix A.

2.2 Review of scale relativity

As the physical approaches moving from descriptive modeling to predictive theory founded on basic principles, physical science evolved through several stages, e.g. Ptolemy's model to Newton's theory to Einstein's general relativity and quantum theory. Scale relativity theory aims to pave the way to unifying the quantum and relativity concept on the basis of first principles. In the framework of scale relativity, the quantum field becomes the manifestation of geometry of space-time, which now includes a scale parameter. (Laurent Nottale, 2011). Using the principles and construct of relativity, scale relativity introduced new operators to account the nondifferentiability of the space-time-scale. A more detailed review of the major principles and

derivation process is included in Appendix B. By giving up the differentiability of space-time, scale relativity redefine derivatives in order to not give up the partial differential equation. For system where nondifferentiability can be neglected, the standard differentiable physics would be sufficient. However, nondifferentiability cannot be ignored with small and large length scale, as well as complex mesoscopic system. To construct the scale relativity theory, the laws of scale at a given point and instant was first constrained by the principle of relativity. Then the laws of motion are derived to include the effects of nondifferentiability and fractality. After that, the law of coupling between scale and motion are developed.

As mentioned in chapter 1, the length of the fractal curve can be estimated using $\mathcal{L}(s,\varepsilon) = s(\frac{\lambda}{\varepsilon})^{\tau}$, where s is a renormalized curvilinear coordinate along the fractal curve and the exponent is defined as $\tau = D_F - D_T$, where D_F and D_T are the fractional and topological dimension respectively. To carry out the scale transformation, an infinitesimal dilation operator is derived as $\widetilde{D} = \varepsilon\frac{\partial}{\partial ln\varepsilon}$, which shows lnε as the natural variable for the resolution. The simplest equation for $\mathcal{L}$ under scale transformation is achieved when it is a function of $\mathcal{L}$ only, i.e. $\frac{\partial \mathcal{L}(s,\varepsilon)}{\partial ln\varepsilon} = \beta(\mathcal{L})$,

Defining $\beta(\mathcal{L})$=a+b$\mathcal{L}$+..., we have$\mathcal{L}(s,\varepsilon) = \mathcal{L}_0(s)\{1 + \zeta(s)\left(\frac{\lambda}{\varepsilon}\right)^{\tau}\}$. Therefore the projection of $\mathcal{L}$ on any direction can be written as $X(s,\varepsilon) = x(s)\{1 + \zeta_x(s)\left(\frac{\lambda}{\varepsilon}\right)^{\tau}\}$. The differential of the projection can be written as $dX = dx + d\xi$, where dx is a classical differential element and $d\xi \propto$

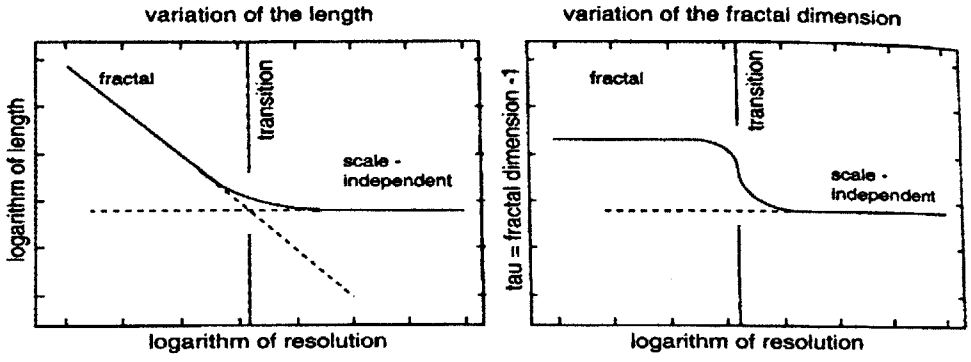

Figure 2.2: Fractal length and fractal dimension for self-similar fractals. The two figures show the scale dependence of a length of a fractal and the fractal dimension in the case of inertial scale laws (i.e.β ($\mathcal{L}$) =a+b$\mathcal{L}$+...,), which are solutions of simple first order scale differential equations. It transforms from scale dependent at small scale to scale-invariant large scale. Figure reproduced from (L. Nottale., 2011)

dx^{1/D_F}. It is obvious that the dx corresponds to the differentiable element while $d\xi$ captures the nondifferentiability. It is easy to see that when (i) for $\varepsilon \ll \lambda$, $\mathcal{L}(s,\varepsilon) \approx \mathcal{L}_0(s)\{\zeta(s)\left(\frac{\lambda}{\varepsilon}\right)^{\tau}\}$, $\mathcal{L}$ follows a power law fractal curve, when (ii) for $\varepsilon \gg \lambda$, $\mathcal{L}(s,\varepsilon) \approx \mathcal{L}_0(s)$ is given by a scale invariant, as shown in Figure 2.2.

The scale symmetry is spontaneously broken by the very existence of standard symmetries, (e.g. translation, rotation) or the introduction of constant a in $\beta(\mathcal{L})$. The symmetry breaking is achieved by domination of one law over the other when moving through different length scales. And this transition is identified with the Einstein-De Broglie scale, which conceptualize the quantum to classical transition as being fractal to nonfractal transition in scale space(L Nottale, 1995).

The relationship can be further generalize by including even higher order term, e.g.. $\frac{\partial \mathcal{L}(s,\varepsilon)}{\partial ln\varepsilon} = a + b\mathcal{L} + c\mathcal{L}^2$ ..., which would leads to two transitions to scale independence (both large and small scales) as shown in Figure 2.3.

By introducing a complex value of b (or fractal dimension) such that , we have $\mathcal{L}(\varepsilon) = \mathcal{L}_0\{1 + \left(\frac{\lambda}{\varepsilon}\right)^{\tau}[1 + bcos(\omega ln\varepsilon)]\}$.

which exhibit log-periodic behavior, like a stationary wave in scale-space.

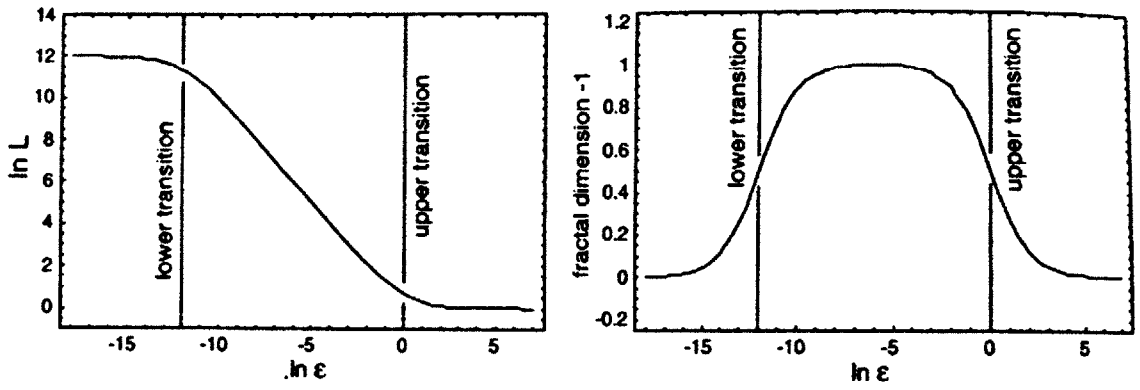

Figure 2.3 Fractal length and fractal dimension for self-similar fractals: two transitions. The two figures show the scale dependence of a length of a fractal and the fractal dimension in the case of inertial scale laws, which are solutions of simple first order scale differential equations. It transforms from scale dependent at small scale to scale-invariant large scale. Figure reproduced from (L. Nottale., 2011)

With the scale transformation (ε→ε') defined, a complex operator $\frac{\hat{d}}{dt} = \frac{\partial}{\partial t} + \mathcal{V} \cdot \nabla - i\mathcal{D}\Delta$ is introduced to deal with the nondifferentiability by replacing d/dt. Here $\mathcal{V}$ is differentiable part of the complex velocity field and $\mathcal{D}$ characterizes the amplitude of fractal fluctuation. This operator enables us to recover the form of physical laws as their differentiable counterpart. Starting from Newton's equation of dynamics $\mathrm{m}\frac{\hat{d}}{dt}\mathcal{V} = -\nabla\phi$ and defining $\varphi = e^{iS/2m\mathcal{D}}$, we obtain

$$\mathcal{D}^2\Delta\varphi + \mathrm{i}\mathcal{D}\frac{\partial}{\partial t}\varphi - \frac{\phi}{2m}\varphi = 0, \qquad (1)$$

When $\hbar = S_0 = 2m\mathcal{D}$, standard Schrödinger equation can be recovered(L. Nottale, 1998). Hence there is natural link between the Compton relation and the Schrödinger equation, where $\mathcal{D}$ can be

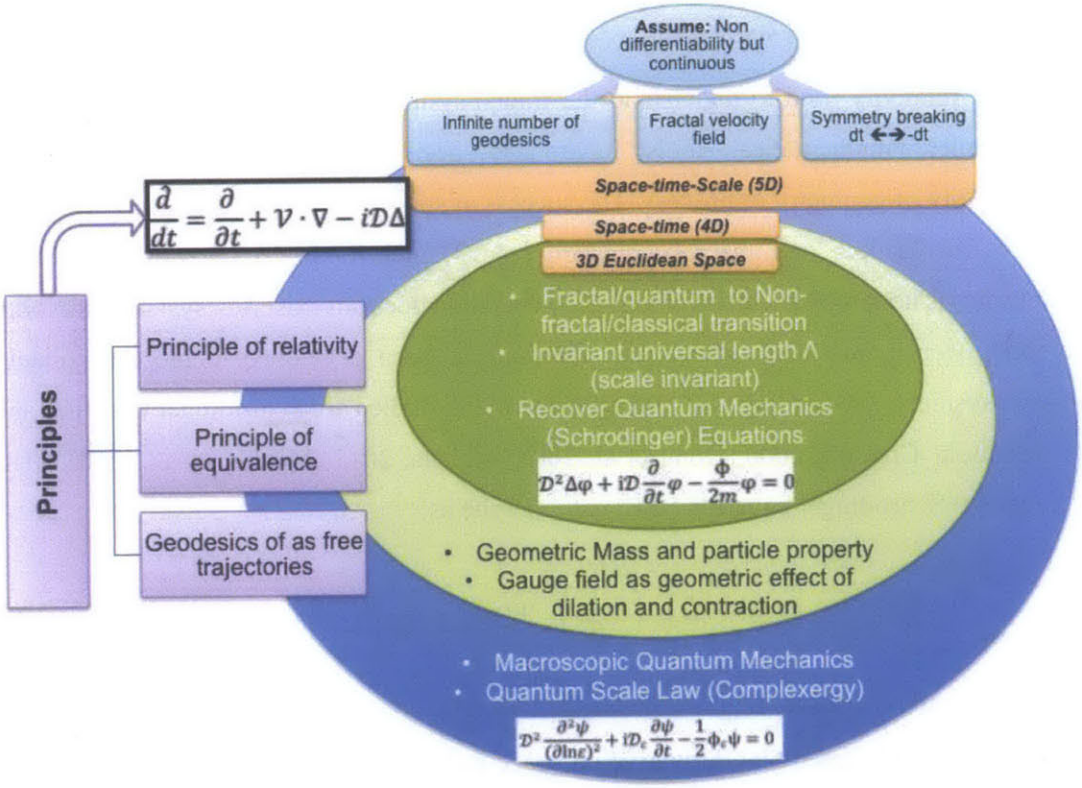

Figure 2.4: Fractal length and fractal dimension for self-similar fractals: two transitions. The two figures show the scale dependence of a length of a fractal and the fractal dimension in the case of inertial scale laws, which are solutions of simple first order scale differential equations. It transforms from scale dependent at small scale to scale-invariant large scale.

defined by the fractal-nonfractal transaction. Hence the quantum-type mechanics (in regard to laws of motion) in space-time can be derived from the simplest possible scale laws constrained by the scale relativity principle and law of motion. Hence, scale relativity theory provides a new way of looking at the scaling laws the physical laws, its main elements can be summarized in Figure 2.4.

Besides the satisfaction derived from finding the underlying link between geometry (in a broad space-time-scale sense), the theory also has other interesting applications. Quantum behavior might be observed in macroscopic (in traditional sense) for irreversible reflection process that meet the condition described by quantum like tool. The analogy between medium-scatter and space (or space-time) object holds potential for studying material physics to understand fundamental physics (Laurent N, 2005, 2011)

2.3 Physics of fractional operator

While the scale relativity tried to understand the fractal system from the foundation of modern physics principles, mathematical tools have also been developed to deal with the nondifferentiability of geometry or process. The success of statistical physics relies largely on the separation of microscopic and macroscopic processes(Daniel R, 1997). However, ordinary statistical physics is no longer adequate when such separation does not exist (i.e. system with long-time memory). Hence fractional differential equation has been developed to more accurately describe such systems. Two of the most common equations studied are Schrodinger equation and diffusion equation(Cresson, 2000; Dong et al, 2007; Mahata, 2013; Muslih, et al, 2010). The general fractional Schrodinger equation (fSE) can be write as

$$ {}_0^C D_t^\alpha \Psi(r,t) = \frac{i^\alpha}{\hbar} \breve{D}_{\alpha\beta} \left(\hbar \frac{\partial}{\partial x}\right)^\beta \Psi(\mathrm{r},\mathrm{t}) - \frac{i^\alpha}{\hbar} V(r) \Psi(\mathrm{r},\mathrm{t}) $$

where ${}_0^C D_t^\alpha$ is Caputo derivative, $\breve{D}_{\alpha\beta}$ is a new quantum diffusion constant. By varying the value of α and β, we can apply fractional derivative on space and or time depending on the system we study(Bruce W. et al., 2003).

For diffusion equations, the most general transport equation can be written as $D_t^\beta [u(x,t)] - \frac{t^{-\beta} u_0}{\Gamma(1-\beta)} = R^\alpha u(x,t)$

Where D_t^{β} is the fractional time derivative (non integer) operator, R^{α} is the fractional space derivative. Similarly, we can simplify it by applying fractional operative on just space

$(\frac{\partial P(x,t)}{\partial t} = R^{\alpha}[P(x,t)])$ or just time $(D_t^{\beta}[P(x,t)] = D\frac{\partial^2 P(x,t)}{\partial^2 x})$.

The fractional calculus is closely associated with chaotic system. "Chaos can be defined as a sensitive dependence of the solutions to a set of nonlinear, deterministic, dynamical equations, on initial condition". Chaos and noise could be source of confusion. It is well known that chaotic solution can result from a nonlinear system with only a few dynamical variables. Therefore, chaos (i.e. erratic behavior of limited predictability) arises from nonlinear deterministic interaction in an isolated dynamical system. However, noise results from environmental effect on a system since the environment is assumed to have an infinite number of elements coupled to the system(Bruce W et al., 2003).

Fractional random walks will impose an inverse power law memory on system response for a random process. As a signature of fractal statistical process, the inverse power law spectrum can be related to the fractal dimensions of the time using its index. Extending the modal to continuum results in Fractional Brownian Motion (fBM), which is Gaussian but non-Markovian. By applying fractional in time while second order in space, fBM with long-term memory can be modeled for their stochastic dynamical process.

2.4 Generalized geometric design framework

By utilizing the group concept and representation theory, Koh's design framework better revealed the underlying physical principles that govern the wave dispersion behavior in metamaterials, especially phononic metamaterials. Realizing the potential of the geometric approach towards designing materials, a more generalized framework can be developed to expand the horizon of novel designer materials. Inspired by the ubiquitous fractals-like geometry of in nature, scale transformation needs to be included in the framework since fractal geometries show structures at all scales. By giving up the nondifferentiability of the geometries in order to describe the roughness of fractal system/process, scale relativity must be added to the framework in addition other conventional transformations, such as translation, rotation etc. Although this framework employed fractal as a more abstract concepts, it can be helpful to understand fractal material system given

the analogy between medium-scatter and space (or space-time)-object. Based on this foundation, we can develop a generalized framework that would have potential to expand the horizon for designer materials, e.g. those based on complex geometries, such as fractals.

For a material system with fractal-like geometry, its properties must undergo a fractal-nonfractal transition due to the relationship $X(s,\varepsilon) = x(s)\{1 + \zeta_x(s)\left(\frac{\lambda}{\varepsilon}\right)^{\tau}\}$. For natural system with multiple fractal dimensions at different scale intervals (i.e. multifractal)- e.g. the Coast of Britain, the material may go through several transitions $X(s,\varepsilon) = x(s)\{1 + \left(\frac{\lambda_0}{\varepsilon}\right)^{\tau_0} + \left(\frac{\lambda_1}{\varepsilon}\right)^{\tau_1}\}$, as shown in Figure 2.5. If we define the action $\mathcal{S} = 2m\mathcal{D} = \hbar$, one transaction would correspond to the de Broglie relationship in standard quantum mechanics, where $\lambda_{dB} = \hbar/p$, (p is the momentum). Since for phonons, the crystal momentum is defined as $\hbar k$, where k is the wave number for phonons, we have $\lambda_{dB} = 1/k$. Therefore when a fractal geometry comprised of crystalline materials, a transition from the quantum to the classical should occur close to the atomic space should be observed. This is consistent with our observation in the Koh framework, where the displacement can be conceptualized as a smooth and continuous field. Hence we might observe the scale independence behavior resulting from the translational and other symmetries common in classical metamaterials.

Similarly, for materials that still retain translational symmetry yet with fractal-motifs (in their unit cell), this fractal to nonfractal transition could be manifested. Hence Koh's framework would still be applicable when the wavelength is comparable to the unit cell. However when the wavelength is much smaller than the unit cell, the standard Hamiltonian and Schrodinger equation would not be sufficient. For example, power-law behavior is common in fractal geometry and processes, yet it cannot be a general solution to the standard linear time independent Schrodinger equation. To account to the nondifferentiability of the geometry, we could generalize the physical law by redefining the derivatives and integral to maintain the structure of governing equations.

This generalized process can be achieved in a different way: develop the fractional calculus where the order of derivatives and/or integrals do not have to be integer anymore; or complex velocity can be introduced with a modified time derivative operator, as scale relativity did. The similar properties achieved in both approaches maybe a manifestation of the underlying link between these two views.

Hence, the general design framework presented could be tested on both exact-self similar fractal-like samples and random fractal samples. The numerical and experimental study would verify the theoretical construct and serve as general guideline for designing novel engineering materials. Furthermore, by introducing fractal geometry to metamaterials, it expended the repertoire for materials scientists. It might also be helpful to understand natural materials given their ubiquitous existence in nature.

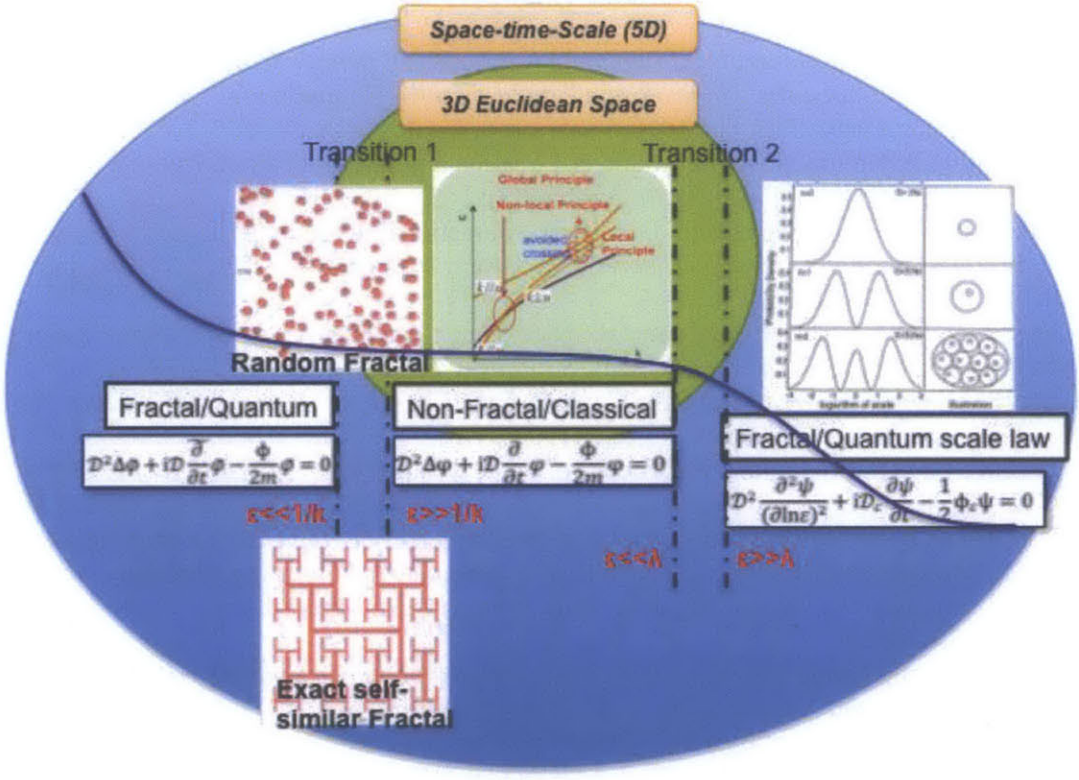

Figure 2.5: Schematics of generalized design framework

2.5 Reference

Bruce J. West Mauro Bologna, P. G. (2003). *Physics of Fractal Operators* (pp. 1–354). Springer. Retrieved from http://www.springer.com/physics/complexity/book/978-0-387-95554-4

Cresson, J. (2000). *Scale Calculus and the Schordinger equation by. Mathematics Subject Classification.* — (pp. 1–55).

Daniel H. Rothman, S. Z. 9780521607605: A. com. B. (1997). *Lattice-Gas Cellular Automata: Simple Models of Complex Hydrodynamics*. Cambridge University Press;

Dong, J., & Xu, M. (2007). Some solutions to the space fractional Schrödinger equation using momentum representation method. *Journal of Mathematical Physics*, *48*(7), 072105. doi:10.1063/1.2749172

Koh, C. Y. (Henry). (2011). *Generalized Phononic Networks: Of Length Scales, Symmetry Breaking and (Non) locality "Controlling Complexity through Simplicity."* Massachusetts Institute of Technology. PhD Thesis

Mahata, A. K. (2013). On Fractional Schrödinger Equation and Its Application. *International Journal of Scientific & Engineering Research*, *4*(2), 1–5.

Muslih, S. I., Agrawal, O. P., & Baleanu, D. (2010). A Fractional Schrödinger Equation and Its Solution. *International Journal of Theoretical Physics*, *49*(8), 1746–1752. doi:10.1007/s10773-010-0354-x

Nottale, L. (1995). Scale Relativity and Fractal Space-Time : Applications to Quantum Physics , Cosmology and Chaotic Systems ∗. *Chaos, Solitons & Fractals,*, *7*(6), 877–938.

Nottale, L. (1998). Scale relativity and Schrödinger's equation. *Chaos, Solitons & Fractals*, *9*(7), 1051–1061. doi:10.1016/S0960-0779(97)00190-2

Nottale, L. (2005). Fractality Field in the Theory of Scale Relativity. *PROGRESS IN PHYSICS*, *1*(7), 12–18.

Nottale, L. (2011). *Scale Relativity And Fractal Space-Time: A New Approach to Unifying Relativity and Quantum Mechanics* (p. 764). World Scientific Publishing Company. Retrieved from http://www.amazon.com/Scale-Relativity-And-Fractal-Space-Time/dp/1848166508

Raoul Bourquin, Vasile Gradinaru, G. A. H. (2011). *Non–Adiabatic Transitions near Avoided Crossings: Theory and Numerics* (pp. 1–24). Retrieved from http://www.ma.utexas.edu/mp_arc/c/11/11-67.pdf

Redding, R. W. (1973). A MODEL CALCULATION ON THE AVOIDED-CROSSING PROBLEM FOR DIATOMIC MOLECULE BOUND STATES. Retrieved from http://kb.osu.edu/dspace/handle/1811/15998

Sun, J. Q., & Lin, C. D. (1992). Diabatic states in the avoided crossing region. *Journal of Physics B: Atomic, Molecular and Optical Physics*, *25*(7), 1363–1373. doi:10.1088/0953-4075/25/7/008

3.Metamaterials based on Deterministic Fractal

3.1 Overview of deterministic fractal

As mentioned before, a fractal can be derived as a secondary property from a continuous and nondifferentiable manifold with scale divergence in the limit resolution $\varepsilon \rightarrow 0$. It does not necessarily imply self-similarity at different scales; vice versa, self-similarity at different scale does not necessarily mean fractal geometry. One typical example is a coastline, which is not self-similar (even statistically) yet is still a fractal(Mandelbrot, 1983). Hence strictly speaking self-similar fractals are a more restrictive view of fractals. However, we shall focus on self-similar fractals given their potential for broadband and subwavelength behaviors that we are particularly interested in.

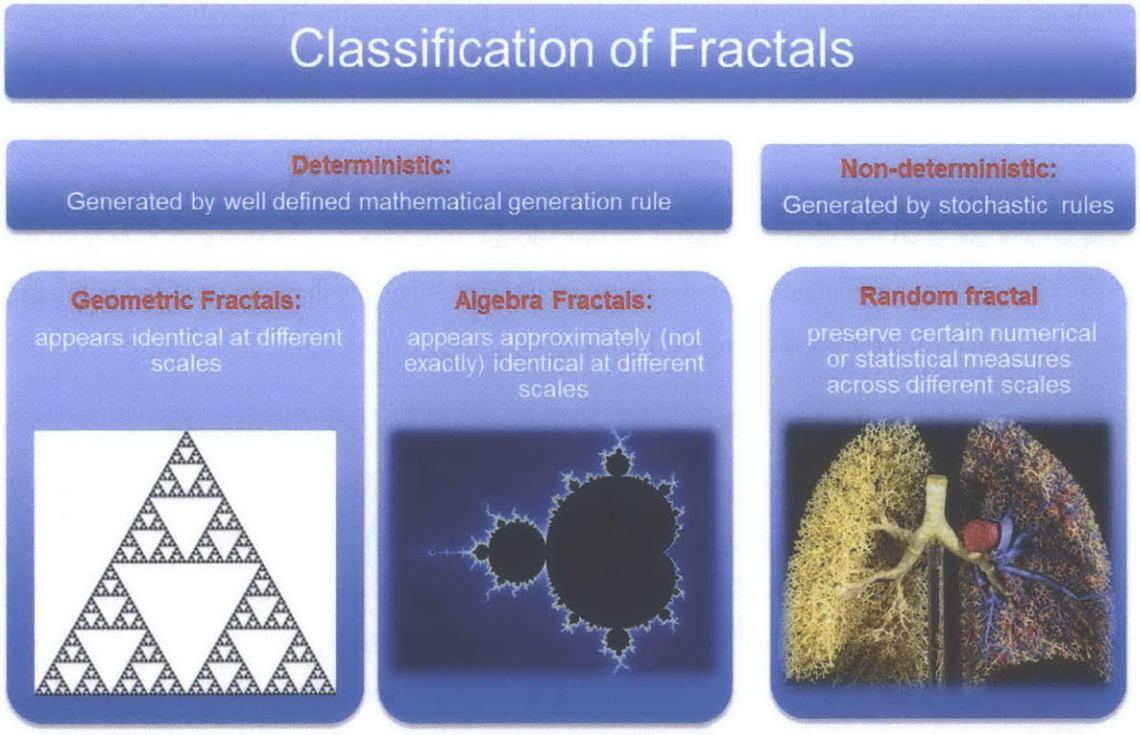

Figure 3.1: One common way of classifying fractals according to their correlation at different scales. The examples shown below are Sierpinski triangle, Mandelbrot set and Lung branching. Many natural objects do display some degree of "statistical" self-similarity over a limited range of spatial or temporal scales, for example, lung branching shows self-similarity over 14 dichotomies.

Self-similar fractals can be divided into deterministic and random fractals according to their correlation relationship. Deterministic fractals can be further divided into geometric and algebraic fractals(Edgar, 2007). Geometric fractals are composed of several scaled down and related copies, hence they can be created by repeating a process infinitely many times. The most common geometric fractals created are Sierpinski Triangle and the von Koch snowflake. Algebraic fractals can be created by calculating an equation (i.e. nonlinear iteration map) many times, such as Julia Set and Mandelbrot Set (Wareham et al., 2010). Their development was accelerated after the invention of personal computer. Both fractals are determined by their initial condition and usually exhibit exact self-similarity or semi self-similarity. Random fractals have an additional element of randomness and are commonly used to model natural phenomenon. However, randomness is not equivalent to chaos, which itself is deterministic process(Kaye, 2008). Random fractals usually have the property of statistical self-similarity, meaning they show similar statistical properties at different scales.

Deterministic fractals would be a natural candidate to start with given that their geometric symmetry elements in the conventional sense are relatively easy to identify. We will first study a system where the scatterer phase is fractal-like geometry with high connectivity, e.g. H tree; and then we will study a metamaterial system where the interface between the scatterers and the matrix phase is the space filling fractal curve - Hilbert Curve.

3.2 Theoretical Study of Metamaterials based on H tree motifs

A fractal using H pattern has been studied and investigated in an electromagnetic metamaterials based on fractal geometry(Huang et al., 2009)(Hou et al., 2008). Their geometrical properties enable quite diverse applications. Since the distance between the center and all the distal points are equal, the H tree prefractal has been used as a clock distribution network for routing timing signals to all parts of a chip in VLSI design(Ullman, 1984)(Burkis, 1991). Similarly, microstrip antenna arrays with H tree geometry have also been used to enable radio signals to read each individual antenna with equal propagation delay (Yang et al., 2004). Since it is a more space efficient way of interconnecting processors than conventional binary tree layout, H tree geometry has been used in parallel supercomputing(Browning, 1980).

The H tree curve in strictly mathematical sense is a space-filling curve with Hausdorff dimension of two. The planar H tree curve can also be extended in 3 dimensions by adding branches in 3rd directions, which might be used as artificial building blocks, e.g. atoms, in designing novel metamaterials(Hou et al., 2008). Furthermore, the bifurcation geometries in both trees and river network have been investigated as an optimized geometry for distribution given certain constrain(Leopold, 1971) . For trees, it has been proposed that bifurcation at the stem is necessary result of local biomechanical stress and constrain(Leopold, 1971). Recently, the Htree geometry is found to be a result of resistance minimization principle that allows the volume-to-point flow to continue its outward expansion(Bejan, 2000). Further study has been conducted to study the diamter, branch angle and branch (a)symmetry to find the opitmized geometries for its thermal conductivities and resistence (Liu, 2005; Wang et al., 2007). 2D plate with finte thickness H tree patten has also been used to model the thermal conductivity of vascular branch our epidermal layer(Bejan et al., 2013).

3.2.1 Theoretical study of 2D fractal system based on H tree motif

Since the H tree can only be implemented at a finite level in any real physical system, the level of the iteration is varied to study how the number of generations influences the behavior. Furthermore, other parameters such as the thickness/length ratio and materials properties has also been investigated, as listed in Table 3.1 and Figure 3.2.

Table 3.1: H patterns geometric parameters for system studied, where t and l is the thickness and length as defined in Figure 3.2 below.

Sample Name	Level	t/l	Fill ratio (Htree)	Comments
H2	N = 2	t/l = 1/9	0.2125	only for first level, t is constant
H2_thin	N = 2	t/l = 1/18	0.10625	only for first level, t is constant
H3	N = 3	t/l = 1/9	0.3575	only for first level, t is the same for N =1,2 and t is halved for N = 3
H4	N = 4	t/l = 1/9	0.413	only for the first level, t is the same for N = 1,2 and t is halved for each iteration afterwards

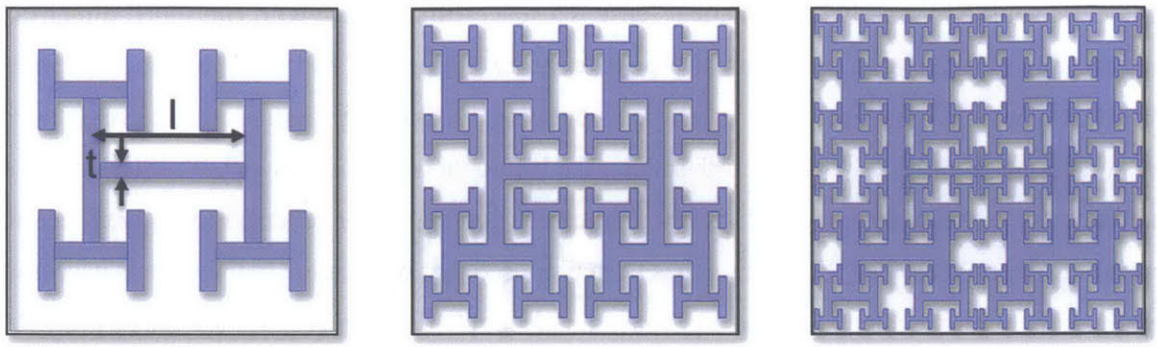

Figure 3.2: Schematics of H tree based binary system unit cell where blue is the scatterer phase and white is the matrix phase, where thickness l and length ratio t are indicated. The symmetry in all units is p2mm.

To define the physics, H like patterns (blue region) are set as scatterers while the background (white region) is set as the matrix material. The dispersion curve is then calculated from MATLAB by exporting the file from COMSOL and sweeping the k vector over the BZ.

Along the ΓX direction, there is mirror plane symmetry along X-axis (Mx) and identity (E), the displacement is either symmetric (mode 2) or antisymmetric (mode1) with respect to the wave vector $k_{\Gamma X}$. The polarizations remain the same along the band. For bands with different symmetry (with respect to $k_{\Gamma X}$,) they can cross each other without avoided crossing happening, (e.g. between band 2 and 3 at 0.7 $k_{\Gamma X}$. Along the XM direction, the symmetry is M_y and E, and the displacement fields are again either symmetric or antisymmetric with respect to the wave vector k_{XM}.

At point X, avoided crossings happen between mode 1(M1) and 9(M9) as well as mode 3(M3) and 11(M11) since their modes are symmetric and antisymmetric with respect to mirror plane. Hence the bands that appear to bound the bandgap are not necessarily the bands that are interacting to form the gap.

3.2.1.1 Plane Strain vs. Plane Stress

We computed for both plane stress and plane strain conditions for H2 pattern. Plane stress occurs for thin samples, where $\sigma_z = 0$. And plane strain occurs for extremely thick samples, where $\varepsilon_z = 0$. Due to the applicability of thin sample for both fabrication and testing, plane stress computation are emphasized. The effect of the plane stress vs plane strain model on the H pattern has also been studied and is shown in Figure 3.4. No significant changes have been observed for the polarization

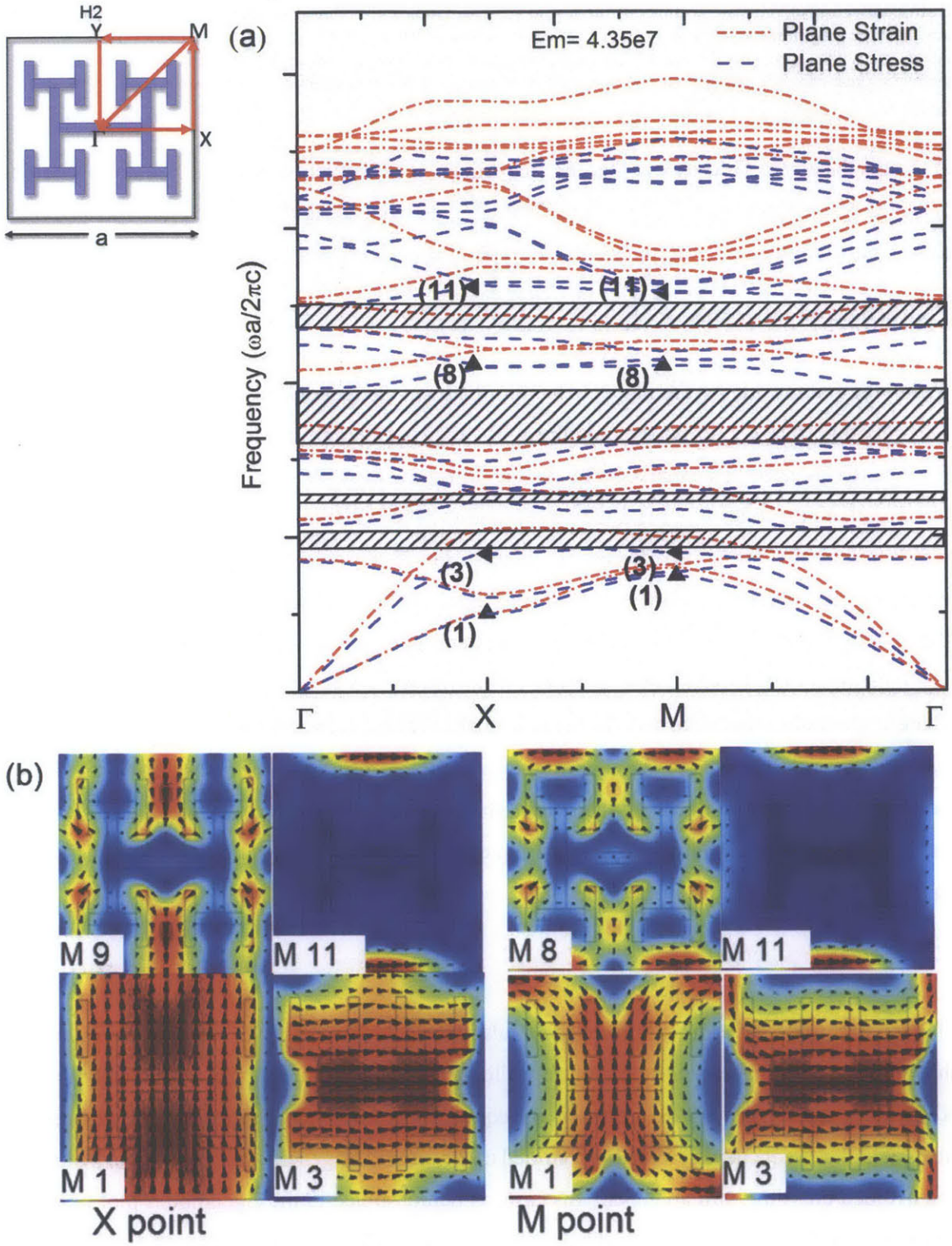
H2
Y
M
I
X
a
(a)
Em= 4.35e7
Plane Strain
Plane Stress
Frequency (ωa/2πc)
(11)
(11)
(8)
(8)
(3)
(3)
(1)
(1)
Γ
X
M
Γ
(b)
M 9
M 11
M 1
M 3
X point
M 8
M 11
M 1
M 3
M point

Figure 3.3: (a) The dispersion curves for sample H2 plane strain (red dot dash line) and H2 plane stress (blue dash line) along the BZ of the unit cell (along Γ→ X→M) as indicated in the unit cells in the bottom right insert. (b)The eigenmodes corresponded are arranged at the side as indicated, where the color (red – large, blue-small displacement) indicates the magnitude and the arrow indicates the direction of the displacement. Both eigenmodes M1 and M9 are symmetric with respect y axis while M3 and M11 are anti-symmetric with respect to y axis at X point. At X point, the interacting pairs are M1 M8 (symmetric with respect y axis), and M3 M11 (anti-symmetric with respect y axis).

of the displacement field except that the frequencies are relatively lower than the corresponding modes at plane strain model. This is predictable given reduced rigidity of the plane stress model, which leads to lower eigenfrequencies. The general framework is still applicable for such system

3.2.1.2 Material Properties

Within the framework for the global behavior, the local interactions can be tuned by varying the material properties, e.g. lower the modulus of the matrix materials, as shown in Figure 3.5, where the eigenfrequencies are reduced due to the lower modulus of the system. While the long wavelength eigenmodes (i.e. M1 and M2 at Γ point) exhibit smaller difference, the eigenmodes at higher frequencies are quite different. In general, the displacement field is more confined with increasing mechanical impedance contrast between the matrix and scatterer phase. . For Em =4.35e 9Pa, the high strain region can exist in both scatterer and matrix, e.g. M17 at Γ, X and M point, where the polarization have been symmetric with respect x axis or y axis. Even for eigenmodes where high strain region are mainly located in the matrix phase, they can still spread into the scatterer phase through higher level H arm, especially the corner of the H arms. For Em =4.35e6 Pa, the fields are well confined in the matrix phase. Given the larger contrast of the scatterer vs. matrix modulus, eigenmodes with higher frequency prefer to be concentrated in at the less rigid phase, i.e., the matrix in this case.

3.2.1.3 Thickness/Length ratio

The geometries of the arms that form the H also affect the behavior of H tree based system, as shown in Figure 3.6. Due to the decreasing filling fraction of the more rigid scatterer phase from H2 (0.2125) to H2_thin (0.10625), the eigenfrequencies of the system decrease. The displacement fields at higher frequency are also less confined in t/l = 1/18. The general guideline about symmetry and avoided crossings still applies in this case, as demonstrated in the eigenmodes plot in Figure 3.6(b). For both sample, the longitudinal and transverse modes at long wavelength again are

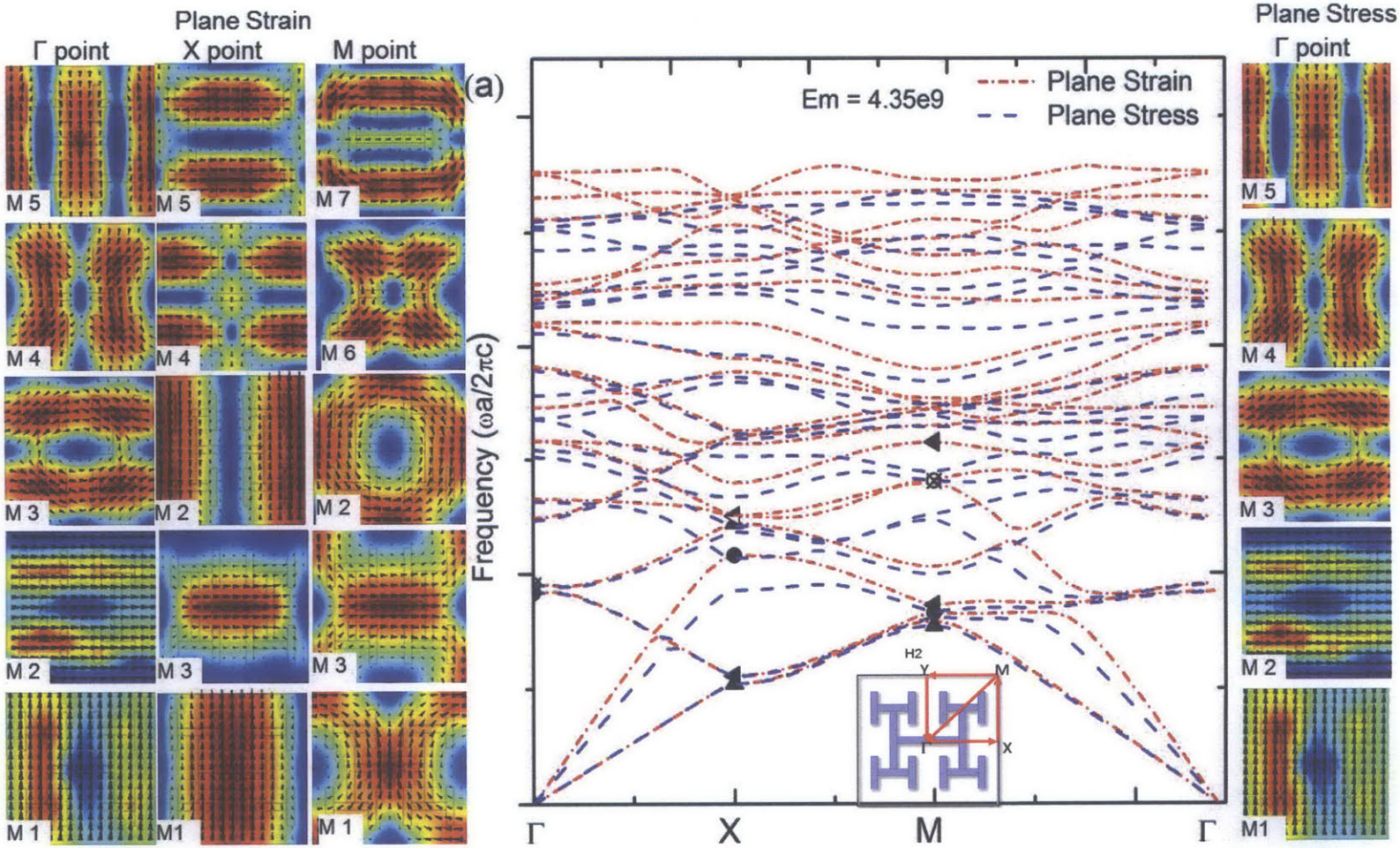

Figure 3.4: The dispersion curves for sample H2 plane strain (red dot dash line) and H2 plane stress (blue dash line) along the BZ of the unit cell (along Γ→ X→M). The eigenmodes corresponded (as highlighted by solid triangle (or circle) are arranged at the side as indicated, Eigenmodes M1, M2 (3) at Γ, X, M point shows are the goldstone modes (longitudinal or transverse displacement). The symmetry of displacement polarization are the same for both plane strain and plane stress at Γ point.

Table 3.2: Material properties used for the simulation for dispersion curves. The scatterer here approximates the properties of lead and the matrix1 has properties similar to the epoxy SU8. The Matrix3 is close to that of a rubber.

Material Properties	Matrix1	Matrix2	Matrix3	Scatterer
Bulk Modulus Pa	4.35e9	4.35e7	4.35e6	4.08e10
Poisson Ratio	0.368	0.368	0.368	0.37
Density kg/m^3	1180	1180	1180	11600

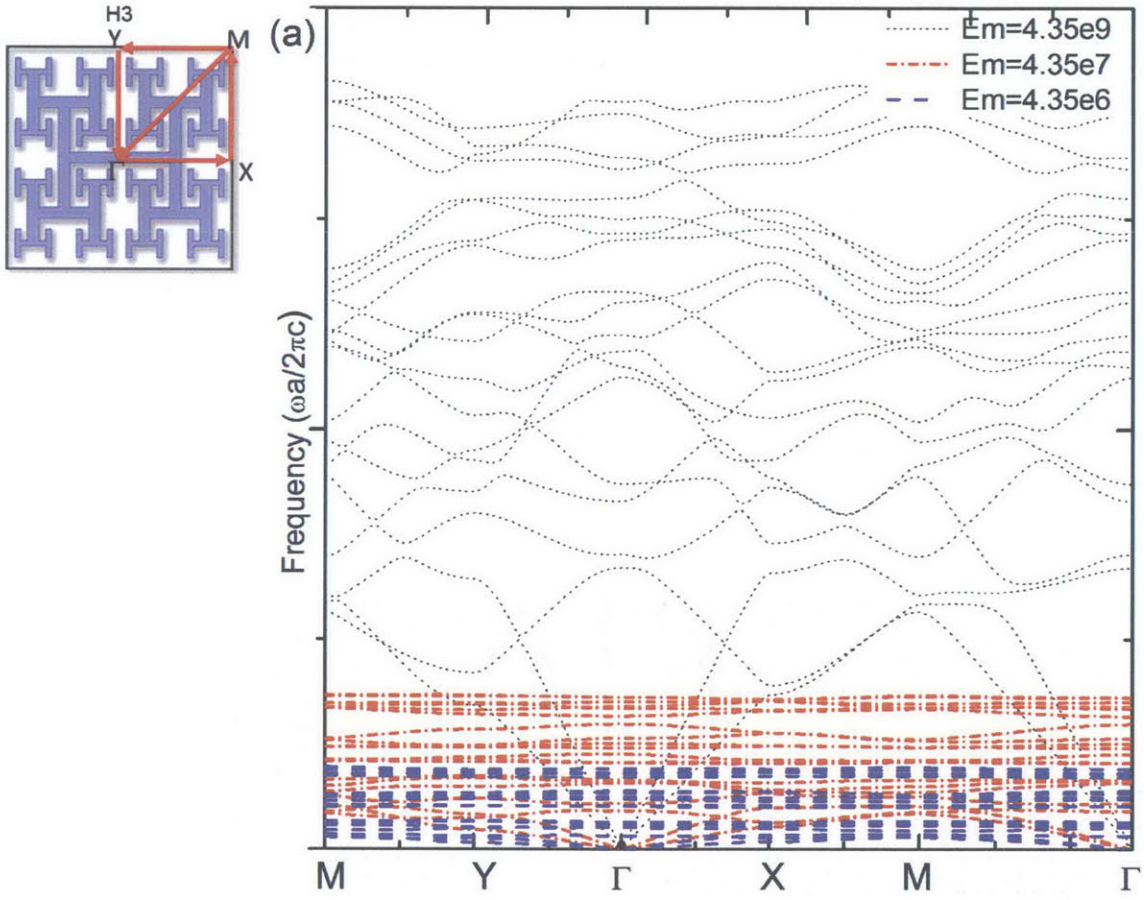

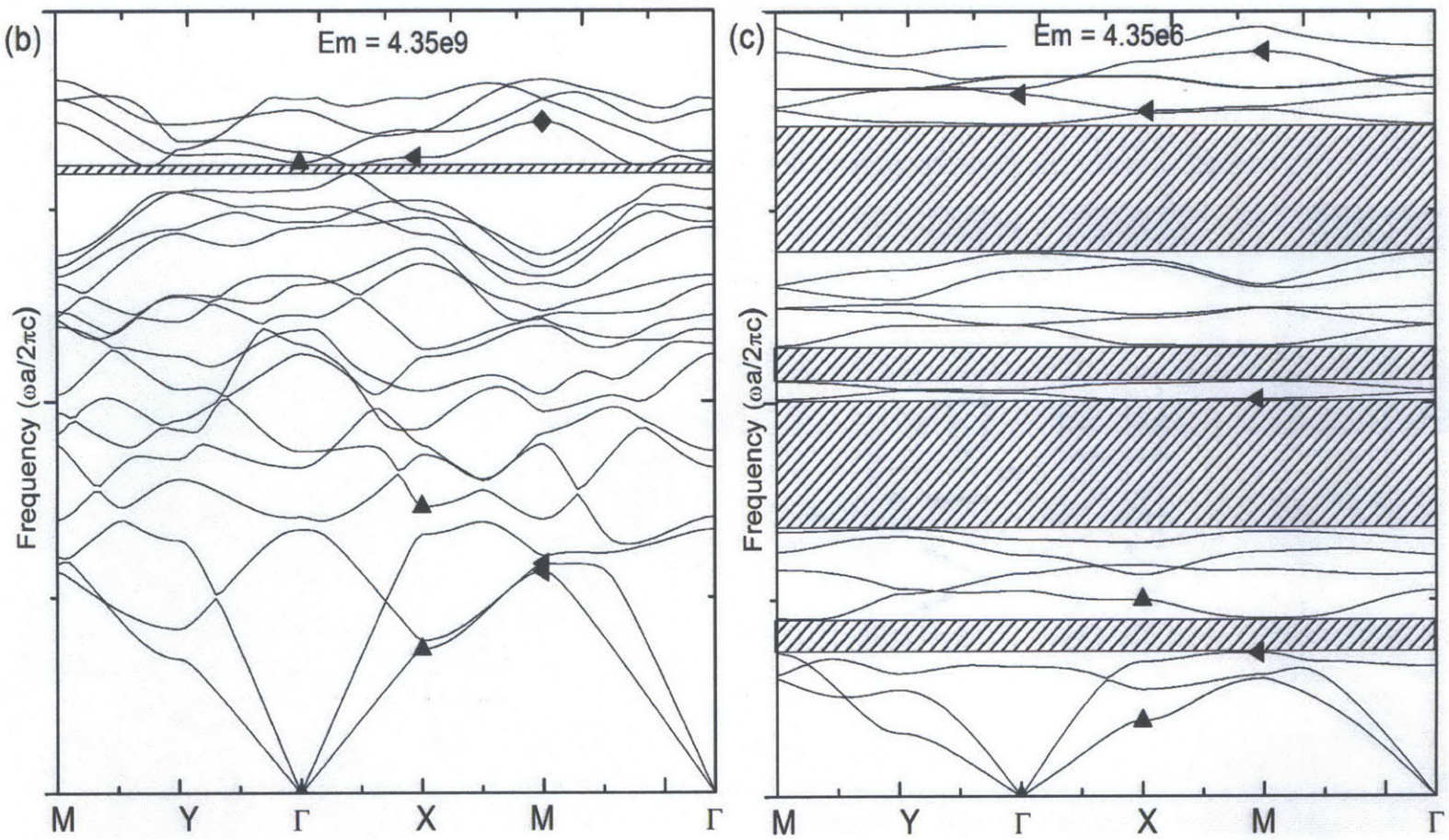
(b)
Em = 4.35e9
Frequency (ωa/2πc)
M
Y
Γ
X
M
Γ
(c)
Em = 4.35e6
Frequency (ωa/2πc)
M
Y
Γ
X
M
Γ

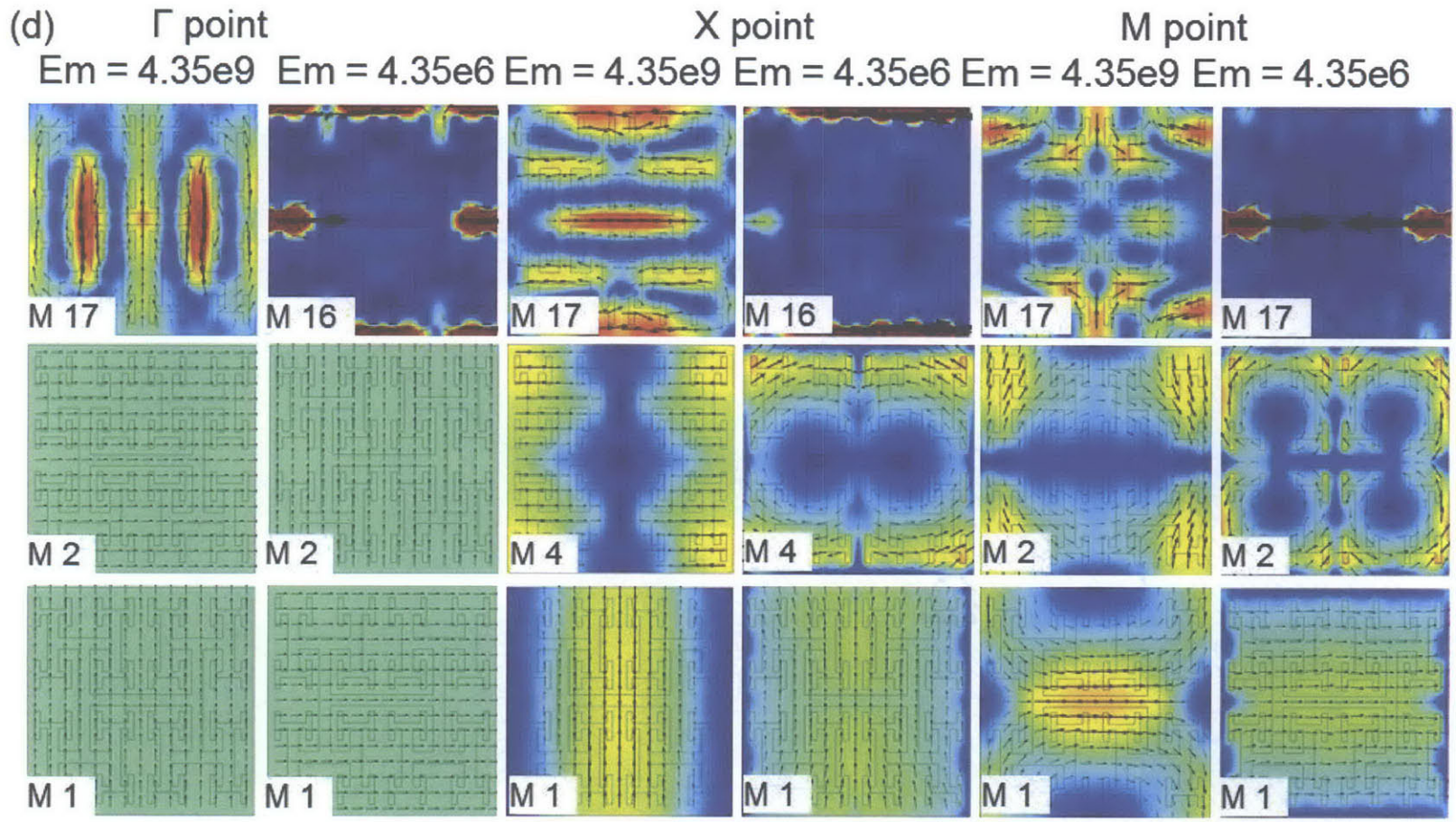

Figure 3.5: (a) The dispersion curves for sample H3 with varying Young's Modulus for Matrix from 4.35e9 to 4.35e6 along the BZ of the unit cell (along M→ Y→ Γ→ X→M) as indicated in the unit cells in the top insert. (b) The dispersion curves along the BZ of the unit cell (along M→ Y→ Γ→ X→M) for sample H3 where Em = 4.35e9 and bandgap is highlighted in hatched rectangle; (c) The dispersion curves for sample H3 along the BZ of the unit cell (along M→ Y→ Γ→ X→M) where Em = 4.35e6 and bandgap is highlighted in hatched rectangle as indicated in the unit cells in the top insert. (d) The eigenmodes corresponding to H3 with different Em (as highlighted by solid triangle). Eigenmodes M1, M2 at Γ, X, M point are the goldstone modes (longitudinal or transverse displacement). The symmetry of displacement are symmetric with respect to either x or y axis or both. For sample with larger impedance contrast, the high strain region are more localized to the matrix, where the high strain region can exist in both scatterer and matrix phase (e.g. M17)

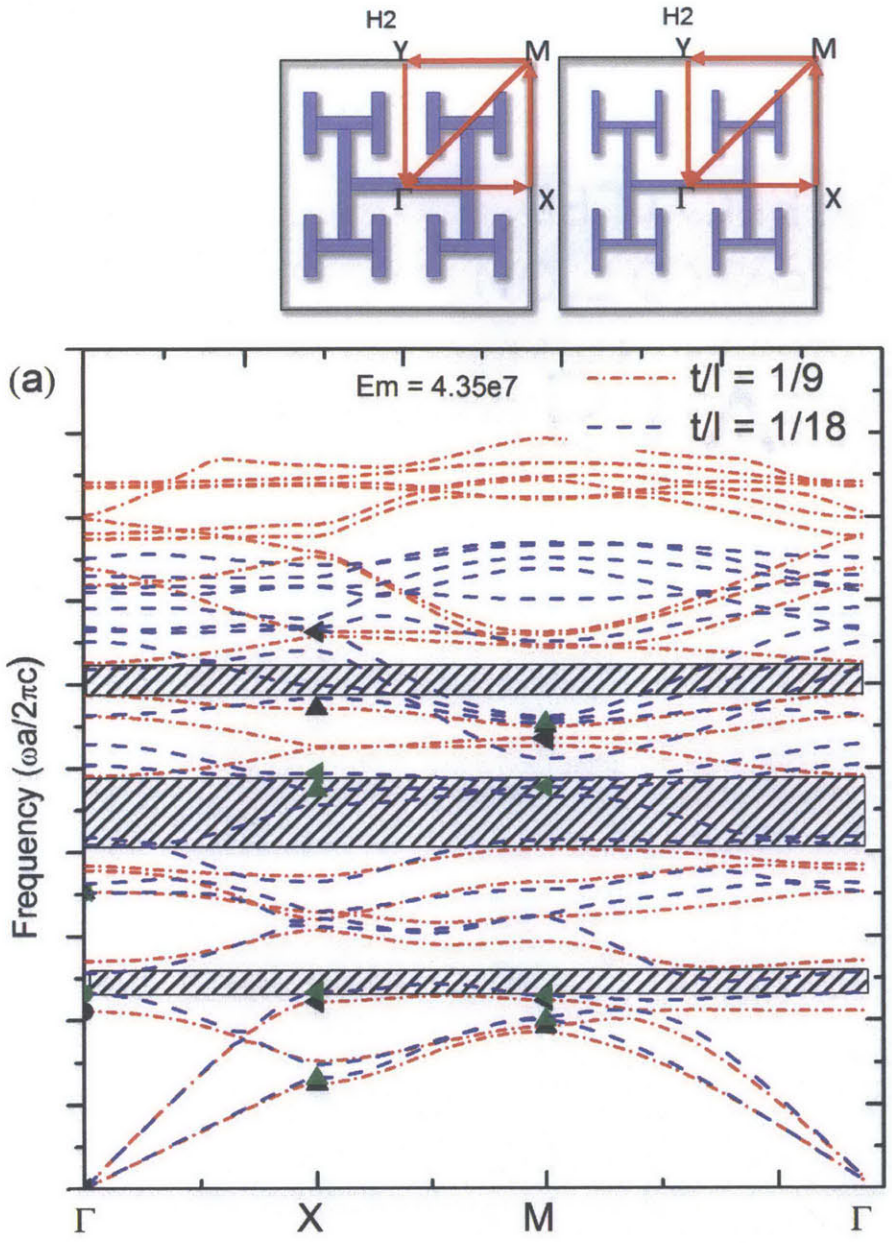
H2
Y
M
Γ
X
H2
Y
M
Γ
X
(a)
Em = 4.35e7
t/l = 1/9
t/l = 1/18
Frequency (ωa/2πc)
Γ
X
M
Γ

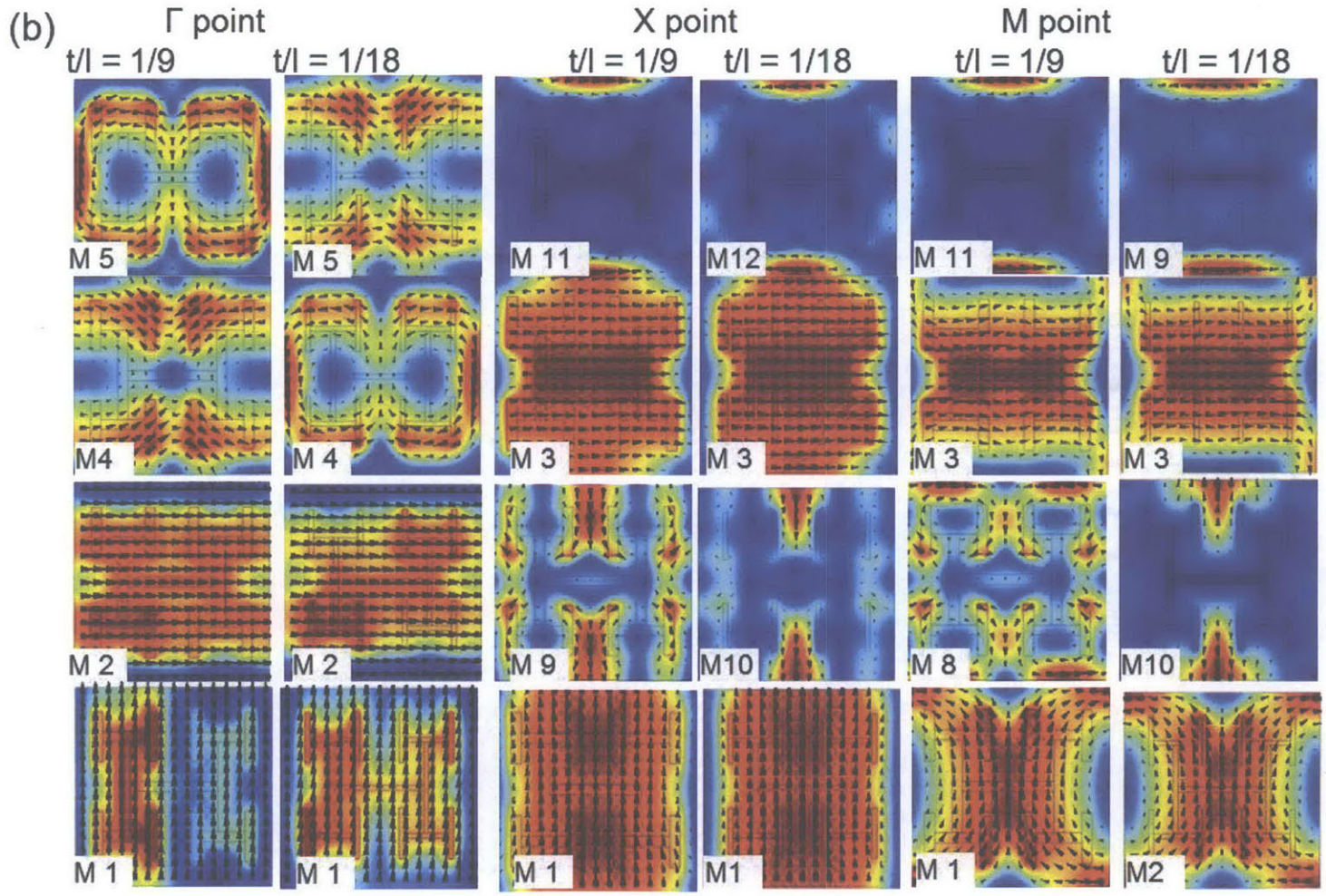

Figure 3.6: (a) The dispersion curves (with plane stress mode) for sample H2 (t/l = 1/9) (red short dash dot) and H2 (t/l = 1/18) (blue dash) along the BZ of the unit cell (along M→ Y→ Γ→ X→M) as indicated in the unit cells in the right insert. (b)The eigenmodes for t/l=1/9 (black solid triangle (or circle)) and t/l = 1/18(olive solid triangle) are arranged at the side as indicated, Eigenmodes M1, M2 at Γ, point are the goldstone modes (longitudinal or transverse displacement). The symmetry of displacement are symmetric with respect to either y (M1 and M9 (10) at X point and M1 (2) and M8 (10) AT M point) and or x axis (M1 and M9 (10) at X point, M3 and M9 (11) at M point). The eigenmodes are more localized with H2 compared to H2_thin.

observed across the BZ boundary (e.g. M1, M2 (3) at Γ, X and M point). Given that both Γ, X and M point has the mirror symmetry with respect to both x and y axis, eigenmodes at higher frequency exhibit polarization that is symmetric with either x axis (e.g. M2 at Γ point, M3 and M11(12) at X and M3 and M11(9) at M point) or y axis (e.g. M1 and M5 at Γ point, M1 and M9(10) at X and M1(2) and M8(10) at M point) or both or two fold symmetry (e.g. M4(5) at Γ point). Eigenmodes with same symmetry would undergo avoided crossing that contributes to the bandgaps formed in Figure 3.6(a). The eigenmodes are H2 and H2_thin have similar symmetry element, while they exhibit slight difference in localization of high strain region. .

3.2.1.4 Levels of Iterations

To study how a fractal like system would behave at different length scale, the level of iterations for H pattern has been studied (Fig 3.7). As the filling fraction of more rigid scatterer phase increase from 0.2125 (H2) to 0.3575(H3), the eigenfrequencies for goldstone mode (long wavelength that corresponds to the unit cell as a whole) increase. Multiple spectral bandgap has been observed for both H2 and H3 (as shown in Fig. 3.7(a)), while the numbers of spectral gaps for higher level of iteration (i.e. H3) is larger. For the frequency range calculated, Sample H2 has only three bandgap clustered towards the lower frequency range of the spectrum. While the bandgap for H3 are spread out to higher frequency range calculated with varying sized. This could due to the interaction of the higher level H tree unit (i.e. the smaller unit) at the frequency comparable to their feature size. Similar trends have been observed in sample pair H2 and H4 (as shown in Figure 3.8(a), where the eigenfrequencies for goldstone mode increases as the fill ratio of scatterer phase from 0.2125 (H2) to 0.413(H4). Compared to H3, H4 has smaller average bandgap size despite the fact it has even larger number of spectrum gap, as shown in Table 3.3.

To investigate the nature of interaction between bands with the same symmetry (with respect to the relevant k vector, the eigenmodes are plotted in Figure 3.7(b). For H3, the longitudinal and transverse modes again are observed across the BZ boundary (e.g. M1, M2 (3) at Γ, X and M point). Then eigenmodes with similar symmetric elements compared to H2 has been observed, i.e. M4 of H2 and M5 of H3 at Γ point (Figure 3.6(b) and Figure 3.7(b). As the eigenfrequency goes higher, the eigenmodes would symmetric with either x axis (e.g. M1 and M7 at Γ point, M3 and M7 at X and M point) or y axis (e.g. M2 and M5 at Γ point, M1 and M4 at X and M point) or both

(e.g. M6 and M11 at Γ point, M5 and M10 at X and M6 and M10 at M point) or exhibit two fold symmetry. Eigenmodes with same symmetry would undergo avoided crossing that contributes to the bandgaps formed in Figure 3.7(a). For medium frequencies range, the H tree on the first level have minimal displacement while the four quarters delineated by it shows mixed displacement (a rotational nature) as if scale the mixed modes by half and arrange with different symmetry element,

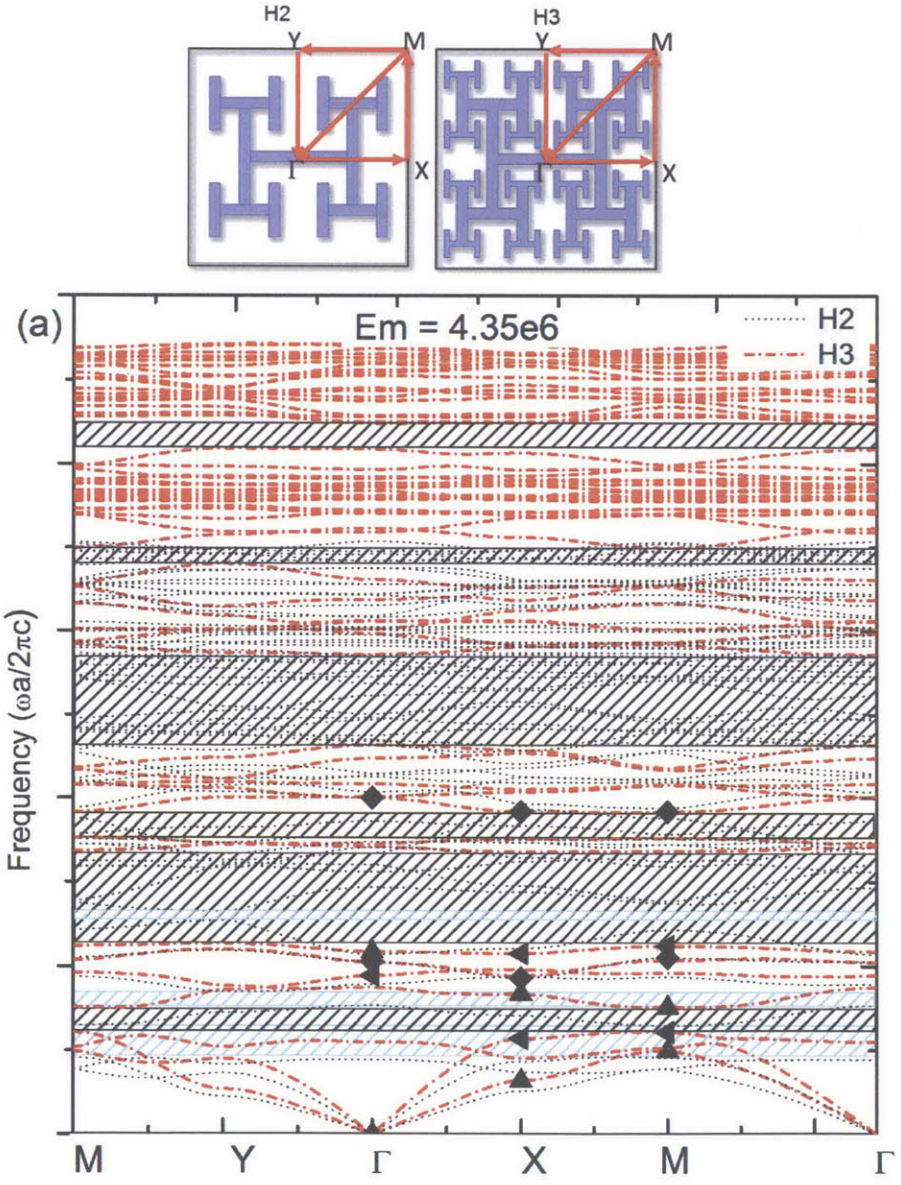

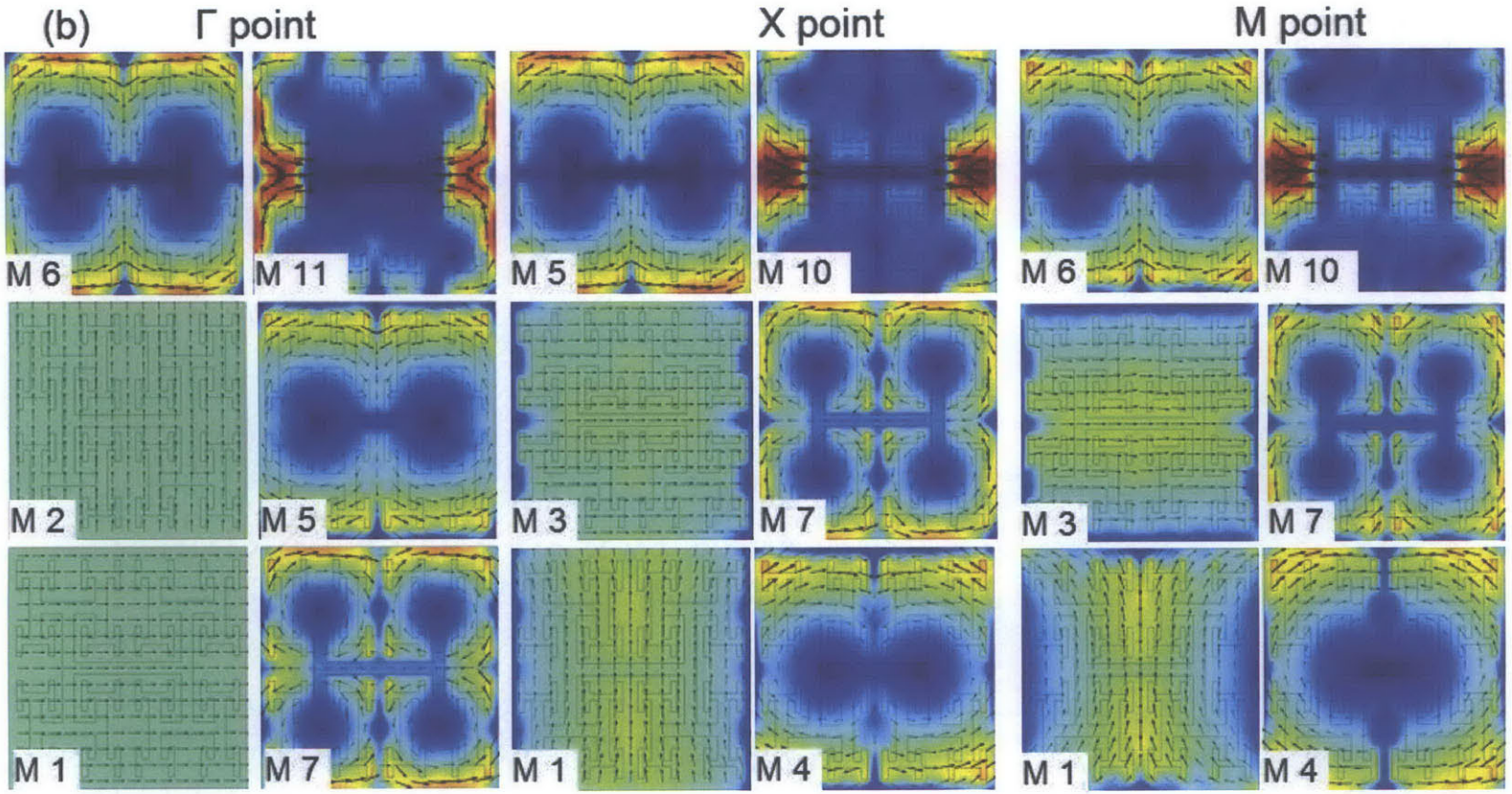

Figure 3.7: The dispersion curves (with plane stress mode) for sample H2 (t/l = 1/9) (red short dash dot) and H2 (t/l = 1/18) (blue dash) along the BZ of the unit cell (along M→ Y→ Γ→ X→M) as indicated in the unit cells in the right insert. (b)The eigenmodes for t/l=1/9 (black solid triangle (or circle)) and t/l = 1/18(olive solid triangle) are arranged at the side as indicated. Eigenmodes M1, M2 at Γ, point are the Goldstone modes (longitudinal or transverse displacement). The symmetry of displacement are symmetric with respect to either y (M3 and M7 at X and M point or x axis (M1 and M4 at X point and M points) or both (M5 (6) and M10 at X and M point).

which only appear in few modes in sample H2. Given the interface grows with the increased number of iteration, the effective path for impedance discontinuity also increase. For H4, the symmetry patterns are retained; it also have eigenmodes that are symmetric with either x axis (e.g. M2 and M5 at Γ point, M1 and M4 at X and M point) or y axis (e.g. M1 and M7 at Γ point, M3 and M6 at X and M point) or both (e.g. M6 and M10 at Γ point, M5 and M9 at X and M point) or

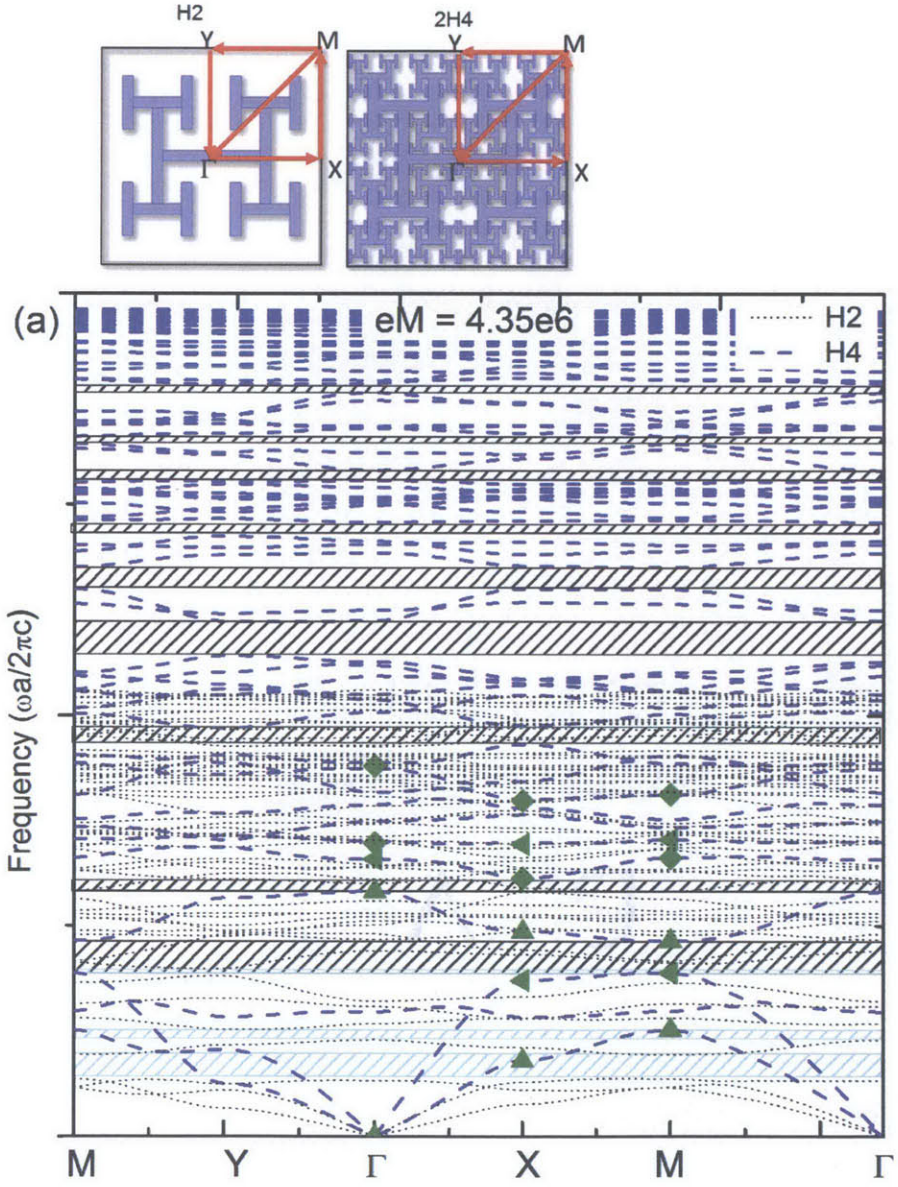

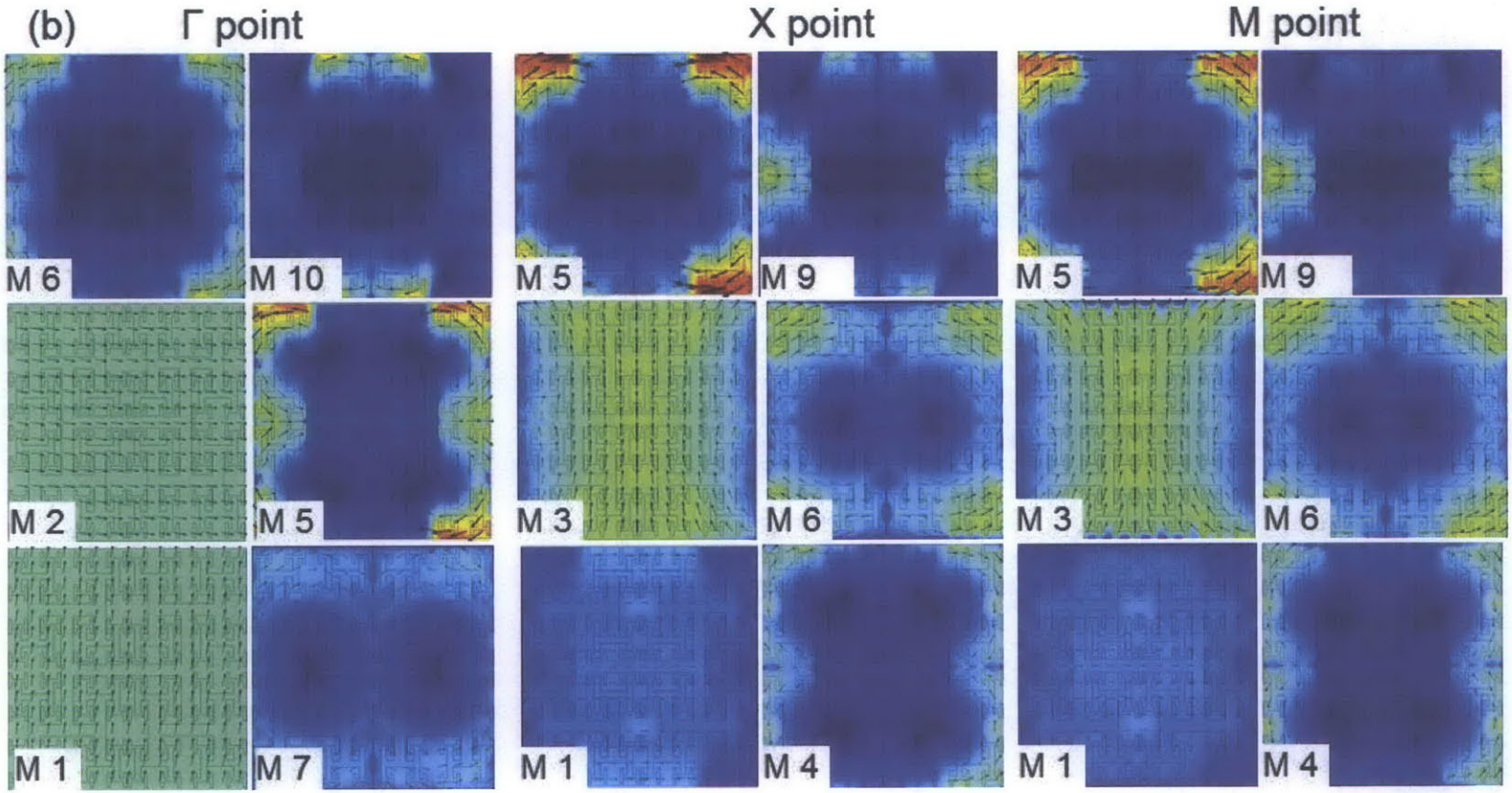

Figure 3.8: (a) The dispersion cur.es for sample H2 (black dot line) and H3 (red short dash dot) along the BZ of the unit cell (along M→ Y→ Γ→ X→M) as indicated in the unit cells in the right insert. (b) The eigenmodes for t/l=1/9 (black solid triangle (or circle)) and t/l = 1/18(olive solid triangle) are arranged at the side as indicated, Eigenmodes M1, M2 at Γ, point are the Goldstone modes (longitudinal or transverse displacement). The symmetry of displacement are symmetric with respect to either y (M3 and M6 at X and M point) or x axis (M1 and M4 at X point and M points) or both (M5 and M9 at X and M point).

Table 3.3: Bandgaps data formed for samples with different levels of iteration and impedance contrast (for the frequency range we investigated)

Sample Name	Number of bandgap	Size of bandgap	Impedance contrast
H2	3	0.265	$Ks/Km = 96.022$
H3	6	0.312	$Ks/Km = 96.022$
H4	6	0.171	$Ks/Km = 96.022$
H2	5	0.327	$Ks/Km = 303.022$
H3	6	0.591	$Ks/Km = 303.022$
H4	9	0.293	$Ks/Km = 303.022$

exhibit two fold symmetry, as shown in Figure 3.8(b). Compared to H3, the absolute displacement is lowered while the eigenfrequencies is higher since the fill fraction of the softer matrix phase actually decreases from H3 to H4. However, the increase in effective Young's modulus is not sufficient to explain the difference, since normalized eigenfrequencies for H3 (i.e. $\omega a/2\pi c$) are still lower than H4. This can be further explained by the more flattened dispersion curve of H3 due to the more localized nature of its eigenmodes compared to H4 with same impedance contrast. Furthermore, the transition from large to small strain in the unit cell does not have the 1 generation H tree acting as the rough interface anymore, comparing Figure 3.7(b) and Figure 3.8(b).

3.2.2 Theoretical Study of 2D plate with finite thickness Metamaterials based on H tree motifs

The study of eigenmodes in 2D in previous section provides interesting insight in the behavior of H tree based system. To accelerate the implementation of such system in devices application, 2D plate with finite thickness systems are investigated for both in plane displacement In this case, the single unit with the H tree prefractals would be the sample of interest, where the periodic boundary condition is removed at four edge faces. The dimension of the sample is chosen such that it would be optimal for the acoustic/ultrasonic setup. The edge of the square is the 20mm (equivalent of a in 2D system) and the thickness is 3mm (for thick sample) and 1mm (for thin samples). The dimensions of the H tree slits obtain the same ratio as a/t/l of H2_thin sample in the above section,

as shown in Figure 3.8 insert. To ensure structural integrity, we define the matrix as the solid phase while the scatter phase are silts filled with medium (water or air) later.

The 2D plate with finite thickness sample geometry is drawn in AutoCAD and the imported into COMSOL to find its eigenmodes through full wave simulation. After the eigenfrequencies are obtained, they would be used as the frequency of a point source at certain distance from the sample (Fig 3.8). Then stimulated eigenmodes (by the point source) are investigated to better understand how the source wave would activate the eigenmodes. The boundary of the sample were set to be acoustic-structure boundary and the fluid domain is bounded by sound radiation boundary condition.

For samples with two levels of H trees in water, the lowest eigenmode dominated by in plane displacement has a frequency of 2090.5Hz with two fold symmetry, so does the fluid pressure field with a high and low pressure region on each edge of the sample (Fig 3.8). As the frequency increases, eigenmodes with other in plane symmetries have also been observed, e.g. symmetric with both x and y axis (e.g. 3583.2Hz), symmetric with y axis (e.g. 7475.1Hz). It is likely the lowest eigenmode corresponds to the stretch and compression along the longest dimension possible (diagonal) and then move to the edges (half a sinusoidal wave) and then decreasing wavelength of displacement with increasing frequencies. As the frequency increase, the number of nodes in the fluid pressure field also increase (e.g. 35445Hz), which is consistent with the relationship between the energy and displacement nodes. The eigenfrequency is then used as the frequency for waves from a point source and the resultant displacement field and fluid pressure

Table 3.4: Bandgaps data formed for samples with different levels of iteration and impedance contrast (for the frequency range we investigated)

	Water	Air	Sample Material
Modulus		-	3.2e9
Density	1000	Rho(pA[1/Pa],T[1/K])(kg/m^3)	1190
Poisson Ratio	-	-	0.35
Speed of Sound	1497	346.65	2800

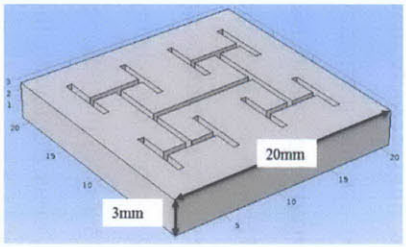

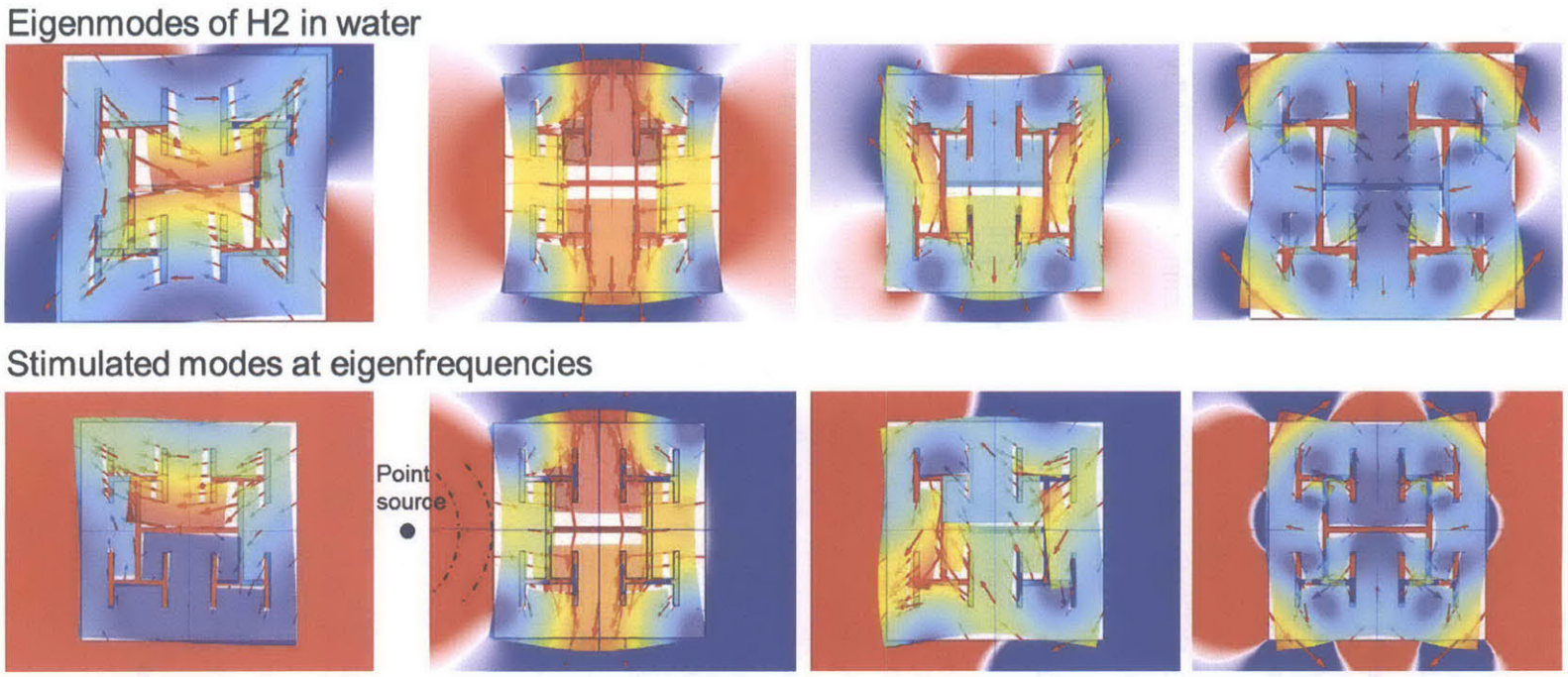

Figure 3.9: The displacement field (on the sample) and the pressure field (outside the sample) of 2D plate with finite thickness Htree (level two) at the top row with eigenfrequencies 2090.5Hz, 3583.2Hz, 7475.1Hz, 35445Hz (from left to right), and stimulated modes (in water) at eigenfrequency of the 1st row, where the color indicates the magnitude and the arrow indicates the direction of the displacement. The point source and the wave front (black short dash dot) are indicated in the second row second column.

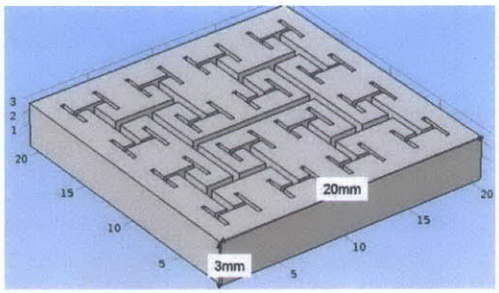

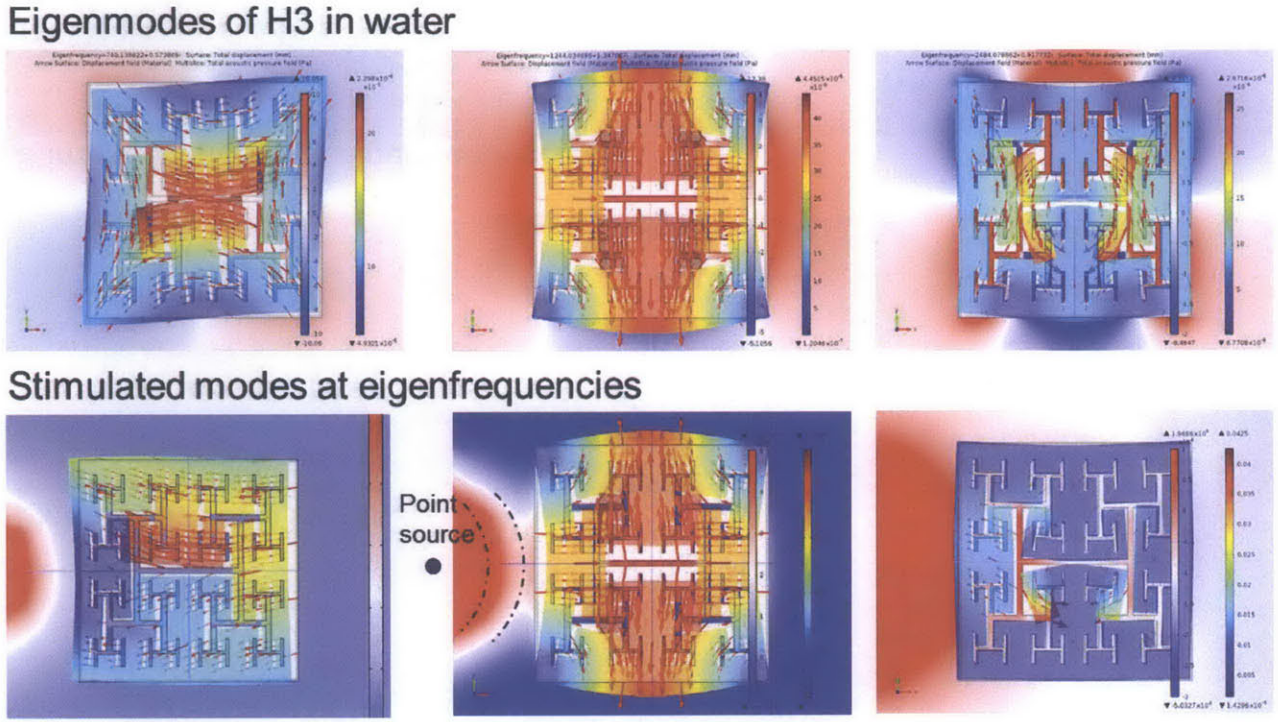

Figure 3.10: The displacement field (on the sample) and the pressure field (outside the sample) of 2D plate with finite thickness Htree (level three) at the top row with eigenfrequencies 740.1Hz, 1224.0Hz, 2484.1 Hz and stimulated modes (in water) at eigenfrequency of the 1st row, where the color indicates the magnitude and the arrow indicates the direction of the displacement. The point source and the wave front (black short dash dot) are indicated in the second row second column.

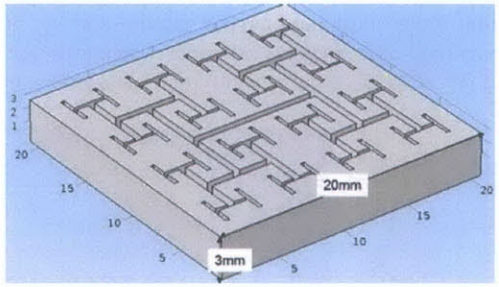

Eigenmodes of H3 in air

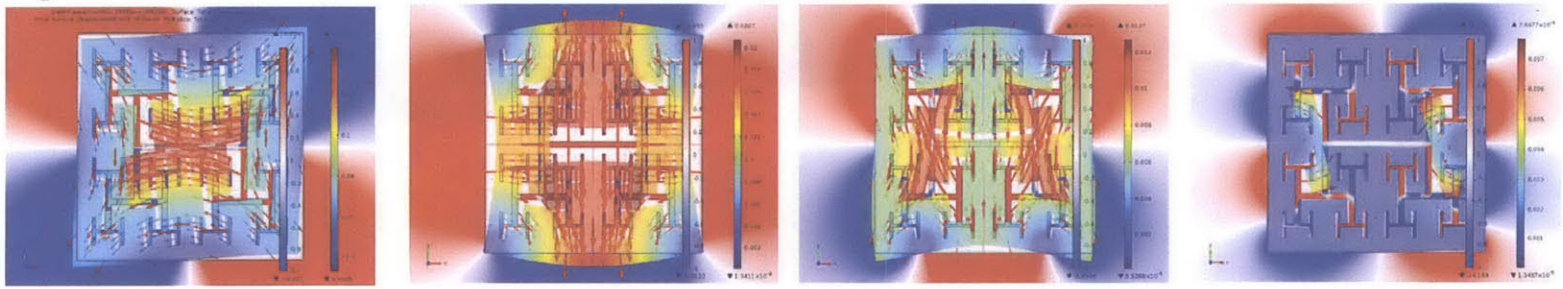

Stimulated modes at eigenfrequencies

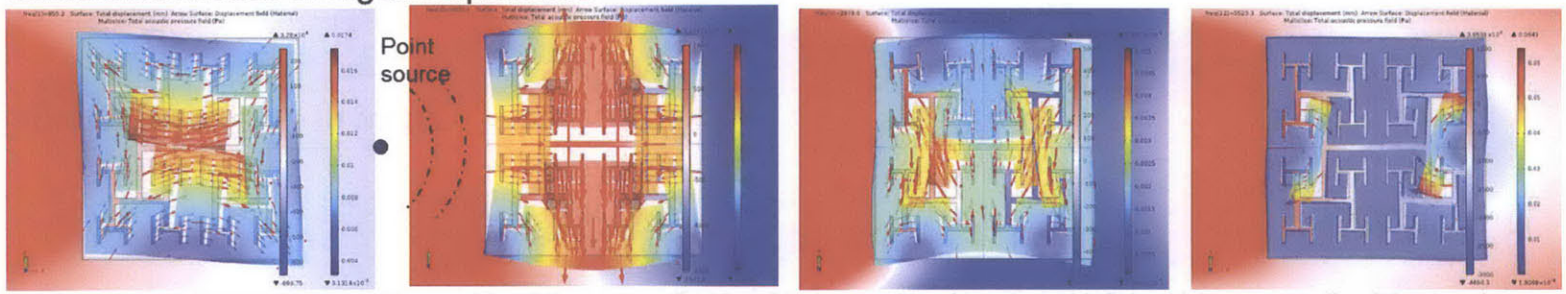

Figure 3.11: The displacement field (on the sample) and the pressure field (outside the sample) of 2D plate with finite thickness Htree (level three) at the top row with eigenfrequencies 855.2 Hz, 1630.6Hz, 2879.6Hz, 5525.3Hz and stimulated modes (in air) at eigenfrequency of the 1st row, where the color indicates the magnitude and the arrow indicates the direction of the displacement. The point source and the wave front (black short dash dot) as the same as above

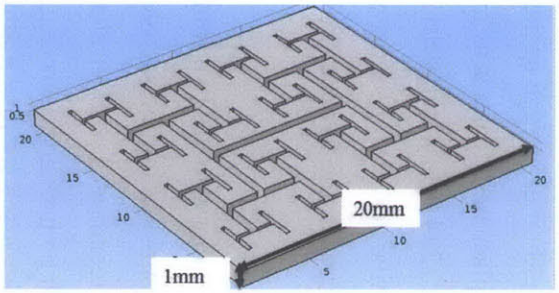

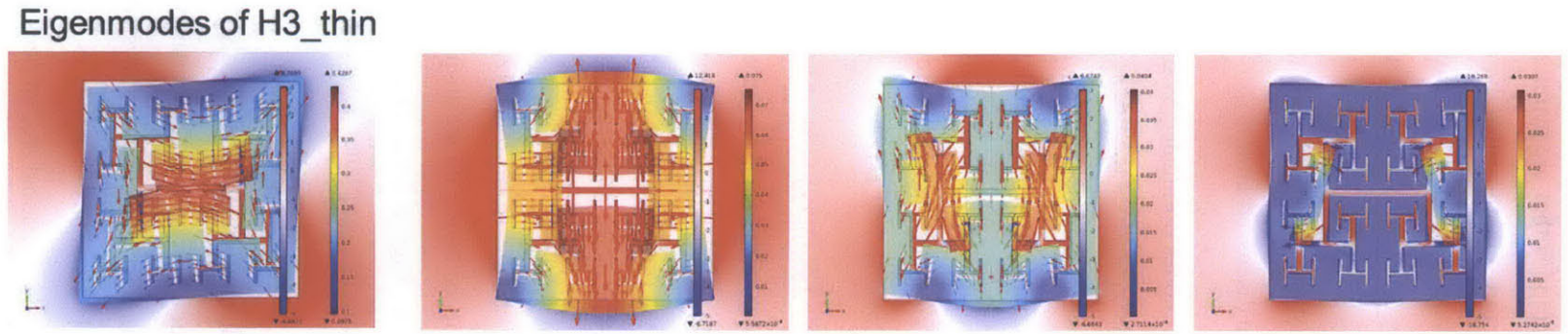

Figure 3.12: The displacement filed (on the sample) and the pressure field (outside the sample) of 2D plate with finite thickness Htree (level three thin) at the top row with eigenfrequencies 830.7Hz, 1582.6Hz, 2785.1Hz, 5374.7Hz, and stimulated modes (in air) at eigenfrequency of the 1st row, where the color indicates the magnitude and the arrow indicates the direction of the displacement. The point source and the wave front (black short dash dot) as the same as above

field is plotted in second row. For eigenmodes that are symmetric with x axis, their symmetry properties are retained with little variation. On the other hand, for eigenmodes that are not symmetric with respect x axis, their displacement vary significantly (e.g. 2090.5Hz, 7475.1Hz). It is worth point out that the eigenfrequency of the in-plane eigenmodes (2090.5 Hz) is much lower compared to the frequency corresponding to the dimension of the plate (i.e. 1500m/s / 20 mm = 75 kHz). To understand this deep subwavelength behavior, we proposed a simple analytical model using Helmholtz resonator tree, as will be discussed later.

For samples H3 in water, the lowest eigenmodes dominated by in plane displacement also has two fold symmetry with a frequency of 740.1Hz, so does the fluid pressure field on each edge of the sample (Fig 3.9). As the frequency increases, eigenmodes with similar displacement features as in H2 (level 2) have been observed, e.g. symmetric with both x and y axis (e.g. 1224.0Hz,), symmetric with y axis (e.g. 2484.1 Hz). For displacement of stimulated modes, similar features have been observed as with H tree (level two). Therefore, as the level of iteration increases, the frequency of eigenmodes further decreases from 2090.5Hz to 740.1Hz.

For H3 trees in air, the lowest eigenmodes dominated by in plane displacement also has two fold symmetry with a frequency of 855.7Hz, while the fluid pressure field on surrounding the sample also have a two-fold symmetry (Fig 3.10). As the frequency increases, eigenmodes with similar displacement features as in water have been observed, e.g. symmetric with both x and y axis (e.g. 1630.6Hz,), symmetric with y axis (e.g. 2879.6 Hz). For displacement of stimulated modes, similar features have been observed as with H3 (in water). Therefore, by varying the surrounding fluids medium, the frequency of eigenmodes change from 740.1Hz to 855.7Hz. To study how the thickness of the sample would affect the behavior of the in-plane behavior, the H3 thickness decrease from 3cm to 1cm, as shown in Figure 3.11. The frequency for the corresponding eigenmodes (i.e. similar symmetry properties in-plane) lowered with the decreasing sample thickness.

Besides the full wave simulation, a simple analytical model has also been implemented to develop a physical intuition of the system and shine lights on the mechanism of subwavelength eigenmodes observed. The Helmholtz resonator is simple acoustic resonant system (Fig 3.12(a)) with a hollow spherical shell connected to an open neck. Its acoustic properties can be characterized by cavity volume V_0, the neck length l_{neck} and the cross sectional area of neck S as well as speed of sound v

and density of surrounding medium ρ. A close analogy can be established between propagation of sound in pipes/champers and electricity flow in electric circuits, i.e. the closed end of chamber is like a capacitor, the narrow neck can be modelled by a resistor and inductor in series as shown in Figure 3.12 (b). In this model, the impedance of an open tube can be represented by its inductance$L = \rho l/S$, the capacitance of the chamber can be written as $C = V_0/\rho v^2$, and the resistance can be modeled by $R = \rho v/S$. For the circuit, the external and internal pressure can be represented by

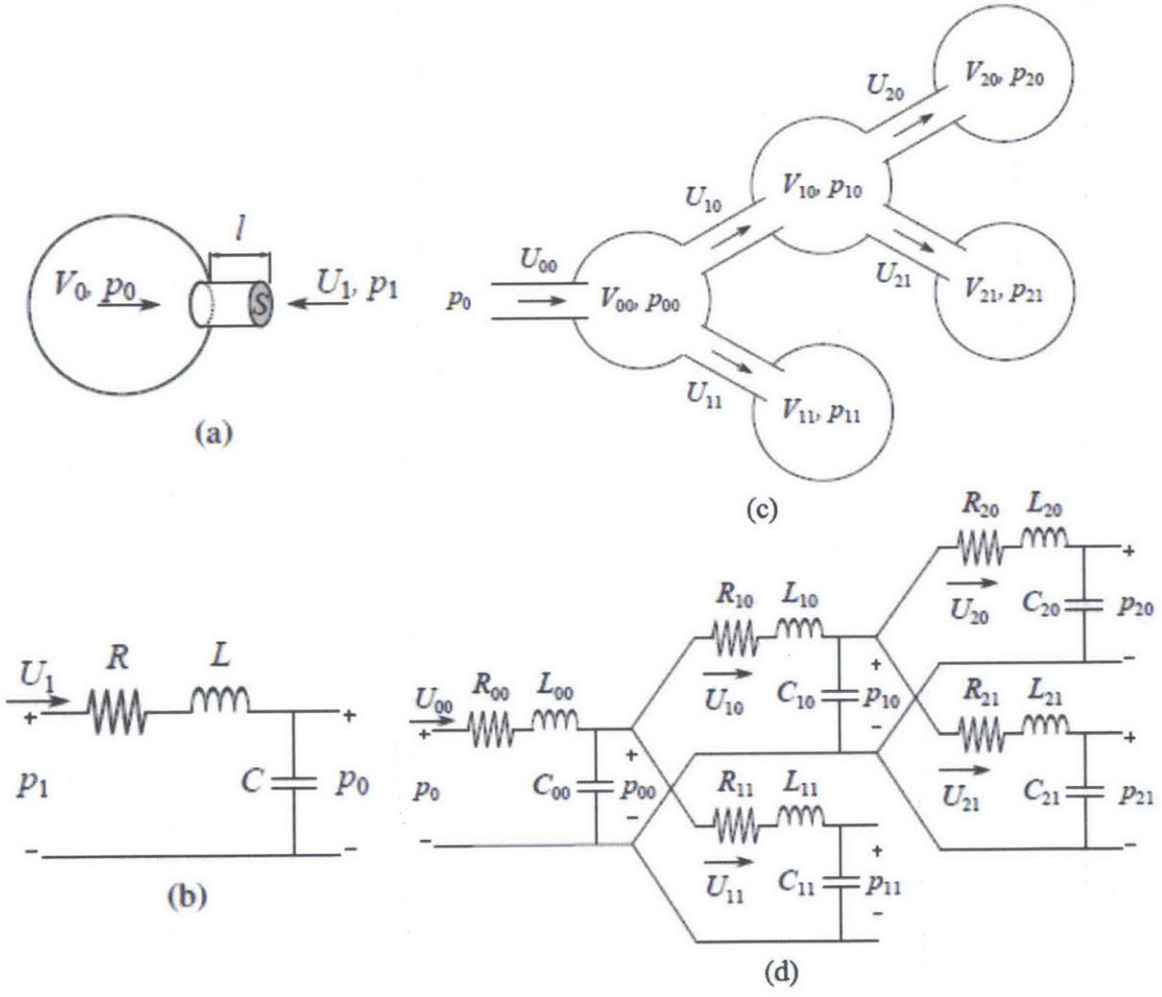

Figure 3.13: (a) Helmholtz resonator and (b) its equivalent circuit (c) Example of a Helmholtz resonator tree; (d) its equivalent circuit. Source: Rafael P. and Vesa V. Proc. of the 15th Int. Conference on Digital Audio Effects (DAFx-12), 2012

the voltage p1 and p0 respectively, while the medium flow through the neck can be represented by current. The acoustic impedance of a single resonator is given by

$$Z_1(\omega) = \frac{(j\omega)^2 LC + j\omega RC + 1}{j\omega C}$$

Where ω is the frequency in rad/s and j is square root of -1.

The Helmholtz resonator has been extended further to build a resonator tree to represent a musical instrument better (Fig 3.12(c)). Since many acoustic problems have been studied using acoustic circuit by applying electric circuit theorems, the equivalent circuit framework has also been used to study this system. Hence the impedance of a Helmholtz resonator tree with N branches can be determined through iteration process

$$Z_K(\omega) = \frac{(j\omega)^2 LC + j\omega RC + 1}{j\omega C + \sum_{n=1}^{N} \frac{1}{Z_{K-1,n}(\omega)}}$$

Where K is the level of iteration and N is the number of branches.

The Helmholtz resonator tree can also be used to model the Htree structure given the branching quality of both systems. The impedance of the Helmholtz resonator tree structure has been calculated by implementing the equation in MATLAB. With increasing level of iteration, the lowest resonance of the system continuous decreasing as shown in Figure 3.13. For 7 level of iteration, the lowest eigenfrequency is about 520 Hz, corresponding well with Htree (level 3) and 5 level of iteration has the lowest resonance frequency of 5400Hz, corresponding to Htree (level 2). Moreover, within increasing level of iteration, the number of resonance dips also increase as shown in Figure 3.12 and Figure 3.13. Both features are a demonstration of the properties of the iterative impedance generation function, which shows that the number of the dips are relates to the poles in the equation (i.e. level of the iteration) and the lowest dips are related to the effective path of the current.

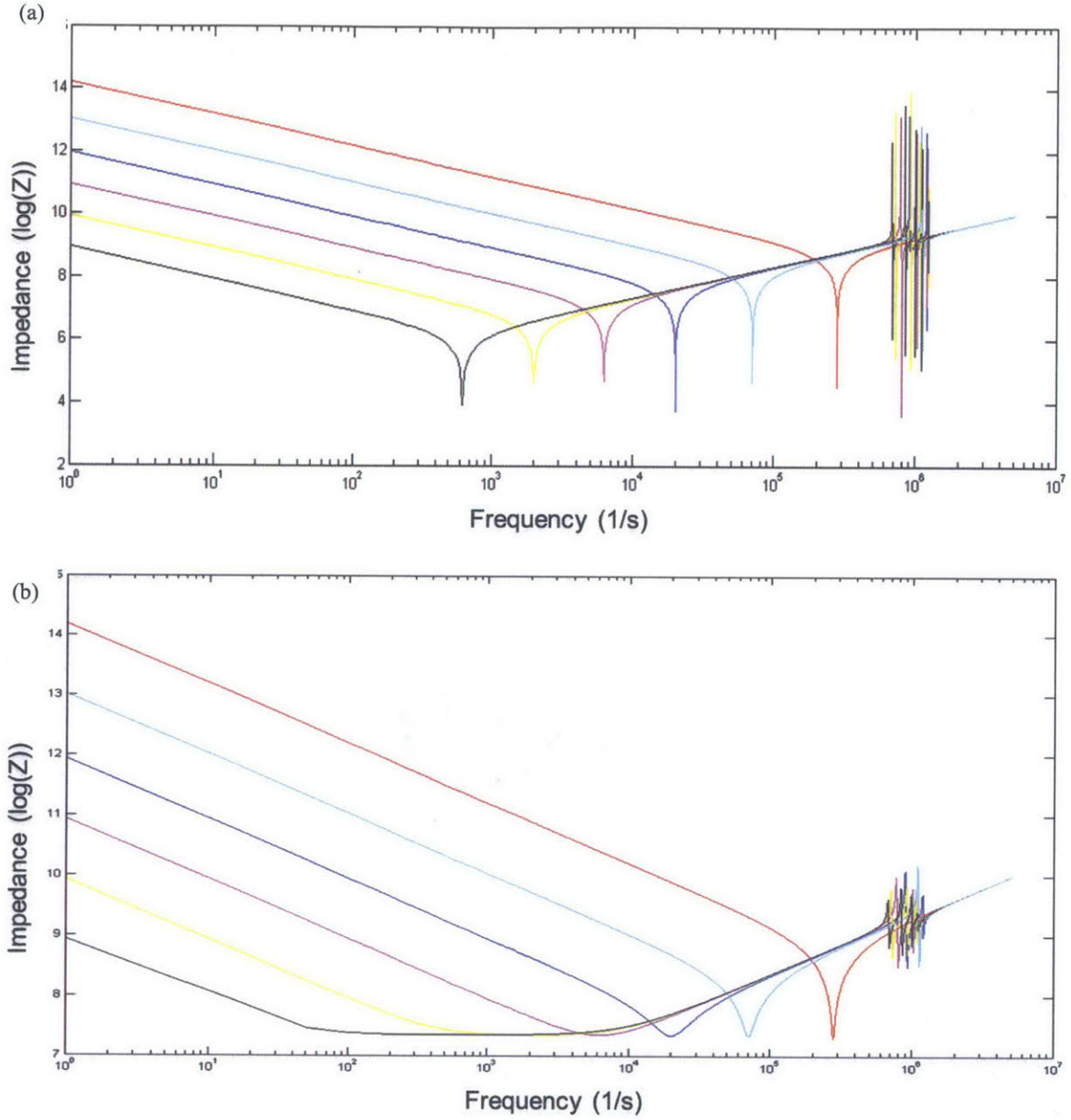

Figure 3.14: Magnitude response showing the effect of changing the number of branch division for the Helmholtz resonator tree for Lower resistance R circuit (a) and High Resistance R circuit (b).

3.2.3 Fabrication of 2D plate with finite thickness Metamaterials based on H tree motifs

Fabrication of fractals can be done with both top-down and bottom up approaches(Kubota, 2009; Pawlak, 2010; Seuront, 2010a; Shalaev, 2000c). Small particle aggregates can be prepared through atomic deposition onto a cold substrate by gravitational deposition. Self-affine random metal-

dielectric plate has also been fabricated by thermal evaporation or sputtering of metal onto an insulating substrate. More regular fractal pattern has also been fabricated with standard lithographic techniques.

H tree based system has been fabricated using a high resolution 3D printer (Project 6600) using 3D design software AutoCAD, as shown in Figure 3.14. The contact point and scaffolding geometry have to be optimized to ensure both the reliability of the fine features and easy removal of supporting scaffolding. Too sparse contact point might result in closure or defects in the fine slit feature, while too dense contact point may result in cracking of fine feature when breaking off the supporting scaffold.

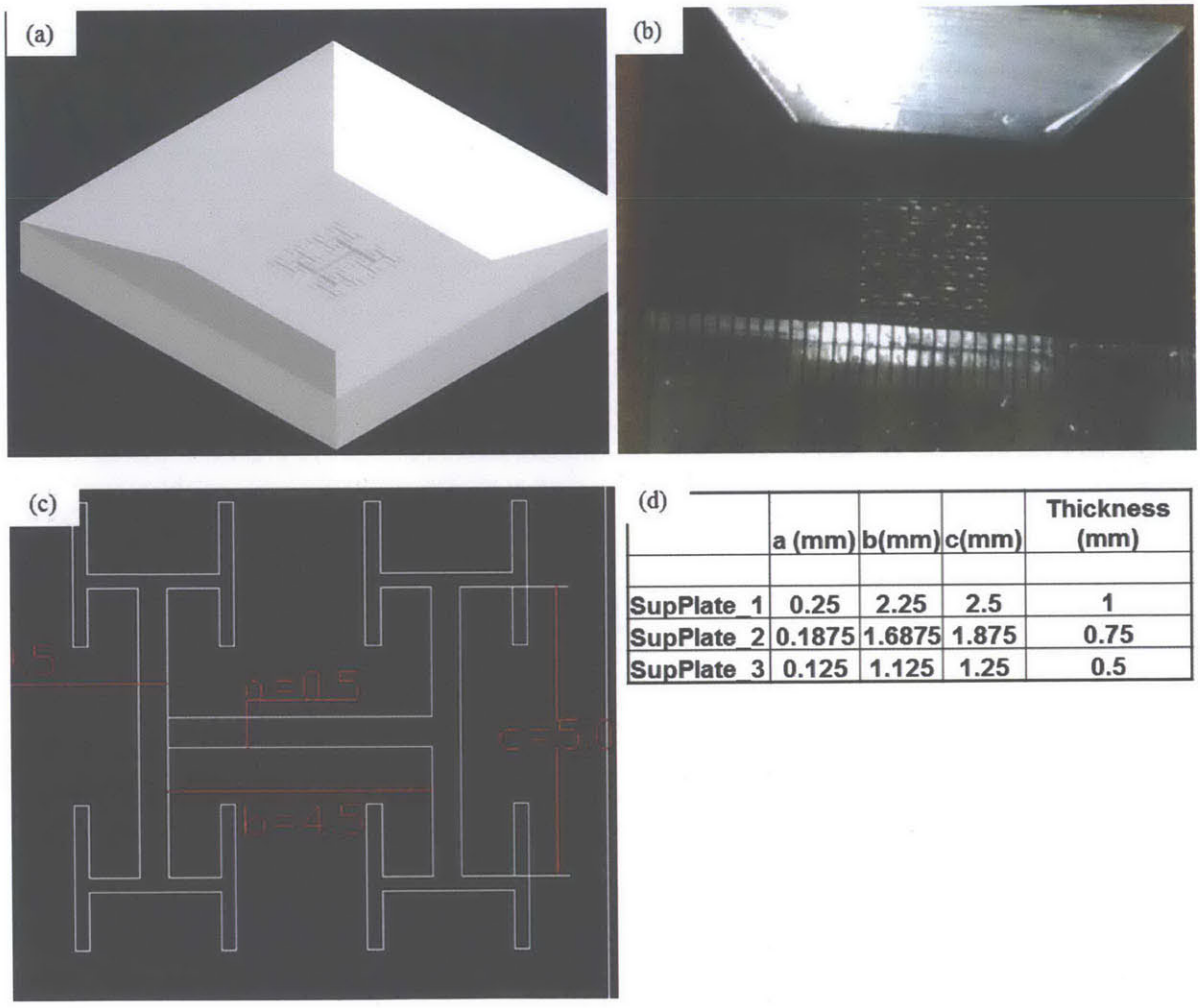

	a (mm)	b(mm)	c(mm)	Thickness (mm)
SupPlate_1	0.25	2.25	2.5	1
SupPlate_2	0.1875	1.6875	1.875	0.75
SupPlate_3	0.125	1.125	1.25	0.5

Figure 3.15: 3D drawing of H tree based sample for SAM measurement tapered platform (a) Fabricated samples using 3D printer (Project 6000) (b) detailed dimension schematics of the H tree (c) and samples dimension (d)

3.2.4 Characterization of Metamaterials based on Fractal Geometry

Another robust technique that can be used to test the phononic behavior of the system is Scanning Acoustic Microscopy (SAM). A Scanning acoustic microscope is a characterization tool that uses focused acoustic waves to image a sample (Briggs, 1982). However, the mechanism for image formation is very different from optical microscope (OM) or scanning electronic microscope (SEM)(Maev, 2008). As shown in Fig 3.15, an acoustic wave is generated using piezoelectric materials (e.g. PVDF or quartz) with in house electronic circuit to control their frequency and profile. The acoustic wave will be focused by acoustic lens (usually made of sapphire and spherical) and will then propagate through a coupling medium (e.g. water) to interact with the sample sited beneath. The reflected and transmitted wave consists information about the properties of the materials and microstructures within the sample. Therefore, a mechanical image can be obtained by scanning a stationary sample with focused acoustic wave.

Since sound can interact with opaque materials, SAM can be used to imaging subsurface features in samples, and as such, SAM is as a common Non-destructive testing technique commonly used in semiconducting industry(Maev, 2008; Manual, n.d.; Sam, 2008). To filter relevant information for testing or imaging for specific purpose, SAM offers several scanning modes, which allows insight into of the materials properties in xy plane, xz plane, 3D etc. (Fig 3.15). Since SAM is very sensitive to mechanical properties and discontinuity in materials, it can be used to map a mechanical composition of a surface by setting a reference signals. For example, it can be used to image the texture structure (e.g. crystallographic orientation) of polished surfaces without the need for etching.

Moreover, SAM can also be used to investigate composite materials, once such example is concrete sample made with granitic aggregate grains and Portland cement. Using a transducer centered around 400 MHz, SAM can clearly identify the boundaries between different materials as well as their distribution, some of which are hardly distinguishable from SEM. Therefore, a SAM image carries rich information that is valuable for mapping out mechanical composition of an object.

Besides hard materials, SAM has also been used to investigate soft materials in biological and medicine studies (Maev, 2008). For example, SAM has been used to study the physiochemical processes of cell during heating. It was found that cell delamination-detachment would happen,

followed by cell death if the temperature was increased further. Due to its unique imaging formation mechanism, SAM can be used to obtain distinct information about samples, which are difficult to accesses from other techniques. The SAM apparatus at MIT currently has an imaging resolution of around 6 um, which could be potentially attractive for samples with comparable or larger features sizes. The SAM can also be used in both transmission and reflection modes, although reflection modes is preferred in many case due to the less strict requirement in the thickness of the sample. Despite its robust and versatile capacities, few studies have been done to use SAM to probe structures with micrometer feature sizes. By modifying the profile of the incident acoustic waves and tailor making the samples, SAM could potentially be a powerful tool to probe the phononic properties, especially surface/interface phonic properties, which are really attractive for device design and applications.

To fully leverage on the capacity of SAM, we tested a sample made of transparent resin from high-resolution 3D printer as described from the last section. The H tree pattern is the slits (i.e. scatter phase) while the matrix phase are plastic solid surrounding the slits. The edge of the matrix square a is 5mm, while the a/l/t ratio is the same as sample H2_thin. The center frequency we used for

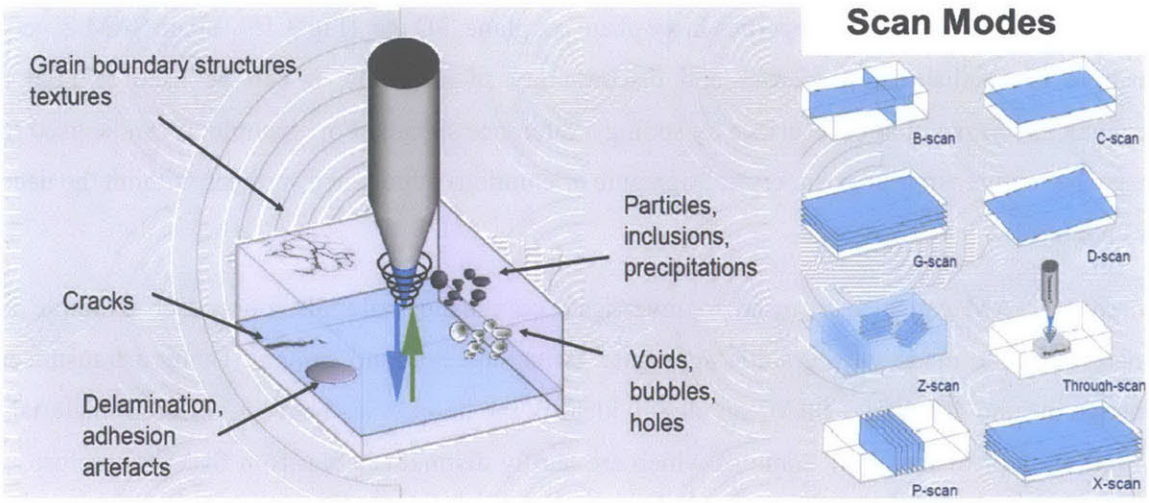

Figure 3.16: Schematics for image forming mechanisms of the scanning acoustic microscope (SAM). The transducer generates acoustic waves that are incident on sample containing microstructures, such as cracks, delamination, voids or particle inclusions. Different scanning modes in SAM offer various applications, C scan is the most common xy plane scanning, where B scan is xz or yz plane, which can be used for thickness analysis using time of flight.

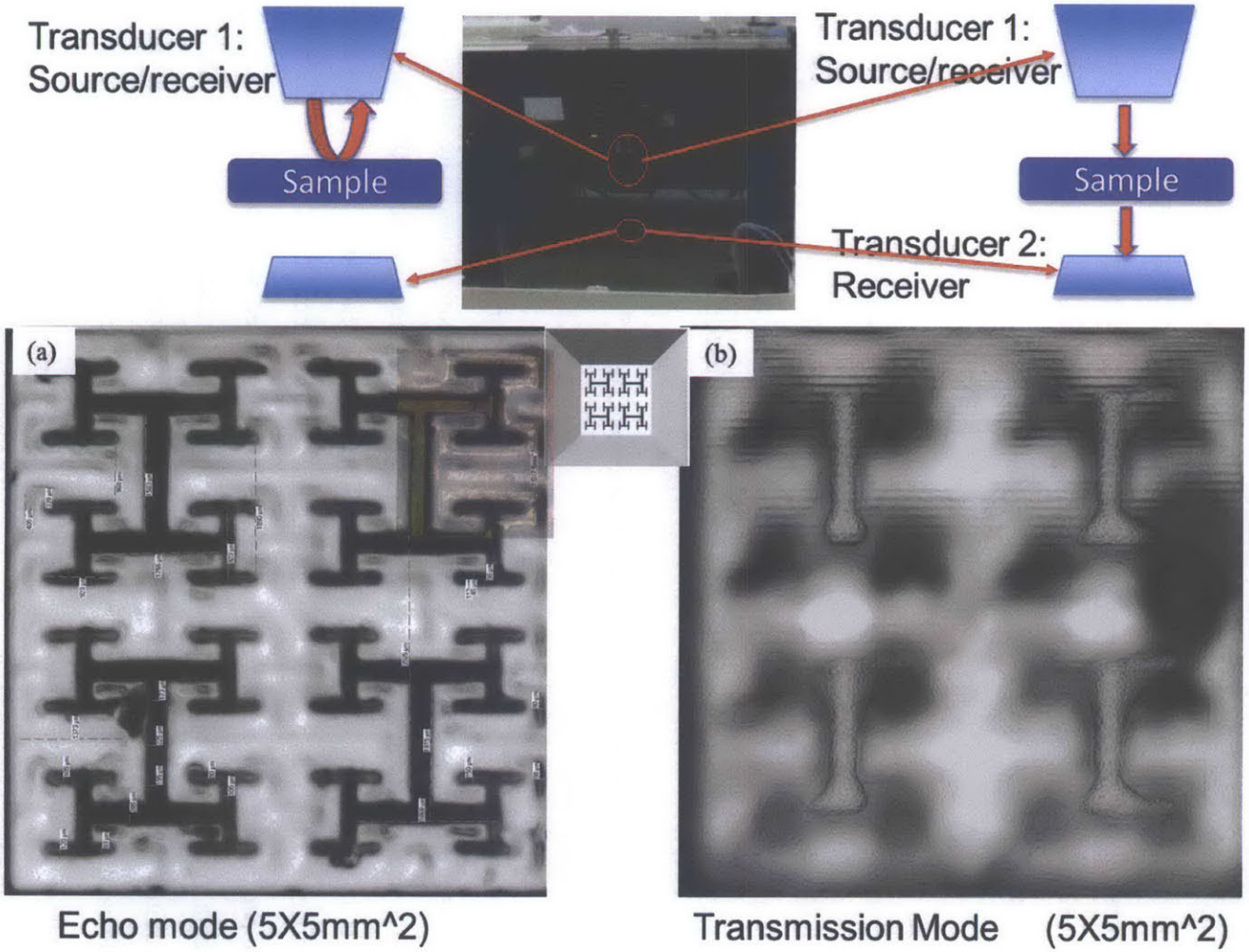

Figure 3.17: Scanning Acoustic Microscope (SAM) image of the 4XH2 tree sample (middle insert) in both reflection (a) and transmission (b) modes with the optical image of the corner overlap on top of the SAM images. The schematics of both modes has been shown on top of the images with the instrument in the middle.

imaging is 50 MHz (i.e. um), where both reflection and transmission mode are used for the imaging. As mentioned above, SAM is very sensitive to surface features of the sample in reflection modes, especially in a defocused position. The surface finish of the sample from our 3D printer around the slits shows clearly in the image in the reflection modes, where the height difference between immediate vicinity of the slit and those further away is reflected in the different grey value of the image. Furthermore, the sharp corners in the 3D drawing are rounded in the images, which could result from limitation of both the 3D printing and the SAM imaging. Furthermore, the dimension of the slits and other features has also been measured, which correspond well with the design parameters defined in the AutoCAD software. The transmission mode is a complementary technique to the reflection modes. The sharp corner is not preserved for the images which is likely due to the diffraction at the sharp corner.

3.3 Metamaterials with Hilbert Curve as the binary phase boundary

3.3.1 Theoretical study

Hilbert curve is a continuous space-filling curve that can visit every point in a square grid with a size of 2×2, 4×4, 8×8, 16×16, or any other power of 2. It was first described by David Hilbert in 1892 as a variant to other spacing-filing curve developed by Giuseppe Peano(David, 1869). Its length in Euclidean space varies with the level of iteration as$2^n - 2^{-n}$, which grows exponentially yet is bounded within a finite area.

Since Hilbert curve as well as its prefractal preserves locality when mapping between 1D and 2D space, (i.e. points are close by along the curve would also have nearby coordinate values in xy plane), they have been used widely in computer science(Nikos Mamoulis et al., 2009). They have been used to in linear mapping between multidimensional data warehouse by utilizing its unique clustering properties(Moon et al., 2001; Nguyen et al. , 2012; Zhou et al., 2012). To further improve their performance, modified Hilbert Curves have been used to adapt to constrains and demands of data applications(Hamilton et al., 2008; Meng et al., 2007). It also been used for visualization of genome data to get better insight than conventional way of presenting data(Anders, 2009). A triple band flexible loop antenna based on third order Hilbert Curve was found to exhibit omnidirectional radiation pattern and circular polarization(Yang, 2012).

The subdomains of the scatterer and matrix are separated by the approximate Hilbert curve with different level of literation, as shown in Figure 3.18, where periodic boundary condition is applied at the edge of the square cell. To investigate the scale dependent behavior of the system, the iteration level has been varied. Similarly, Young's modulus and the arrangement have also been varied to study their effect on Hilbert Curve bounded system.

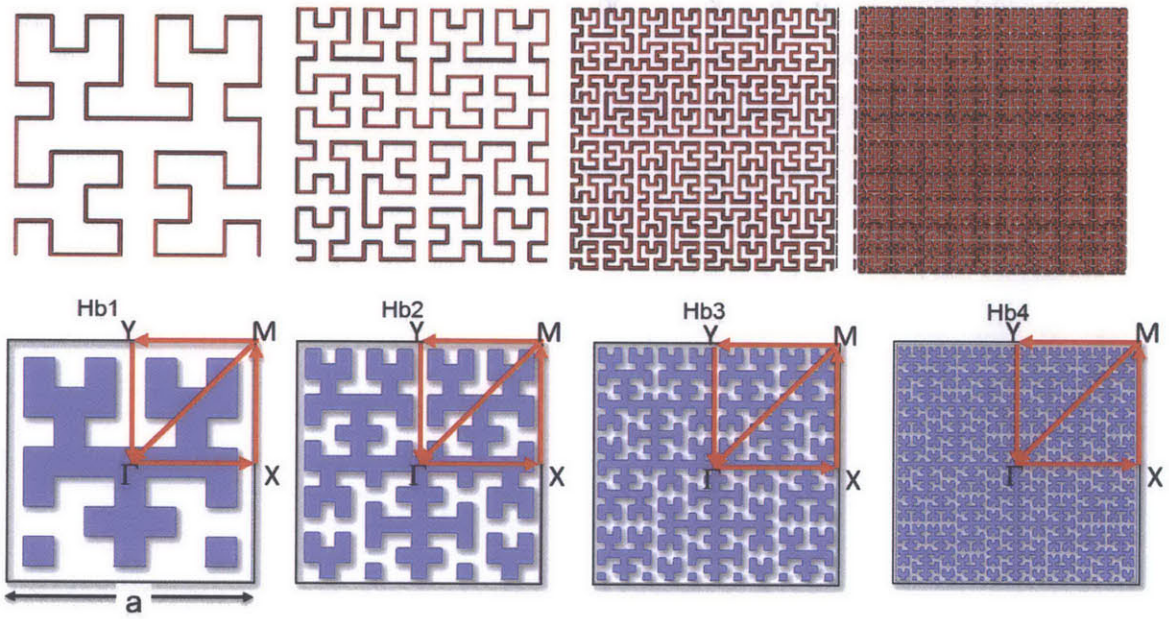

Figure 3.18: Top row is Hilbert curve with iteration level of 3, 4, 5 and 6 respectively, the corresponding unit cells Hb1, Hb2, Hb3 and Hb4 are plotted in second row, where blue is the scatterer phase and the white region is the matrix phase. The filling ratio η of Hb1, Hb2, Hb3 and Hb4 are 0.4373, 0.4708, 0.4862 and 0.4868 respectively. The BZ zone is also superimposed on top of the unit cell, where the edge length of the unit cell is indicated for Hb1 too.

Table 3.5: Hb patterns fill fraction for system studied

Sample Name	Level of Hilbert Curve iterations	Fill ratio (Scatterer phase)
Hb1	N = 3	0.437
Hb2	N = 4	0.471
Hb3	N = 5	0.486
Hb4	N = 6	0.487

3.3.1.1 General framework

As shown in Figure 3.19, the Hilbert curve bounded pattern has a mirror plane along y axis and identity at Γ point while the symmetry element reduced to identify along ΓX and MΓ direction. Along the XM direction, the symmetry is again mirror along y axis and identity, where the displacement can be either symmetric or antisymmetric with respect to the wave vector k_{XM}. At point X, mode 1 and 4 as well as mode 13 and 14 are both antisymmetric with respect to y axis mirror, and an avoided crossing leads to the band gaps. Similarly, two other pairs, mode 3 and 8 as well and mode 11 and 12, are antisymmetric with respect to y axis mirror. At point M, the y

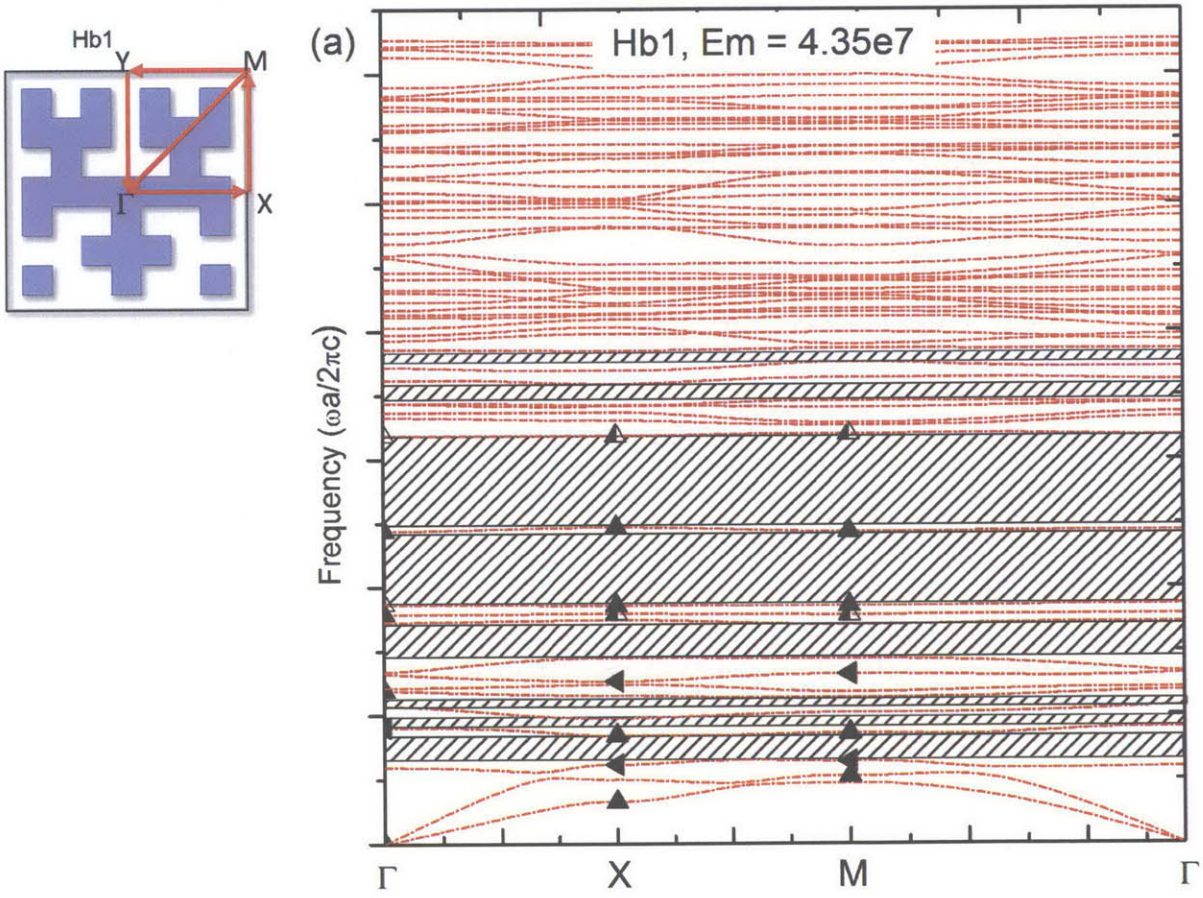

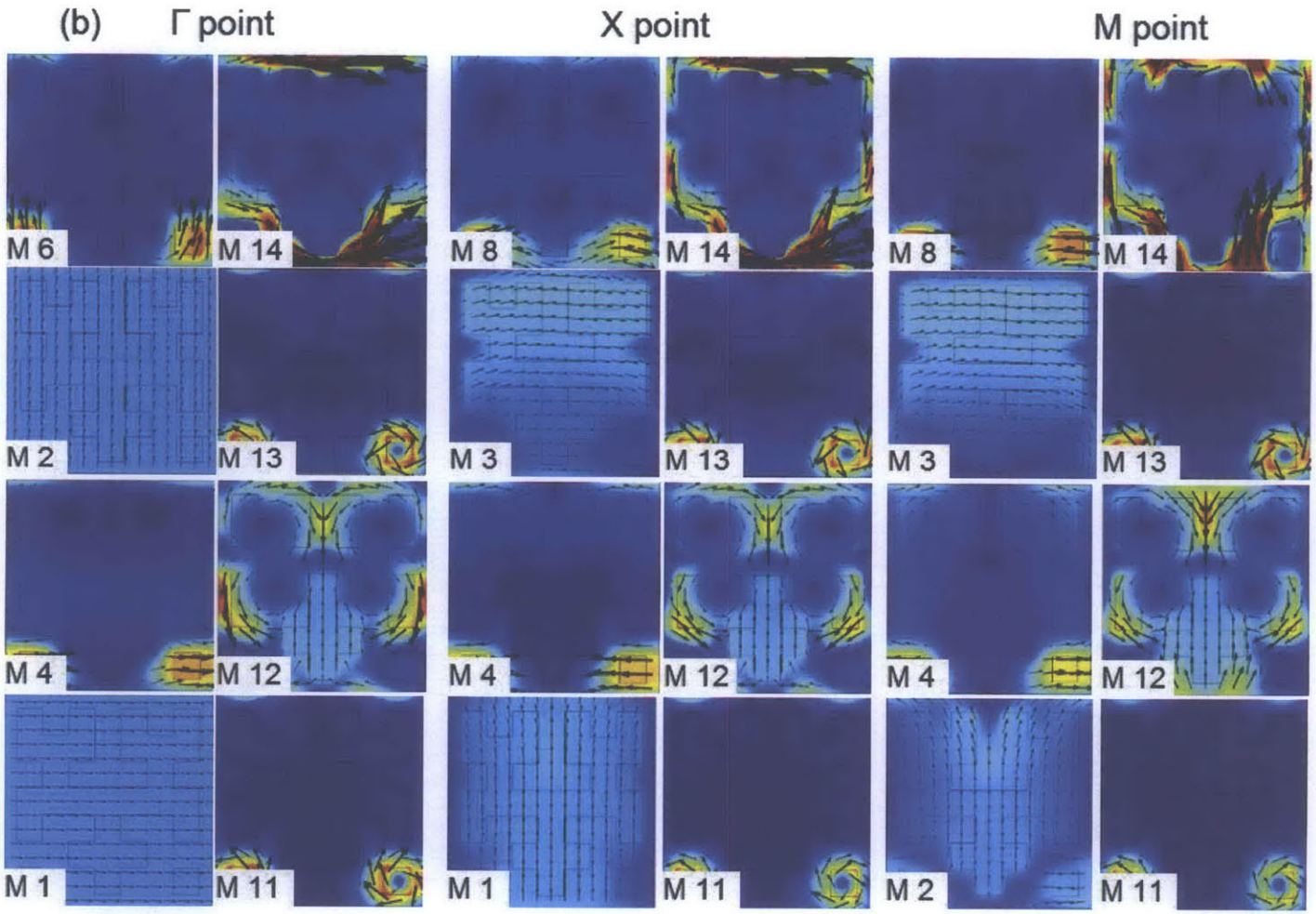

Figure 3.19: (a) The dispersion curves for sample H2 (Es = 4.35e7Pa) (red short dash dot) along the BZ of the unit cell (along Γ→ X→M) as indicated in the unit cells in the right insert. (b)The eigenmodes (highlighted as black solid triangle (or circle) are arranged at the side as indicated, Both eigenmodes M1 and M9 are symmetric with respect y axis while M3 and M11 are anti-symmetric with respect to y axis at X point. At X point, the interacting pairs are M1 M8 (symmetric with respect y axis), and M3 M11 (anti-symmetric with respect y axis).

axis mirror symmetry and the identity also enable the possibility of avoid crossing. The pairs with symmetric (with respect to y axis) eigenmodes are M2 (M4) and M11 (M12); the pairs with antisymmetric (with respect to y axis) eigenmodes are M3 (M8) and M13 (M14).

3.3.1.2. Material Properties

The materials properties investigated are listed in Table 3.2 for the binary system, where the Young's Modulus of the scatterer phase is varied. When the modulus of the scatterer decreases from 4.35e10 Pa to 4.35e6 Pa, the eigenfrequencies will decrease as expected, as shown in Figure 3.20. For long wavelength (or lower frequency) eigenmodes, the eigenmodes of samples with rigid and soft scatterers looks similar except the Hilbert curve boundary is more conspicuous at a higher impedance contrast, (e.g. M1 and M3(4) at X point in Figure 3.19 eigenmodes plot). This high impedance contrast between scatterers and matrix results in more localized displacement fields, i.e. the displacement are better confined in the soft scatterer phase. Hence, the eigenmodes at higher frequency appear to be more localized, hence the dispersion curve are flattened (as shown in Figure 3.19 eigenmodes M14 (15) at X point and M16 (15) at M point).

3.3.2.3 Levels of iterations

The effect of the level of iteration has also been studied for the Hilbert curve pattern, as shown in Figures 3.21, 3.22 and 3.23. As mentioned above, the filling fraction of scattering phase increases gradually with increasing N (i.e. 0.4373, for iteration level N = 3, 0.4708 for iteration level N = 4, 0.4862 for iteration level N = 5). When the scatterer phase has a higher Young's modulus, the eigenfrequency increases with increasing N, as shown in Figure 3.21. However, when scatterer become the softer phase (i.e. Es < Em), the eigenfrequencies decrease from sample Hb1 to Hb3, Therefore, filling fraction itself is insufficient to determine the eigenfrequency even the material properties are the same for the binary phase. At the low frequency, the eigenmodes correspond to the longitudinal and transverse mode, hence the salient features of the eigenmode are retained since the wavelength is much larger than the feature size in the binary composite. However, with increasing level of iteration, the number if bandgaps and size seems to increase from Hb1 to Hb2 and then decrease Hb3. For Hb3, the dispersion curve seems to indicate more extended displacement field, which is reflected in the than the feature size in the binary composite. However, with increasing level of iteration, the number if bandgaps and size seems to increase from Hb1 to

Hb2 and then decrease Hb3. For Hb3, the dispersion curve seems to indicate more extended displacement field, which is reflected in the localization characteristic of eigenmodes.

Table 3.6: Material properties of the system studied for binary and matrix phase, the Young's Modulus of the scatterer phase is varied. The scatterer1 here approximates the properties of lead and Scatterer2 has Young's Modulus similar to the epoxy. The Matrix3 is close to that of a rubber. The properties of matrix is close to PMMA.

Material Properties	Scatterer1	Scatterer2	Scatterer3	Matrix
Young's Modulus Pa	4.35e10	4.35e7	4.35e6	4.35e8
Poisson Ratio	0.329	0.329	0.329	0.375
Density kg/m^3	972	972	972	2500

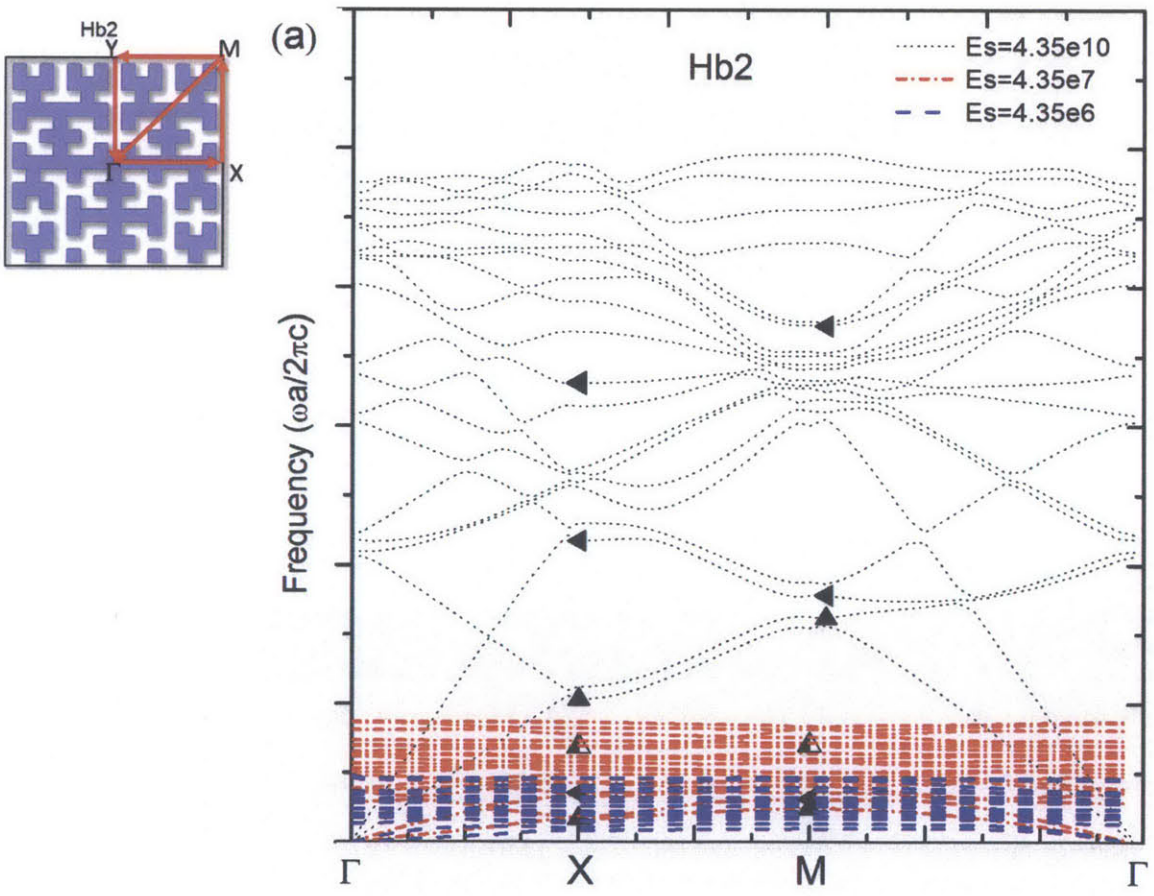

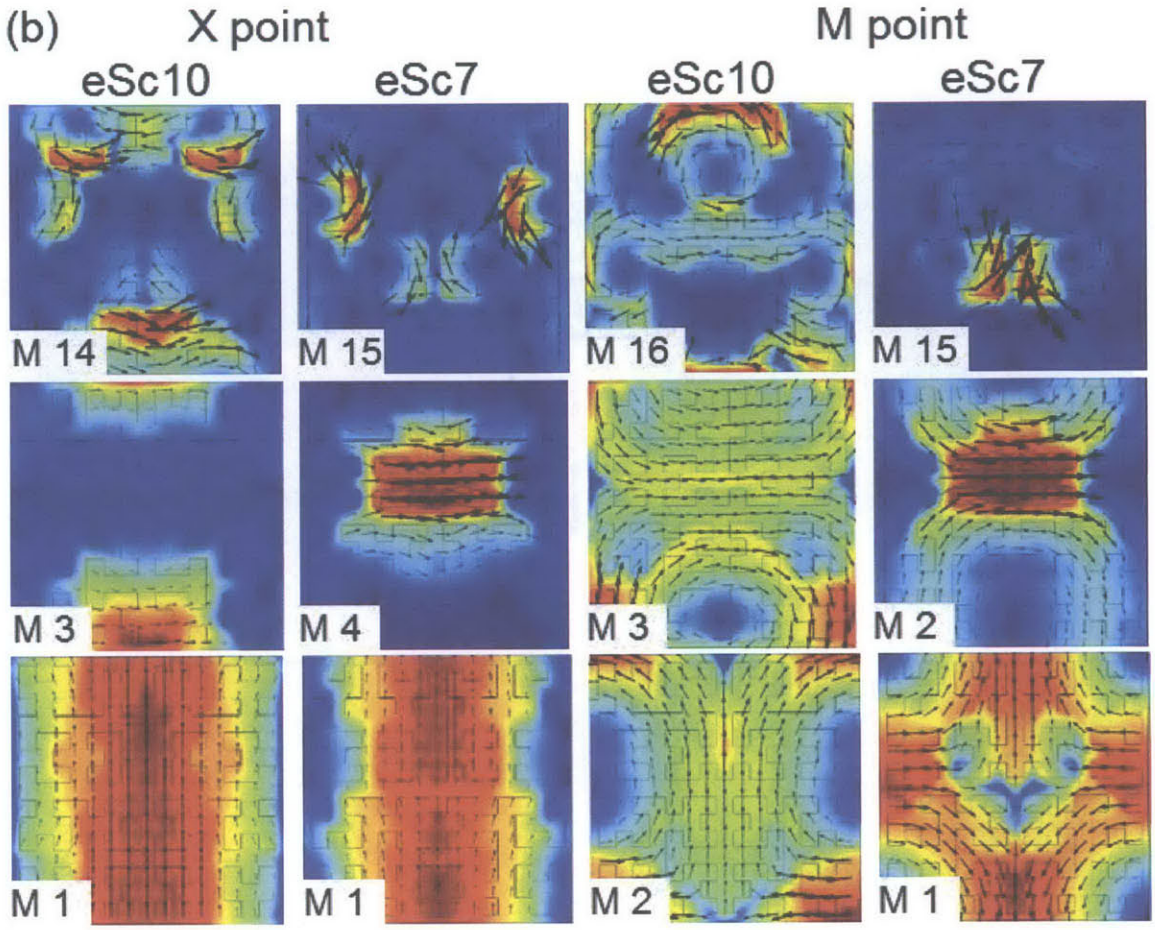

Figure 3.20: (a) The dispersion curves for sample Hb2 with varying Young's Modulus for scatterer phase, e.g. Es = 4.35e10Pa (black dot line), Es = 4.35e7Pa (red short dash dot) and Es = 4.35e6Pa (blue dash) along the BZ of the unit cell (along Γ→ X→M→ Γ) as indicated in the unit cells on the right insert. (b)The eigenmodes (highlighted as black solid triangle are arranged at the side as indicated, , All eigenmodes are symmetric or anti-symmetric with respect to y axis where the high strain region is more localized for samples with higher mechanical impedance contrast.

Table 3.7: Material properties used for the simulation for dispersion curves. The scatterer here approximates the properties of lead and the matrix1 has properties similar to the epoxy SU8. The Matrix3 is close to that of a rubber.

Material Properties	Matrix1	Matrix2	Matrix3	Scatterer
Bulk Modulus Pa	4.35e9	4.35e7	4.35e6	4.08e10
Poisson Ratio	0.368	0.368	0.368	0.37
Density kg/m^3	1180	1180	1180	11600

Furthermore, given multiple spectral band gaps formed, several avoided crossings happened between eigenmodes with the same symmetry even at higher frequencies, as shown in Figure 3.23 (c). Furthermore, as the level of iteration increases, the location of lowest bandgaps shifted upward comparing Hb2 and Hb3, as shown in Figure 3.22 and Figure 3.23.

At higher frequency, the displacement are also more spread out for Hb3 than for Hb2 and Hb1 (Fig 3.19, 3.21 eigenmodes). Although all the eigenmodes still possess antisymmetric/symmetric with respect to y axis or identity, the eigenmodes no longer resemble one another. While the transition for high strain/high energy (i.e. high displacement) and low strain/low energy (i.e. low displacement) region at smaller N (i.e. Hb1) are smoothed over sharp corners of Hilbert Curve boundary, the transition follows the Hilbert Curve more closely at higher N, such as M5 (7) and M7 (6) at M point for Hb1 (3) (Fig 3.19, 3.21 eigenmodes).

When the literation level becomes relatively high (N = 5 and N = 6), the difference at lower frequency become less and less since the composite becomes almost homogeneous given the ratio of wavelength/feature size of phase boundary), as shown in dispersion curves of Hb3 and Hb4 from Figure 3.23. With increasing level of iteration and torturous nature of the boundary, the transition for hot (i.e. high displacement) and cold (i.e. low displacement) region are more linear compared to lower level iteration (i.e. the displacement direction have less rotational component).

For all the four samples we studied, two impedance contrast are chosen since increase impedance would affect the dispersion behavior locally. By tabulating the features of bandgaps in table 3.8,

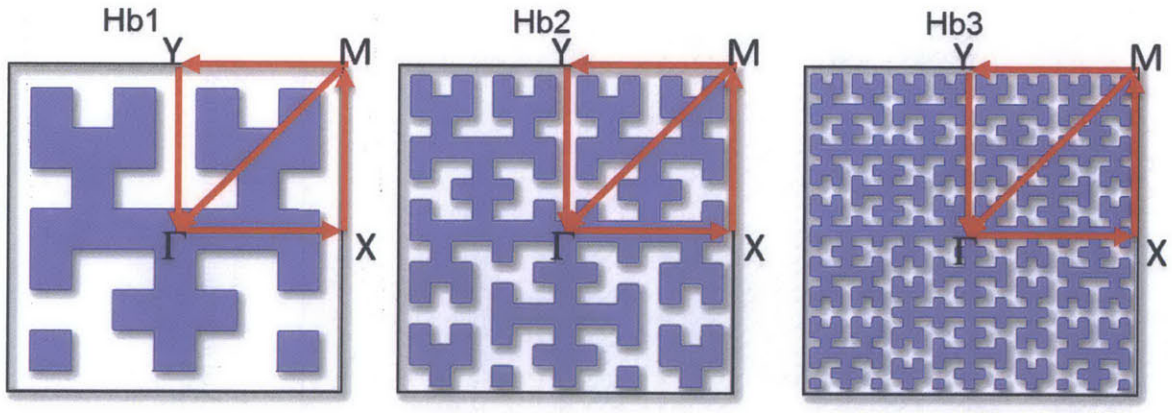

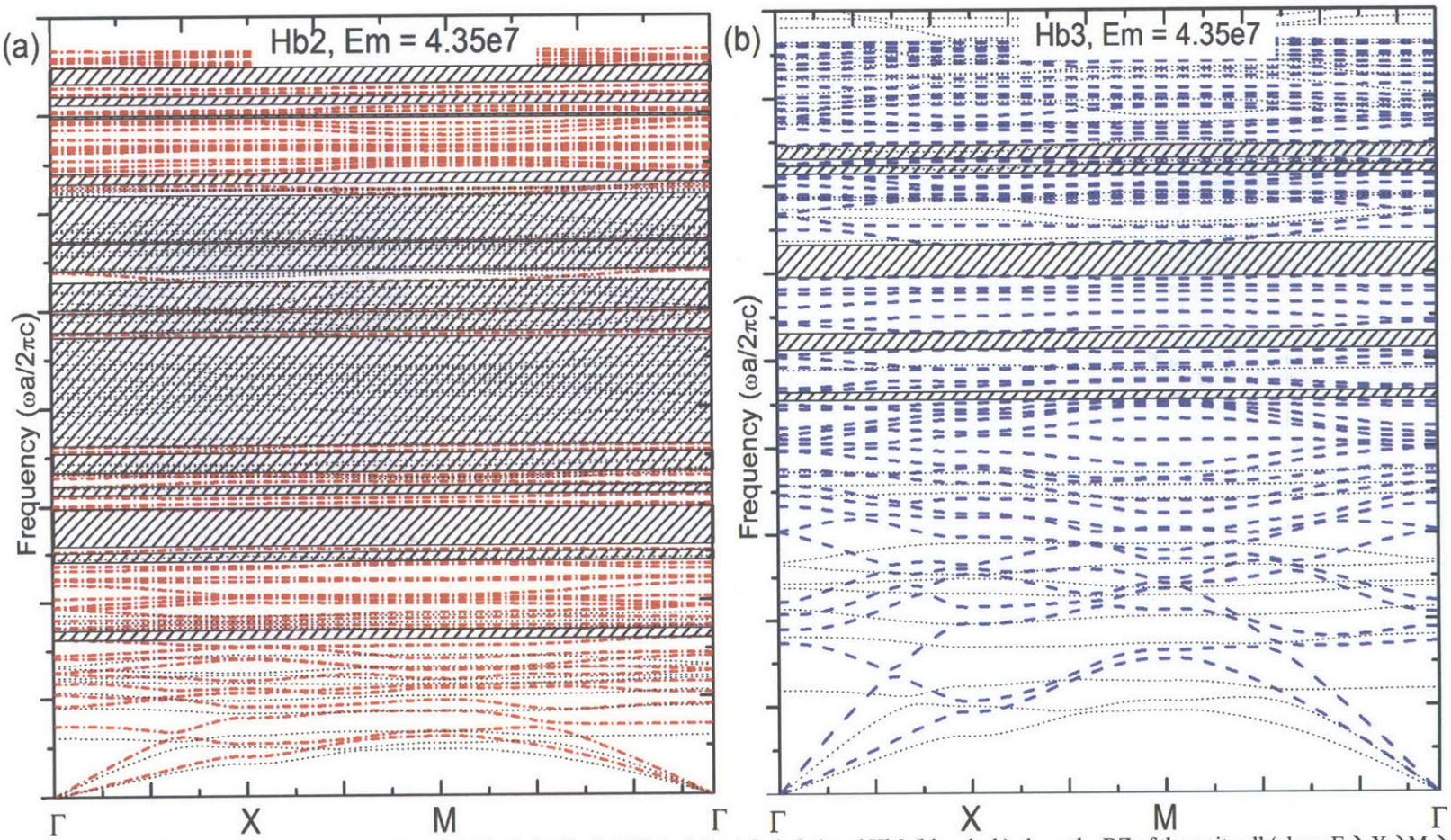

Figure 3.21: The dispersion curves for samples Hb1 (black dot line), Hb2 (red short dash dot) and Hb3 (blue dash) along the BZ of the unit cell (along Γ→ X→M→ Γ) as indicated in the unit cells in the Figure 3.18. The materials constants used are Em = 4.35e7, others are listed in Table 3.2

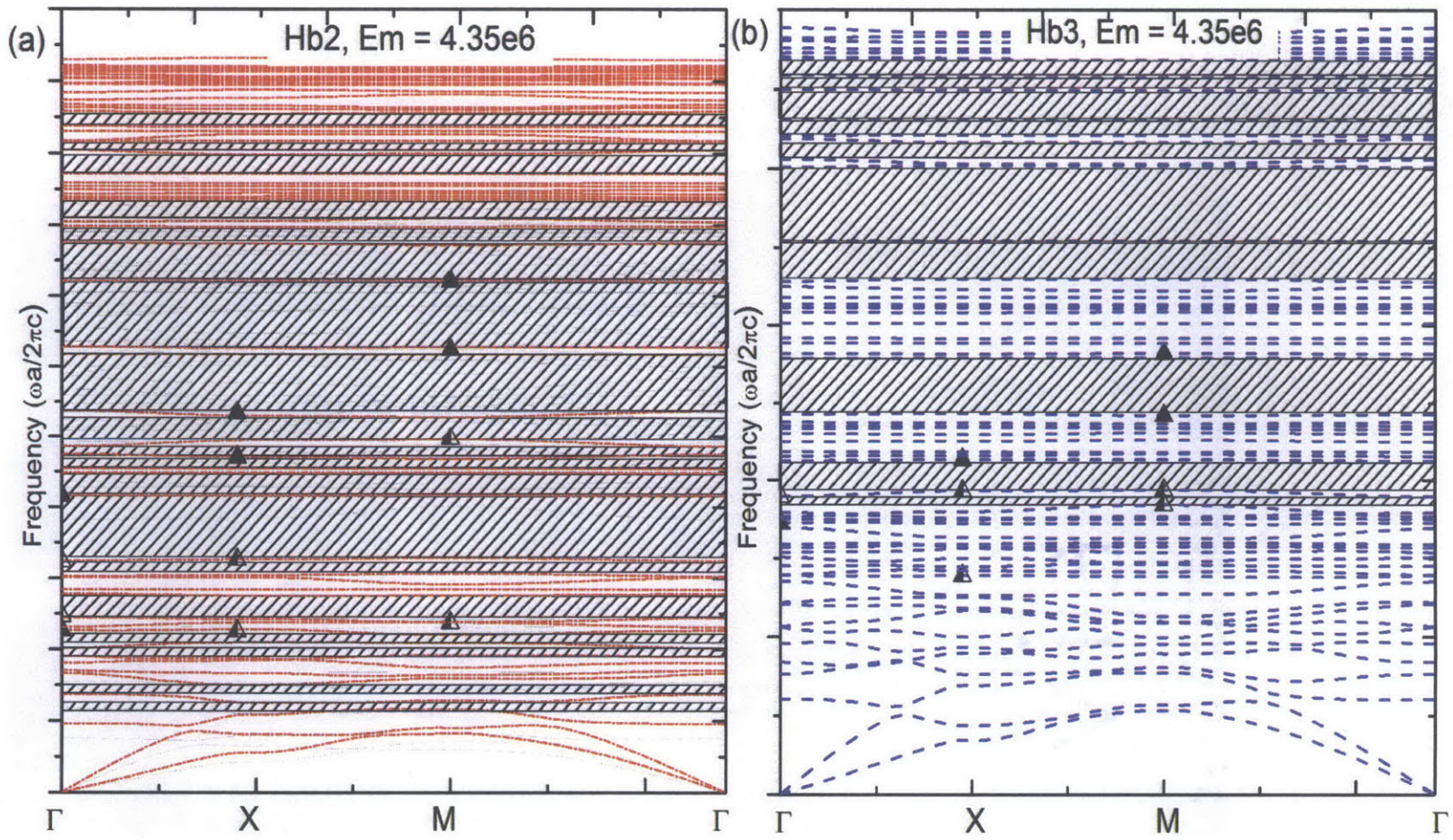
(a)
Hb2, Em = 4.35e6
Frequency (ωa/2πc)
Γ
X
M
Γ
(b)
Hb3, Em = 4.35e6
Frequency (ωa/2πc)
Γ
X
M
Γ

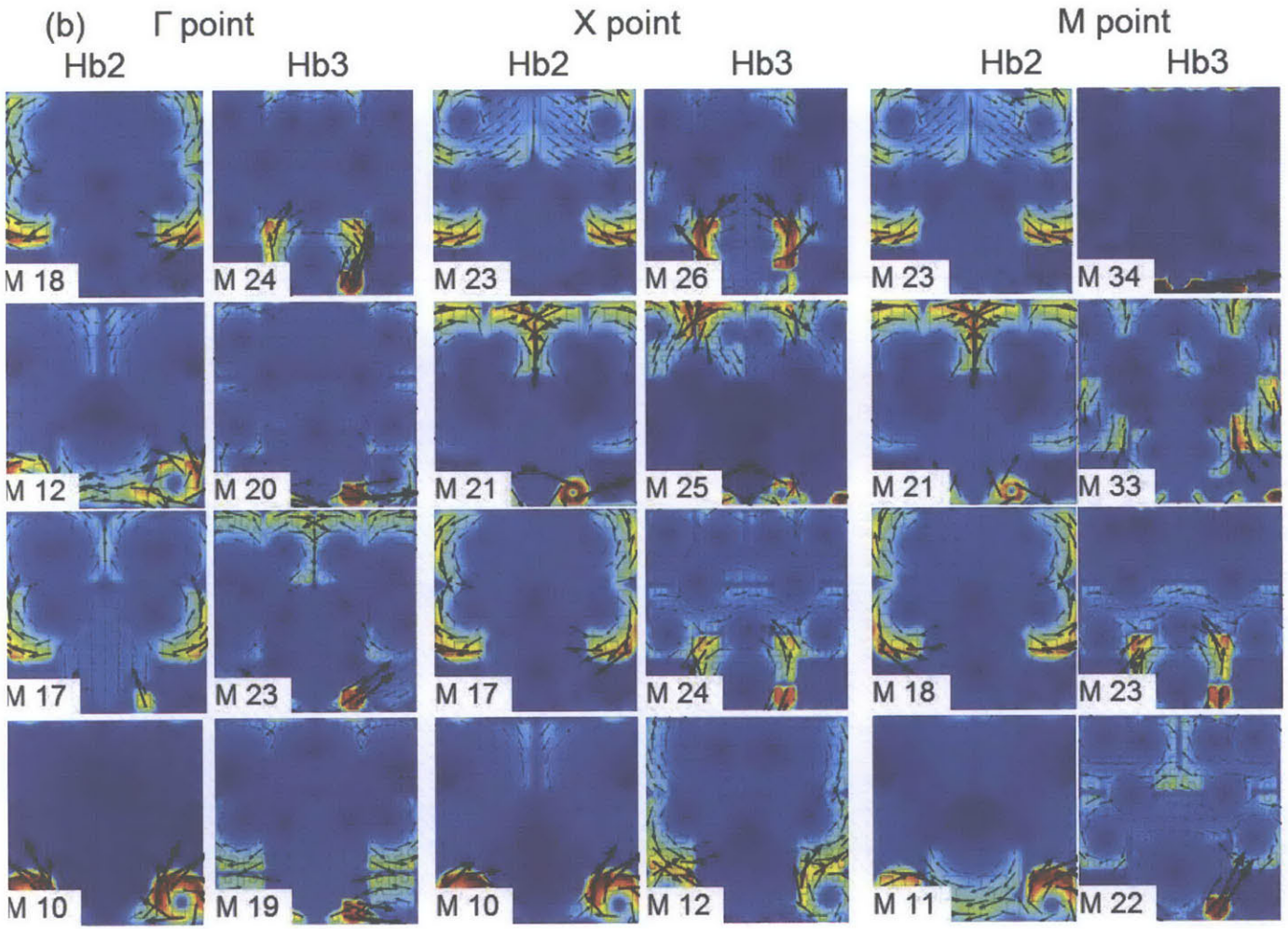

Figure 3.22: (a) The dispersion curves for samples Hb1 (black dot line), Hb2 (red short dash dot) and Hb3 (blue dash) along the BZ of the unit cell (along Γ→ X→M→ Γ) as indicated in the unit cells in the Figure 3.18. The materials constants used are Es = 4.35e7, others are listed in Table 3.2. (b)The eigenmodes for Hb1 (black solid triangle) and Hb3 (olive solid triangle) are arranged at the side as indicated, Both eigenmodes M1 and M9 are symmetric with respect y axis while M3 and M11 are anti-symmetric with respect to y axis at X point. At X point, the interacting pairs are M1 M8 (symmetric with respect y axis), and M3 M11 (anti-symmetric with respect y axis)...

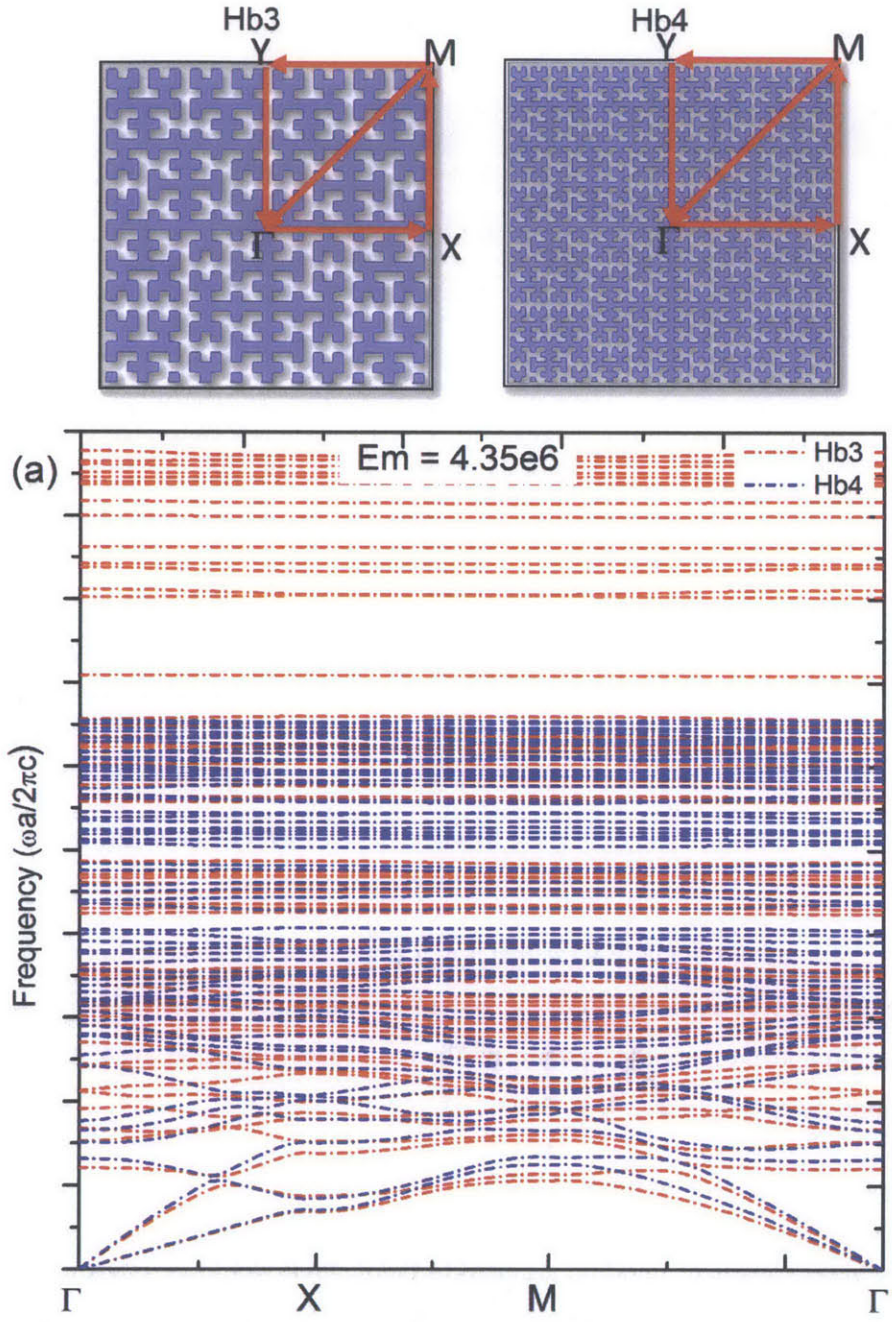

Figure 3.23: (a) The dispersion curves for samples Hb1 (black dot line), Hb2 (red short dash dot) and Hb3 (blue dash) along the BZ of the unit cell (along Γ→ X→M→ Γ) as indicated in the unit cells in the Figure 3.18. The materials constants used are Em = 4.35e6, others are listed in Table 3.2.

Table 3.8: Bandgaps data formed for samples with different levels of iteration and impedance contrast (for the frequency range we investigated)

Sample Name	Number of bandgap	Size of bandgap	Impedance contrast
Hb1	31	0.689	$Ks/Km = 96.023$
Hb2	42	0.572	$Ks/Km = 96.023$
Hb3	28	0.149	$Ks/Km = 96.023$
Hb4	9	0.025	$Ks/Km = 96.023$
Hb1	35	0.769	$Ks/Km = 303.023$
Hb2	54	0.770	$Ks/Km = 303.023$
Hb3	50	0.491	$Ks/Km = 303.023$
Hb4	27	0.133	$Ks/Km = 303.023$
Hb1_2	43	0.684	$Ks/Km = 96.023$
Hb1_2	48	0.821	$Ks/Km = 303.023$
Hb2_3	28	0.124	$Ks/Km = 96.023$
Hb2_2	40	0.342	$Ks/Km = 303.023$

we can see that the size of bandgap increase with increasing impedance contrast, however, the trend with levels of iteration is less obvious. From the system we investigated, Hb1 and Hb2 are both good candidate for broadband response system. Furthermore, Hb1 might be even superior given the number of bandgaps is smaller.

3.3.2.4 Variation of the arrangement of building blocks

Since structures having higher levels of iteration are hard to fabricate, it would be interesting to know if their properties can be mimicked by arranging the building blocks with lower level of iteration. To mimic the behavior of Hilbert Curve with iteration level 4, we arrange the building blocks with Hilbert Curve with iteration level 3 (sample Hb1_2), as shown in unit cell in Figure 3.23. We define the scatterer and matrix in such a way that matrix are connected across the unit cell, similar to original cell Hb2, while the boundary between scatterers and matrix are still similar

to by approximate Hilbert Curve. It can be reorganized that the top portion of Hb1_2 is identical to Hb2 while the bottom portion is complementary to Hb2. The dispersion curves differs from each other significantly for sample Hb1_2 and Hb2 for Young's Modulus of Em = 4.35e7Pa (Fig 3.24 (a)) and Em = 4.35e6Pa (Fig 3.24 (b)). The filling ratio of the stiffer scatterer phase of Hb1_2 (0.455) is smaller than that of Hb2 (0.4708) and the dispersion curve shift downwards from Hb2 (Fig 3.23(a)).

A similar process was applied to Hb2 and Hb3 as shown in the unit cell in Figure 3.24. Again the top portion of Hb2_3 is identical to Hb3 while the bottom portion is complementary to Hb3. The dispersion curves differ from each other for sample Hb2_3 and Hb3 for Young's Modulus of Em = 4.35e7Pa (Fig 3.25 (a)) and Es = 4.35e6Pa (Fig 3.25(b)). The filling ratio of stiffer scatter phase of Hb2_3 (0.4715) is smaller than that of Hb3 (0.4868) By simply modifying the arrangement of the motif, the size of bandgaps increases comparing Hb1_2 to Hb2, as shown in Table 3.8 However, the trend is not preserved for sample Hb2_3 and Hb3.

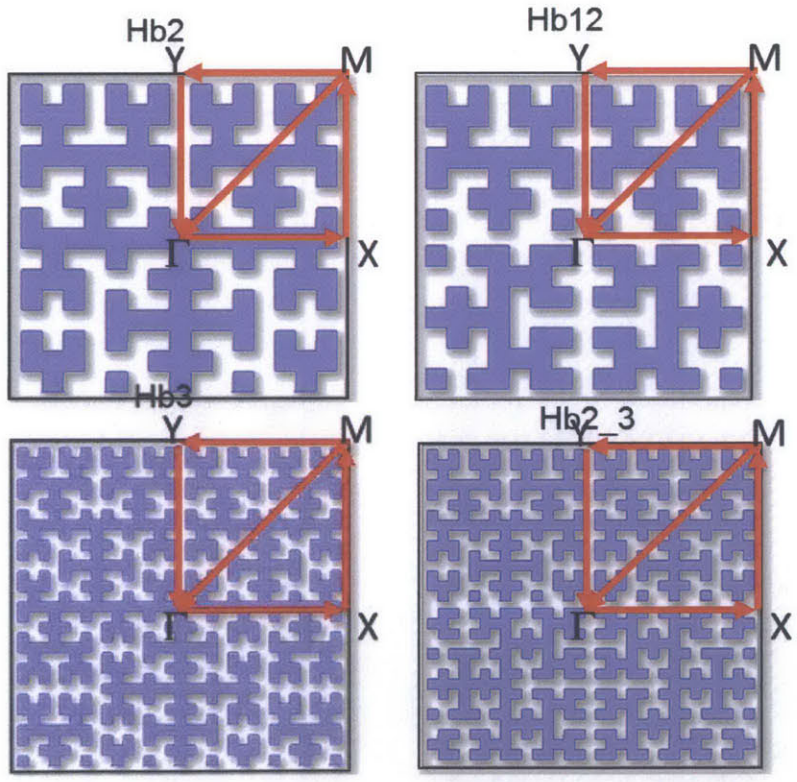

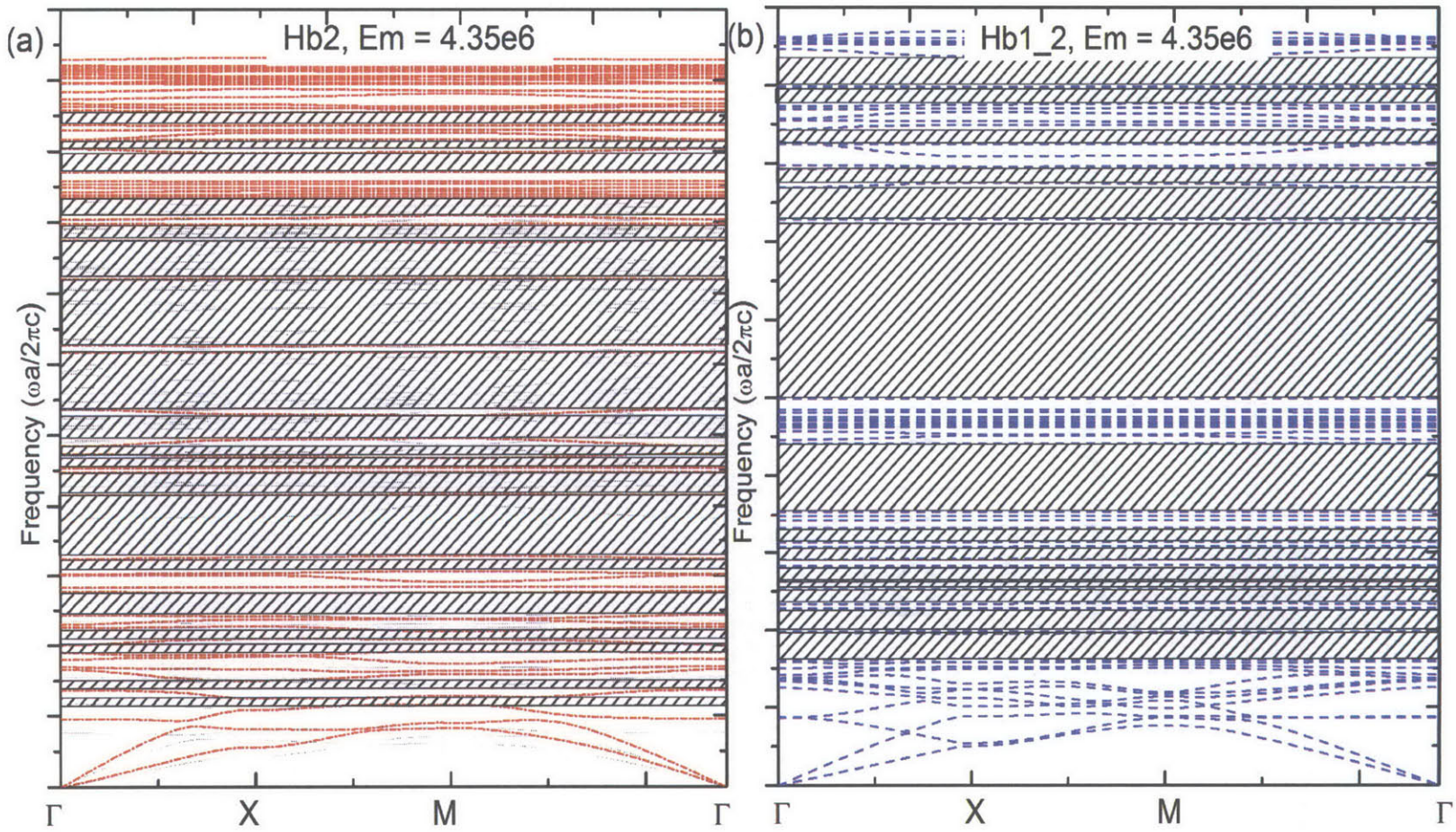

Figure 3.24: The dispersion curves for sample Hb2 (red short dash dot) (a) Hb1_2 (blue dash) (b) with Young's Modulus of scatterer phase Em = 4.35e6 along the BZ of the unit cell (along M→ Y→ Γ→ X→M) as indicated in the unit cells above the dispersion curve. The filling ratio η of Hb2, Hb1_2, are 0.4708 and 0.4550 respectively.

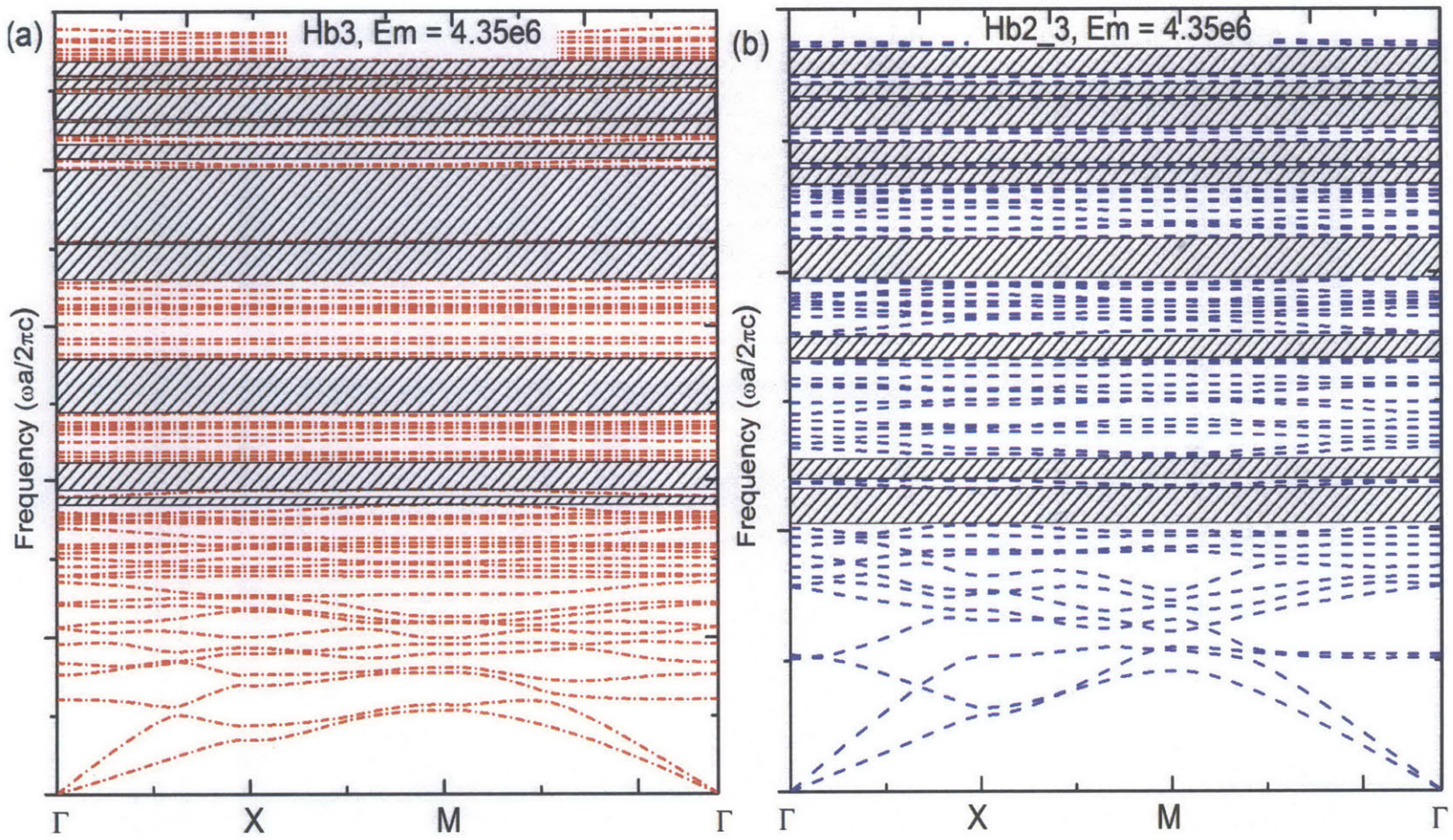

Figure 3.25The dispersion curves for sample Hb3 (red short dash dot) (a) Hb2_3 (blue dash) (b) with Young's Modulus of scatterer phase Em = 4.35e6 along the BZ of the unit cell (along M→ Y→ Γ→ X→M) as indicated in the unit cells above the dispersion curve. The filling ratio η of Hb3 and Hb2_3 are 0.4868 and 0.5715 respectively.

3.3.2 Fabrication of 3D Metamaterials based on Hilbert tree motifs

Hilbert Curve bounded systems with different levels of iterations have been fabricated using high resolution 3D printer (Project 6600) by designing using AutoCAD, as shown in Figure 3.24. As the level of iteration increases, the fabrication process is more challenging since the supporting scaffolding would have more point of contact with sample for facilitate the thin slit structure. The contact point and scaffolding geometry have to be optimized to ensure both the reliability of fine feature and easy removal of supporting scaffolding. Too sparse contact point might result in closure or defects in the fine slit feature, while too dense contact point may result in break of fine feature when braking off the supporting scaffold.

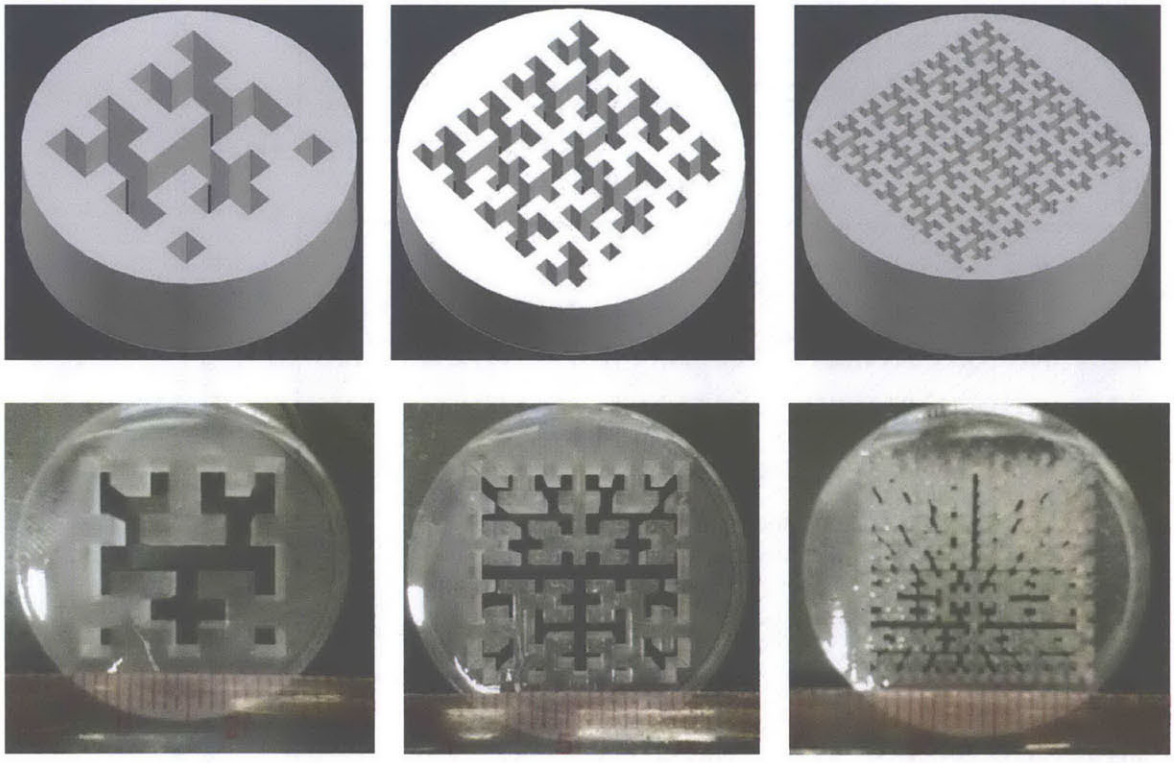

Figure 3.26: 3D drawing of Hilbert Curve based sample for out of plan transmission measurement with increasing level of iterations from left to right, 2nd row are the corresponding samples fabricated from high resolution 3D printer (project 6000) with the clear resin.

3.4 Conclusion

Deterministic fractals, e.g. Sierpinski Triangle and the Koch snowflake, have captured the attention of mathematicians for their unique properties. Their unique properties render them as interesting for applied applications, such as metamaterials, sound absorbing materials and biological diffusion system. Metamaterial based on deterministic prefractals have been studied (e.g. H tree prefractal) and they exhibit novel behavior. In this chapter, we aim to further our understanding of phononic metamaterials based on deterministic prefractal by study two systems using the theoretical framework introduced in chapter 2: one where the scatterer phase has fractal like geometry, e.g. H tree prefractal; the other is fractal interface e.g. Hilbert curve prefractal, between the scatterer and matrix phase

For H tree based metamaterials, we studied both in–plane eigenmodes and out-of-plane transmission behavior for 2D and 2D plate with finite thickness systems. For 2D system, several factors have been studied systematically on how they would impact the behavior of the systems. It was found that the length/thickness ratio, level of iteration and materials properties can all be used to control the wave propagation behavior in the system through different mechanism. By increasing the level of iteration, multiple bandgaps can be achieved across different length scale. For 2D fractal resonator with finite thickness, the lowest eigenmodes exhibit subwavelength frequencies from full wave simulation, which is 1/75 of the frequency comparable to the Euclidean dimension of the plate. A simple equivalent electric circuit is developed to describe the Helmholtz resonator tree, which in turn can be used to explain in-plane eigenmodes of the 2D plate with finite thickness slab with H tree prefractal. The resonance frequency obtained are consistent with the full wave simulation. 2D fractal resonators with finite thickness have been fabricated using high resolution 3D printer, where the scaffolding and other parameters have to be optimized to achieve the precision and robust mechanical properties of the final sample. To study their mechanical behavior, SAM has also been used for imaging the surface and subsurface of sample (in reflection mode) as well as the transmission characteristic of such samples (in transmission mode). The reflection images revealed topographic features informative of the surface finish of the sample.

For Hilbert Curve prefractal bounded sample, their in-plane eigenmodes have been studied for 2D system. Again multiple spectral band gaps have been observed for the samples studied. It was

found that higher impedance contrast between scatterers and matrix are preferred for band opening since high strain region are more localized in softer phase, hence flatten the dispersion curves. Furthermore, the bandgap size increases and decrease with increasing level of iteration (as well as filling ratio of scatterer phase), which might indicate an optimal fill fraction. Furthermore, the eigenmodes are less confined with increasing level of iterations although they still obey the symmetry of the relevant k vector. Besides the level of iterations, arrangement of the building blocks also influence the behavior, although the symmetries of the unit cell is retained, their variation in local dynamics also changed the dispersion behavior system. The bandgap size of modified system can be larger or smaller than the pure prefractal system depending on the level of iteration. Furthermore, it was found the bandgap size of the fractal interface is larger than that of a fractal phase (although the interface of H tree prefractal also exhibit certain fractal like properties).

Hence, both broadband behavior and subwavelength (for compact devices) has been observed for metamaterials based on deterministic prefractals, which could be beneficial for a wide range of applications. The knowledge gained can further be used to understand and model the fractal system in nature since it can serve as a transition from crystal material to fractal system observed in nature. Their unique properties can be used to control and manipulate wave propagation through such systems. Hence studying metamaterial systems based on deterministic fractal would further expand the horizon for novel designer materials.

3.5 Reference

Shalaev, V. M. (2000). Small-Particle Fractal Aggregates. In *Nonlinear optics of Random Media: Fractal composites and metal-Dielectric Films* (pp. 21–73). Springer.

Anders, S. (2009). Visualization of genomic data with the Hilbert curve. *Bioinformatics (Oxford, England)*, *25*(10), 1231–5.

Bejan, A. (2000). *Shape and Structure, from Engineering to Nature* (p. 324). Cambridge University Press.

Bejan, A., & Zane, J. P. (2013). *Design in Nature: How the Constructal Law Governs Evolution in Biology, Physics, Technology, and Social Organizations* (p. 296). Knopf Doubleday Publishing Group.

Briggs, A. (1982). *An introduction to scanning acoustic microscopy* (p. 70). Oxford science publications.

Browning, S. A. (1980, January 1). The Tree Machine: A Highly Concurrent Computing Environment. California Institute of Technology.

Burkis, J. (1991). Clock tree synthesis for high performance ASICs. In *[1991] Proceedings Fourth Annual IEEE International ASIC Conference and Exhibit* (pp. P9–8/1–3). IEEE.

David Hilbert. (1869). Ueber die stetige Abbildung einer Linie auf ein Flächenstück. *Mathematische Annalen*, *12*.

Edgar, G. (2007). *Measure, Topology, and Fractal Geometry (Google eBook)* (p. 288). Springer.

Group,. Scanning Acoustic Microscope. *Image (Rochester, N.Y.)*.

Hamilton, C. H., & Rau-Chaplin, A. (2008). Compact Hilbert indices: Space-filling curves for domains with unequal side lengths. *Information Processing Letters*, *105*(5), 155–163.

Hou, B., Xie, H., Wen, W., & Sheng, P. (2008). Three-dimensional metallic fractals and their photonic crystal characteristics. *Physical Review B*, *77*(12), 125113.

Huang, X., Xiao, S., Zhou, L., Wen, W., Chan, C. T., & Sheng, P. (2009). Photonic Metamaterials Based on Fractal Geometry. In *Metamaterials: Theory, Design, and Applications* (pp. 215–245).

Kaye, B. H. (2008). *A Random Walk Through Fractal Dimensions (Google eBook)* (p. 452). John Wiley & Sons. Retrieved from http://books.google.com/books?id=Kp582WW-GkcC&pgis=1

Kubota, S., Miyamaru, F., & Takeda, M. W. (2009). *Terahertz response of fractal metamaterials. 2009 34th International Conference on Infrared, Millimeter, and Terahertz Waves* (pp. 1–2).

Leopold, L. B. (1971). Trees and Streams: The Efficiency of Branching Patterns. *J. Theor. Biol.*, *31*, 339–354.

Liu, T. (2005). Optimum Bifurcating-Tube Tree for Gas Transport. *Journal of Fluids Engineering*, *127*(3), 550.

Maev, R. G. (2008). *Acoustic Microscopy: Fundamentals and Applications*. *New Journal of Physics* (1st ed., Vol. 15, p. 291). Wiley-VCH;

Mandelbrot, B. B. (1983). *The fractal geometry of nature* (p. 468). San Francisco : W.H. Freeman, c1983.

Manual, U. (n.d.). User manual. *Data Base*.

Meng, L., Huang, C., Zhao, C., & Lin, Z. (2007). An improved Hilbert curve for parallel spatial data partitioning. *Geo-Spatial Information Science*, *10*(4), 282–286.

Moon, B., Jagadish, H. V., Faloutsos, C., & Saltz, J. H. (2001). Analysis of the clustering properties of the Hilbert space-filling curve. *IEEE Transactions on Knowledge and Data Engineering*, *13*(1), 124–141.

Nguyen, G., Franco, P., Mullot, R., & Ogier, J. (2012). Mapping high dimensional features onto Hilbert curve:

Nikos Mamoulis, Thomas Seidl, Torben Bach Pedersen, Kristian Torp, I. A. (2009). *Advances in Spatial and Temporal Databases: 11th International Symposium, SSTD 2009 Aalborg, Denmark, July 8-10, 2009 Proceedings (Google eBook)* (p. 466). Springer.

Pawlak, D. A., Turczynski, S., Gajc, M., Kolodziejak, K., Diduszko, R., Rozniatowski, K., … Vendik, I. (2010). How Far Are We from Making Metamaterials by Self-Organization? The Microstructure of Highly Anisotropic Particles with an SRR-Like Geometry. *Advanced Functional Materials*, *20*(7), 1116–1124.

Sam, X.-R. (n.d.). Scanning Acoustic Microscopy. *Science*, 1–89.

Seuront, L. (2010). Self-Similar Fractals. In *Fractals and Multifractals in Ecology and Aquatic Science* (pp. 25–98). CRC press Taylor & Francis Group.

Shalaev, V. M. (2000). Small-Particle Fractal Aggregates. In *Nonlinear optics of Random Media: Fractal composites and metal-Dielectric Films* (pp. 21–73). Springer.

Ullman, J. D. (1984). *Computational aspects of VLSI* (p. 495). Computer Science Press.

Wang, X.-Q., Mujumdar, A. S., & Yap, C. (2007). Effect of bifurcation angle in tree-shaped microchannel networks. *Journal of Applied Physics*, *102*(7), 073530.

Wareham, R. J., & Lasenby, J. (2010). Generating Fractals Using Geometric Algebra. *Advances in Applied Clifford Algebras*, *21*(3), 647–659.

Yang, D.-O. K. C.-Y. K. D.-G. (2012). Flexible Hilbert-Curve Loop Antenna Having a Triple-Band and Omnidirectional Pattern for WLAN/WiMAX Applications. *International Journal of Antennas & Propagation;*, *2012*, 9.

Yang, L. T., Guo, M., Gao, G. R., & Jha, N. K. (Eds.). (2004). *Embedded and Ubiquitous Computing* (Vol. 3207). Berlin, Heidelberg: Springer Berlin Heidelberg.

Zhou, Y., & Jiang, L. (2012). Hilbert Curve Based Spatial Data Declustering Method for Parallel Spatial Database. In *2012 2nd International Conference on Remote Sensing, Environment and Transportation Engineering* (pp. 1–4). IEEE.

4. Metamaterials based on Random Fractal

4.1 Why these systems are interesting?

Random fractals are more common than deterministic fractals in nature. This is due to the aggregation of many small parts in the physical objects (spatial fractal process) or in the process itself (temporal random fractal process). The randomness for the objects or processes implies scale-related repetitions of overall complexity but not of an exact pattern. Random Fractal analysis have applications in many areas, such as ecology system, biological growth, distribution of galaxies, solar activities, stock market, seismic wave, internet traffic, turbulence etc.

Coastlines are examples of random fractals that have been studied extensively by Mandelbrot, who showed that the fractal dimensions of coastlines vary within certain range. How would they behave differently with respect to reflecting waves (e.g. tsunami or just regular tide)? To go one step further, what is the cause of the variation in their fractal dimension? The fractal dimension of lungs are correlated to the health of the individual. Since several organs and their vitals exhibit fractal properties, modern medicine could use analysis of fractal properties to help differentiate between health and diseased individuals. For example, it was found that the fractal dimension of the lung and the lung sound spectrum appears to vary between healthy and sick lungs, which might provide a new way to help diagnosis. Hence study metamaterial systems that exhibit randomness would increase the repertoire for novel designer materials; moreover, it may also contribute our understanding of natural physical systems and processes.

4.2 Overview of Random Fractal

4.2.1 Fractional Brownian motion

After the discovery of Brownian motion, it is one of the most common stochastic processes used in a variety of applications. However, the assumption of independent increment is limited for modeling systems with long-range correlation or long-term memories. To meet the demands of such applications, the independent increments assumption is removed, resulting in a more generalized stationary Gaussian process called fractional Brownian motion (fBM). Given its statistical nature, correlation functions have been valuable approaches to give quantitative description of the fractal random/stochastic system (Heory, 2010; Mandelbrot, 1977; Seuront,

2010a).

If we define a general density function as, where is density at position r and averaging over all possible r_0, then for self-similar fractals (isotropic scaling), the general density function would obey a homogeneous power-law:

Where α = d-D, where d is the Euclidean dimensionality of the embedding space, and D is usually the fractal dimension. For anisotropic scaling (i.e. scale differently along different dimensions), a new concept self-affine has been introduced. For a set of points $\vec{x} = (x_1, x_2, \ldots\ldots\ x_{D_E})$, a self-affine transformation would result in a new set of points as $\overrightarrow{\lambda x} = (\lambda_1 x_1, \lambda_2 x_2, \ldots\ldots\ \lambda_{D_E} x_{D_E})$, where the scale ratios $(\lambda_1, \lambda_2, \ldots\ldots, \lambda_{D_E})$ are all different. Brownian motion is a self-affine process since it scales differently with respect to time and space (Mandelbrot, 1977, 2006; V. M. Shalaev, 2000d).

Fractional Brownian motion can be applied to both spatial and temporal processes. The fractional Brownian diffusion process can be described by both fractional calculus and stochastic calculus. One of the continuum models often used is the KPZ equation (Rothman, D. H. 2008):

$$\frac{\partial h(x,t)}{\partial t} = \nu \nabla^2 h(x,t) + \frac{\Lambda}{2} |\nabla h(x,t)|^2 + \eta(x,t)$$

where ν is diffusivity, η is the Gaussian noise, and Λ is average normal velocity

For a spatial process, self-affine surfaces are common in nature (e.g. mountains) and can be described by $h(x) = b^{-H} h(bx)$, where h(x) is the height of the surface and H is called Hurst exponent. We define W(L) as the root mean square fluctuation of height over length L, then the fluctuation of the height over length L (Rothman, D. H. 2008) can be described as

$$W^2(L) = \frac{1}{L}\int_0^L |h(x)|^2 dx \propto L^{2H},$$

For 0<H<1, the surfaces are called fractional Brownian surfaces, and the surfaces can be categorized according to value of H

- 0<H<1/2 is anti-persistent or sub-diffusive case,
- H = ½ corresponds to pure diffusion

- 1/2<H<1 is persistent or super-diffusive cases

Various models have been proposed to construct a self-affine surface with different features, one of them will be explained in detail in next section.

4.2.2 Methodology to generate random fractal based on fractional Brownian motion

To generate a random fractal with binary phases/components, we use a spatial generation process to obtain the fractional Brownian field/surface (Dirk P. K. 2013). Starting from generating fBm on a uniform grid, the increment processes ($X_i = W_i - W_{i-1}$), also known as *fractional Gaussian noise*, can be obtained from a discrete zero-mean stationary Gaussian process with covariance $cov(X_i, X_{i+k}) = \frac{1}{2}(|k+1|^{\alpha} - 2|k|^{\alpha} + |k-1|^{\alpha}), k = 0,1,2 \ldots.$

Where H=α/2 is the Hurst constant that measures the self-similarity of the process.

Fractional Gaussian noise can be generated using a circulant embedding approach to exploit the structural properties of the stationary Gaussian process. The stationary process is characterized by constant expectation function and an invariant covariance function under translation. This approach is implemented by four steps: 1) the covariance matrix is built and stored, the matrix is uniquely characterized by its first block row and has a symmetric block-Toeplitz structure, where the matrix contains blocks repeated down the diagonals of the matrix, just as Toeplitz matrix has elements repeated along the diagonals of the matrix. This step is usually the most time consuming step in typical applications. 2) Each Toeplitz matrix is embedded in upper left corner of a circulant

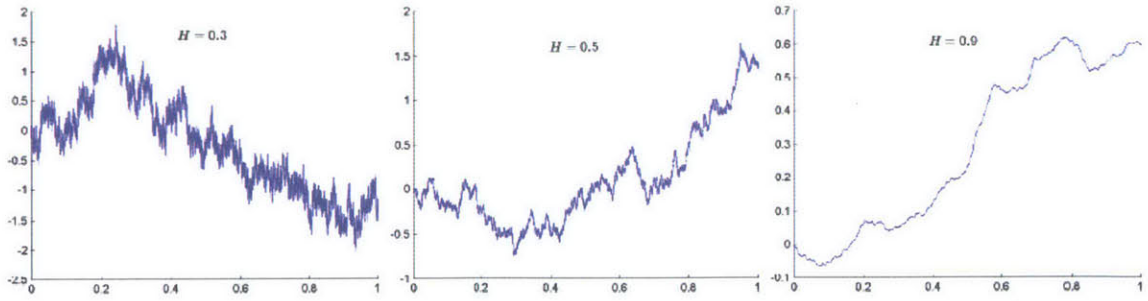

Figure 4.1: Self-affine fractional Brownian motion (fBm) characterized by various Hurst constants. Image from Dirk P. K., Zdravko I. B. (2013).

matrix. 3) square root of the block circulant matrix is computed. 4) The appropriate sub-block is extracted to obtain the Gaussian field on the grid. Using this approach, fBms with different Hurst constant are generated as shown in Figure 4.1.

To extend this process into two dimensions, fractional Brownian field/surface can be obtained, which is a zero mean Gaussian process with non- stationary covariance function defined by

$$Cov(\tilde{X}_s, \tilde{X}_t) = \tilde{\rho}(s,t) = \| s \|^{\alpha} + \| t \|^{\alpha} - \| s - t \|^{\alpha}$$

Where H = α/2 is Hurst constant that controls the roughness of the surface, and the Hausdorff dimension can be found by $D_H = 2 - H$.

To obtain an fBms on a unit disk in the first quadrant, a stationary Gaussian field $\breve{X}_t$ is generated over the quarter disk with the covariance function

$\square(s,t) = c_0 + c_2 \| s \square t \|^2 \square \| s \square t \|^{\square}$ where constants $c_0, c_2 \square 0$.

Once $\breve{X}_t$ is generated, $\tilde{X}_t$ can be obtained via the adjustment

$\breve{X}_t$ can be generated using intrinsic embedding via the following covariance function

$$\square(h) = \begin{cases} c_0 + c_2 \| h \|^2 \square \| h \|^{\square} & \| h \| \square 1 \\ \dfrac{\square(R \square \| h \|)^3}{\| h \|} & 1 \square \| h \| \square R \\ 0 & \| h \| \square R \end{cases}$$

where the value of the constant depends on the value of α. As an example, for a grid size of m=n = 1000, the fBms with different Hurst constants are generated as shown in Figure 4.2. Hence higher Hurst constants lead to smoother surfaces while the smaller ones lead to rougher surfaces.

A 2D binary system can be then obtained from fractional Brownian surface/field(fBs) following the follow procedure: Defining a plane with height h_c to intersect the fractional Brownian surface with grid numbers N (i.e. N numbers of unit per edges, hence NxN total grid squares in the yellow plane), where N is also the grid number for generating the fBs. Then if the height of the fBs is larger than the value of hc, we would draw a circle at the grid; otherwise, it would be left empty. After this procedure, there would be random distributed circles (serving as a scatterer) reflecting

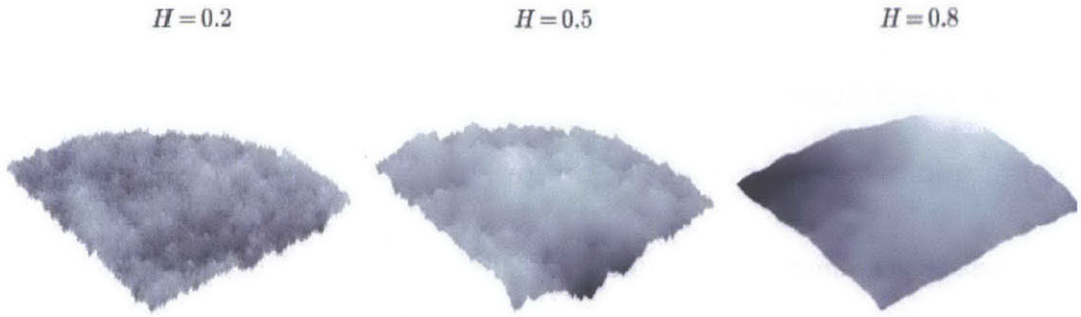

Figure 4.2: Examples of the fractional Brownian surface generated using the code for different Hurst constants. Image from Dirk P. K., Zdravko I. B. (2013).

the spatial relationship of the heights, as shown in Figure 4.4 To implement this concept in MATLAB, we first generated the matrix of height and then sort them to find our critical value h_c.

Once we find the h_c, all the nodes with height above it would be center of circles. The distributions generated with H = 0.1, 0.3, 0.5, 0.7, 0.9 are shown in Figure 4.4. Therefore, the filling ratio (area of scatterer/total area) is determined by the h_c, if we fix the diameter of the circles to be the same as the grid size (more detail can be found at Appendix C: MATLAB code for the 2D geometry). The two dimensional image generated is then imported into COMSOL as the geometric object, where the circles are scatterers, where the rest of region is defined as matrix. The materials properties are listed in Table 1 below. By saving the COMSOL models as m files, the full wave eigenfrequency varies with respect to the wave vector k) can be calculated to gain insight in overall

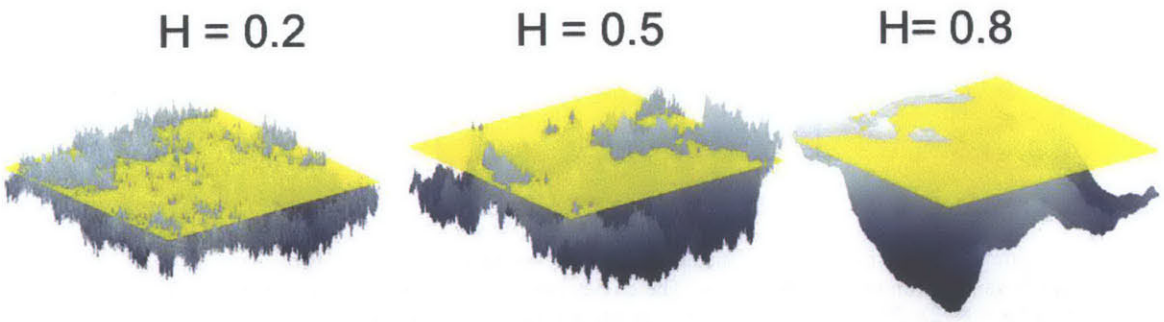

Figure 4.3: Demonstration of a cap plane intersecting fractional Brownian surface generated with different Hurst constants, the transparent yellow planes are the cap plane.

behavior of the system (more detail can be found at Appendix C: MATLAB code for calculating the dispersion curve of the system. Then individual eigenmodes at a particular k vector will be studied further using COMSOL.

4.3 Metamaterials system based on random fractals

To obtain translational symmetry for the system, periodic boundary conditions are applied to both left-right and top-bottom pairs of edges on the unit cell. Therefore, the scatterers inside the unit cell would have certain spatial correlation as defined by the Hurst constant while the translational symmetry is also obeyed by the samples.

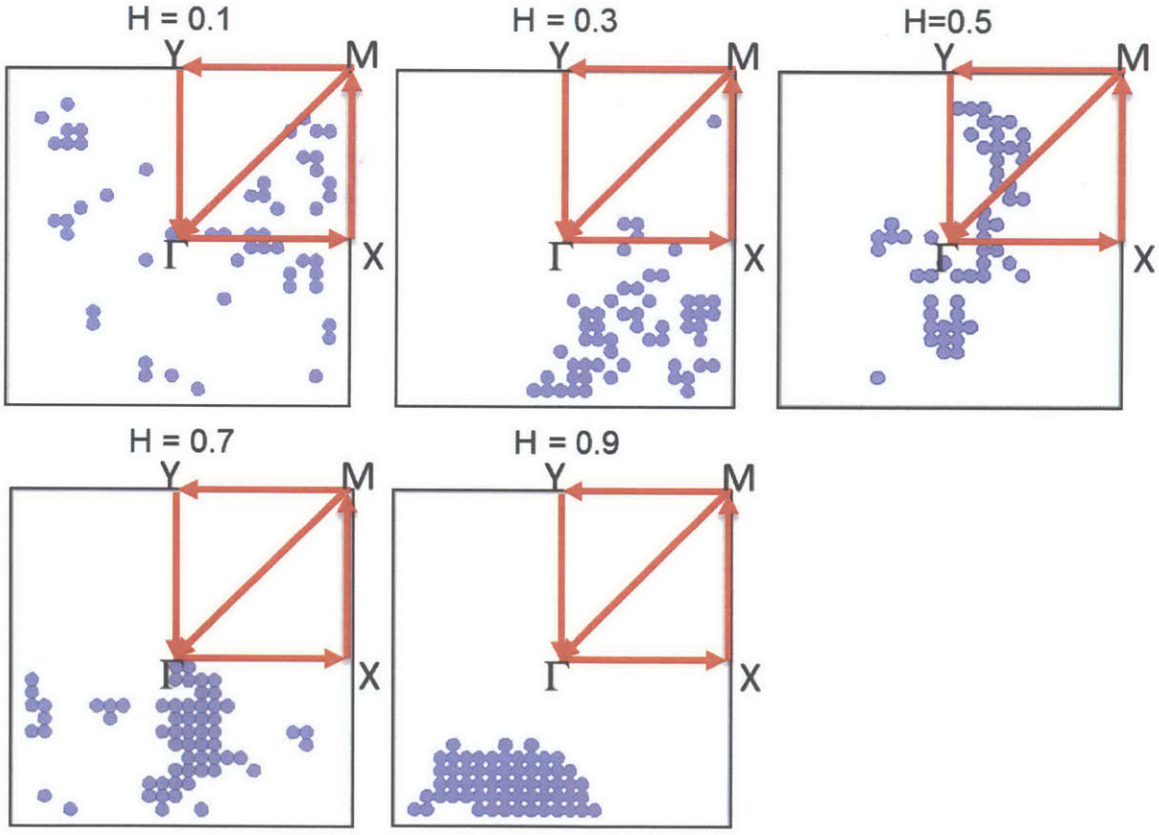

Figure 4.4: Examples of the planar binary metamaterials unit based on a fractional Brownian surface with different Hurst constants as listed on top of the unit cell. The circles are scatterer phase and its diameter is determined by the grid number ($d/a = N/2 = 25$). The white phase represents the matrix. Since hc is fixed for the samples, the fill fraction for the samples are the same as 7.85%.

4.3.1 Is the Hurst constant sufficient to represent the behavior of the system?

Due to the random nature, the binary geometry generated each time is not exactly the same, as shown in Figure 4.5. Hence, it would be interesting to find out if the Hurst constant is a unique parameter to characterize the ω(k) properties of the systems. Three random fractal based unit cell with same Hurst constant (H = 0.1) and same fill fraction (hc = $0.9h_{max}$) were generated as shown in Figure 4.5. Their dispersion behavior has been studied to find out if they would be invariant under same Hurst constant and fill fraction despite the apparent differences from sample to sample. From the dispersion curves given in Figure 4.6, it can be seen at long wavelength/high eigenfrequency, the dispersion curves nearly coincide with each other for the three different unit cells. However, when the frequency increase to higher values (i.e. shorter wavelength), there are slight deviation of the dispersion bands observed. To further verify the features of different iterations, their eigenmodes have also been studied. It was found that for dispersion the similar eigenmodes exhibit nodes similar to homogeneous slab (i.e. M9 at X point) while the deviation of frequencies can be reflected in difference of high/low displacement features too (i.e. M10 at M point), as shown in the eigenmodes plot in Figure 4.6

To further confirm that the Hurst constant could be a good indicator of the system behavior, the Young's Modulus of scatterer phase is varied by a factor of 1000, as listed in Table 4.1. The difference between different iterations would increase relatively comparing to system where the impedance contrast of scatterers and matrix are smaller (i.e. Scatterer1 and matrix). Given the

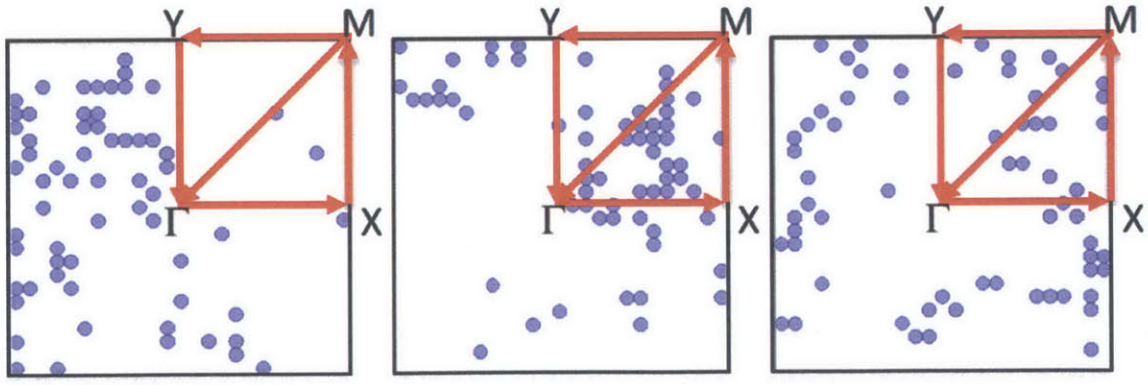

Figure 4.5: Unit cells of random fractal based metamaterials with the same Hurst constant (H = 0.1) and same fill fraction ($h_c = 0.9h_{max}$) as 7.85%, where the blue circle are the scatterers, and the white background are the matrix phase.

consistency of the dispersion behavior between different iterations, the Hurst constant and fill ratio can be used to characterize the systems based on random fractals for binary system. However, it should also be kept in mind that the exact distribution of scatterers could have nuance effect in the dispersion behavior, especially when the impedance contrast increase further, as shown in Figure 4.7 with eigenmodes plotted at X and M point.

Table 4.1: Material properties used for the simulation for dispersion curve.

Material Properties	Scatterer1	Scatterer2	Scatterer2	Matrix
Young's Modulus Pa	4.35e10	4.35e7	4.35e6	3e9
Poisson Ratio	0.329	0.329	0.329	0.375
Density kg/m^3	972	972	972	2500
Impedance contrast	Ks/Km = 2.374	Ks/Km = 0.075	Ks/Km = 0.024	-

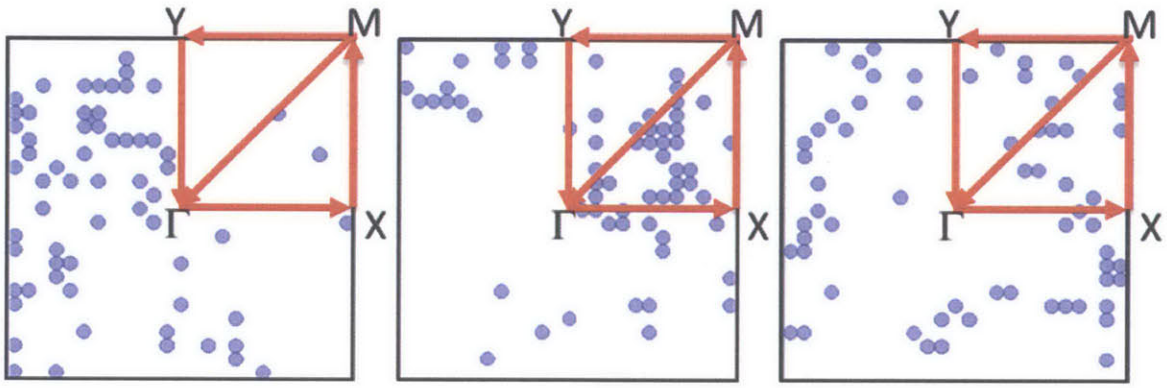

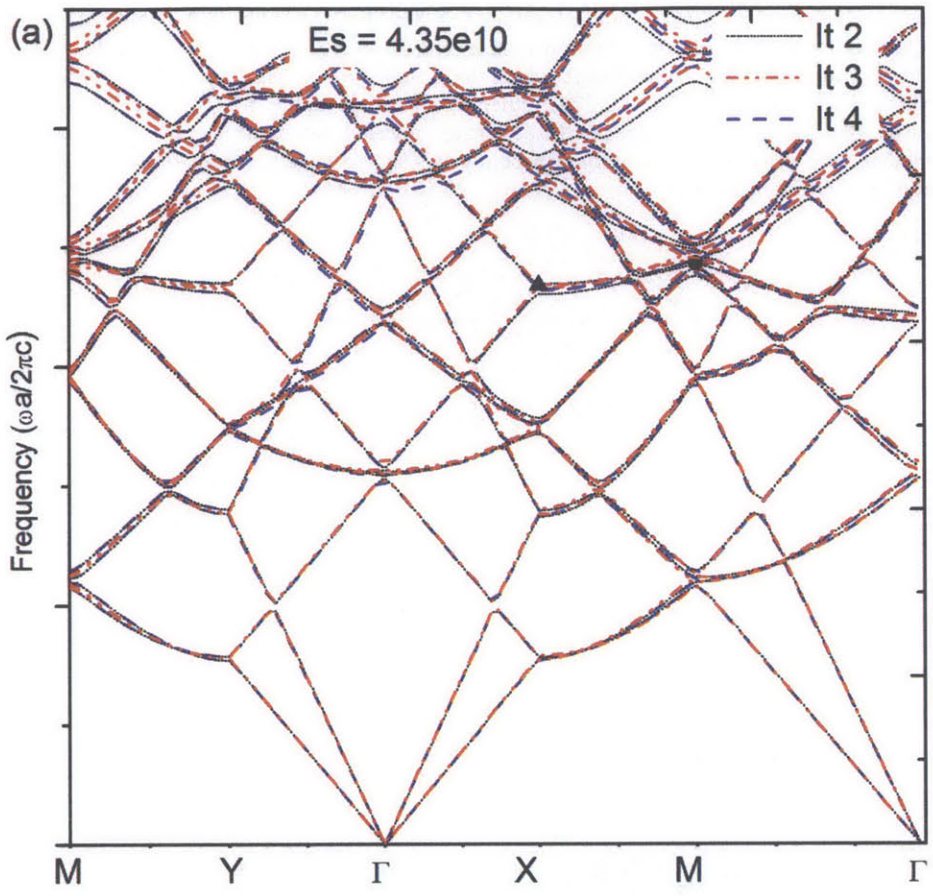
(a)
Es = 4.35e10
lt 2
lt 3
lt 4
Frequency (ωa/2πc)
M
Y
Γ
X
M
Γ

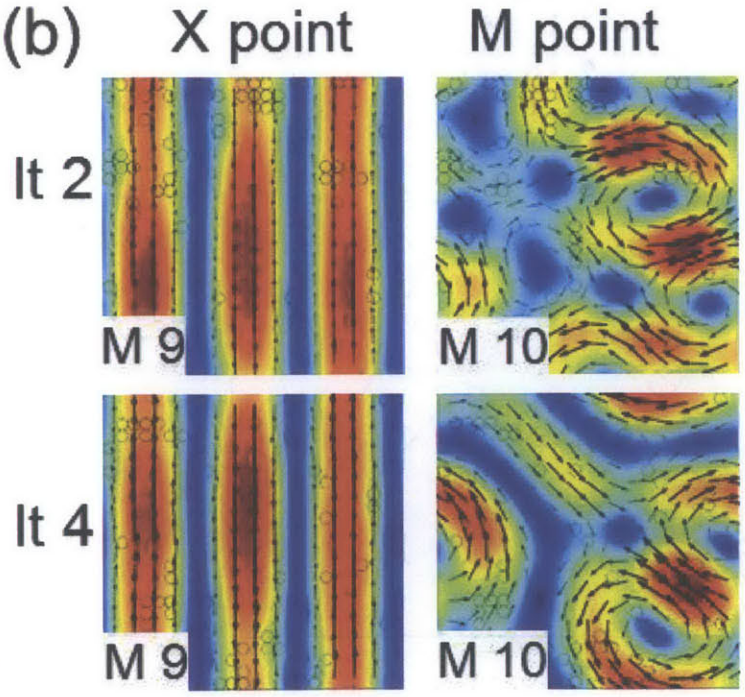
(b)
X point
M point
lt 2
M 9
M 10
lt 4
M 9
M 10

Figure 4.6: (a) Dispersion curves along the BZ of the unit cell (along Γ→ X→M→ Γ) as indicated in the unit cells in the Figure 4.5 for different iterations of random fractal based sample with H = 0.1 (i.e. iteration 2 (black dot line), iteration 3 (red short dash dot) and iteration 4 (blue dash)), where the Young's modulus of the scatterers are Es = 4.35e10Pa (where impedance contrast is Ks/Km = 2.374), others are listed in Table 4.1. (b) The eigenmodes corresponded (highlighted as solid triangle) are arranged at the bottom as indicated, where the Mode 9 of It 2 and It 4 have similar displacement that have mirror symmetry with respect to y axis approximately. On the other hand, Mode 10 of It2 and It4 at M point have different features.

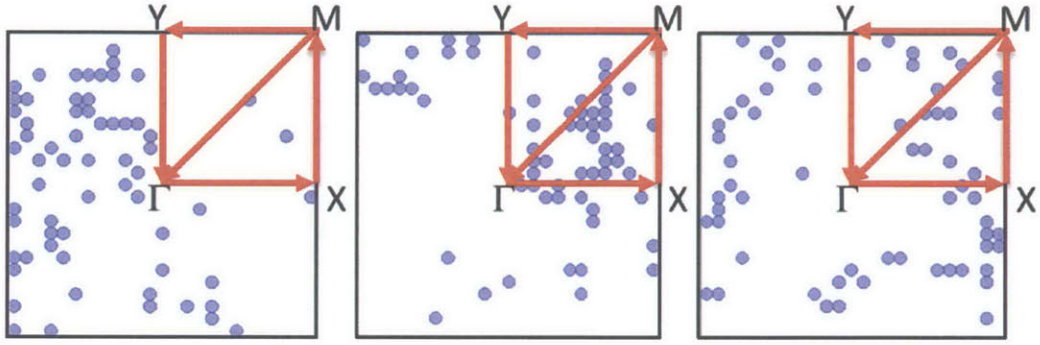

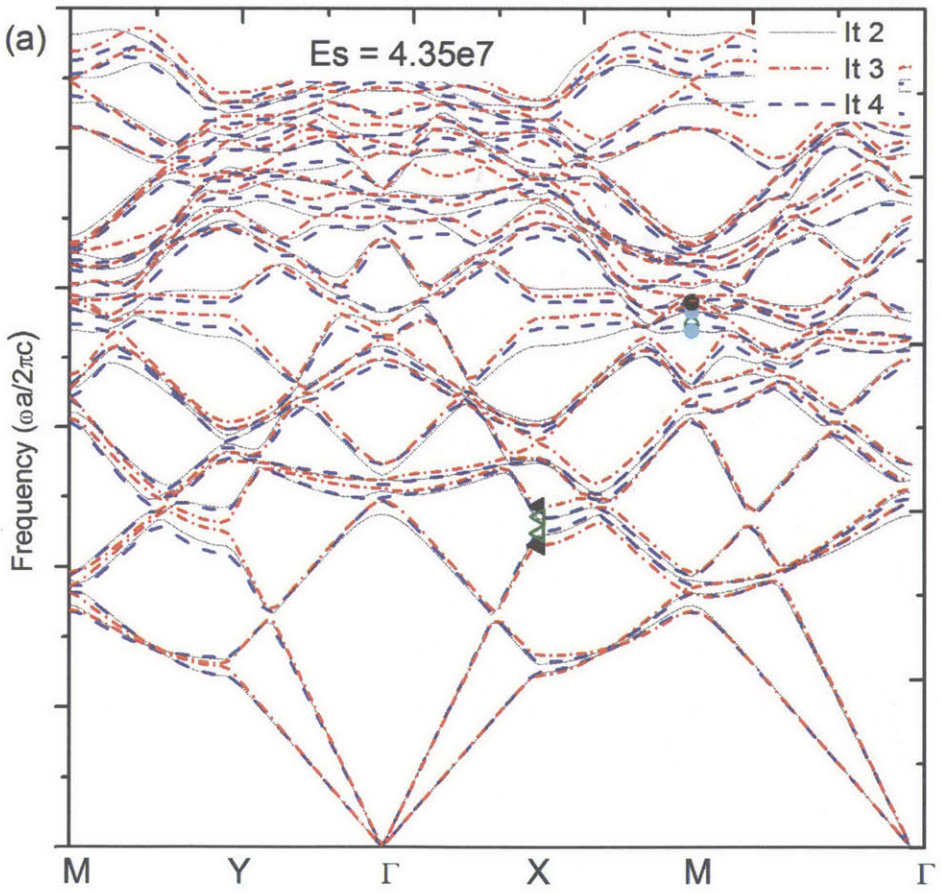

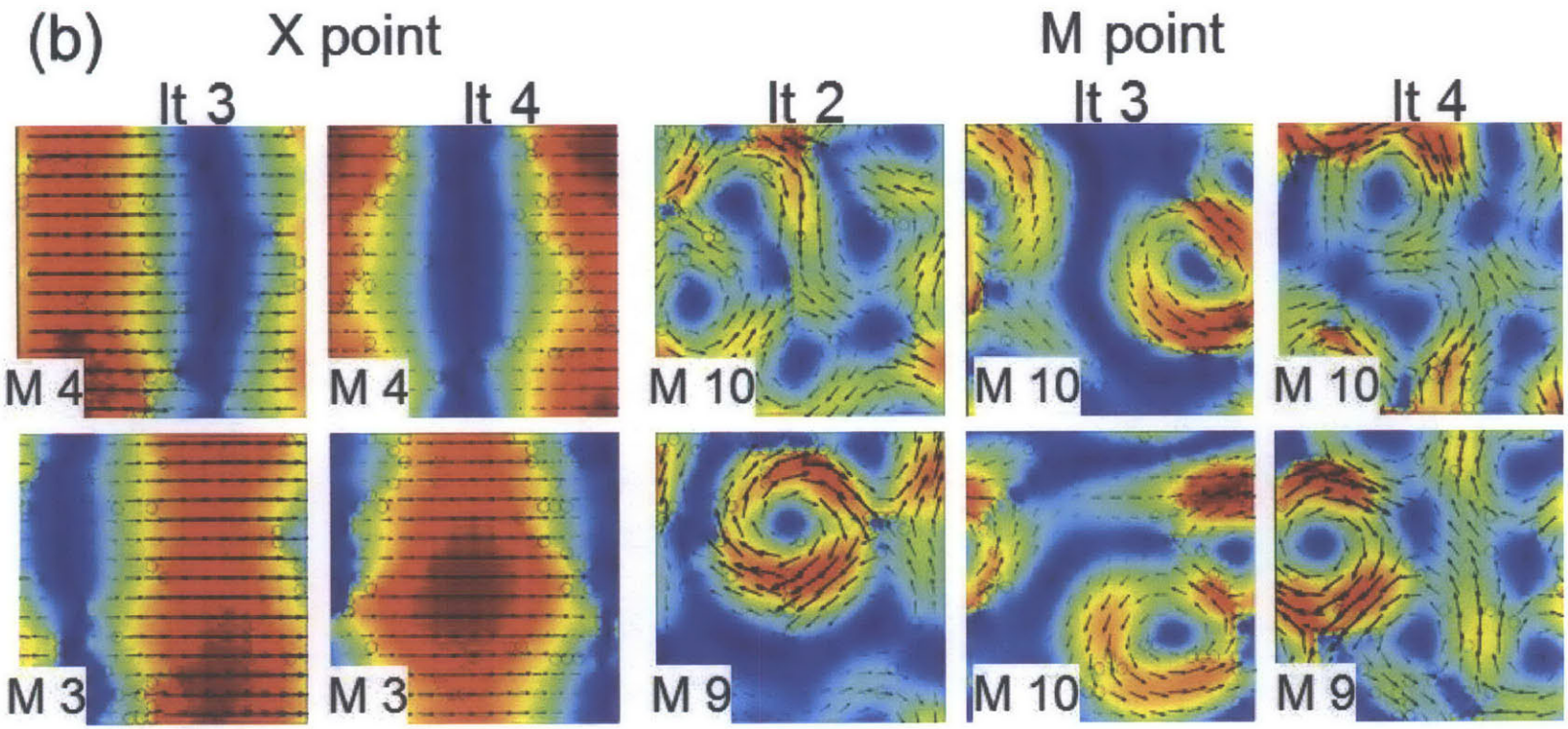

Figure 4.7: (a) Dispersion curves along the BZ of the unit cell (along Γ→ X→M→ Γ) as indicated in the Figure 4.5 for different iterations of random fractal based sample with H = 0.1 (i.e. iteration 2 (black dot line), iteration 3 (red short dash dot) and iteration 4 (blue dash)), where the Young's modulus of the scatterers are Es = 4.35e7Pa (where impedance contrast is Ks/Km = 0.075), others are listed in Table 4.1. (b) The eigenmodes corresponded to It 2 (cyan circle), It 3 (black solid triangle) and Iter4 (olive triangle/circle) are arranged at the bottom as indicated, where the Mode 3 and Mode 4 of It 3 and It 4 exhibit complementary displacement pattern (i.e. high/low strain) where the interaction between M3 and M4 for It 4 seems to be larger compared to It 3 from dispersion curve. On the other hand, Mode 9 and Mode 10 of It2, It3 and It4 at M point have different features.

4.3.2 Varying the Hurst constant of the system

Since the Hurst constant characterize the spatial distribution of the scatterers, we studied binary systems with different Hurst constants and the material properties used are shown in Table 4.1. The filling ratio is also kept at 0.0785 (for $h = 0.9h_{max}$) for all the samples, which means only the node with height on the top 10% is used as the centers for the scatterers.

Since waves with small frequency (i.e. long wavelength relative to certain scale) are not very sensitive to the heterogeneous nature in the material properties (i.e. the sample appears to be homogeneous to the wave), the extended modes for samples with different Hurst constant are relatively small (as shown in the lowest dispersion curves Figure 4.8). The extended nature is reflected in the linear bands along the ΓX direction, where the group velocity can be derived from the tangent of the curve. In general, for H = 0.1, the scatterers are more distributed and isolated, the average cluster size is small and comparable to individual scatterer size (as shown in Figure 4.4 and 4.5). As the H value increases, the scatterer are more connected and clustered together, hence the average cluster size also increases. Since the critical scale are related to the feature size, which can be approximated by cluster size in this case, the critical scale increases with increasing H value. Therefore, sample with H = 0.1 exhibits dispersion behavior similar to a homogeneous square unit cell since its transition scale is the smallest (hence shortest wavelength), as shown in Figure 4.8 dispersion curves. At the Γ point, the eigenmodes up to 4^{th} mode resemble the homogeneous plate closely (M1 in Fig 4.8) while the higher eigenmodes also retain certain degree of regularity observed in homogeneous samples (M20 in Fig 4.8). At X and M point, the eigenmodes are relatively extended with more dispersion curves have a larger slope along XM and M Γ at higher frequency comparing to sample with H value of 0.5 and 0.9.

As the H value increase, the presence of scatterer clusters would become more obvious at lower frequencies, which reflect in both localized displacement (i.e. relatively flat dispersion bands) and the lowered frequencies. For H = 0.5, the lowest eigenmodes still exhibit longitudinal and transversal like modes, as shown in M1 or M 3 at X M point in Figure 4.8 eigenmodes plot. They eigenmodes exhibit regular high/low displacement region like homogenous plate up to bands six. However, at higher frequency (shorter wavelength), the eigenmodes become more localized at the

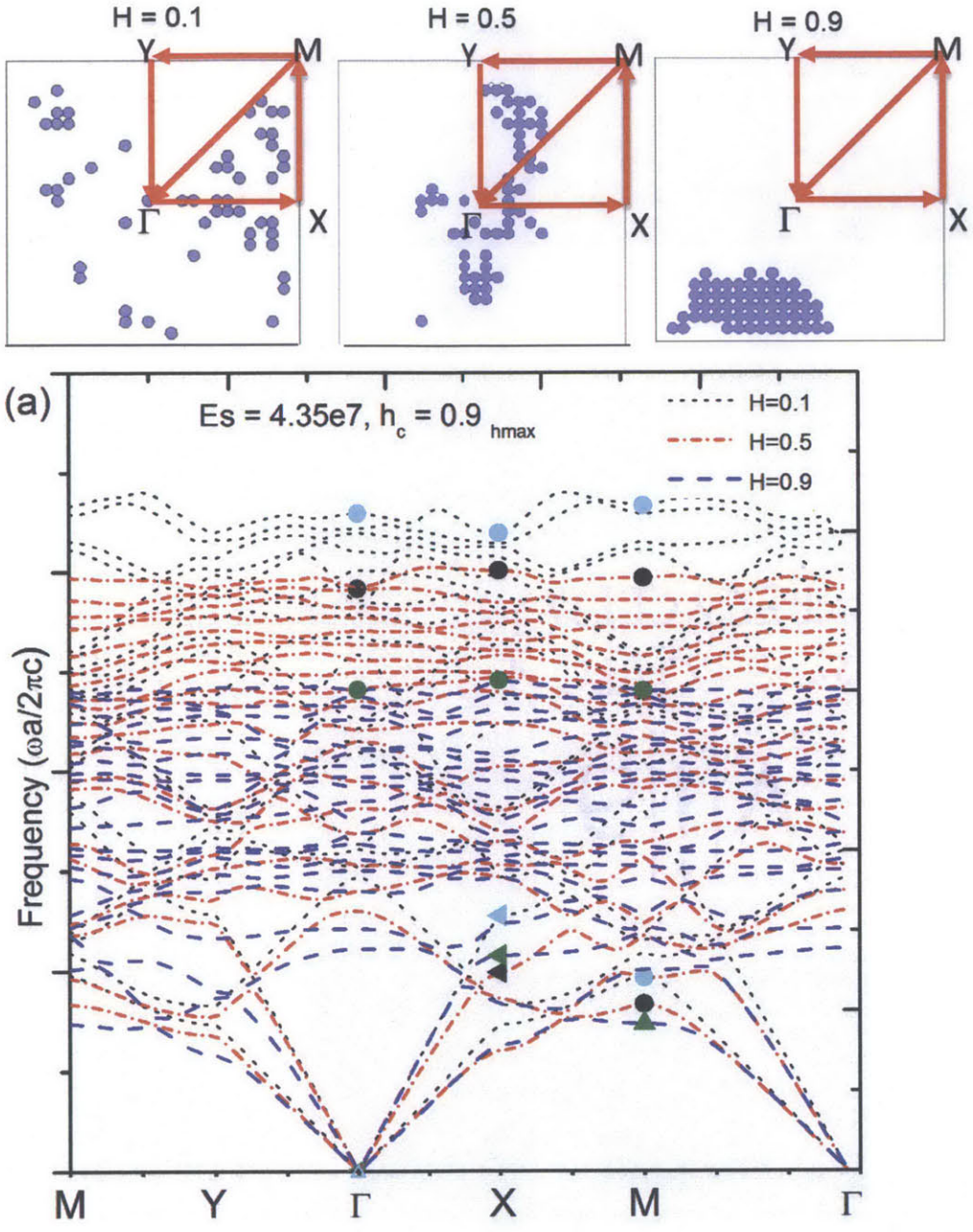
H = 0.1
H = 0.5
H = 0.9
Y
M
Γ
X
(a)
Es = 4.35e7, h_c = 0.9 hmax
H=0.1
H=0.5
H=0.9
Frequency (ωa/2πc)
M
Y
Γ
X
M
Γ

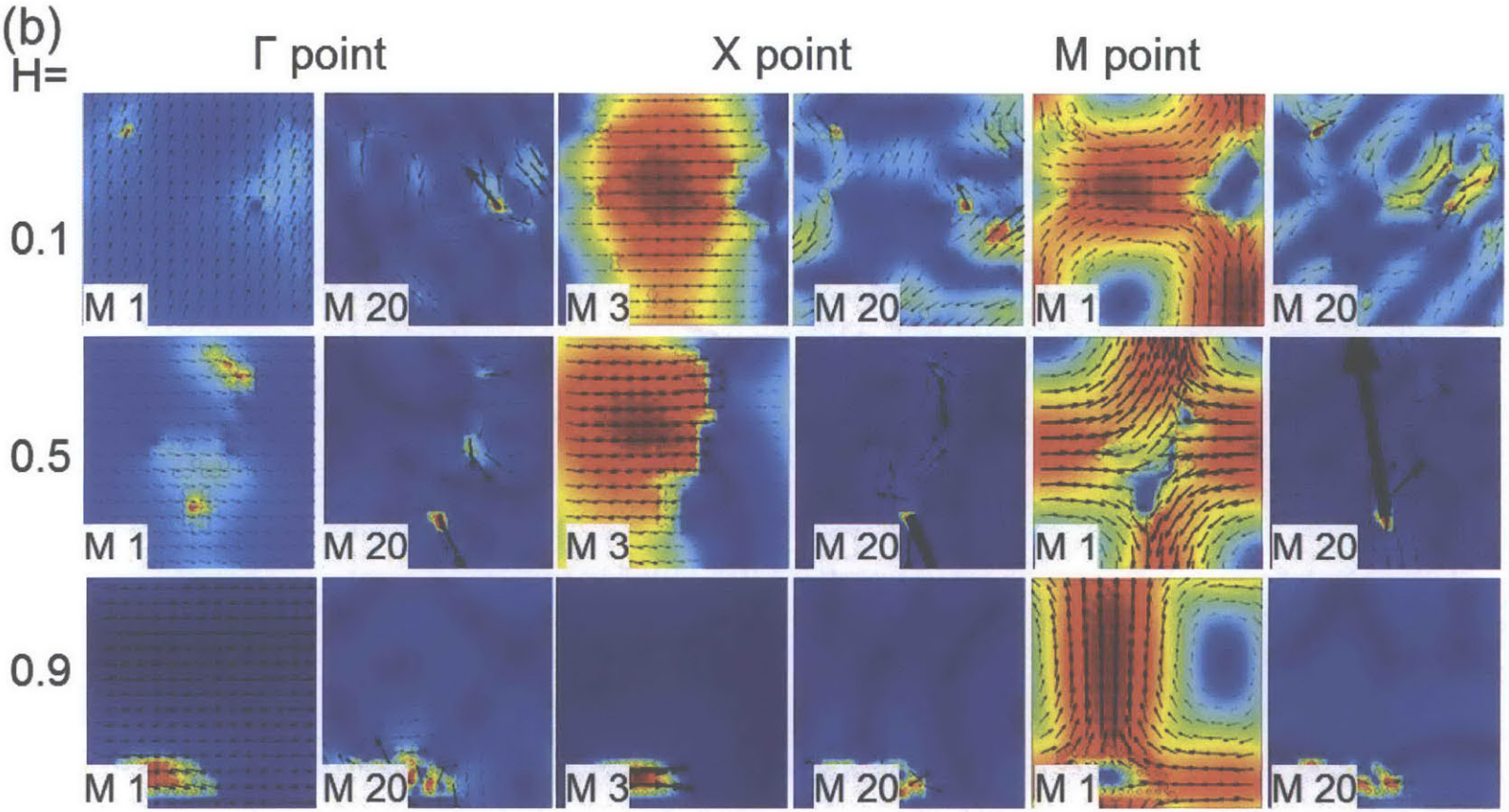

Figure 4.8: (a) Dispersion curves along the BZ of the unit cell (along Γ→ X→M→ Γ) as indicated in the Figure 4.5 for random fractal based sample with different Hurst constant, e.g. H = 0.1 (black dot line), H = 0.5 (red short dash dot) and H = 0.9 (blue dash)), where the Young's modulus of the scatterers are Es = 4.35e7Pa (where impedance contrast is Ks/Km = 0.075),,, others are listed in Table 4.1. (b) The eigenmodes corresponded to H = 0.1 (cyan circle), H = 0.5 (black solid triangle) and H = 0.9 (olive triangle/circle) are arranged at the bottom as indicated, where the longitudinal and transverse modes are observed at Γ point for all three samples (e.g. M1), where at higher frequencies, the high strain regions are more concentrated in the softer scatterers (e.g. M20). At X point, the eigenmodes of sample with H = 0.9 differs from the other two significantly with high strain more confined to scatter phase (M3 of H = 0.9) given its largest cluster size. While the M1 for all samples are extended at M point, the eigenmodes of high frequencies are more confined (e.g. M 20) for H = 0.5 and H =0.9.

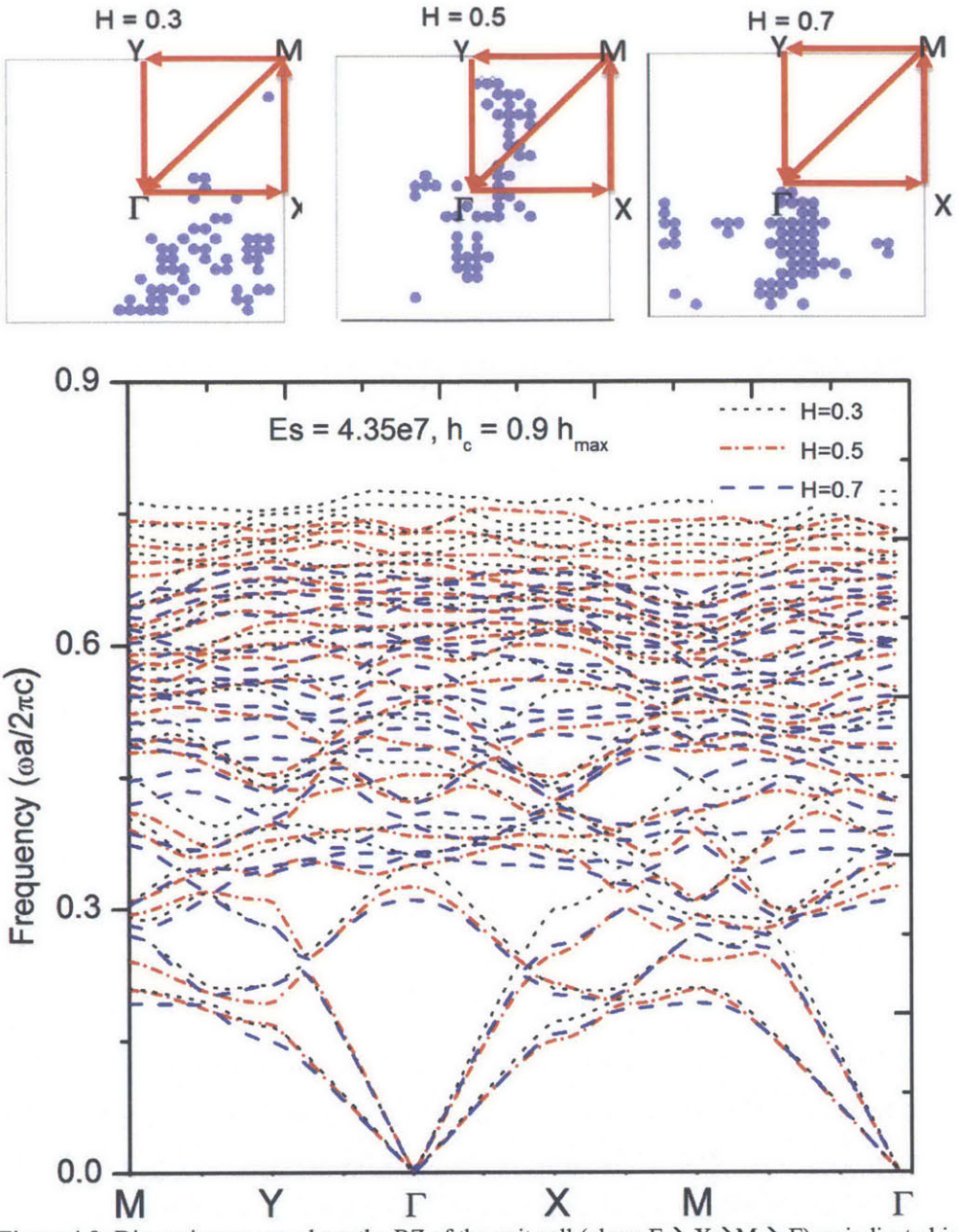

Figure 4.9: Dispersion curves along the BZ of the unit cell (along Γ→ X→M→ Γ) as indicated in the Figure 4.5 for random fractal based sample with different Hurst constant, e.g. H = 0.3 (black dot line), H = 0.5 (red short dash dot) and H = 0.7 (blue dash)), where the Young's modulus of the scatterers are Es = 4.35e7Pa (where impedance contrast is Ks/Km = 0.075), others are listed in Table 4.1.

scatterer phase, from larger scatterer size to smaller scatterer size (M20 at Γ, X and M point in Fig 4.8 eigenmodes). Following similar trend, for samples with H = 0.9, their eigenfrequency decreased further since the cluster sizes are much larger and this begin to affect the dispersion

behavior at longer wavelength. Although they still retain the longitudinal and transverse like eigenmodes (M1 and M 3 in Fig 4.8 eigenmodes), the displacement quickly localized in the soft scatterer phase, where the nodes and antinodes start to develop within the scatterer cluster region as if it is the pseudo unit cell. Similar trends of dispersion behavior can be observed for samples with H = 0.3, H =0.5 and H =0.7, as shown in Figure 4.9. However, as the frequency increases, the dispersion bands begin to differentiate from each other, as shown in Figure 4.5. As the average cluster size S increases with H, the eigenfrequency also shifted downwards. Hence, the H constant can be used to tune the phononic behavior of the system through the average cluster size with a fixed filling ratio.

4.3.3 Varying the filling ratio of scatterers

Besides the distribution of the scatterers, their filling ratio is another factor that affects how they interact with waves. Since the filling ratio is controlled by h_c for our system, the cap value of height h is varied to study how the behavior of the system would change with it. $h_c = 0.5$ is chosen since it is close to the bond percolation threshold value in 2D. The filling ratio is increases from 0.0785 (for $h = 0.9h_{max}$) to 0.3927 (for $h = 0.5h_{max}$) for all the samples. Samples with different H value are again generated, as shown in Figure 4.0 (a), where the average cluster size increases with increasing value of H. As expected, the eigenfrequency of the system shifted downwards with decreasing h_c, even when the impedance contrast is relatively small between matrix and scatterers, as shown in Figure 4.10.

For all the samples, the longitudinal and transverse like eigenmodes are still retained at lower frequency at X and M points (M1, M 3 as shown in Figure 4.11 eigenmodes). However, as the frequency increases, the eigenmodes now localized in the scatterer phases at longer wavelength (compared to $h=0.9h_{max}$) and no longer resemble the homogeneous plate eigenmodes. The cluster with largest sizes would dominate in the lower frequency (as shown in M3 and M4 at X and M point) while the number of node/antinode increases with increasing frequency) (M20 at X and M point). The localized features of the eigenmodes at higher frequencies is demonstrated through the relatively flat dispersion bands. Therefore, the clusters serve as a pseudo unit cell where higher order harmonics appears as the frequency increases.

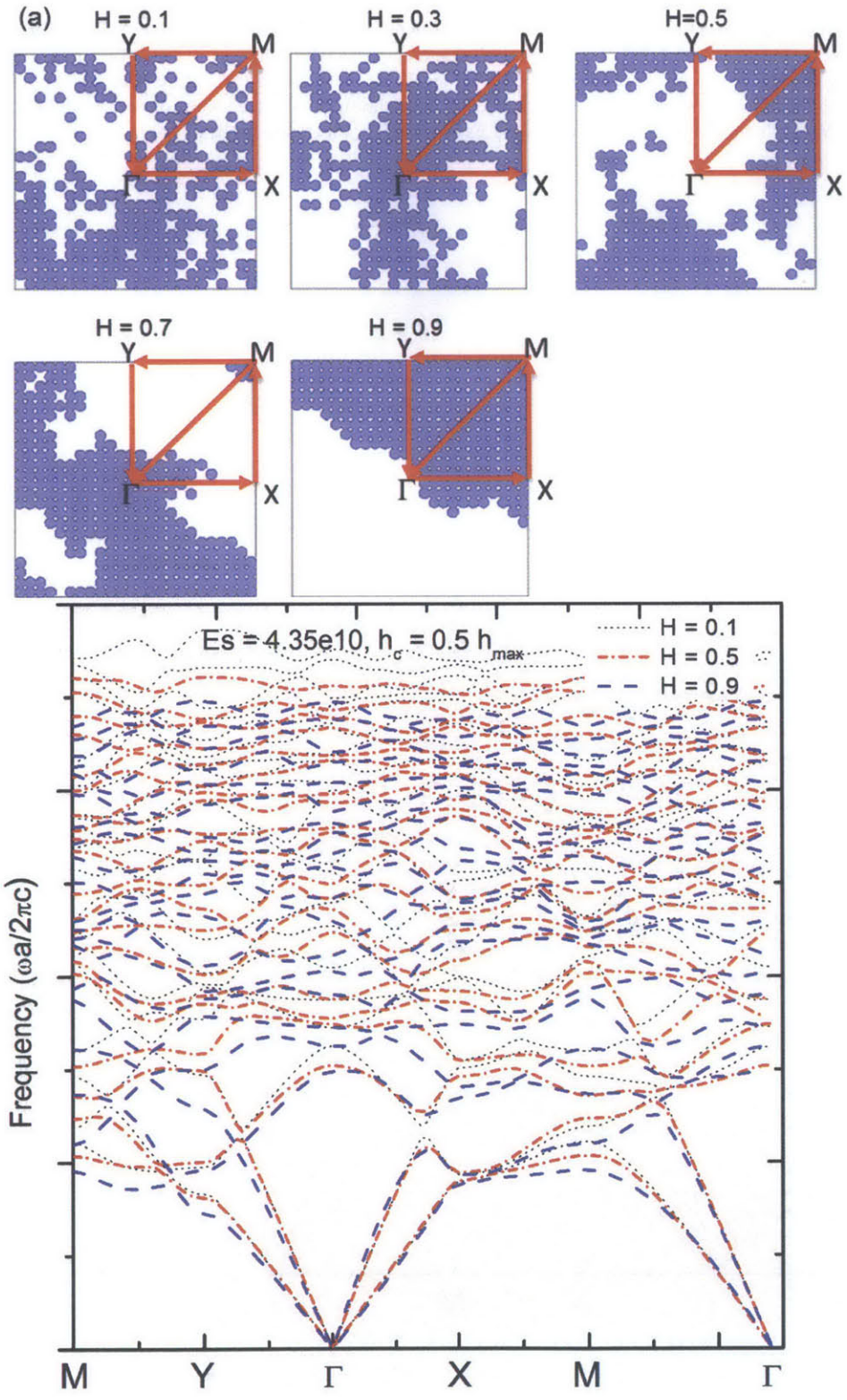
(a)
H = 0.1
H = 0.3
H=0.5
H = 0.7
H = 0.9
Y
M
Γ
X
Es = 4.35e10, h_c = 0.5 h_max
H = 0.1
H = 0.5
H = 0.9
Frequency (ωa/2πc)
M
Y
Γ
X
M
Γ

Figure 4.10: a) Examples of the planar binary metamaterials unit based on fractional Brownian surface with different Hurst constants as listed on top of the unit cell. The circles are scatterer phase while the rest is the matrix phase. b) Dispersion curves along the BZ of the unit cell (along Γ→ X→M→ Γ) as indicated in the Figure 4.10 for random fractal based sample with different Hurst constant, e.g. H = 0.1 (black dot line), H = 0.5 (red short dash dot) and H0.9 (blue dash)), where the Young's modulus of the scatterers are Es = 4.35e7Pa, others are listed in Table 4.1.

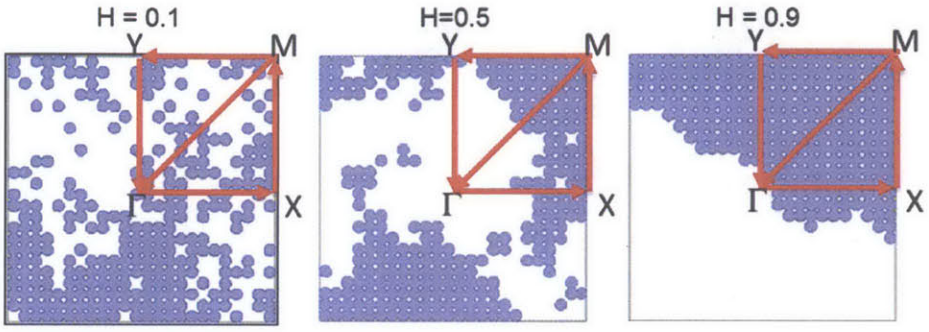

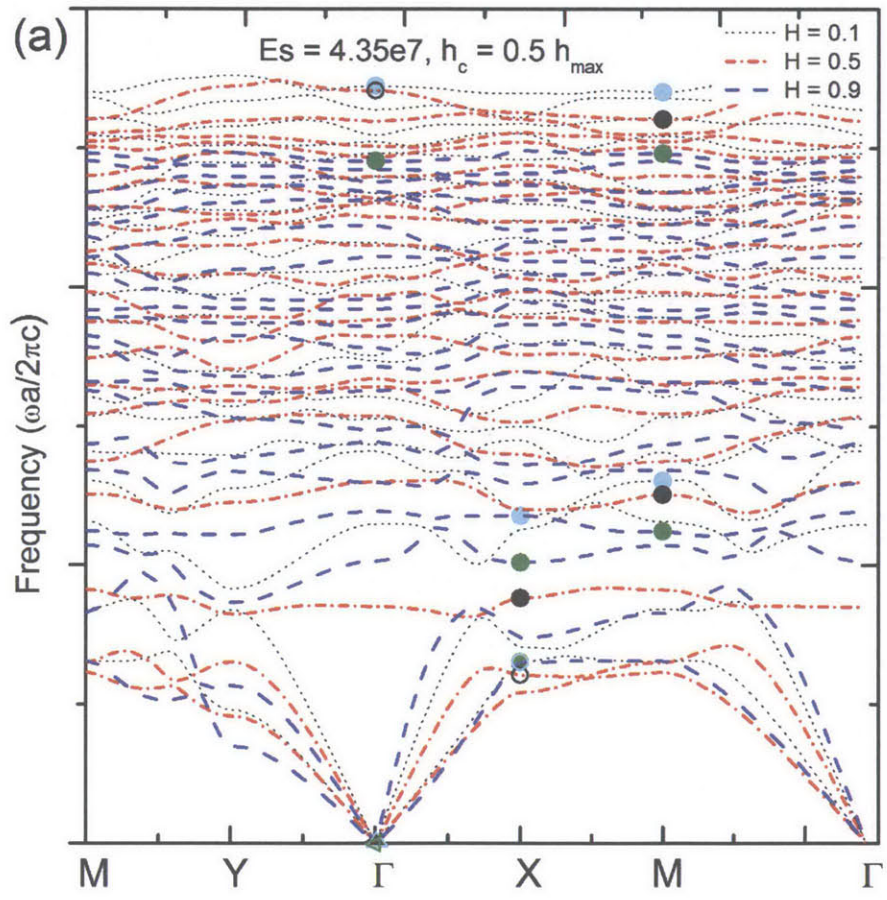

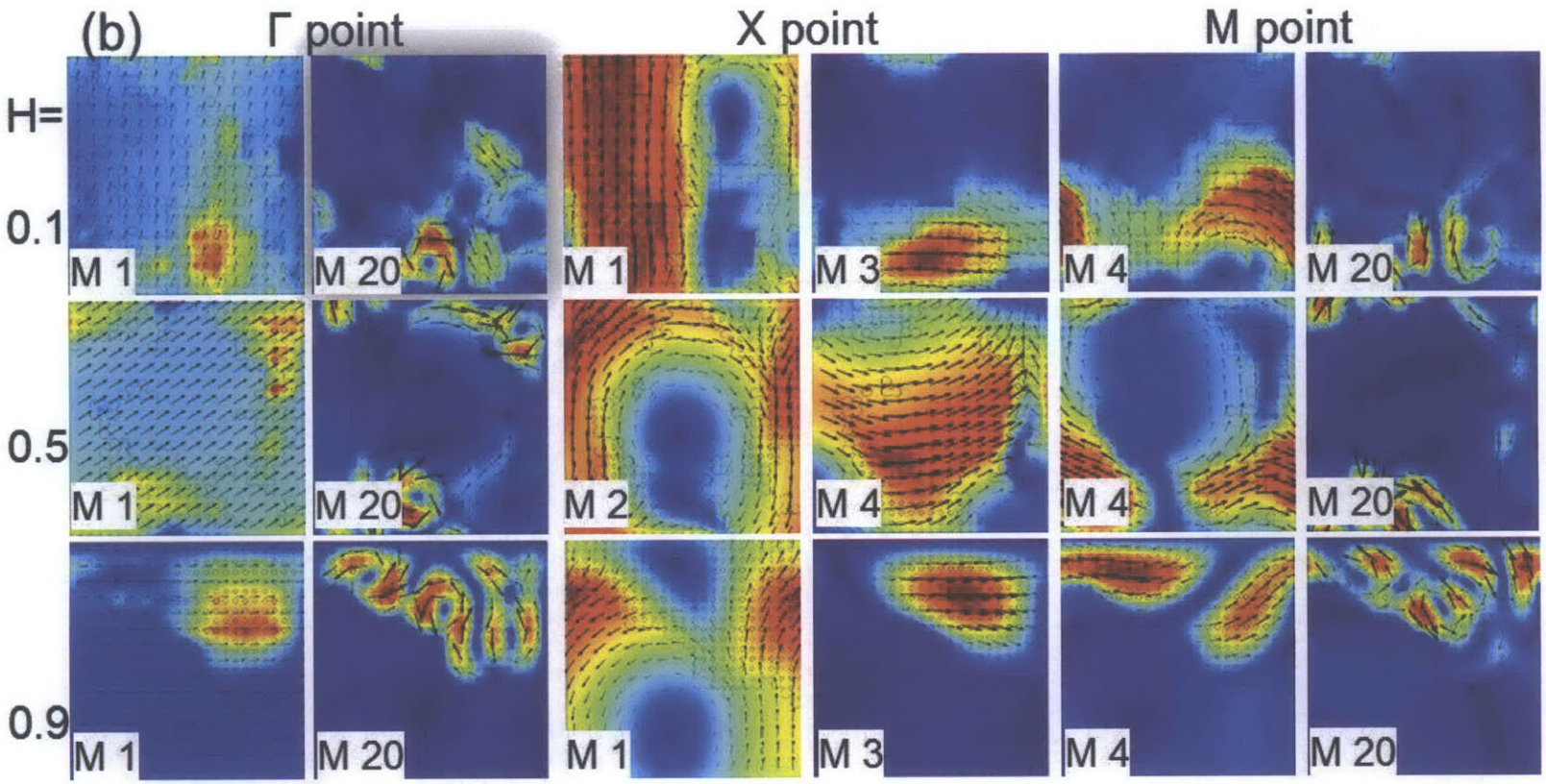

Figure 4.11: (a) Dispersion curves along the BZ of the unit cell (along Γ→ X→M→ Γ) as indicated in the Figure 4.5 and 4.10 for random fractal based sample with different Hurst constant, e.g. with H = 0.1 (black dot line), H = 0.5 (red short dash dot) and H = 0.9 (blue dash)), where the Young's modulus of the scatterers are Es = 4.35e7Pa (where impedance contrast is Ks/Km = 0.075),, others are listed in Table 4.1. (b) The eigenmodes corresponded to H = 0.1 (cyan circle), H = 0.5 (black solid triangle) and H = 0.9 (olive triangle/circle) are arranged at the bottom as indicated. The longitudinal and transverse modes are observed at Γ point for all three samples (e.g. M1). At higher frequencies, the high strain regions are more concentrated in the softer scatterers (e.g. M20). At X point, the eigenmodes of samples started to have high strain region confined to scatterer phase even at relatively low frequency (M3 (4) M1 (2) at X point) given the increased cluster size.

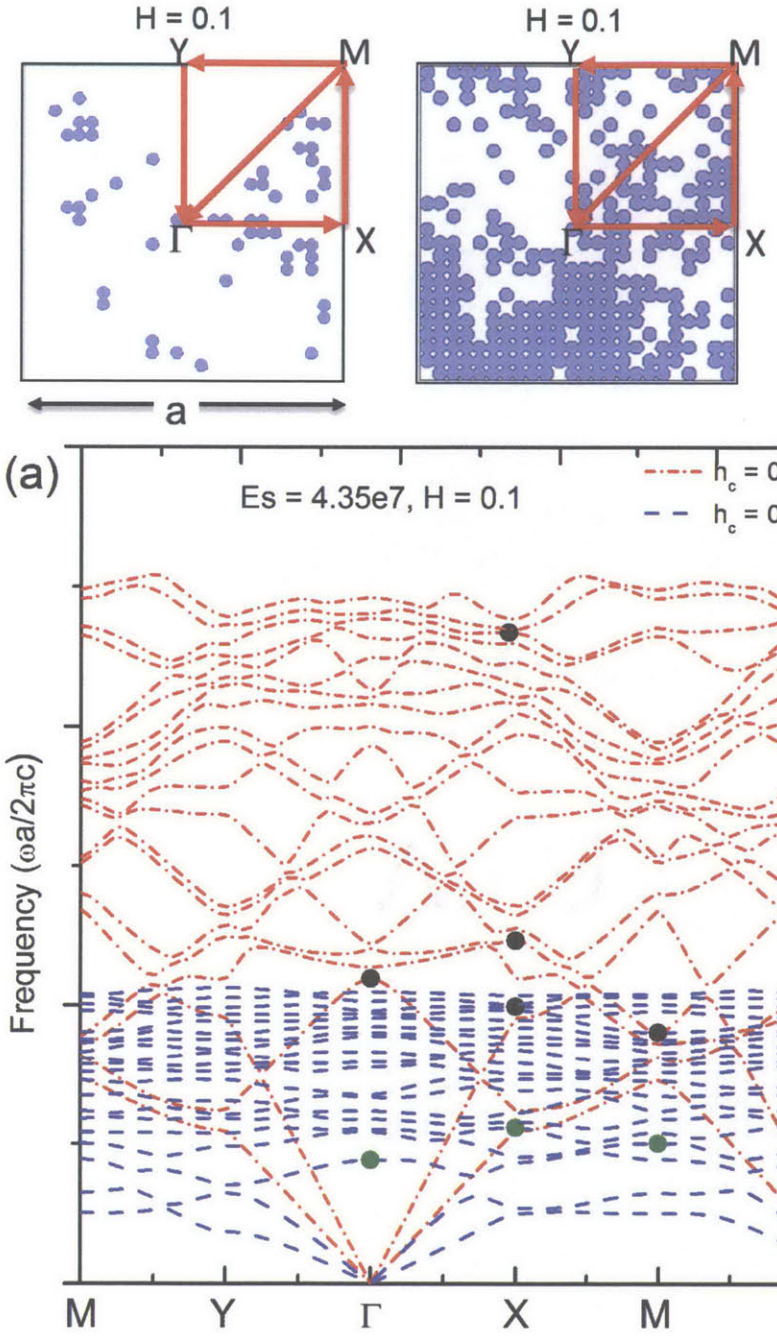
H = 0.1
Y
M
Γ
X
a
H = 0.1
Y
M
Γ
X
(a)
Es = 4.35e7, H = 0.1
h_c = 0.9h_max
h_c = 0.5h_max
Frequency (ωa/2πc)
M
Y
Γ
X
M
Γ

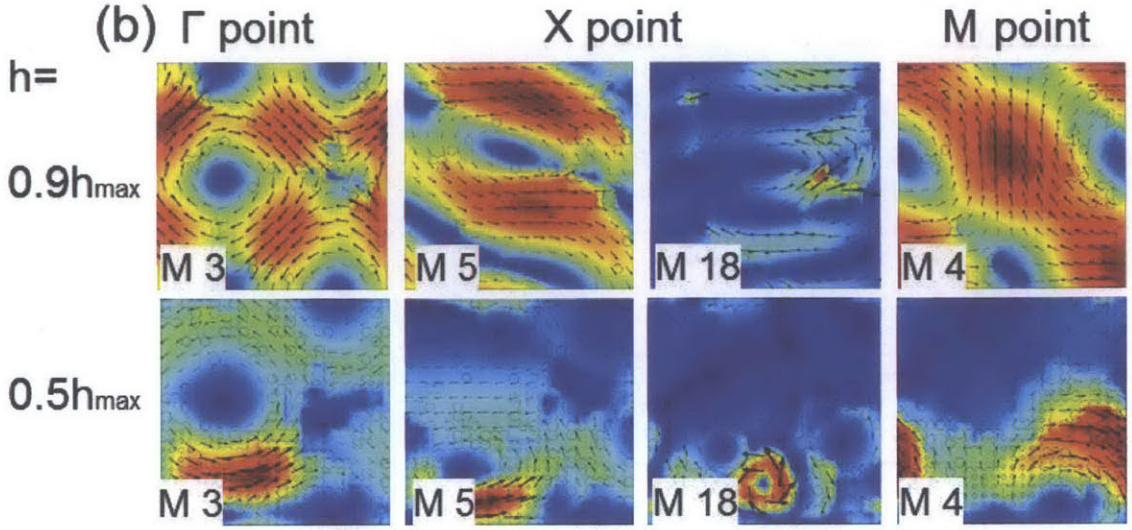

Figure 4.12: (a) Dispersion curves along the BZ of the unit cell (along Γ→ X→M→ Γ) as indicated in the Figure 4.5 and Figure 4.10 for random fractal based sample with H = 0.1 yet different filling ratios 0.0785 (i.e. h = 0.9hmax) (red short dash dot) and or 0.3927 (i.e. h = $0.5h_{max}$) (blue dash), where the Young's modulus of the scatterers are Es = 4.35e7Pa(where impedance contrast is Ks/Km = 0.075),, others are listed in Table 4.1. (b) The eigenmodes corresponded to h = $0.9h_{max}$ (black solid triangle) and h = $0.5h_{max}$ (olive triangle/circle) are arranged at the bottom as indicated, the eigenmodes of $h_c = 0.9h_{max}$ are more regular (in terms of high/low strain regions) displacement pattern compared to $h_c = 0.5h_{max}$. On the other hand, the transition from high to low strain region are more influenced by the shape of clusters for samples of $h_c = 0.5h_{max}$.

For H = 0.5, the eigenmodes become localized in the cluster with the largest cluster size in the unit cluster (i.e. top right and bottom left of the unit cell), as M20 shown at X and M point in the eigenmodes plot in Figure 4.11. While for the sample with H =0.9, the eigenmodes are localized at the top right corner, demonstrated in M3 at X and M4 at M point as well as M20. For the scatterer to form spanning cluster, $h_c \approx 0.4$ is required, which corresponds to fill fraction for site percolation threshold (0.593).

To have a more direct comparison of samples with different value of the fill fraction, samples with the same H value are plotted in Figure 4.12 and 4.13. In both cases, the eigenfrequency decreases with increasing fill fraction of the softer scatterer phase. For H = 0.1, the regularity of high/low displacement regions also decreases as the fill fraction of scatterer increases at the frequency range we studied, (M3, M5 and M4 shown in eigenmodes plot in Figure 4.12). For H = 0.9, both samples exhibit eigenmodes localized to the soft scatterer phase, where the largest size of cluster for h = $0.5h_{max}$ is larger than those of h = $0.9h_{max}$. Therefore, the corresponding eigenfrequency of h = $0.5h_{max}$ is smaller than those of h = $0.9h_{max}$, as shown in Figure 4.12.

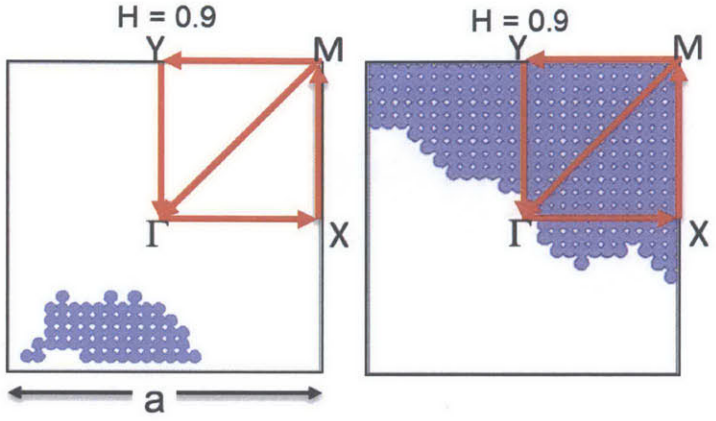
H = 0.9
Y
M
Γ
X
a
H = 0.9
Y
M
Γ
X

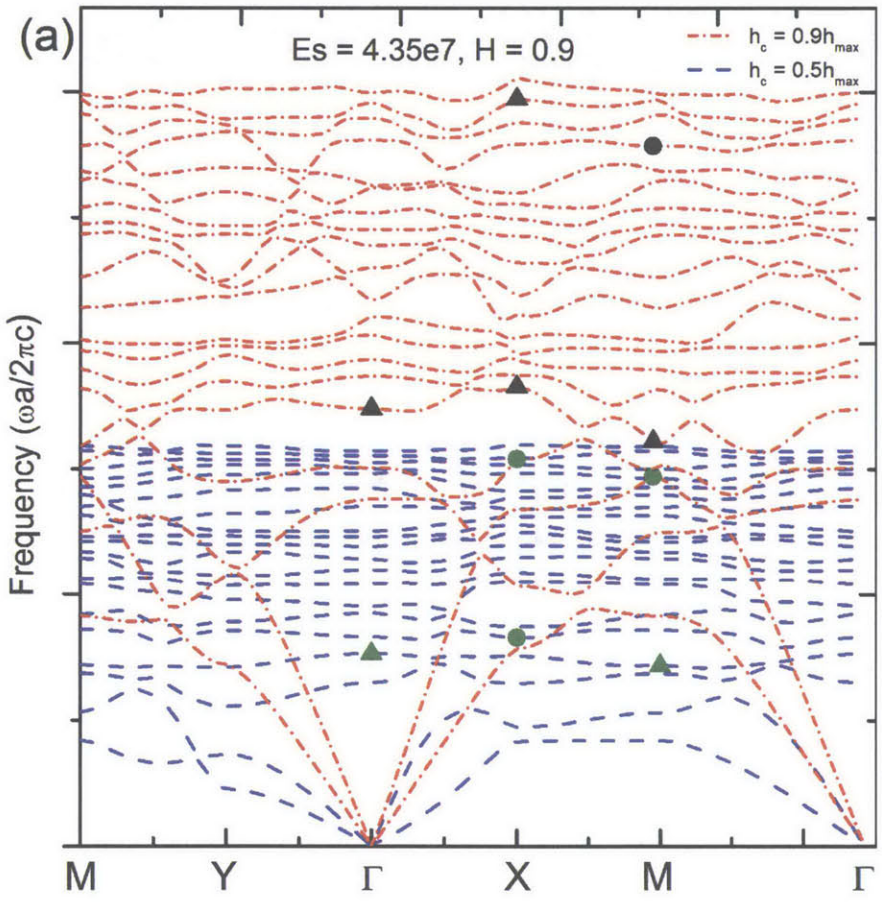
(a)
Es = 4.35e7, H = 0.9
h_c = 0.9h_max
h_c = 0.5h_max
Frequency (ωa/2πc)
M
Y
Γ
X
M
Γ

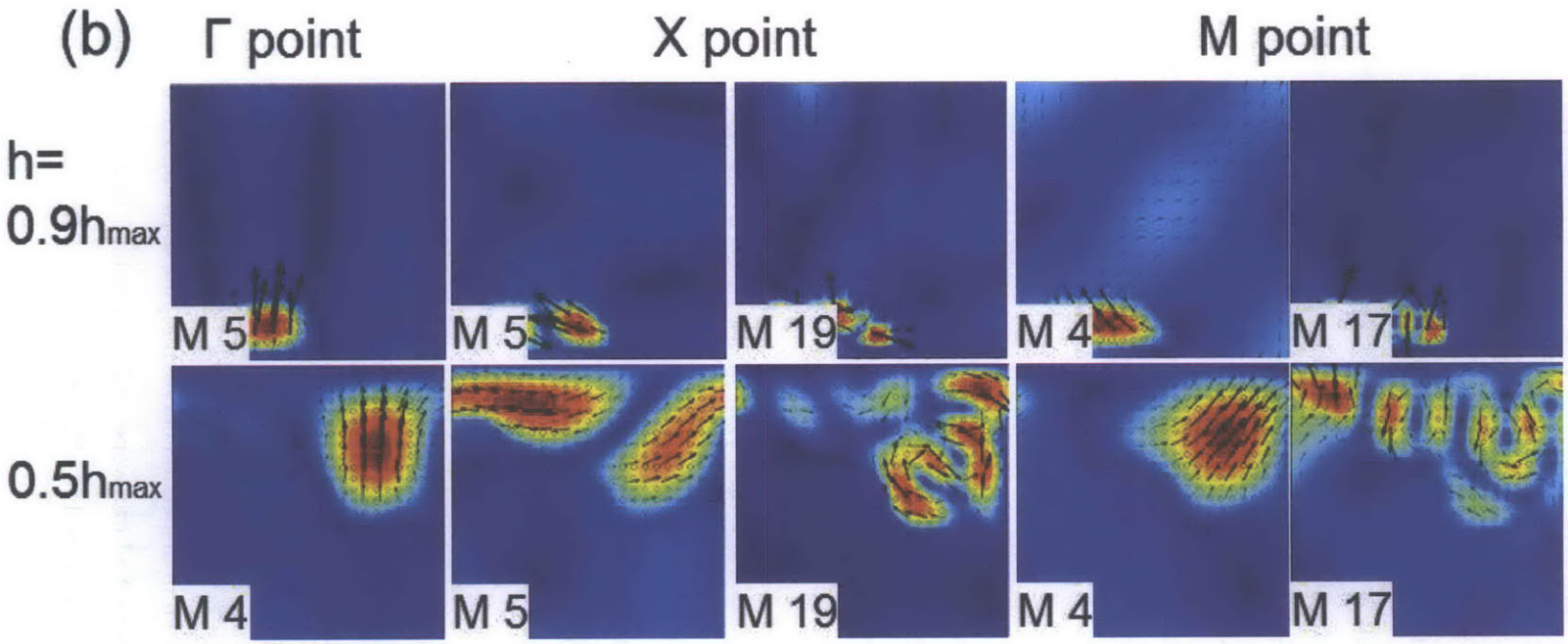

Figure 4.13: (a) Dispersion curves along the BZ of the unit cell (along Γ→ X→M→ Γ) as indicated in the Figure 4.5 and Figure 4.10 for random fractal based sample with H = 0.9 yet different filling ratios 0.0785 (i.e. h = 0.9hmax) (red short dash dot) and or 0.3927 (i.e. h = 0.5hmax) (blue dash), where the Young's modulus of the scatterers are Es = 4.35e7Pa(where impedance contrast is Ks/Km = 0.075),, others are listed in Table 4.1. (b) The eigenmodes corresponded to h = 0.9hmax (black solid triangle) and h = 0.5hmax (olive triangle/circle) are arranged at the bottom as indicated, where the color indicates the magnitude and the arrow indicates the direction of the displacement. The eigenmodes for both samples has the high strain confined to softer scatterers region since the average size of the scatters are comparable to the wavelength investigated.

4.3.4 Varying the scale of the system

As mentioned before, the scale, or more precisely the relative scale of individual scatterer diameter and unit cell, can be varied artificially by introducing more grid numbers (i.e. N = 100 and N =150) per unit cell in the system, as shown in Figure 4.14.And it is likely that by including the number of scatters per unit cell, it would represent the system more accurately, given the statistical nature of the system It should be mentioned that this is different from self-similarity in strict sense since periodic boundary condition has been applied at the unit cells in all cases. To investigate whether N = 50 would be sufficient to simulate the behavior of the system based on random fractal, we increase grid number to N = 100 and N = 150 and compared their behavior with the case for N = 50.

For H = 0.1, the dispersion curves traces closely for samples with grid number m=n=100 and m=n=150, as shown in Figure 4.15 (a), especially at lower frequencies, since they corresponds to the extended modes of homogeneous plate closely. This might due to the fact the wavelength studied are larger than the critical length scale (corresponding to the scatterer/cluster size of m=n=100 and m=n=150); Hence the wavelength studied cannot sense the difference in the numbers of scatterers per unit cell. This could be beneficial for the simulation since it allow for choice of a small unit cell, hence less demanding for the simulation. For H = 0.5, the dispersion curves start to deviate more from each other at higher frequency (as circled in the figure) while the dispersion curves at lower frequency still overlap with each other closely, as shown in Figure 4.15 (b). For H = 0.9, the dispersion curves for harder scatterer/soft matrix have less a clear trend with increasing grid number per unit cell, as shown in Figure 4.16(a). For softer scatterers, the dispersion varies significantly with increasing number of grid number per unit cell, as shown in Figure 4.16(b). At Γ point, the longitudinal and transverse like eigenmodes occurred with the homogeneous plate like eigenmodes M4 for grid number 50 and 100 (as shown in Figure 4.17). However, as the number increase to 150, this regular periodic eigenmodes is replaced by a more localized modes (despite the four lower displacement region at M4). Hence, its frequency is also lowered with increasing grid number as shown in dispersion curve in Figure 4.16 (b). At X and M point, the lowest few eigenmodes exhibit disturbed transverse and longitudinal like eigenmodes, where the frequency split is the smallest for N = 150. Hence it is important to choose the

appropriate length scale for averaging, otherwise, misrepresentation and loss of information could happen.

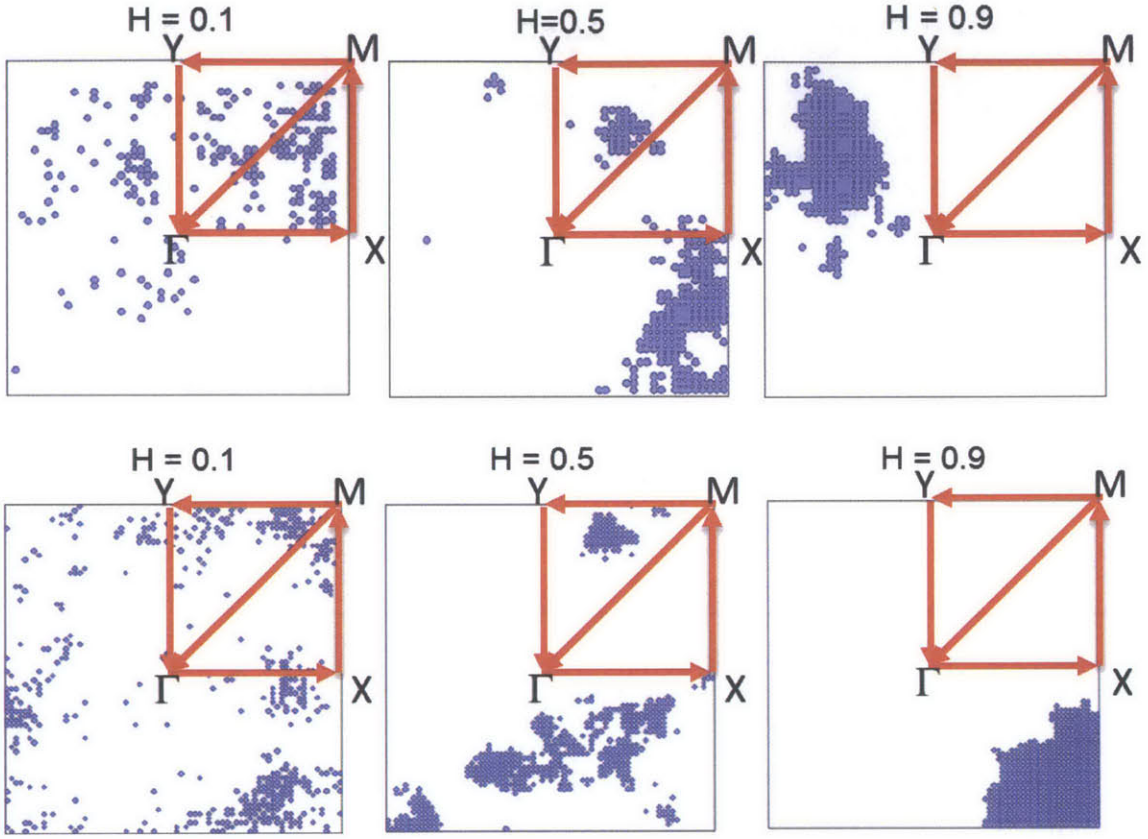

Figure 4.14: Examples of the binary metamaterials unit based on fractional Brownian surface with different Hurst constants as listed on top of the unit cell and grid number per unit cell of m=n=100 (first row) and m=n=150 (second row). The circles are scatterer phase while the rest is the matrix phase.

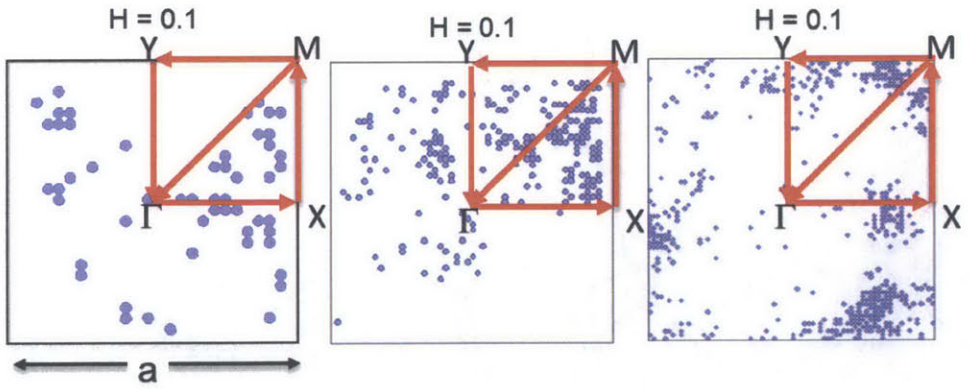

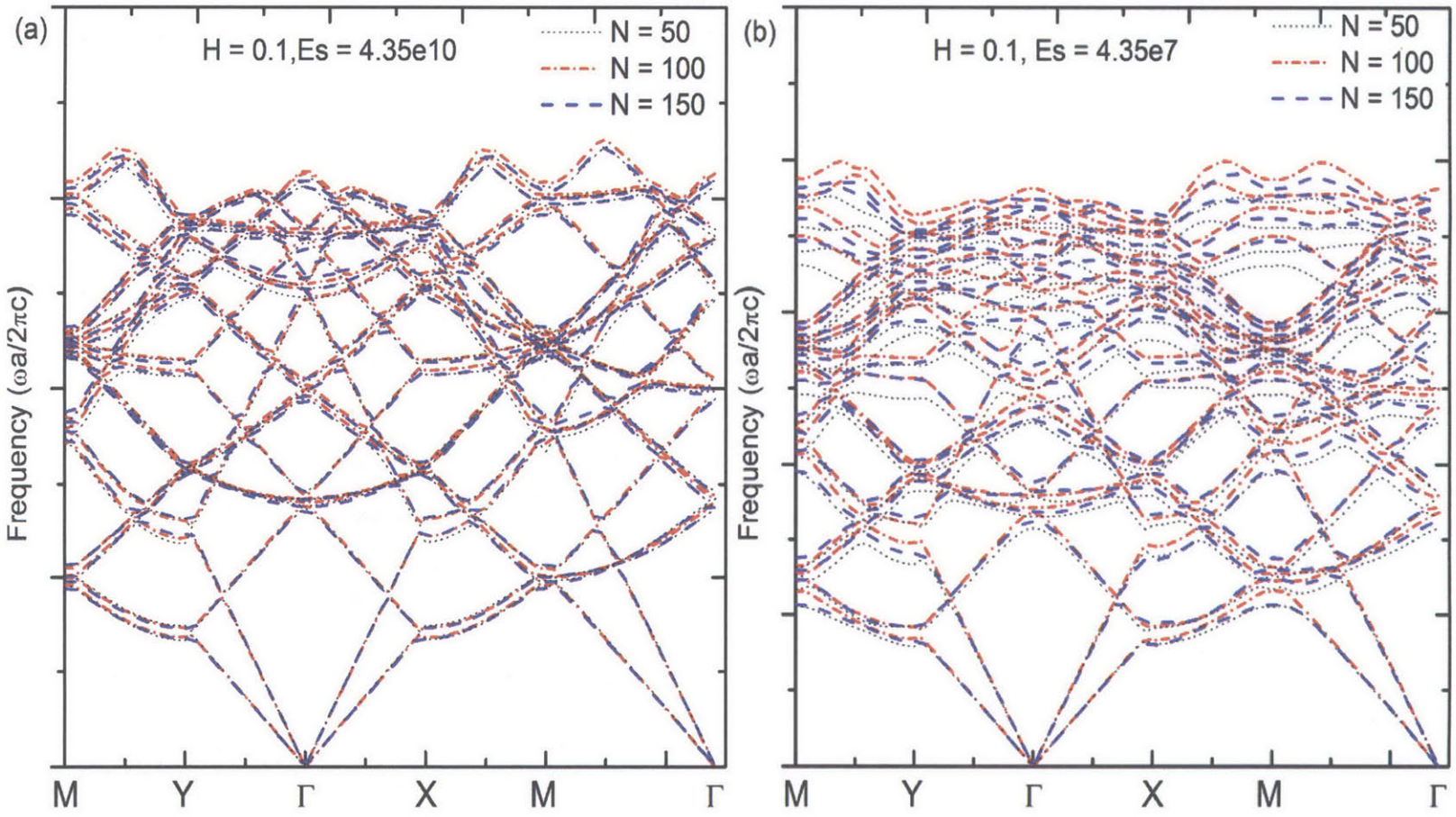

Figure 4.15: Dispersion curves along the BZ of the unit cell (along Γ→ X→M→ Γ) for random fractal based sample with H = 0.1 for Es = 4.35e10Pa(where impedance contrast is Ks/Km = 2.374), a) and Es = 4.35e7Pa(where impedance contrast is Ks/Km = 0.075), b) yet different number of grid point in the unit N = 50(black dot line), N = 100 (red short dash dot line) and N = 150 (blue dash line) others are listed in table 4.2.

4.3.5 Varying the arrangement of the system

Even though the fractal dimension description greatly extends our ability to describe artificial and natural geometry and processes, sometimes a single fractal dimension is not sufficient to describe the complex and/or dynamic system occurring in nature. Hence a multifractal system was proposed where a spectrum of exponent I used to characterize systems/processes in nature. They have been used to study fully fluid dynamics, stock market, biological system, geophysics, astronomy, image modeling. As mentioned before, multifractal can be demonstrated as varying fractal dimension at different resolution (both spatial and temporal) in scale relativity framework. In practice, the multifractal analysis algorithms have been developed to describe natural systems and even used to predict their behavior. To mimic the multifractal system, we studied two system: one with a Hurst constant H = 0.5, and the other is a multifractal super-cell consist of four cells with pairs of H = 0.3 and H = 0.7 arranged diagonally, as shown in Figure 4.16. The grid number and unit cell are adjust such that the two systems have same filling ratio and unit cell size. The dispersion curve were studied to find out how they phononic behavior would be affected by different spatial arrangement of two system having an average H = 0.5

The dispersive behavior of the two systems are plotted in Figure 4.18. Significant differences develop due to rearranging the distribution of scatterers. In general, the multifractal sample with a mixture of H values (i.e. MixedH) have eigenmodes with more extended displacement compared with samples with the single H (i.e. SingleH) value (as shown in eigenmodes plot in Figure 4.18.

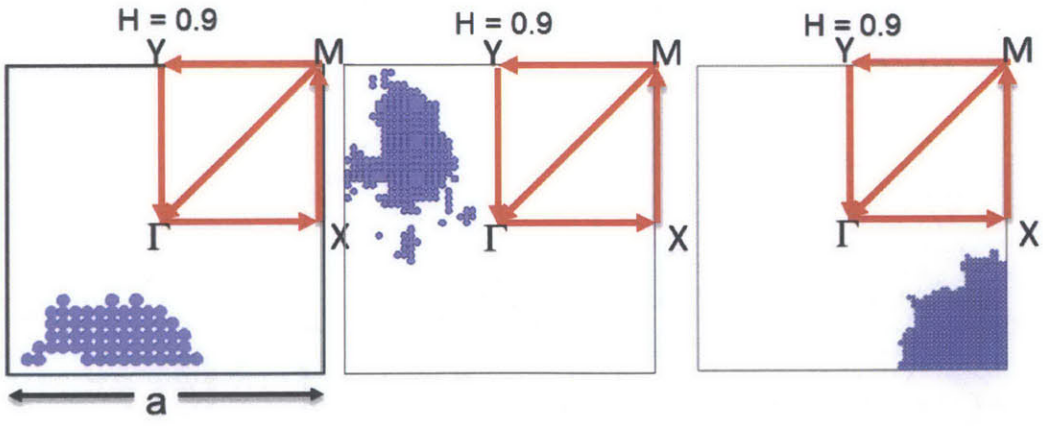

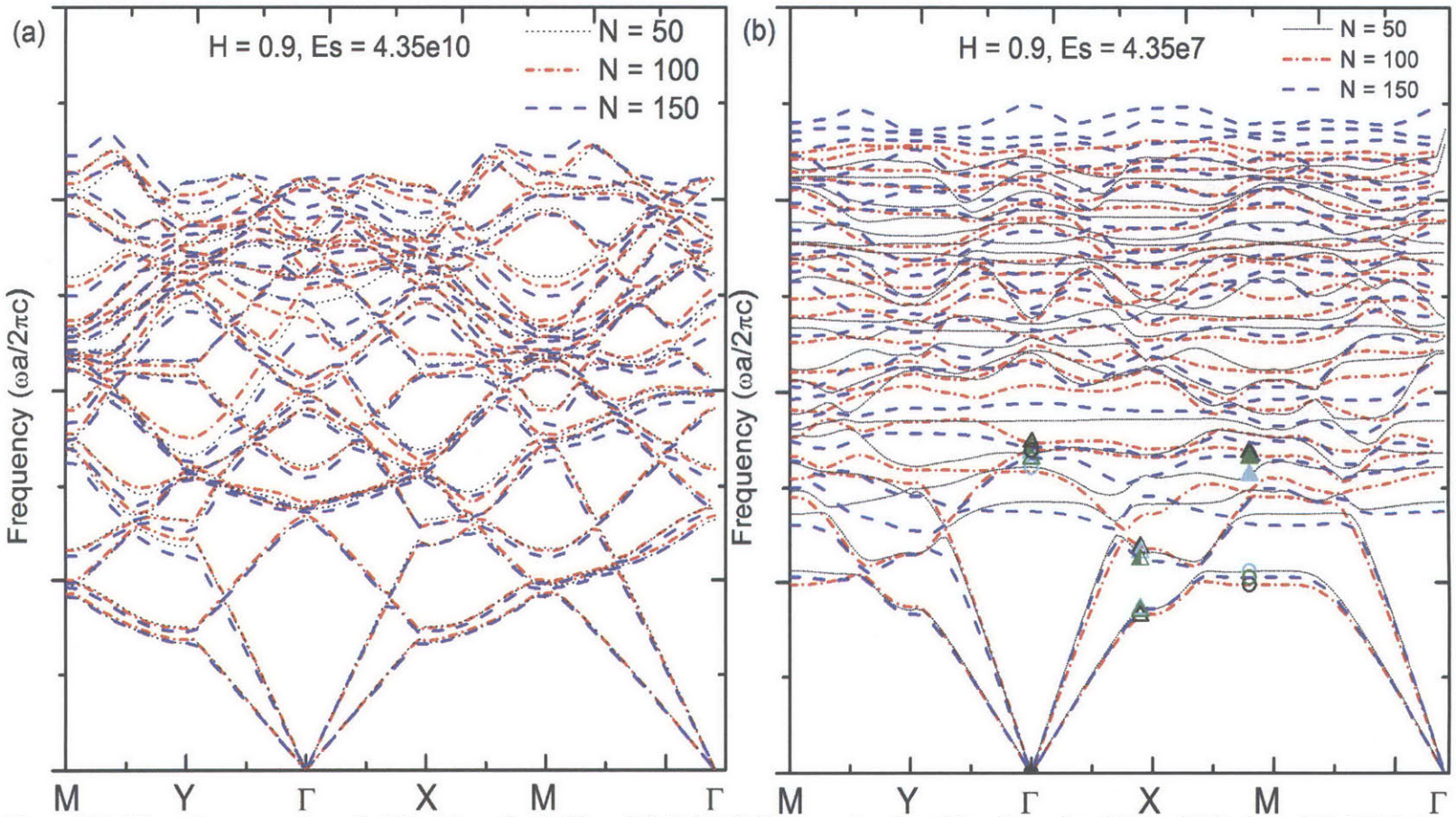

Figure 4.16: Dispersion curves along the BZ of the unit cell (along Γ→ X→M→ Γ) for random fractal based sample with H = 0.9 for Es = 4.35e10Pa(where impedance contrast is Ks/Km = 2.374), a) and Es = 4.35e7Pa (where impedance contrast is Ks/Km = 0.075), b) yet different number of grid point in the unit N = 50(black dot line), N = 100 (red short dash dot line) and N = 150 (blue dash line) others are listed in Table 4.1.

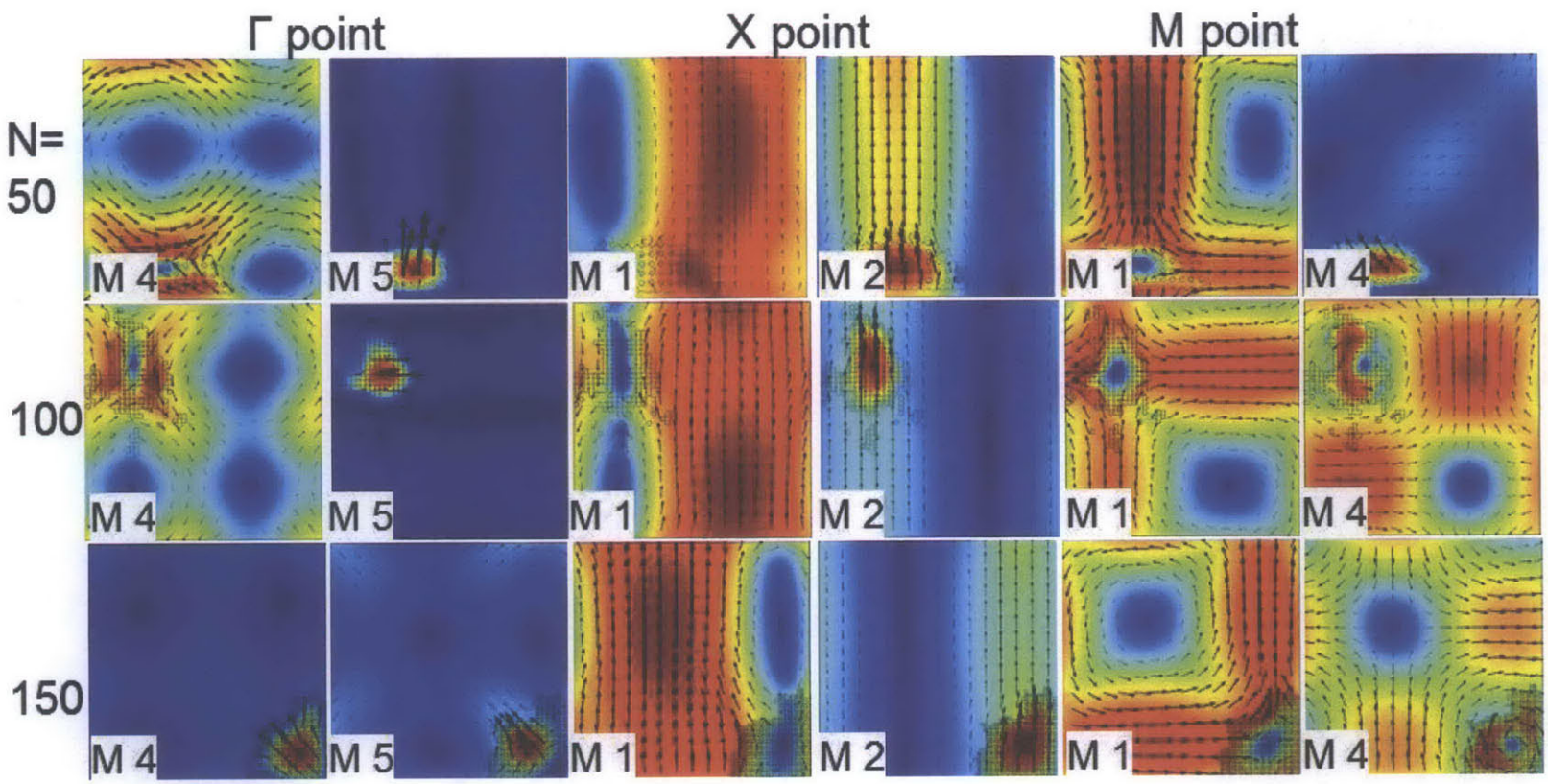

Figure 4.17: The eigenmodes corresponding to Figure 4.16(b) from sample with grid number N = 50 (Cyan solid triangle/circle), N = 100 (Cyan solid triangle/circle) and N = 150 (olive triangle/circle).The longitudinal and transverse like modes are observed at X point for all three samples (e.g. M1 and M2) where the location of the super-cluster define the low/high strain transition. At M point, the diagonal half without the cluster would become the low strain region where (as well as the center of super-cluster) while the displacement are relative antisymmetric with respect to the diagonal of the unit cell (M1 (4) at M point.

At the Γ point, M3 for the sample MixedH, a regular arrangement of high/low displacement is found, while M3 for sample SingleH have its transition region affected by the boundary of scatterers at the lower right corner. The M4 mode for sample SingleH is localized while M4 for sample MixedH still shows features similar to regular square plate (M4 at Figure 4.18 eigenmodes plot). At M point, the longitudinal and transverse like modes exhibit themselves with different degrees of distortion due to scatterer clusters, as shown in M1, M2 and M3 at X point in Figure 4.18. The localized M4 modes for sample SingleH is retained while it is more extended for sample MixedH. At M point, all eigenmodes with the lowest frequencies show all eigenmodes with the lowest frequencies show extended features. However, the eigenmodes are similar to nodes and antinodes features of homogeneous plate more closely with more regular node/antinode in displacement. This might be explained by the fact that the arrangement of mixed H value block are artificially periodic (i.e. in a 2by2 fashion), which could define the dispersion behavior at lower frequencies.

This indicates that the arrangement of the unit cell does affect the behavior of the super cell significantly; Hence H value of supercell cannot be simply averaged over its cells with different H value.

4.3.6 Vary the modulus of the system

With an understanding of the non-locality of dispersion behavior, we can further fine tune the system by varying the material properties of the system, e.g. Young's Modulus of the scatterer phase as shown in Table 4.2.

For all the systems studied, the eigenfrequency shifted downwards with decreasing Young's modulus of the scatterer phase. For H = 0.1, the extended modes become more localized with

Table 4.2: Material properties used for the simulation for dispersion curve of sample H=0.1, H=0.5.

Material Properties	Scatterer1	Scatterer2	Scatterer3	Matrix
Young's Modulus Pa	4.35e10	4.35e7	4.35e6	3e9
Poisson Ratio	0.329	0.329	0.329	0.375
Density kg/m^3	972	972	972	2500

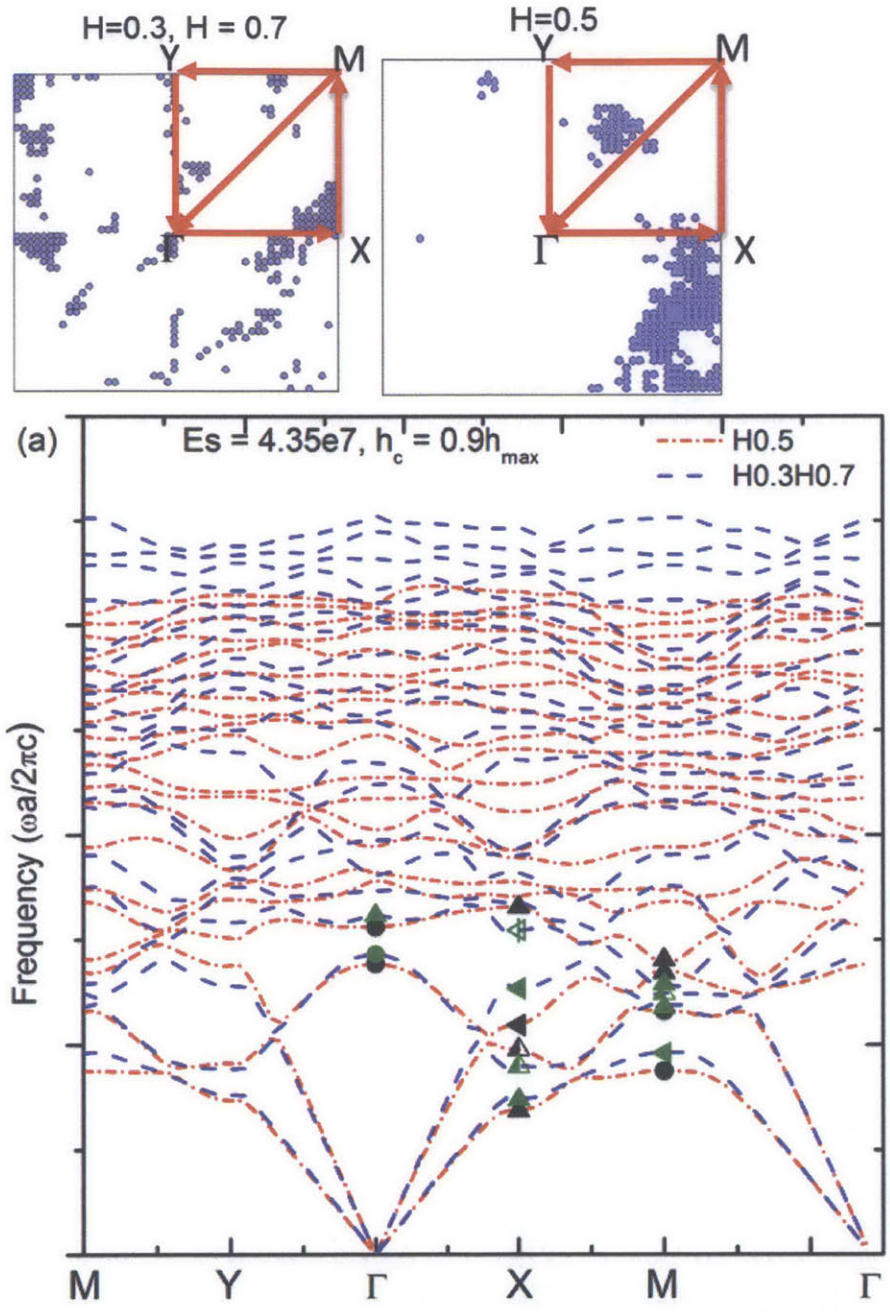
H=0.3, H = 0.7
Y
M
Γ
X
H=0.5
Y
M
Γ
X
(a)
Es = 4.35e7, h_c = 0.9h_max
H0.5
H0.3H0.7
Frequency (ωa/2πc)
M
Y
Γ
X
M
Γ

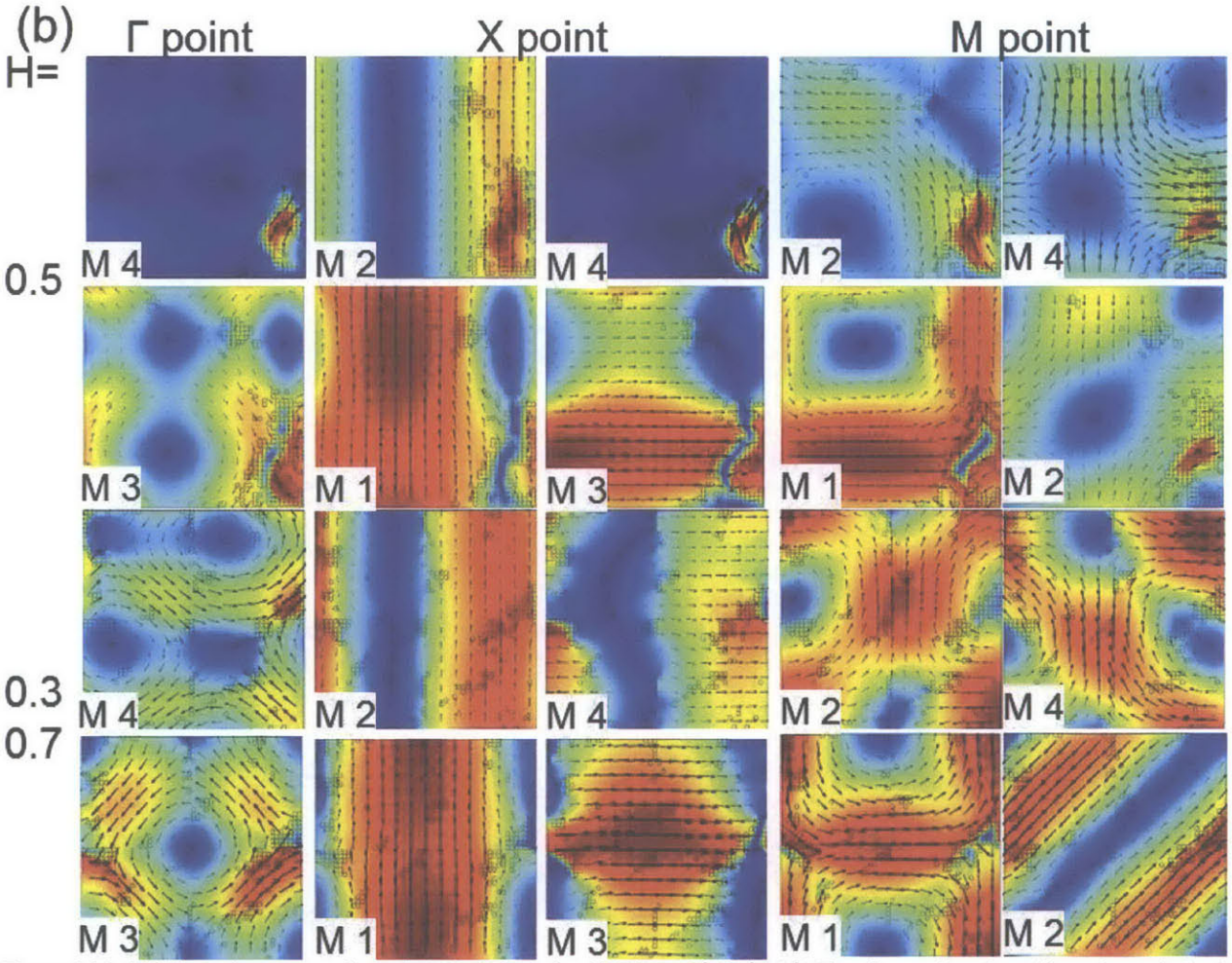

Figure 4.18: (a) Dispersion curves along the BZ of the unit cell (along Γ→ X→M→ Γ) as for random fractal based sample having H = 0.5 (red short dash dot) and H = 0.3, H =0.7 mix (blue dash), where the insert of the second sample are shown in the insert on the right, (where impedance contrast is Ks/Km = 0.075), and other materials properties are listed in Table 4.1. b) The eigenmodes corresponded to H = 0.5 (black solid triangle) and H = 0.7/0.3 (olive triangle/circle) are arranged at the bottom as indicated, the longitudinal (M3 (4)) and transverse (M1 (2)) like modes are observed at X point for all three samples (e.g. M1). Samples with mixed H value seems to exhibit eigenmodes with an underlying size of a quarter of the unit cell (same of the unit cell used to build the super cell).

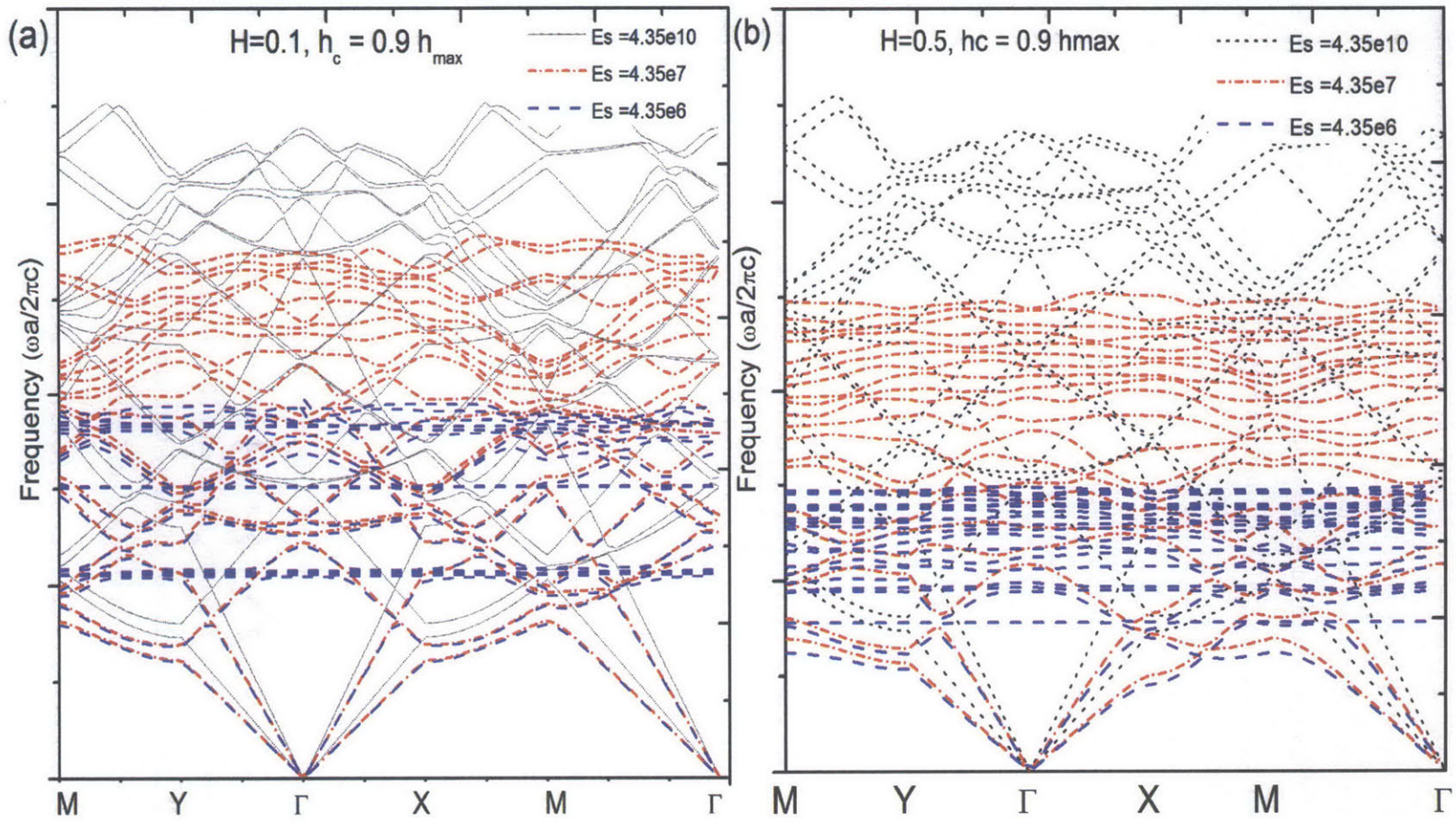

Figure 4.19: Dispersion curves along the BZ of the unit cell (along Γ→ X→M→ Γ) as for random fractal based sample for sample H = 0.1 m=n=50 a) and H = 0.5, m=n=100 b) for varying Young's Modulus of scatterers: Es = 4.35e10Pa (black dot line) (where impedance contrast is Ks/Km = 2.374), Es = 4.35e7Pa (red short dash dot) (where impedance contrast is Ks/Km = 0.075), and Es = 4.35e6Pa (blue dash) (where impedance contrast is Ks/Km = 0.024), other material properties are listed in Table 4.2.

increasing impedance contrast, as shown in Figure 4.19 (a). When the Young's Modulus change by from 4.35e7 to 4.35e6, the longitudinal and transverse modes varied little since the dispersion curve coincide. However, the higher frequency modes are more localized, as reflected in the flat dispersion curves (blue dash line compared to red dash dot line). Similar behavior have been observed with samples of H = 0.5 and N = 100, as shown in Figure 4.19 (b).

4.4 Conclusion

Although quasicrystals attracted a great deal of attention in recent years, metamaterials design is still based primarily on periodic structure, due to both theoretical and experimental limitations (Pawlak, D. A 2010). However, many "rough surface" exist in nature and biological system, therefore metamaterials based on fractal geometry might introducing new materials/systems with novel properties for various applications. This chapter utilized the concepts of fractional Brownian surface to study a binary system based on random fractals. It has been found that Hurst constant, which characterizes the fluctuation or width of the surface height, could be used to characterize the behavior of random fractal based system with moderate impedance contrast (i.e. $\frac{Ks}{Km} < 1/\sqrt{10}$. Although the statistical variable Hurst constant can be used to describe the statistical properties of random fractals of different iterations, the detailed distribution of scatterers does affect the nuanced dispersion behavior of the system, especially at higher frequencies, whose fluctuations in the scatterers influence the behavior. By varying the Hurst constant H, the dispersion behavior also varies as their cluster sizes vary with different H value. Moreover, the filling fraction also affects the behavior of the system by influencing both the effective properties at long wavelength and the largest cluster size.

It was also found that the dispersion behavior seems to vary little with different grid number/cell (i.e. relative scale) with small impedance contrast. This could be beneficial since smaller system can be used to study pseudo-random fractal system, which would reduce computation time and resource consumption. It was also found that for supercell with different H value at local cells, the arrangement of the cell affects the behavior of the system. However this might be due to the periodic arrangement of the local cell since they are artificially defined as 2by2 array.

By taking a systematic approach to study fractal based metamaterials, the factors that could influence the dispersion behavior have been identified and discussed. Although this likely is an incomplete list, this chapter shines light on the mechanisms of such system. The knowledge gained can further be used to understand the abundant fractal systems in nature; it can also be used to design system that can control and manipulate wave propagation through such systems. Hence studying metamaterial systems based on random fractal would increase the repertoire for novel designer materials; moreover, it may also contribute our understanding of natural physical system and processes.

4.5 Reference

Bader, R. (2005). Turbulent k − model of flute-like musical instrument sound production. In L.-V. Jacques & L. Evelyne (Eds.), *Fractals in Engineering* (pp. 109-121). Springer.

Chin, J. Y., Liu, R., Cui, T. J., & Smith, D. R. (2009). Rapid Design for Metamaterials. In R. L. Tie Jun Cui, David R. Smith (Ed.), *Metamaterials: Theory, Design, and Applications* (pp. 61-89). Springer.

Crnojevic-Bengin, V., Radonic, V., & Jokanovic, B. (2008). Fractal Geometries of Complementary Split-Ring Resonators. *IEEE Transactions on Microwave Theory and Techniques*, *56*(10), 2312-2321.

Evelyne Lutton, J. L.-V. (2005). *Fractals in Engineering: New Trends in Theory and Applications*. (J. Lévy-Véhel & E. Lutton, Eds.). © Springer-Verlag London Limited2005.

Feng, Y. (2009). Compensated Anisotropic Metamaterials : Manipulating Subwavelength Images. *Metamaterials: Theory, Design, and Applications* (pp. 155-181).Springer.

Huang, X., Xiao, S., Ye, D., Huangfu, J., Wang, Z., Ran, L., & Zhou, L. (2010). Fractal Plasmonic metamaterials for subwavelength imaging. *Optics Express*, *18*(10), 10377.

Huang, X., Xiao, S., Zhou, L., Wen, Weijia, Chan, C T, & Sheng, Ping. (2009). Photonic Metamaterials Based on Fractal Geometry. *Metamaterials: Theory, Design, and Applications* (pp. 215-245).

Ito, S. (2010). *Fractal THz slow light metamaterial devices*. Oklahoma State University. Jacquin, A. (1994). An introduction to Fractals and Their Applications in Electrical Engineering. *Journal of the Franklin Institute*, *331*(6), 659-680.

Koh, C. Y. (Henry). (2011). *Generalized Phononic Networks: Of Length Scales, Symmetry Breaking and (Non) locality "Controlling Complexity through Simplicity."* Massachusetts Institute of Technology. PhD thesis

Kubota, S., Miyamaru, F., & Takeda, M. W. (2009). *Terahertz Response of Fractal Metamaterials. 2009 34th International Conference on Infrared, Millimeter, and Terahertz Waves* (pp. 1-2). IEEE.

Mandelbrot, B. B. (1977). *Fractals: Form, Chance, and Dimension* (p. 365). San Francisco: W. H. Freeman, c1977.

Mandelbrot, B. B. (1983). *The fractal geometry of nature* (p. 468). San Francisco: W.H. Freeman, c1983.

Mandelbrot, B. B. (1997). *Fractals and Scaling in Finance: Discontinuity, Concentration, Risk: Selecta volume E* (p. 541). New York: Springer, c1997.

Mandelbrot, B. B. (2006). Self-Affine Fractals and Fractal Dimension. *Physica Scripta*, *36*(4), 21-260.

Mejdoubi, A., & Brosseau, C. (2009). Reflectance and absorbance of all-dielectric metamaterial composites with fractal boundaries: A numerical investigation. *Journal of Applied Physics*, *105*(2), 024110. American Institute of Physics.

Pawlak, D. A., Turczynski, S., Gajc, M., Kolodziejak, K., Diduszko, R., Rozniatowski, K., Smalc, J., et al. (2010). How Far Are We from Making Metamaterials by Self-Organization? The Microstructure of Highly Anisotropic Particles with an SRR-Like Geometry. *Advanced Functional Materials*, *20*(7), 1116-1124.

Woloszyn, P. (2005). Acoustic Diffraction Patterns from Fractal to Urban Structures: Applications to the Sierpinski Triangle and to a Neoclassical Urban Facade. *Fractals in Enginering* (pp. 97-108). Springer-Verlag London.

Rothman, D. H. (2008). Statistical Topography, lecture notes from MIT opencourseware, retrieved from http://ocw.mit.edu

Dirk P. K., Zdravko I. B. (2013). Spatial Process Generation. To appear in: V. Schmidt (Ed.).Lectures on Stochastic Geometry, Spatial Statistics and Random Fields, Volume II: Analysis, Modeling and Simulation of Complex Structures, Springer-Verlag, Berlin Retrieved fromhttp://www.maths.uq.edu.au/~kroese/ps/MCSpatial.pdf

5. Mesoscopic Metamaterials

5.1 Surface Acoustic Wave Device

Since the introduction of planar integrated circuits in the early 1960s, surface acoustic wave (SAM) become dominant in acoustic technology. Compared to conventional bulk acoustic device, SAW can provide many advantages such as compatibility with the microelectronic fabrication technology. Since the acoustic wavelength is about 10^{-5} of that of electromagnetic wave with the same frequency, it enables miniaturization of the devices(Campbell, 1989). Over the last few decades, SAW has become a sophisticated, versatile technology using piezoelectric films and other semiconducting materials(Balin, et al., 2009; Bohlein, et al., 2012; Bonello, et al., 2006; Dutcher et al., 1992; Glass, et al., 1983; Länge, et al., 2008). Given the flexibility of this technology, SAW has been used widely in various applications both high volume consumer products and specialized applications such as microfluidics, sensor etc. The high demand from telecommunication products further fueled the development SAW devices for high-frequency applications in the range of 100 MHz to a few GHz (Laude, Wilm, Benchabane, & Khelif, 2005; Lima & Santos, 2005; Maznev & Wright, 2009; Nardi et al., 2009; Tanaka & Tamura, 1998; Wu, Huang, & Lin, 2004; Zhang, 2009).

Surface acoustic wave can be generated in different ways and the interdigital transducer (IDT) is the most common one since it is especially adapted to signal processing applications. Invented by White and Voltmer, IDT uses sets of finger electrodes on piezoelectric substrates, where the shape and arrangement of the finger electrodes can control the characteristic of the surface acoustic wave. Since the acoustic energy is strongly confined at the surface of the devices in the range of the acoustic wavelength, the wave is potentially very sensitive towards changes on the surface(Länge et al., 2008). For specialized sensors, the device can be coated with sensitive functional polymer for various species, such as gas, protein etc. The challenges they face are attenuation of the displacement and fragile property with the thin thickens.

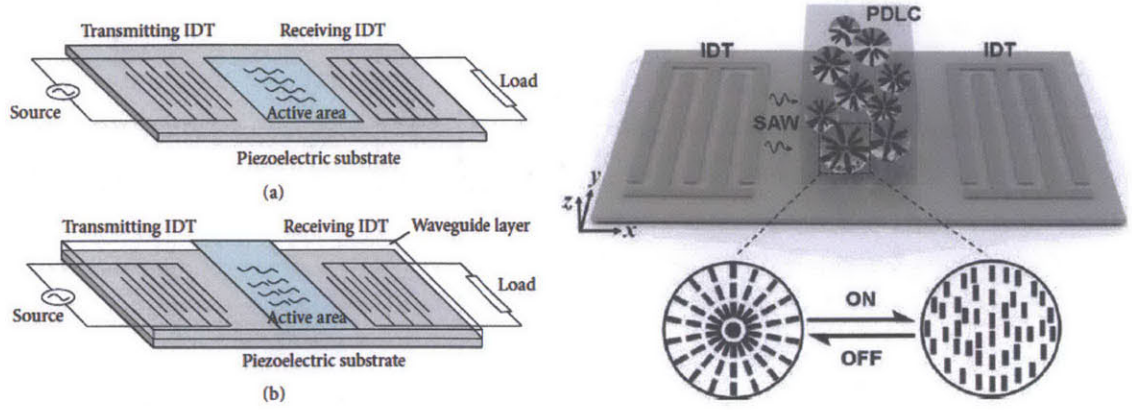

Figure 5.1: Schematic representations of a two-port delay-line SAW sensor (a) and a Love-mode SAW sensor (b) Source J. Sensors V 2009. The device structure and working principle for the SAW-driven PDLC light shutter. The magnified part shows a reversible switching process between two different LC droplet configurations. c) Source Adv. Mater. 2011, XX, 1–4,

Besides sensing, surface acoustic wave can also be used as actuating element for special applications. By interacting with special materials, they can be used to switch on and off by transform transparent materials into translucent/opaque, as shown in Figure 5.1(Liu et al., 2011)(Zhang, 2009).

Hence an understanding of the surface acoustic wave behavior would be beneficial for the designing surface acoustic wave devices with specific applications. Therefore it would be really attractive to engineer surface that can interact with acoustic wave in specific ways for targeted applications. In this chapter, we studied mesoscopic surface wave system where the system has two characteristic featured periodicity, one is the pitch of 1d grating while the other is scatters.

5.2 Mesoscopic Metamaterials with spherical scatters in 2D

As mentioned before, there are two periods in the mesoscopic, one from the grating and the other is the period of scatters. Starting from 2D system with grating and scatter represented by rectangles and circles (Figure 5.2 insert below). To mimic the final 3 dimensional system with only the gratings and scatters as the active features on silicon substrate, the thickness of the silicon (represented by red) in the 2D system has been reduced compared to grating and the scatters. From principles listed in the framework, a few factors are identified to affects the dispersion behavior and studied systematically.

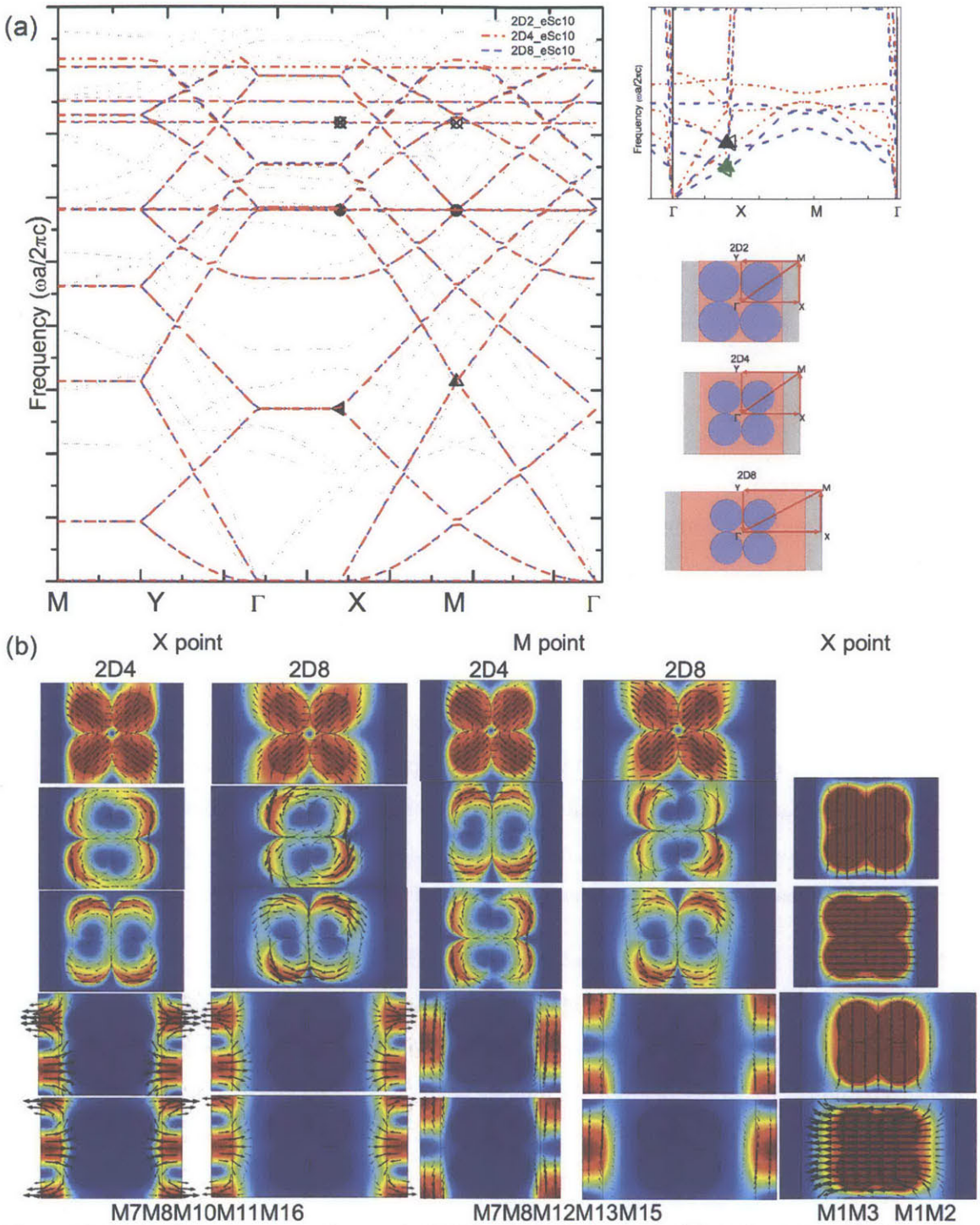

Figure 5.2: (a) the dispersion curves for sample 2D2 (black dot line), 2D4 (red dash dot dot) and 2D8 (blue dash) along the BZ of the unit cell (along M→ Y→ Γ→ X→M) as indicated in the unit cells in the bottom right insert. The top right inserts is zoomed in dispersion curve for the 3 samples. (b) The eigenmodes corresponded for 2D4 (black triangles/circle) and 2D8 (olive triangle/circle) are arranged at the bottom as indicated by the arrow and circles, where the color indicates the magnitude and the arrow indicates the direction of the displacement.

5.2.1Vary the period of the 1D grating

We choose samples 2D2 (as shown in insert 5.2) as reference system, since all the scatters are in contact with both grating and scatters. For sample pair 2D4 and 2D8, the scatters would cluster together at the center of the trench bounded by 1d grating with different period of 1D grating a_x, while other parameters remain the same. Similarly for sample pair 2D5 and 2D9, the scatters are in contact with 1d grating with different period of 1D grating a_x changed while other parameters remain the same. Compared to reference system 2D2, the dispersion behavior changed significantly along ΓX direction by simply removing the mutual contact point. This is not surprising since the wave propagate along ΓX direction can pass from 1d grating and scatters without passing through Si phase (despite the point contacts) in 2D2, but not for the rest of the samples. Therefore, the eigenfrequencies along ΓX direction is suppressed with relatively flat dispersion curve in the rest of the samples.

To zoom in at the frequencies along ΓX direction, the eigenfrequencies along ΓX direction would decrease with increasing a_x (Figure 5.2 zoom in inserts). For sample pair 2D4 and 2D8, the dispersion behavior along X→M→Γ and M→ Y→ Γ for extended modes overlap with each other, since they corresponds to eigenmodes of 1D grating, as shown in Figure 5.2. Since the 1d grating along XM direction are identical for 2D4 and 2D5, the eigenmodes restricted to 1d grating are also identical propagating modes (i.e. extended modes with linear dispersion curves). Moreover, the eigenfrequencies corresponds to the cluster modes (i.e. flat bands) vary little by increasing the a_x 1d grating, which indicates that coupling between the cluster and 1d grating is weak. However, to zoom in at the lower frequencies and their eigenmodes (fig 5.2 inserts and eigenmodes M1M2 (3)), the eigenmodes correspond to the displacement of center cluster and their frequencies decrease with increasing a_x along ΓX direction and XM direction.

Meanwhile, the dispersion curves for sample pair (2D5 and 2D9) with different ax are found to behave differently (Fig 5.3) where the extended modes along X→M→Γ and M→ Y→ Γ no longer overlap with each other. In general, the eigenmodes are relatively lower with larger ax (sample 2D9) along all Brillouin zone boundaries. The eigenmodes at lower frequencies vary by only a little since their displacement eigenmodes are similar to each other, as shown in Fig 5.3 eigenmodes. At M point, the degeneracies pairs for both samples appear to have shifted along y axis by half of period, i.e. symmetric with y axis mirror and antisymmetric with x axis mirror

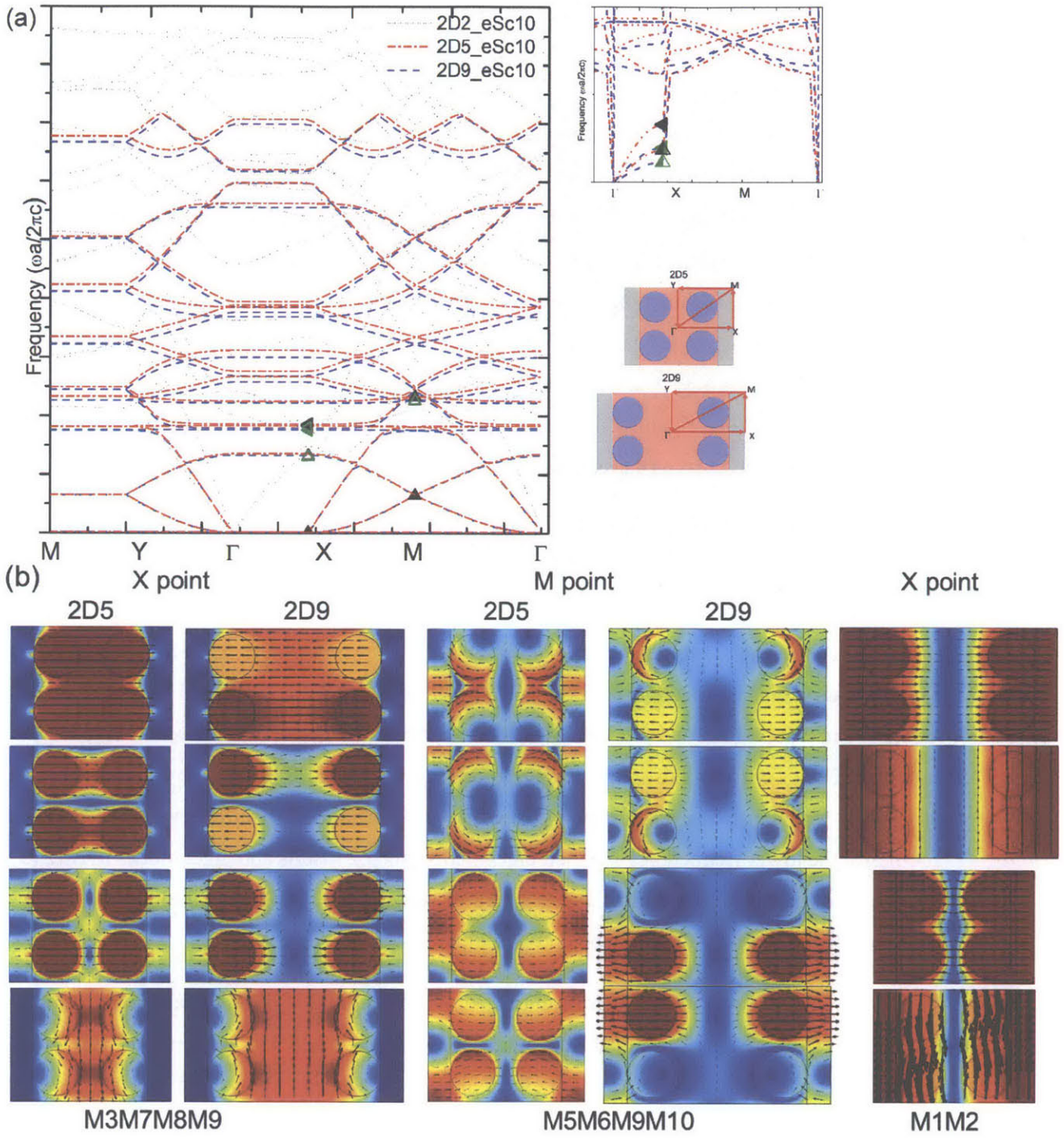

Figure 5.3: (a) the dispersion curves for sample 2D2 (black dot line), 2D5 (red dash dot dot) and 2D9 (blue dash) along the BZ of the unit cell (along M→ Y→ Γ→ X→M) as indicated in the unit cells in the bottom right insert. The top right inserts is zoomed in dispersion curve for the 3 samples. (b) The eigenmodes corresponded for 2D5 (black triangles/circle) and 2D9 (olive triangle/circle) are arranged at the bottom as indicated, where the color indicates the magnitude and the arrow indicates the direction of the displacement.

(Fig 5.3 eigenmodes). Similarly, at the extreme low frequencies, the eigenfrequencies decrease with increasing a_x along ΓX directions, since they behave as dump bell with thin link (Si substrate) in between (Fig 5.3 eigenmodes).

For both pairs, the dispersion bands along Y→ Γ→ X are relatively flat given they have to pass through the Si substrate (much thinner link) while the dispersion along other direction are extended. Therefore, to introduce more localized modes along these direction, a defects can be introduced to induce more tight-band like behavior.

5.2.2 Vary the arrangement of the scatter

It has been demonstrated above that the dispersion behavior depends on the arrangement of the scatters inside the trench, since that scatters are moved from the center of the trench (pair 2D4 2D8) to be in contact with the 1d grating and 2D5 2D9. By connecting the scatters with 1d grating, 2D5 and 2D9 allow eigenmodes with lower frequency to appear along X → M →Γ direction. This is because by coupling the scatter to the 1d grating, it allows the wave to curve along the circular scatters, as shown in Fig 5.2 and Fig 5.3. The analogy can be drawn with circular cavity coupled with straight waveguide in photonic devices, where the electromagnetic wave demonstrate whisper modes by circling along the circumference of the cavity before exiting into the straight waveguides again. In other words, the effective path for the wave has been extended by coupling the scatter with 1D grating, which effectively decreased the eigenfrequencies along all direction for the system. Furthermore, the eigenmodes of 2D5 (2D9) at X point with frequencies close of 2D4 (2D8) have similar nodes and antinodes (e.g. nodes number and position), as shown in Figure 5.4(5.5). Moreover, no degeneracy is observed at X point for sample 2D5 (2D9) where M10 and M11 exhibit same symmetry along both x axis and y axis; while the quarter period shifting along y axis change the symmetry with respect to the y axis.

5.2.3Vary the materials properties (e.g. Young's Modulus)

Since the mechanical bonds were used to conceptualize the bonding among building blocks, the impedance properties of the materials can be fined tuned to vary the bonding among building blocks. For sample 2D4, as the Young's Modulus of the scattering materials is lowered (as shown in Table 5.1), the eigenfrequencies of the flat bands from both samples also dropping with

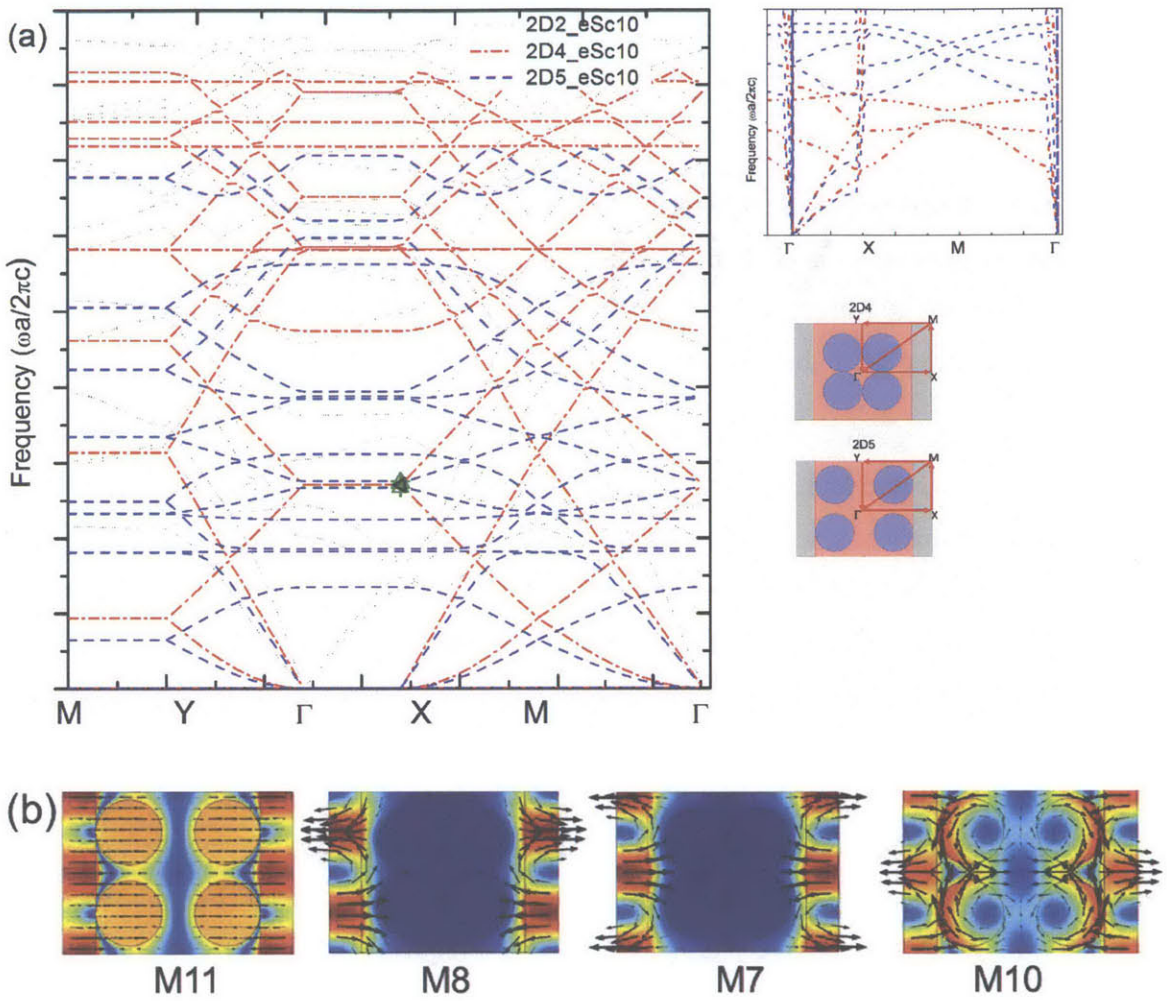

Figure 5.4: (a) the dispersion curves for sample 2D2 (black dot line), 2D5 (red dash dot dot) and 2D9 (blue dash) along the BZ of the unit cell (along M→ Y→ Γ→ X→M) as indicated in the unit cells in the bottom right insert. The top right inserts is zoomed in dispersion curve for the 3 samples. (b) The eigenmodes corresponded for 2D4 (black triangles/circle) and 2D5 (olive triangle/circle) are arranged at the bottom as indicated, where the color indicates the magnitude and the arrow indicates the direction of the displacement.

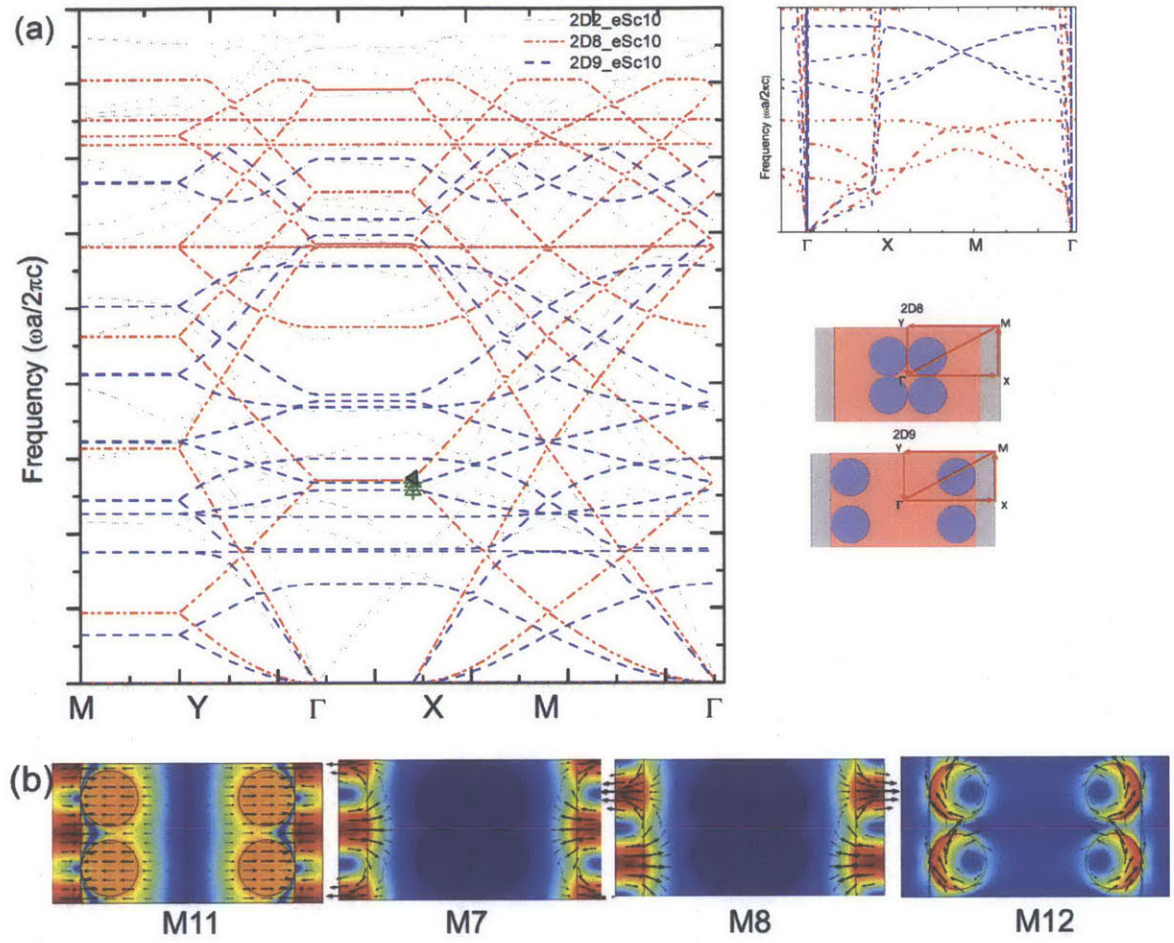

Figure 5.5: (a) the dispersion curves for sample 2D2 (black dot line), 2D5 (red dash dot dot) and 2D9 (blue dash) along the BZ of the unit cell (along M→ Y→ Γ→ X→M) as indicated in the unit cells in the bottom right insert. The top right inserts is zoomed in dispersion curve for the 3 samples. (b) The eigenmodes corresponded for 2D8 (black triangles/circle) and 2D9 (olive triangle/circle) are arranged at the bottom as indicated, where the color indicates the magnitude and the arrow indicates the direction of the displacement.

Table 5.1 Material properties used for the simulation for dispersion curve.

Material Properties	Scatter1	Scatter2	Matrix
Young's Modulus Pa	4.35e10	4.35e7	3e9
Poisson Ratio	0.329	0.329	0.4
Density kg/m^3	972	972	2500

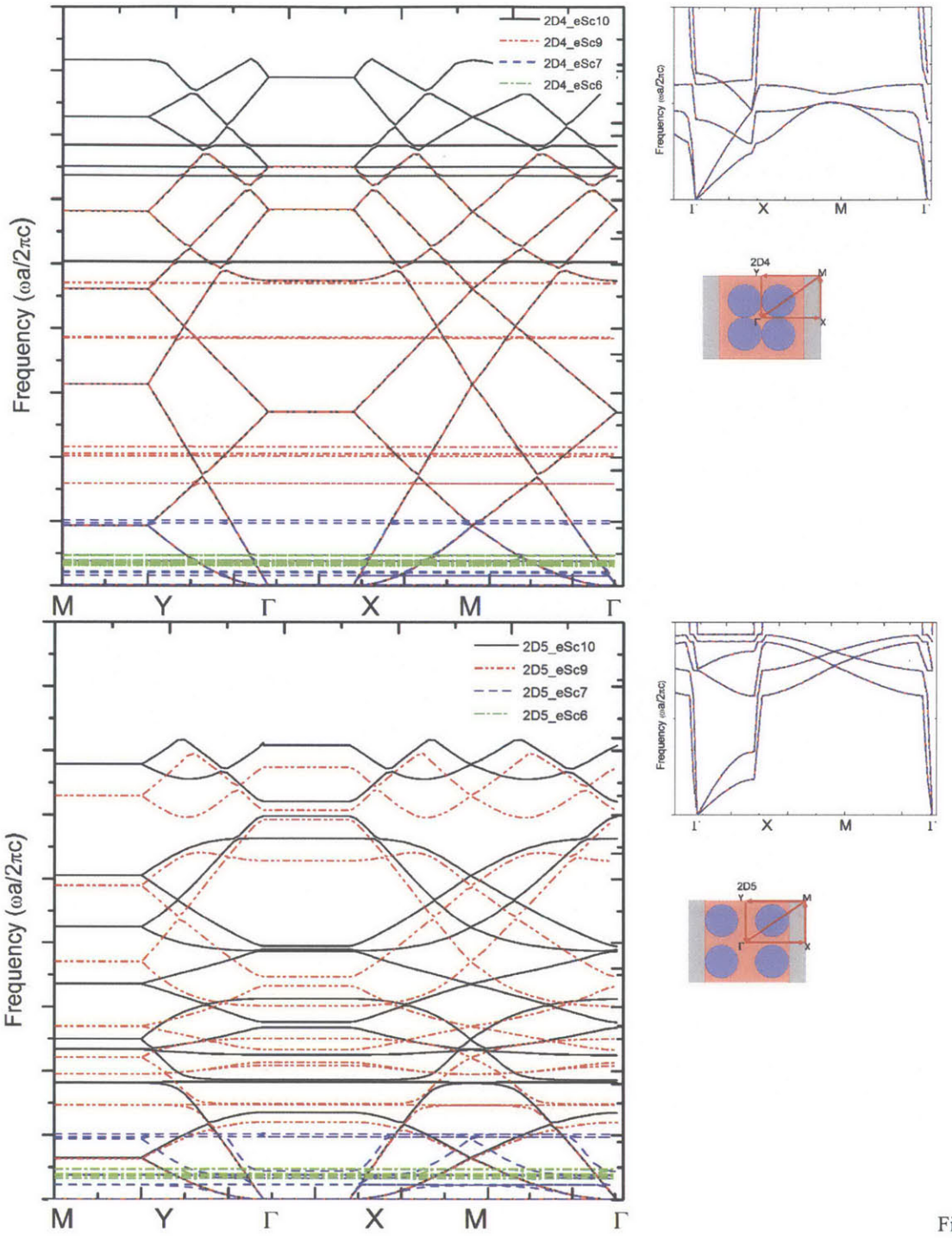

Figure 5.6: the dispersion curves for sample 2D4 (top), 2D5 (bottom) along the BZ of the unit cell (along M→ Y→ Γ→ X→M) with varying Young's modulus of scatters. The top right inserts is zoomed in dispersion curve for the 2 samples.

minimal changes to the extended modes that corresponds to the 1d grating, as shown in Figure 5.6. This again demonstrates the weak link between the center cluster and the 1d grating in the system. As the Young's Modulus of scatters drop further, they dispersion curves is flattened since the displacement are more localized now. For 2D5, the general features of the dispersion bands retained while the frequencies decrease with decreasing Young's Modulus, since the scatter and 1d grating are now coupled.

5.3 Mesoscopic Metamaterials with spherical scatter in 3D

As mentioned before, there are two characteristic length-scales in the mesoscopic, one from the grating and the other is the period of scatters, as shown in Figure 5.7 below. The diameters and periods of both grating and scatters have been retained to study the dispersion behaviors by varying a few factors identified to affects the dispersion behavior from the framework. By allowing the boundary condition to Si substrate to be free, the extended Golden modes would appear at Γ point as expected. However, since our interests focus mostly on the surface waves along the system, the extended modes are not included in the dispersion curves except the one from reference system 3D2 where the all scatters are in contact with the other scatters and 1D grating simultaneously.

5.3.1Vary the period of the 1D grating

For sample pair 3D4 and 3D8, the scatters would cluster together at the center of the trench bounded by 1D grating with different period of 1D grating a_x, while other parameters remain the same. Similarly for sample pair 3D5 and 3D9, the scatters are in contact with 1D grating with different period of 1D grating a_x. The dispersion bands are relative flat along ΓX and MY direction and extended along X→M→Γ. Similarly, the dispersion curves along the BZ zone closely follow each other for pair 3D4 and 3D8 with features similar to 2D system studied in last section (Fig 5.2). The extended modes correspond to displacement along 1D gratings, resemble the features of nodes (antinodes) from the 2D systems, as shown in Figure 5.7. For sample 3D4, the flat bands reflect localized eigenmodes dominated by spherical scatters. At X point, for eigenmodes dominated by 1D grating (Fig 5.7 eigenmodes M9M10 for 3D4), the shift in quarter period (in y direction) occurs again, which transform its symmetry from symmetric (with respect

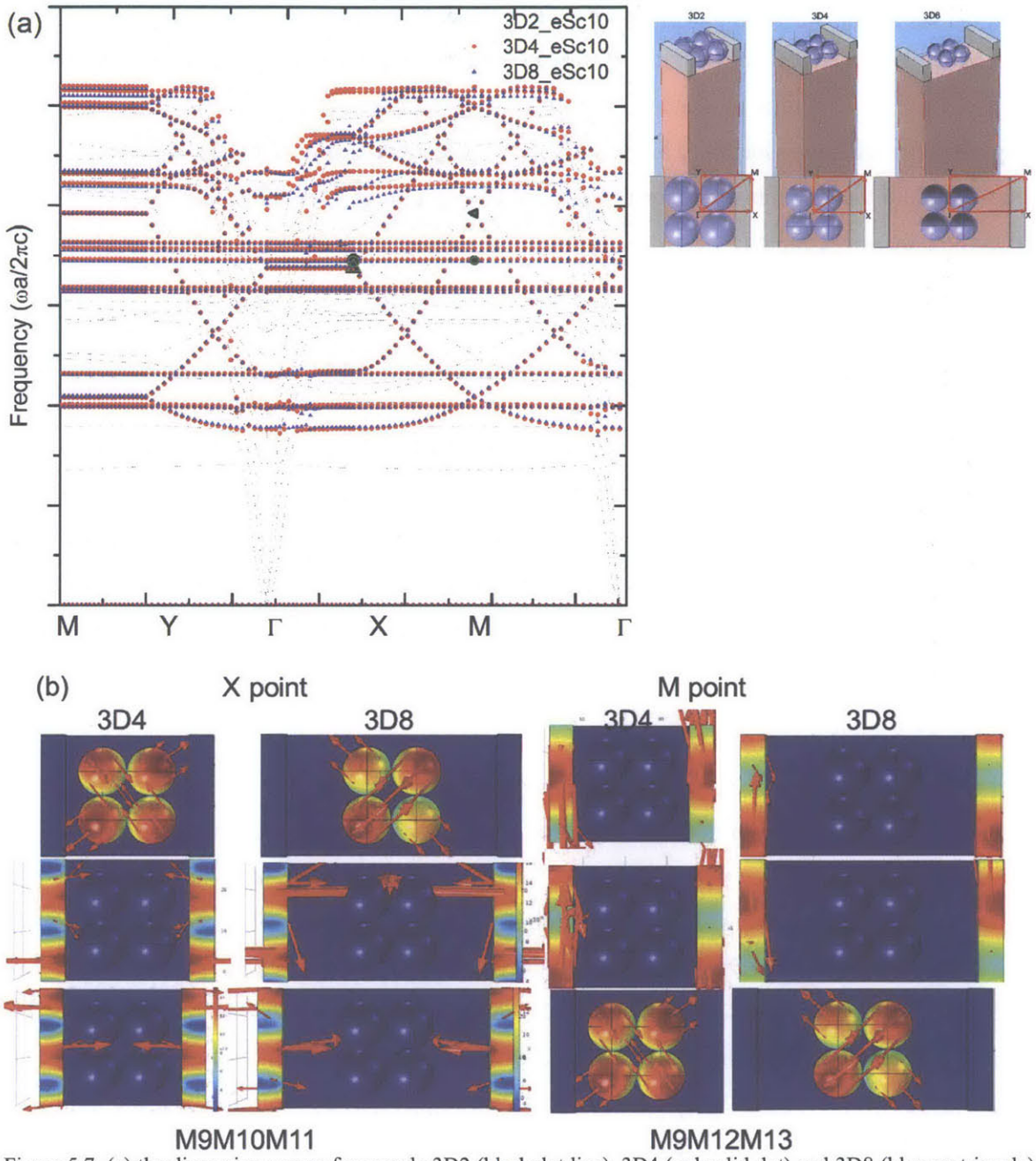

Figure 5.7: (a) the dispersion curves for sample 3D2 (black dot line), 3D4 (red solid dot) and 3D8 (blue up triangle) along the BZ of the unit cell (along M→ Y→ Γ→ X→M) as indicated in the unit cells in the bottom right insert. The right inserts is zoomed in dispersion curve for the 3 samples corresponds to extended modes around Γ. (b) the eigenmodes corresponded for 3D4 (black triangles/circle) and 3D8 (olive triangle/circle) are arranged at the bottom as indicated, where the color indicates the magnitude and the arrow indicates the direction of the displacement.

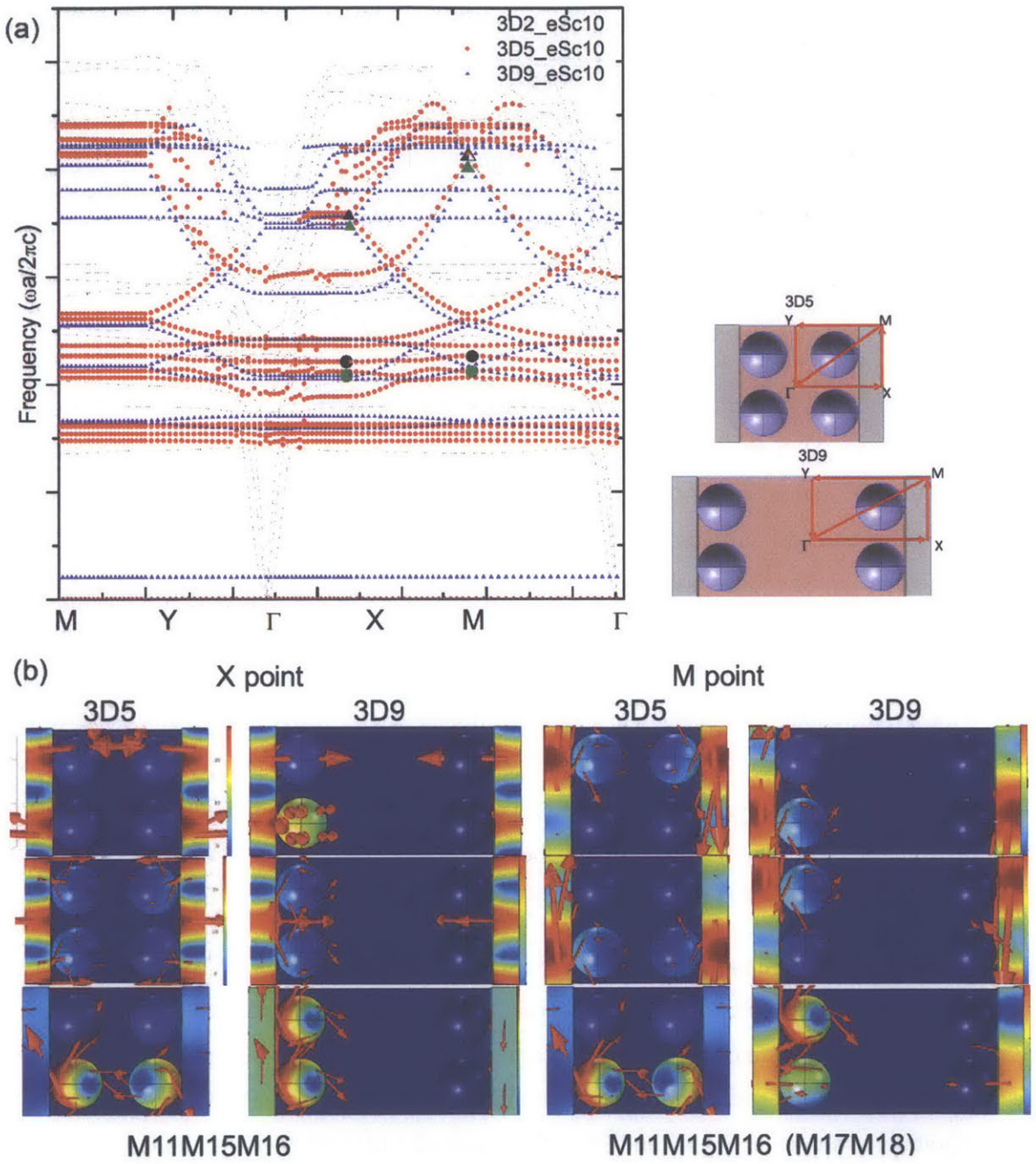

Figure 5.8: (a) the dispersion curves for sample 3D2 (black dot line), 3D5 (red solid dot) and 3D9 (blue up triangle) along the BZ of the unit cell (along M→ Y→ Γ→ X→M) as indicated in the unit cells in the bottom right insert. The top right inserts is zoomed in dispersion curve for the 3 samples. (b) The eigenmodes corresponded for 3D5 (black triangles/circle) and 3D9 (olive triangle/circle) are arranged at the bottom as indicated, where the color indicates the magnitude and the arrow indicates the direction of the displacement.

to x Axis) to antisymmetric with a slight jump in frequencies. To zoom in at the frequencies along ΓX direction, the eigenfrequencies (for longitudinal and transverse wave of the whole unit cell) along ΓX direction would decrease with increasing ax. Moreover, the dispersion curve of 3D4 and 3D2 also overlap with each other for the three branches since the substrates and 1D grating in the unit cell dominate the displacement in this case.

On the other hand, sample pair 3D5 and 3D9 behave differently as in 2D case studied in last section, where the extended modes along X→M→Γ and M→ Y→ Γ no longer overlap with each other and the degeneracies observed along MY and XM for sample 3D4(8) have been lifted as shown in Figure 5.8. For sample 3D5, the flat bands reflect localized eigenmodes dominated by spherical scatters. At X point, for eigenmodes dominated by 1D grating (Fig 5.8 eigenmodes M15M16 for 3D5 and 3d9), the shift in quarter period (in y direction) occurs again with a small jump in frequencies, which transform its symmetry from symmetric (with respect to x Axis) to antisymmetric. At M point, the eigenmodes with dominant 1D grating displacement are antisymmetric with both x Axis and y Axis and leave a tiny gap when the two bands are close to cross each other. As the coupling of the scatters in contact with opposite grating weakened with increasing ax, the coupling of scatters in contact with same grating starts to dominant, as shown in M11 at X and M point for the pair. Furthermore, the longitudinal and transverse modes of the whole unit cell is not observed at low frequencies in sample 3D9 close to Γ point. This could have important implication in membrane design, they can restrict movement of substrate by simply increasing the period of the 1D grating.

5.3.2 Vary the arrangement of the scatter

As demonstrated above, by connecting the scatters with 1D grating instead of the cluster together, 3D5 and 3D9 allow eigenmodes with lower frequency to appear. This is because weakly coupled scatters allow for low frequency eigenmodes to appear with frequencies relatively independent of the 1D grating, as shown in Fig 5.9 and Fig 5.10 eigenmodes M1M5M9. These modes correspond to the expansion and relative movement of scatters since the scatters are not attached to the substrate or grating physically (i.e. a free contact), hence they usually appear in a group of four (for sample 3D5) or two (for sample 3D9) with frequencies close to each other since the four scatters are equivalent. However, the cluster in 3D4 (8) form an entity that moves together (Fig 5.9). Furthermore, the eigenmodes with similar nodes and

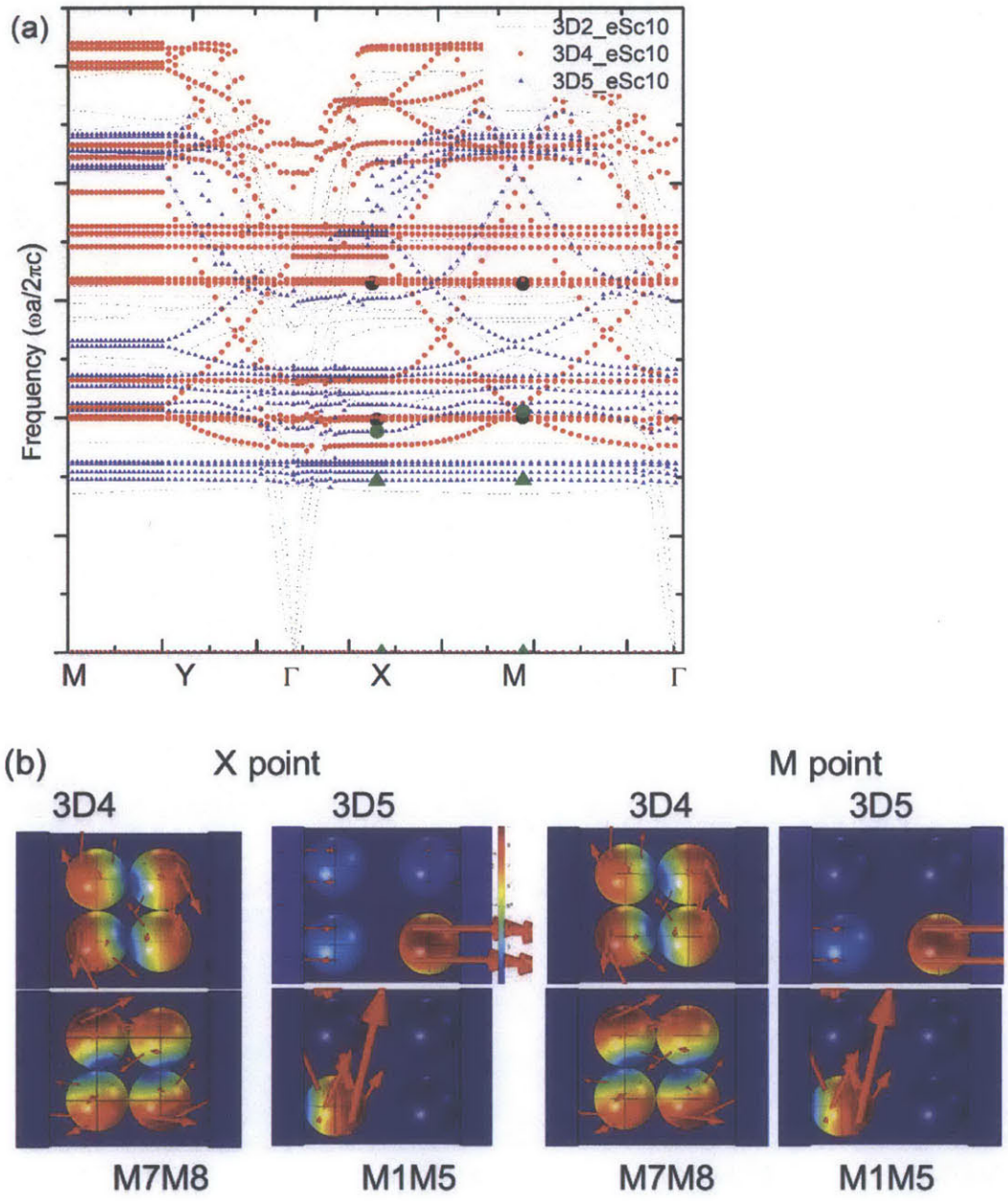

Figure 5.9: (a) the dispersion curves for sample 3D2 (black dot line), 3D4 (red solid dot) and 3D5 (blue up triangle) along the BZ of the unit cell (along M→ Y→ Γ→ X→M) as indicated in the unit cells in the bottom right insert. The top right inserts is zoomed in dispersion curve for the 3 samples. (b) The eigenmodes corresponded for 3D4 (black triangles/circle) and 3D5 (olive triangle/circle) are arranged at the bottom as indicated, where the color indicates the magnitude and the arrow indicates the direction of the displacement.

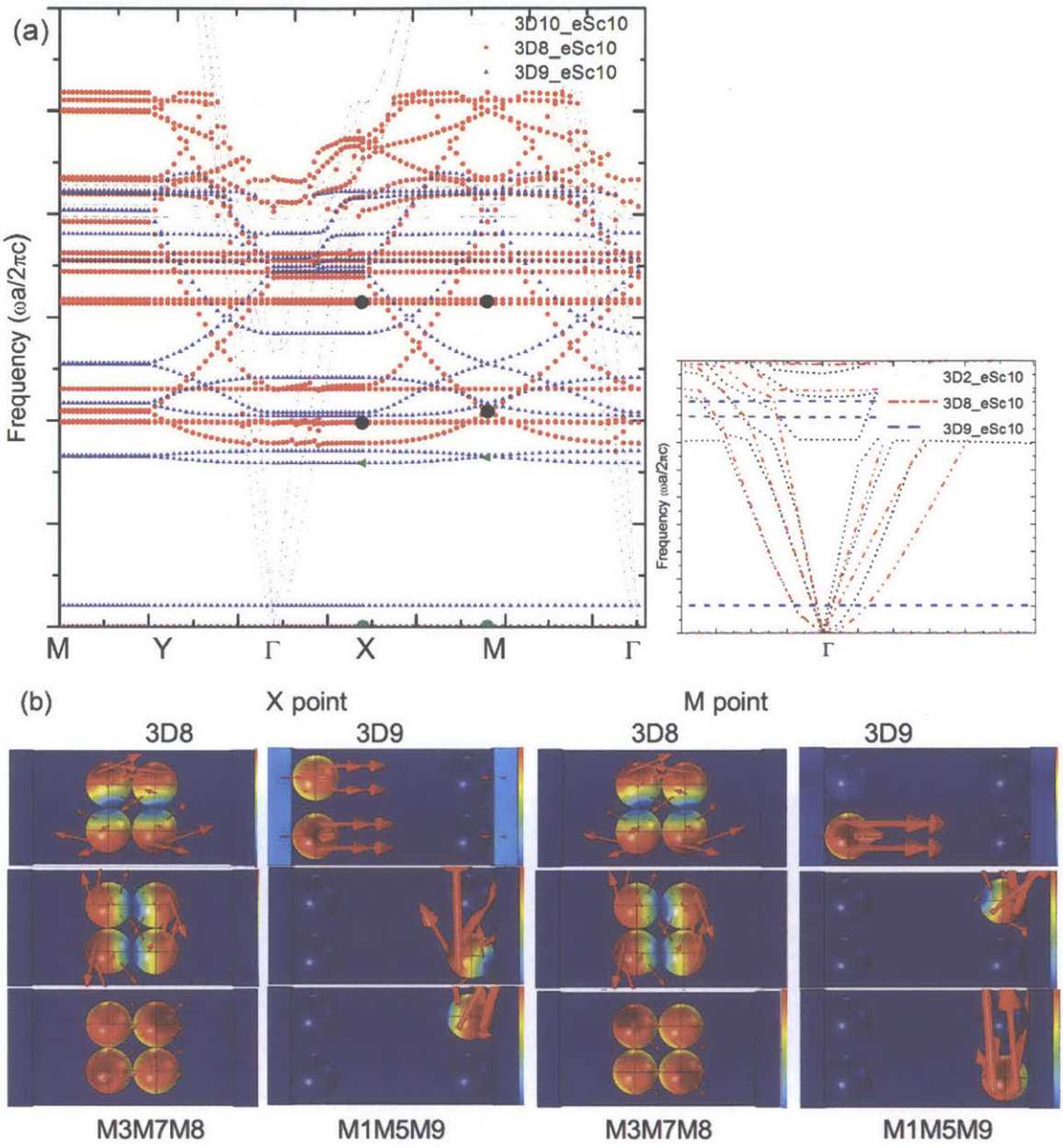

Figure 5.10: (a) the dispersion curves for sample 3D2 (black dot line), 3D8 (red solid dot) and 3D9 (blue up triangle) along the BZ of the unit cell (along M→ Y→ Γ→ X→M) as indicated in the unit cells in the bottom right insert. The top right inserts is zoomed in dispersion curve for the 3 samples. (b) The eigenmodes corresponded for 3D8 (black triangles/circle) and 3D9 (olive triangle/circle) are arranged at the bottom as indicated, where the color indicates the magnitude and the arrow indicates the direction of the displacement.

antinodes (e.g. nodes number and position) has frequencies closer to each other, e.g. M10M11 for 3D4 (5) and M15M16 for 3D8 (9), as shown in Figure 5.7(5.8). As in 2D case, the dispersion

bands along X → M →Γ direction are suppressed separated scatters system compared to clustered scatter system. And the extended bands correspond to pure grating are perturbed in 3D5 (9) due to the coupling between the scatters and gratings. Comparing clustered system scatters and separated scatters, the latter is a preferred for application where band gaps are desired. Furthermore, different grating period would impact features of band gaps (Fig 5.10)

5.3.3Vary the size of the spherical scatters

To further fine tune the system properties, the size of scatters has also been reduced by 20 percent for both 3D4 and 3D5 to generate 3D6 and 3D7. For clustered scatters, the extended bands dominated by grating vary little with decreasing size (80%) of the scatters (Fig 5.11a), demonstrated by the overlapping bands of 3D4 and 3D6. However, the flat bands of localized eigenmodes have a higher frequencies with smaller scatters. The symmetry and patterns of the eigenmodes also vary little for 3D4 and 3D6.

On the other hand, for sample 3D5 and 3D7, both the eigenfrequency of both flat bands and extended modes have been affected with decreasing scatter size, where the symmetry and features of eigenmodes at the X and M point varied little for both the grating and scatters. Therefore, the band gaps for surface acoustic wave can be adjusted by varying the size of the scatters. Meanwhile, given the sensitivity of the dispersion behavior to the size of the scatters, they can be leveraged on to characterizing the size of nanoparticles or micro particles or even a dynamic system where sizes of the particles varies continuously.

5.3.4 Vary the materials properties (e.g. Young's Modulus)

For all the systems, as the Young's Modulus of the scattering materials is lowered (as shown in Table 5.1), the eigenfrequencies of the localized modes lowered accordingly, since they dropped lower than eigenfrequencies of the extended modes dominated by grating, only flattened dispersion bands are observed for the first few lower bands, as shown in Figure 5.12. As the Young's Modulus of the scatters lowered, their eigenfrequencies become lower than eigenfrequencies of 1D grating, hence only localized eigenmodes are observed for the first twenty bands in the dispersion curves.

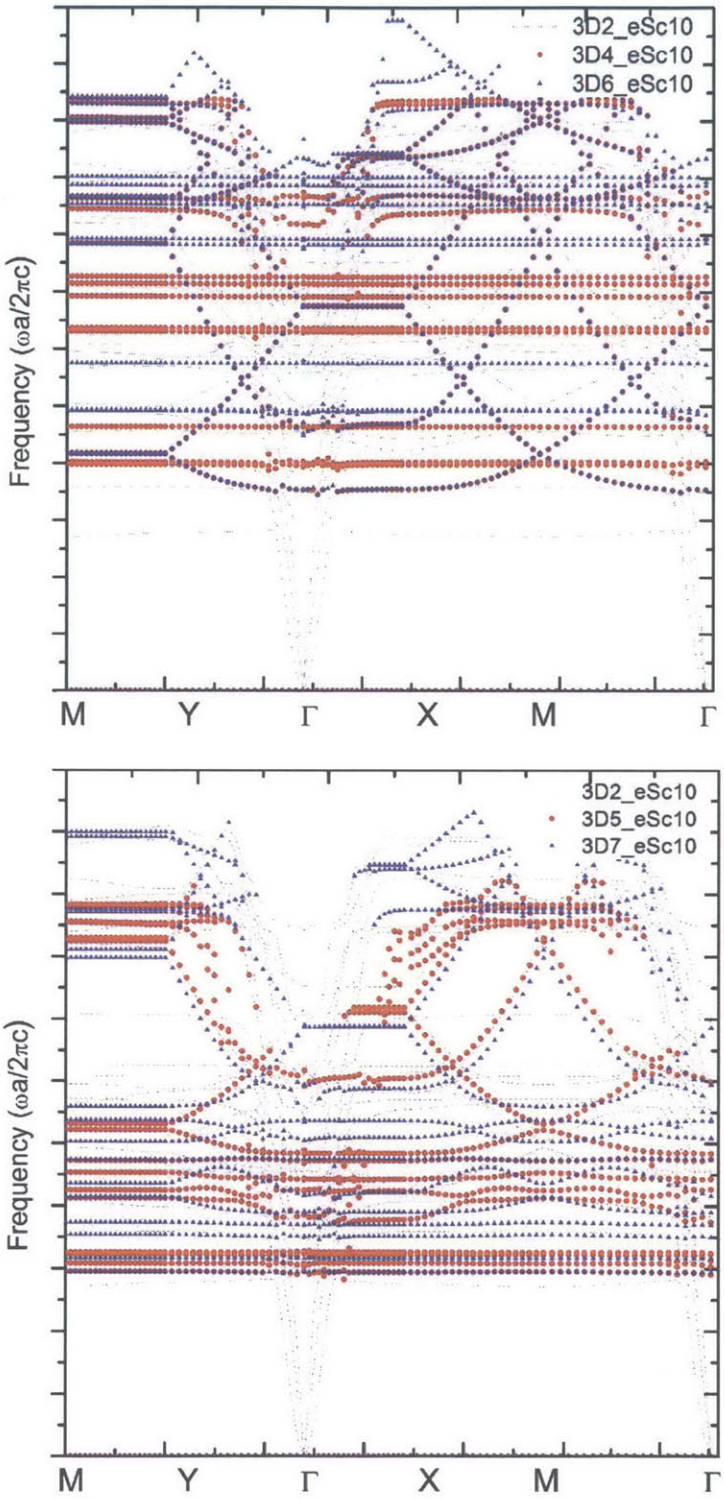

Figure 5.11: The dispersion curves for sample a) 3D2(black dot line), 3D4(red solid dot) and 3D6 (blue up triangle) and b) 3D2(black dot line), 3D5(red solid dot) and 3D7 (blue up triangle) along the BZ of the unit cell (along M→ Y→ Γ→ X→M).

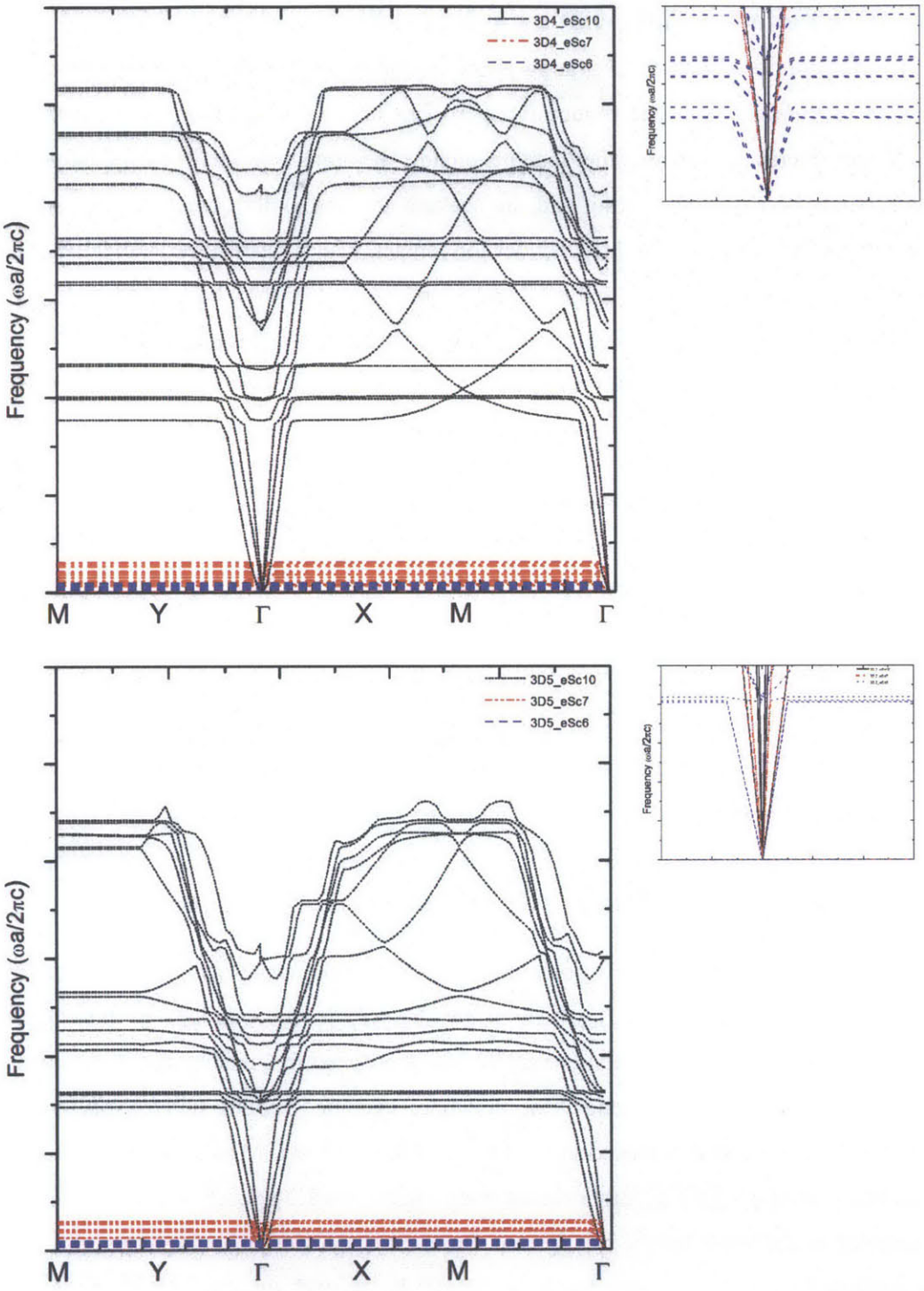

Figure 5.12: the dispersion curves for sample 3D4 (top), 3D5 (bottom) along the BZ of the unit cell (along M→ Y→ Γ→ X→M) with varying Young's modulus of scatters. The top right inserts is zoomed in dispersion curve for the 2 samples.

5.4 Mesoscopic metamaterials with cylinder scatter and soft bridge

It is seen from the last section that 1D grating allow extended modes along XM direction, by coupling scatters to grating, it would introduce avoid crossing between bands with same symmetry with respect to k of interest. To gain further insights on how the bonds would affects the behavior of the system, bonds between the grating and the scatters are artificially defined with a softer rubber phase. The scatters was changed to cylinder for contact, which can also be fabricated with common lithography techniques as 1D grating. Furthermore, it is clear that the gratings facilitate the extended modes along the X→ M → Γ direction, which is not optimal if spectral gaps are the desirable properties of applications. Therefore, defects are introduced to study how they would affects the behavior of the system by disturbing the extended modes along X→ M → Γ direction.

5.4.1 Vary the coupling among the scatters

The coupling among the scatters is varied by linking along the edges (P4) or diagonal (P4m) of the square defined by the four cylindrical scatters, as shown in Figure 5.13 below. By introducing rubber as the soft block, eigenmodes with lower frequencies (compared to reference sample) are dominant by the softer linking blocks. Although both cylindrical scatters and rubber links have p4mm symmetry, they demonstrate different properties. Since the four linking blocks are equivalent to each other for P4, a group of four closely packed eigenmodes can be observed, which reflect the four fold symmetry of the center motif (scatter and links). The representative eigenmodes of first few groups are plotted in Fig 5.13: 1) bending of rubber links in xy plane; 2) flex or twisting in one of the linking blocks; 3) bending in z direction of the links, etc.

For sample P4m, there are several closely positioned dispersion bands pairs with the eigenmodes rotate by $\pi/2$ (Fig 5.13 M2M3 at X point), which usually are symmetric along x (or y) axis. Since there are only two diagonal links equivalent to each other, their eigenfrequencies are more spread out compared to sample P4. Also along XM, the more extended modes with displacement dominated by the 1d grating still persisted in both system (Fig 5.13 M13M14 at X and M13M14 at M point) and they overlap with each other consistently. Hence, the 1D grating and linked scatters are weekly coupled in both case for the two system. From the dispersion behavior along, the first structure is preferred to generate large bandgap; while the second structure is more apt for multispectral frequency gaps for surface gaps.

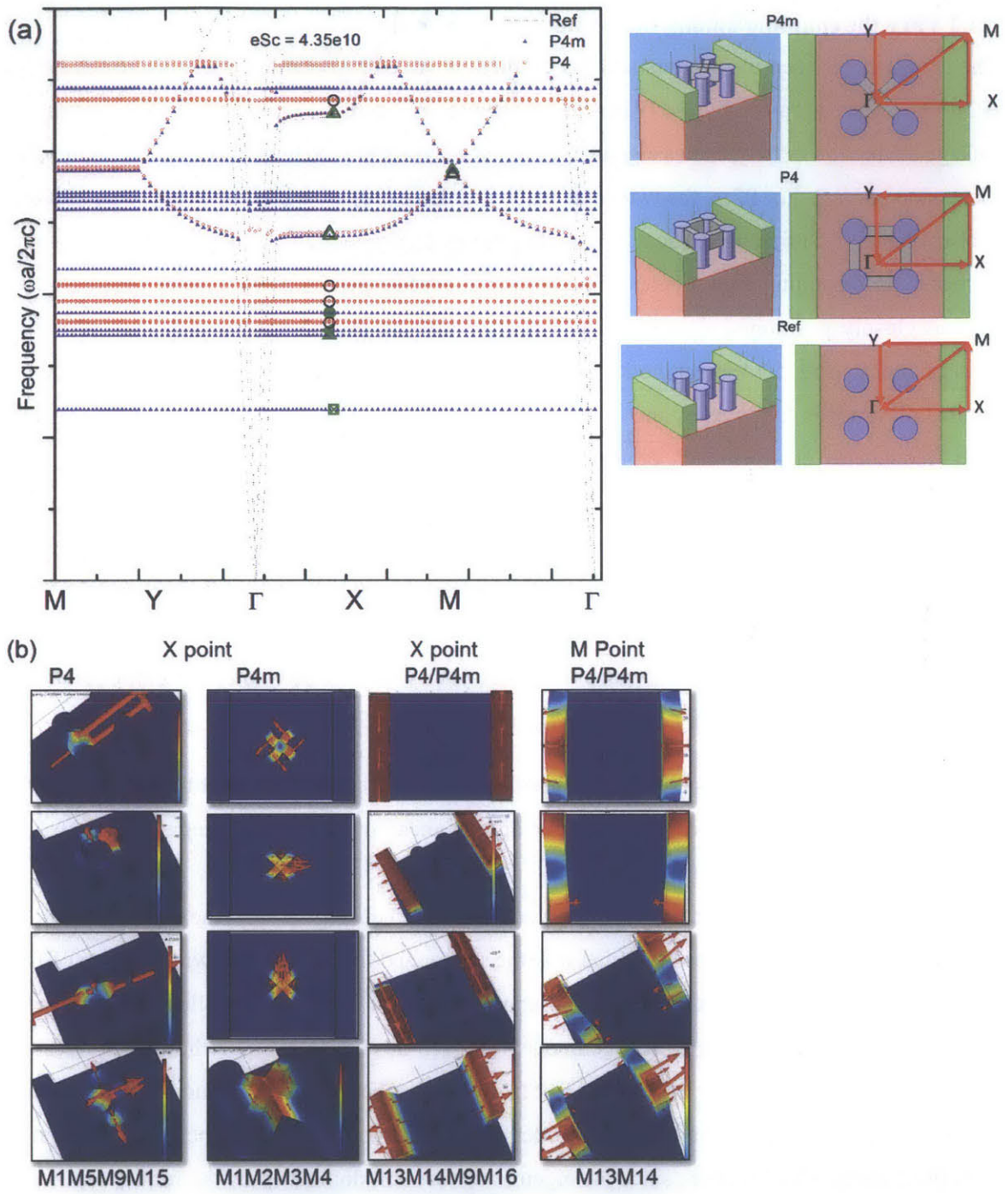

Figure 5.13: (a) the dispersion curves for sample P4m (open red circle), P4 (blue up triangle) along the BZ of the unit cell (along M→ Y→ Γ→ X→M). (b) The eigenmodes corresponded for P4m (black triangles/circle) and P4 (olive triangle/circle) are arranged at the bottom as indicated, where the color indicates the magnitude and the arrow indicates the direction of the displacement. The 3D and top view schematics of mesoscopic surface acoustic wave system are on the right: Reference (top), P4 and P4m, with the BZ indicated on the top view of the three systems, consisting of 1D grating (green), scatters (blue), rubber (gray) and red (silicon substrate).

5.4.2 Vary the coupling among the scatters and 1D grating

The coupling between the scatters and 1D gratings is varied by connecting them through bridge (P2m) or over the top cap blocks (P2mCap), as shown in Figure 5.14 schematics. The soft rubber linkage enable lower frequencies eigenmodes to appear compared to the Ref Samples (Figure 5.14 dispersion curves). For P2m, the two center rubber linkage (10) are a little bit longer than the four rubber blocks (7.5) linking the scatter and 1D grating. Hence the lowest frequencies eigenmodes corresponds to bending of the center linking block (Fig 5.14 eigenmodes M1), followed by a group of four closely positioned flats bands whose displacement demonstrates bending of four side linking block (Fig 5.14 eigenmodes M5); twisting of the middle linkage block (Fig 5.14 eigenmodes M5) is followed by the twisting of the side linkage block (group of four eigenmodes with frequencies close to each other). Then the block would band upward (downward) in z direction (Fig 5.14 eigenmodes M17). Hence the eigenmodes of rubber blocks follows similar trends for P4 and P4m sample, where bending in xy plane, twisting and then bending upwards/downwards). Furthermore, the extended modes corresponds dominated 1D grating along XM have also be observed (as shown in Fig 5.14), which shift downward a little compared to reference samples. The side links disturb the frequencies slightly while the scatters and center link block remains almost stationary (Fig 5.14 eigenmodes M19M20 at X point).

For P2mcap, the eigenfrequencies of eigenmodes are lower further compared to p2m. Similarly, the lowest eigenmodes corresponds to the displacement of the middle segments (Fig 5.14 eigenmodes M1), since movement in xy plane is more restricted now by the changed width/thickness ratio, a slight twist is observed instead of bending in xy plane; it is followed by the displacement of the side portion (that link the scatter and the 1D grating) with a group of four bands (Fig 5.14 eigenmodes M3); The twisting of the middle segment followed the upward bending of the cap link (Fig 5.14 eigenmodes M7M13 at X point). Since the eigenmodes are relatively localized, they vary little at M point from X point, hence only eigenmodes at X point are listed below. Furthermore, the extended modes is not observed at the frequencies around that of P2m (Ref) along XM direction, since the eigenmodes are still dominated by the rubber cap link.

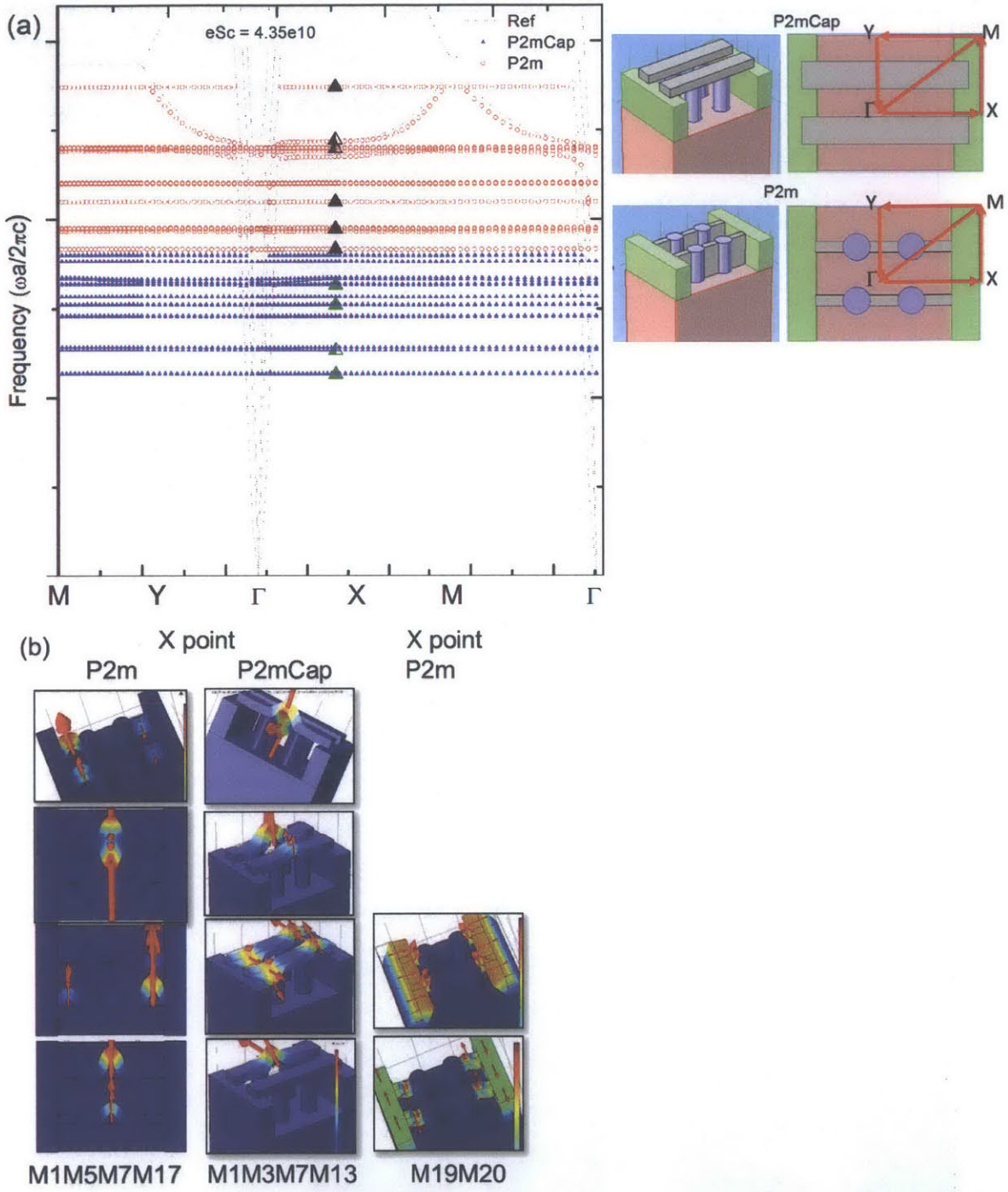

Figure 5.14: the dispersion curves for sample P2m (open red circle), P2mCap (blue up triangle) along the BZ of the unit cell (along M→ Y→ Γ→ X→M). The eigenmodes corresponded is arranged at the bottom as indicated by the arrow and circles, where the color indicates the magnitude and the arrow indicates the direction of the displacement. The 3D and top view schematics of mesoscopic surface acoustic wave system are on the right: P4m, and P4mCap, with the BZ indicated on the top view of the three systems, consisting of 1D grating (green), scatters (blue), rubber (gray) and red (silicon substrate).

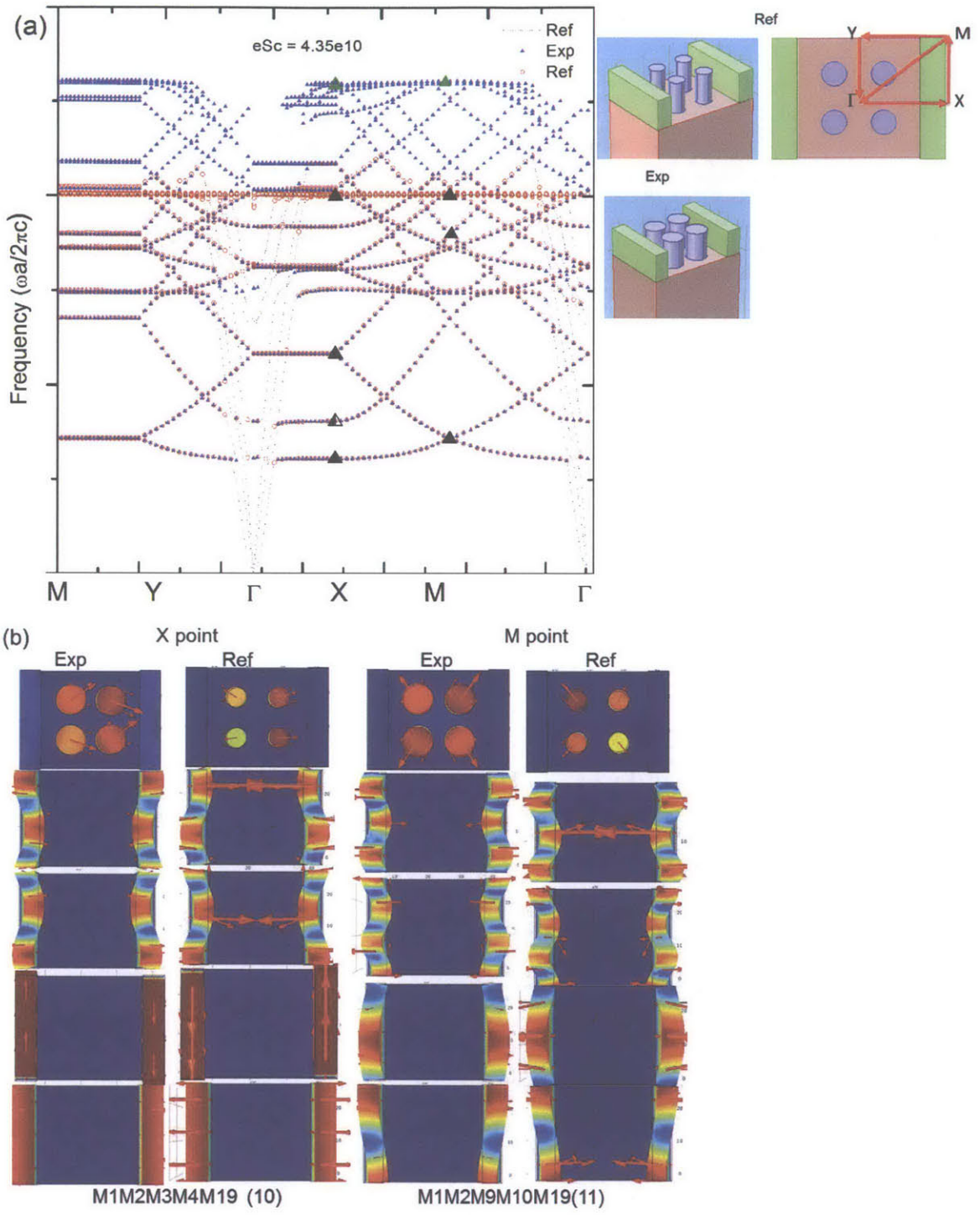

Figure 5.15: the dispersion curves for sample Ref (open red circle), Ext (blue up triangle) along the BZ of the unit cell (along M→ Y→ Γ→ X→M). The eigenmodes corresponded is arranged at the bottom as indicated by the arrow and circles, where the color indicates the magnitude and the arrow indicates the direction of the displacement. The 3D and top view schematics of mesoscopic surface acoustic wave system are on the right: Reference (top) and Exp, with the

BZ indicated on the top view of the three systems, consisting of 1D grating (green), scatters (blue), rubber (gray) and red (silicon substrate).

5.4.3 Vary the diameter the scatters

When the cylinders are expended in radius, the extended modes that corresponds to 1D grating vary little due to the weak coupling between the scatters and the 1D grating (Figure 5.15), as illustrated in last section with sphere scatters. However, the localized modes dominated by scatter changed with the eigenfrequencies lowered with lower radius of the scatter (Fig5.15 eigenmodes M19 (10), since reduced radius decrease the stiffness of the scatters.

5.4.4 Introducing defects along XM direction

As mentioned before, the extended eigenmodes dominated 1D grating can be affected by introducing defects to achieve localized eigenmodes and a flat dispersion curve. Therefore a short segments of the 1D grating is removed for all the samples studied, as shown in Fig 5.16 schematics.

As expected, flat dispersion curves are observed for both P4 and P4m sample, as shown in Fig 5.16. The eigenmodes dominated by scatters and links are not disturbed due to the weak coupling between the 1D grating and the scatter(links) (Fig 5.16 eigenmodes), so their dispersion curves overlap well with each other. Moreover, at X point the frequencies of the 1D grating dominated modes vary little too, since their displacements are similar to the original system with only the center part are removed. The eigenmodes vary little as k travel from X to M point, hence a localized modes, which are very different from the original system.

For sample P2m, the extended modes along XM are also disturbed by introducing the defects as shown in Fig 5.17. The 1D dominated modes also disturbed little at X point, while changed significantly at M point. On the other hands, the introduction of defects affects little on sample P2mCap since the eigenmodes are dominated by the cap link with minimal involvement of the 1D grating.

For sample Ref and Exp, the defects causes drastic change since the extended modes along XM are now disturbed, as shown in Fig 5.17. The eigenmodes are more localized with the two smaller segments along XM direction and flat dispersion bands have been achieved for surface acoustics wave. Furthermore, the eigenfrequencies have also been varied due to the introduction of displacement with changed features.

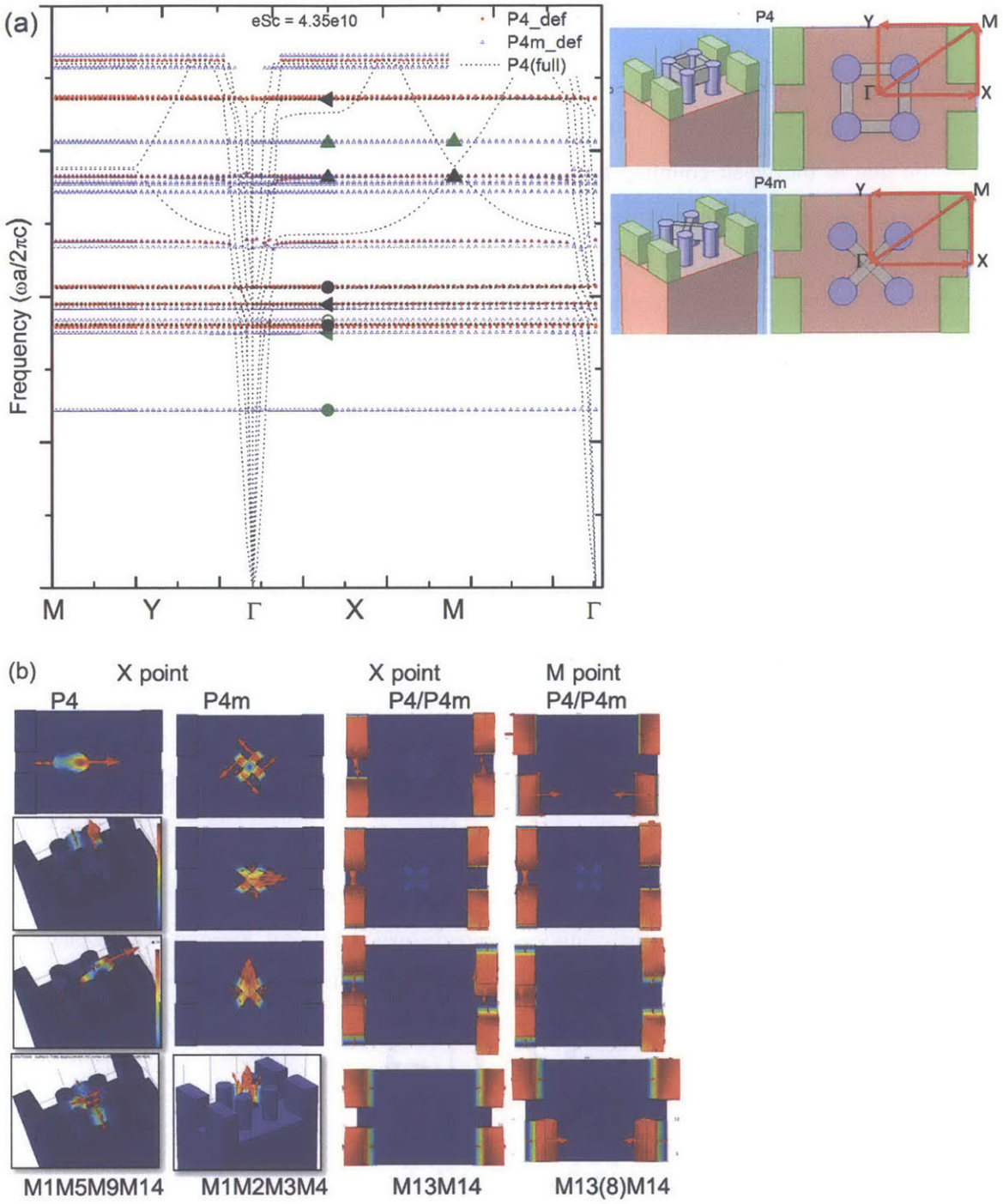

Figure 5.16: the dispersion curves for sample Ref (open red circle), Exp (blue up triangle) along the BZ of the unit cell (along M→ Y→ Γ→ X→M). The eigenmodes corresponded is arranged at the bottom as indicated by the arrow and circles, where the color indicates the magnitude and the arrow indicates the direction of the displacement. The 3D and top view schematics of mesoscopic surface acoustic wave system are on the right: Reference (top) and Exp, with the BZ indicated on the top view of the three systems, consisting of 1D grating (green), scatters (blue), rubber (gray) and red (silicon substrate).

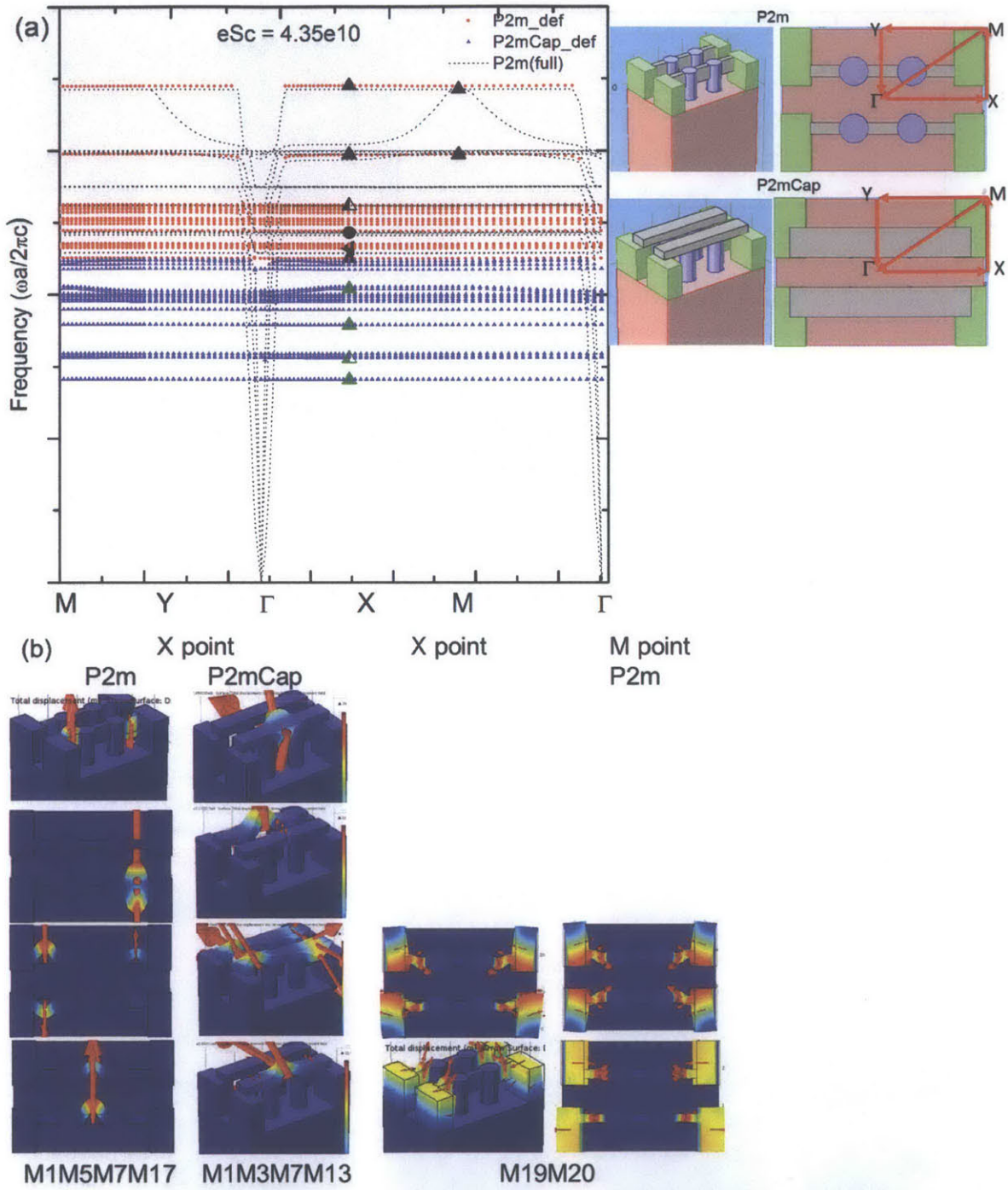

Figure 5.17: the dispersion curves for sample Ref (open red circle), Exp (blue up triangle) along the BZ of the unit cell (along M→ Y→ Γ→ X→M). The eigenmodes corresponded is arranged at the bottom as indicated by the arrow and circles, where the color indicates the magnitude and the arrow indicates the direction of the displacement. The 3D and top view schematics of mesoscopic surface acoustic wave system are on the right: Reference (top) and Exp, with the BZ indicated on the top view of the three systems, consisting of 1D grating (green), scatters (blue), rubber (gray) and red (silicon substrate).

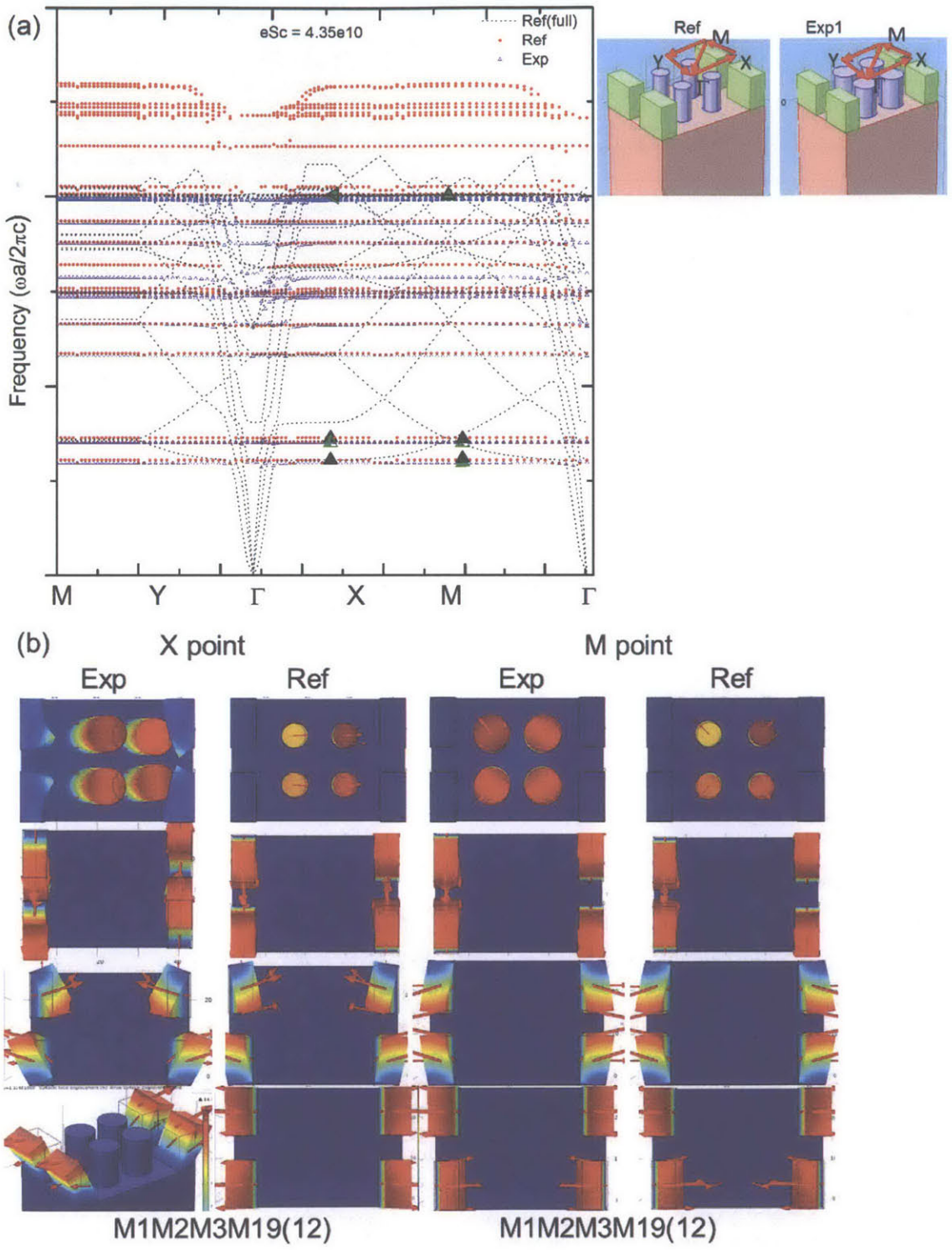

Figure 5.18: the dispersion curves for sample Ref (open red circle), Exp (blue up triangle) along the BZ of the unit cell (along M→ Y→ Γ→ X→M). The eigenmodes corresponded is arranged at the bottom as indicated by the arrow

and circles, where the color indicates the magnitude and the arrow indicates the direction of the displacement. The 3D and top view schematics of mesoscopic surface acoustic wave system are on the right: Reference (top) and Exp, with the BZ indicated on the top view of the three systems, consisting of 1D grating (green), scatters (blue), rubber (gray) and red (silicon substrate).

5.4.5 Change the material properties of the scatters

Similarly to previous system, the eigenfrequencies could be further fine-tuned by changing the Young's modulus of the scatters (or other components) in system of interest, as shown in Fig 5.18. For sample Ref, lowering the Young's modulus of leads to lowered resonance modes of the scatters, hence the lower frequencies are populated by these localized modes, which leads to the flat dispersion curve (Fig 5.18). To take a closer look at gamma point, the transverse and longitudinal eigenmodes corresponds to the entire unit cell is also affected by the scatters' Young Modulus. Therefore, for simple system, the behavior can be manipulated by changing the mechanical impedance of the system.

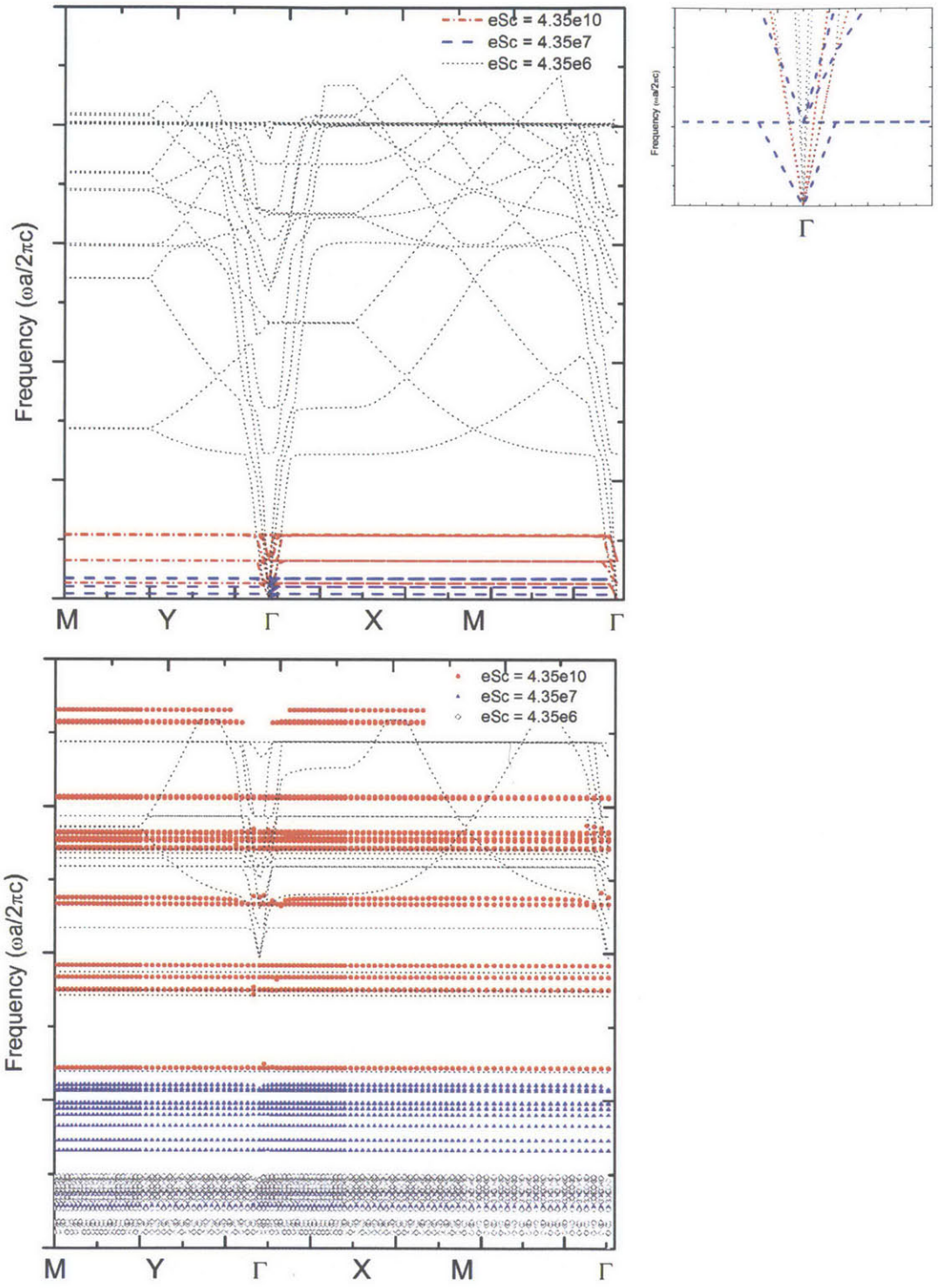

Figure 5.19: the dispersion curves for sample Ref and P2m and (open red circle), Exp (blue up triangle) along the BZ of the unit cell (along M→ Y→ Γ→ X→M).

5.5 Fabrication of Mesoscopic Phononic Metamaterials

Due to scaling properties of the general framework, the feature dimensions as well as the materials can be designed to enable characterization using technique, Brillion Light Scattering (BLS). The feature size and materials would then determine the most suitable fabrication techniques. Both the feature size and materials should be substantially varied in order to test the robustness of the framework.

5.5.1 Vertical deposition methods

As a simple and versatile technique, the vertical deposition method (Retsch, 2009) is used to fabricate local resonance structures. The process is demonstrated in Figure 5.19. To obtain a more uniform distribution of the nanoparticles on the patterned substrate, a more concentrated colloidal system is used, since a large area of the substrate does not need to be covered by nanoparticles. When using the concentrated PS colloidal solution, the coverage is more uniform, as shown in Figure 5.19. However, this might also due to the fact that the 1D grating become thinner, i.e. the trench width/sphere diameter is close to 2/1.

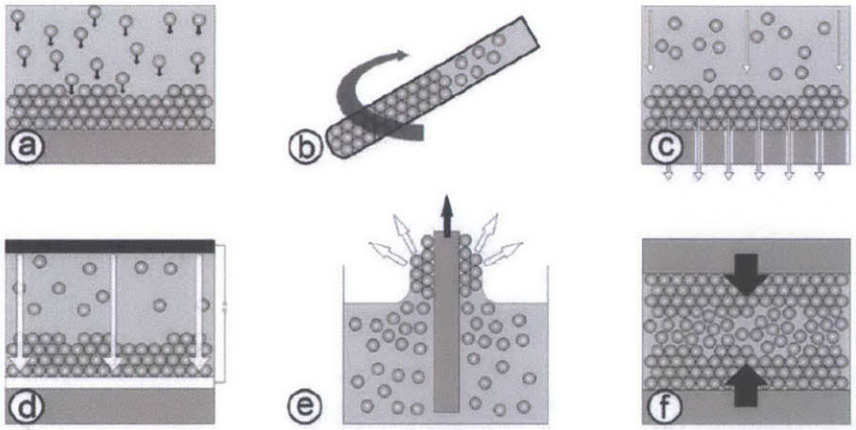

Figure 1.3. Formation of colloidal crystals via a) sedimentation, b) centrifugation, c) filtering, d) electrodeposition, e) vertical deposition, or f) compression molding.[32]

Figure 5.20: Schematics of the vertical deposition method from (Retsch, 2009) . a) sedimentation, b) centrifugation, c) filtering, d) electrodeposition, e) vertical deposition, or f) compression molding.

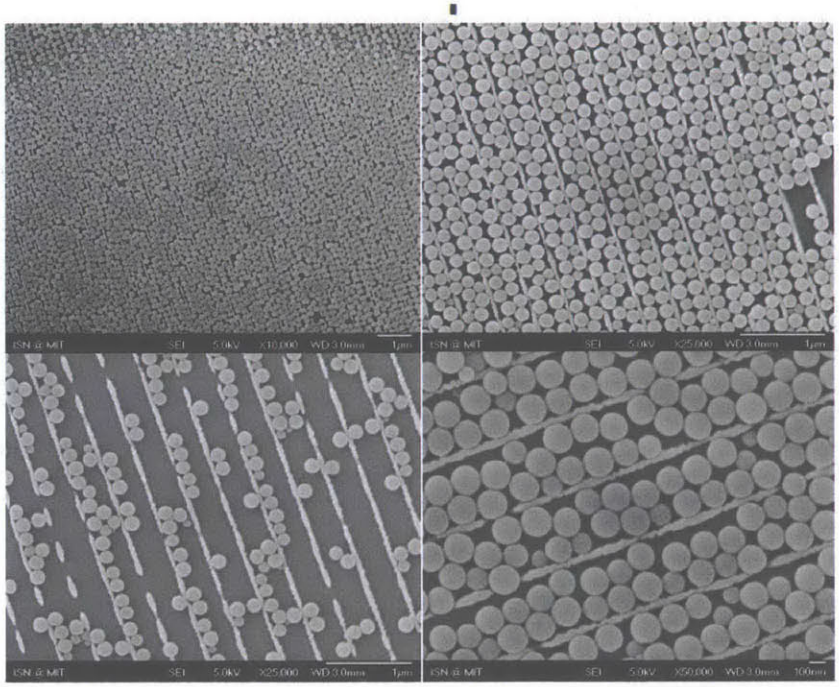

Withdraw speed Is 30 ul/hr

Deposition direction both perpendicular and parallel to line direction

Line pitch is about 350nm and line width is around 40 nm

Figure 5.21: SEM structure of the resulted structure from the vertical deposition of 130nm PS nanoparticles on the fine 1D grating at withdrawing speed of 30ul/hr

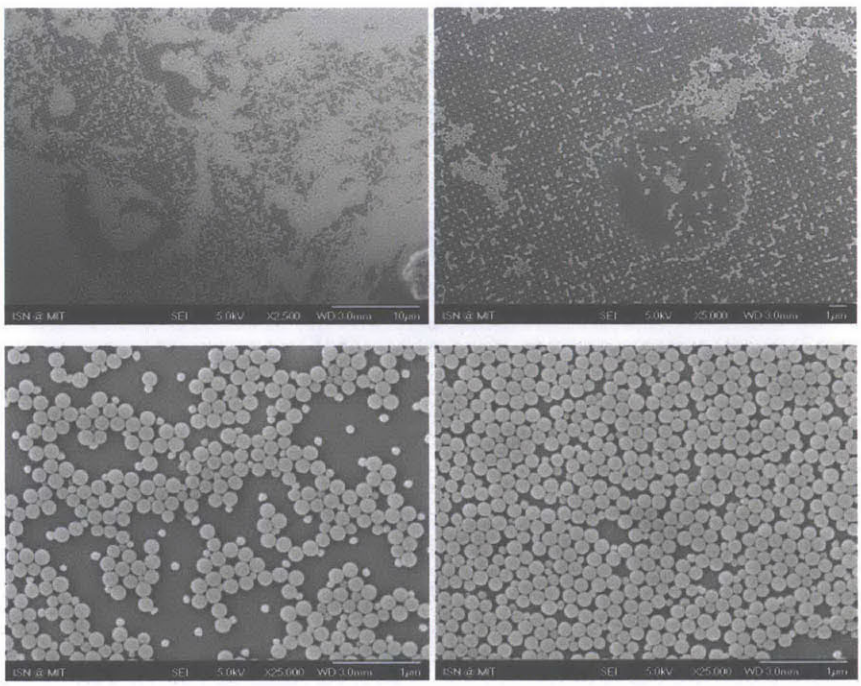

Figure 5.22: SEM structure of the resulted structure from the vertical deposition of 130nm PS nanoparticles on the fine 2D dot (Top) for withdrawing speed of 30ul/hr

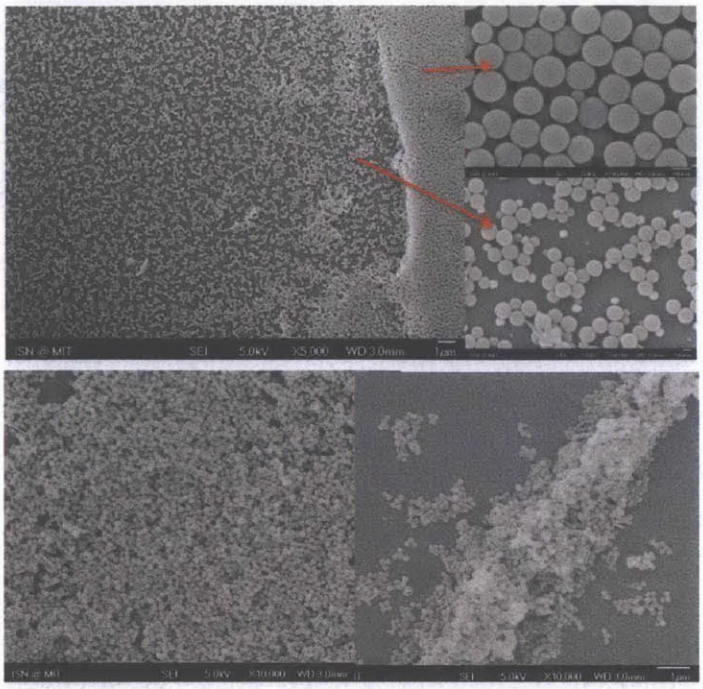

Figure 5.23: SEM structure of the resulted structure from the vertical deposition of 130nm PS nanoparticles with diluted colloidal system for withdrawing speed of 30ul/hr

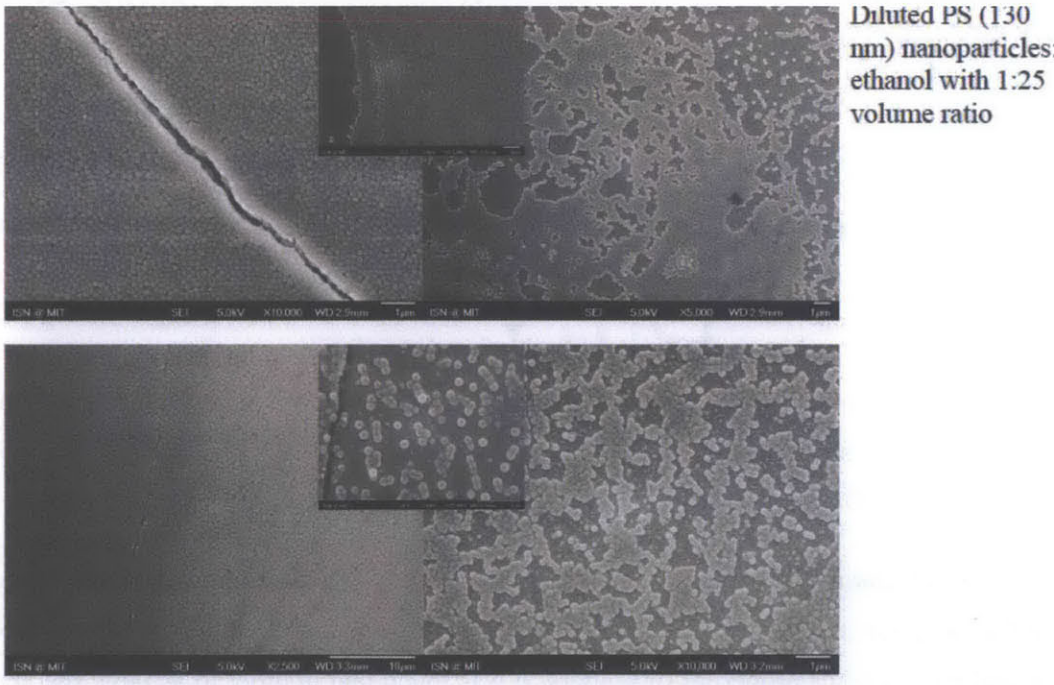

Figure 5.24: SEM structure of the resulted structure from the vertical deposition of 130nm PS nanoparticles with diluted colloidal system on PDMS substrate for withdrawing speed of 30ul/hr

5.5.2 Vary the substrate pattern:

When the pattern changes to 2D square dot structure, the coverage varies accessibility for the nanoparticles changes. The coverage is not uniform from a zoom out image as shown in Figure 5.22. Despite some short-range order hexagonal stack, there is no long range order of the particles

In order to minimize the ratio of the multi-layer colloidal crystal, the colloidal system is diluted with ethanol. SEM image seems to indicate more uniform coverage with less short range order for 1:25 volume ratio. The multi-layer colloidal crystal still persists on this substrate. When the volume ratio is 1:50, the nanoparticles start to cluster in the solutions and deposit on the substrate too, as shown in Figure 5.22. Therefore, other parameters need to be optimized to minimize snapping phenomena in the vertical to obtain more uniform sample.

5.5.3 Vary substrate materials:

PDMS is often used as a substrate for the placement of nanoparticles through convective and capillary assembly(Teh, 2004)(Malaquin, 2007). Hence patterned PDMS (with soft lithography) was also used as substrate for the vertical deposition. The fine grating pattern is not observed on the PDMS stamp and the deposited nanoparticles seems to be "sintered" (Figure 5.23) together with reasons unknown for now.

5.6 Conclusion

Surface acoustic wave device had been wide used in a wide range of applications, from gas sensor to microfluidic devices. Hence, a more in depth understanding of how metamaterials surface can manipulate the surface acoustic wave propagation would accelerate the application the surface acoustic wave device further.

To mimic the surface acoustic wave, we first use a 2D toy system with same dimensions, but reduced thickness for the substrates section. The behavior we obtained shine light on the behavior of system interested in 3D.

For system with 1D grating and spherical scatters, there are several parameters we can use to manipulate the behavior: the period of 1D grating, the size of spherical scatters, arrangement of the scatters and the materials properties of scatters. It was found that in order to achieve spectral gaps for real applications, system where scatters in contact with 1D grating would be preferred.

For system with 2D grating and cylindrical scatters, the bonding between the scatters and/or 1D grating are varied using soft rubber blocks. It was found that the scatter cluster and 1D grating are almost independent with each other. However, by bonding the scatters with 1D grating, localized eigenmodes and flattened dispersion behavior can be achieved. The bonding through cap block on top of both scatters and 1D gratings are shown to be particularly effective.

Furthermore, the extended modes along the XM direction can also be eliminated by remove a short segment of the 1D grating. Both multiple spectrum gap and fewer large spectrum gap can be achieved by varying the bonding between the scatters and/or 1D grating.

Besides the simulations, samples with 1D grating and spherical scatters have also been fabricated using a vertical deposition technique, where the density can be controlled by the deposition parameters.

5.7 Reference

Balin, I., Dahan, N., Kleiner, V., & Hasman, E. (2009). Slow surface phonon polaritons for sensing in the midinfrared spectrum. *Applied Physics Letters*, *94*(11), 111112.

Bohlein, T., Mikhael, J., & Bechinger, C. (2012). Observation of kinks and antikinks in colloidal monolayers driven across ordered surfaces. *Nature Materials*, *11*(2), 126–30.

Bonello, B., Charles, C., & Ganot, F. (2006). Velocity of a SAW propagating in a 2D phononic crystal. *Ultrasonics*, *44 Suppl 1*, e1259–63.

Campbell, C. K. (1989). Applications of Surface acoustic and shallow bulk acoustic wave devices.pdf. *Proceedings of the IEEE*, *77*(10), 1453.

Dutcher, J., Lee, S., Hillebrands, B., McLaughlin, G., Nickel, B., & Stegeman, G. (1992, April). Surface-grating-induced zone folding and hybridization of surface acoustic modes. *Physical Review Letters*.

Glass, N. E., Maradudin, A. A., & Introduction, I. (1983). Leaky surface-elastic waves on both flat and strongly corrugated surfaces for isotropic, nondissipative media. *Glass*, *92717*(February), 796–805.

Länge, K., Rapp, B. E., & Rapp, M. (2008). Surface acoustic wave biosensors: a review. *Analytical and Bioanalytical Chemistry*, *391*(5), 1509–19.

Laude, V., Wilm, M., Benchabane, S., & Khelif, A. (2005). Full band gap for surface acoustic waves in a piezoelectric phononic crystal. *Physical Review E*, *71*(3), 1–7.

Lima, M. M. De, & Santos, P. V. (2005). Modulation of photonic structures by surface acoustic waves. *Reports on Progress in Physics*, *68*(7), 1639–1701.

Liu, Y. J., Ding, X., Lin, S.-C. S., Shi, J., Chiang, I.-K., & Huang, T. J. (2011). Surface acoustic wave driven light shutters using polymer-dispersed liquid crystals. *Advanced Materials (Deerfield Beach, Fla.)*, *23*(14), 1656–9.

Malaquin, L., Kraus, T., Schmid, H., Delamarche, E., & Wolf, H. (2007). Controlled particle placement through convective and capillary assembly. *Langmuir : The ACS Journal of Surfaces and Colloids*, *23*(23), 11513–21.

Maznev, a. a., & Wright, O. B. (2009). Optical generation of long-lived surface vibrations in a periodic microstructure. *Journal of Applied Physics*, *105*(12), 123530.

Nardi, D., Banfi, F., Giannetti, C., Revaz, B., Ferrini, G., & Parmigiani, F. (2009). Pseudosurface acoustic waves in hypersonic surface phononic crystals. *Physical Review B*, *80*(10), 1–8.

Retsch, M. (2009). *Complex materials via colloidal crystallization*. der Johannes Gutenberg-Universität in Mainz.

Tanaka, Y., & Tamura, S. (1998). Surface acoustic waves in two-dimensional periodic elastic structures. *Physical Review B*, *58*(12), 7958–7965.

Teh, L. K., Tan, N. K., Wong, C. C., & Li, S. (2004). Growth imperfections in three-dimensional colloidal self-assembly. *Applied Physics A*, *81*(7), 1399–1404.

Wu, T.-T., Huang, Z.-G., & Lin, S. (2004). Surface and bulk acoustic waves in two-dimensional phononic crystal consisting of materials with general anisotropy. *Physical Review B*, *69*(9), 1–10.

Zhang, G. (2009). Nanostructure-Enhanced Surface Acoustic Waves Biosensor and Its Computational Modeling. *Journal of Sensors*, *2009*, 1–11.

6. Application: Mesoscopic Structure of Kidney Stones and Shockwave Induced Fracture

6.1 Introduction of the kidney stone

Kidney stones are a common clinical problem that affected up to 10% of men and 5% of women throughout the United States. Stone disease can cause pain and suffering, occasional renal failure or even fatal in rare cases. However, the pathology is not well understood despite significant progress made over the last few decades. Moreover, the patients also encounter treatment cost and additional loss of productivity at workplace.

Kidney stones consist of mineral microcrystals aggregates and organic substances incorporated in various ways. They are classified into several categories according to their chemical compositions and morphologies.

6.1.1Major classes of kidney stone

The most common kidney stones consists of calcium oxalate (60~70% of kidneys stones), which crystallizes in three different chemical and crystallographic forms: 1) Calcium oxalate monohydrate $CaC_2O_4 \cdot H_2O$ (COM), also known as whewellite and 2) Calcium oxalate dihydrate $CaC_2O_4 \cdot 2H_2O$ (COD), also called weddellite and 3) Calcium oxalate trihydrate $CaC_2O_4 \cdot H_2O$ (COT). The single crystals usually have a size of 2-3m and packed together tightly with some porosity (Sokol, Nigmatulina, Maksimova, & Chiglintsev, 2005). COM can be present as single crystal or aggregated polycrystalline particles, as shown in Figure 6.1 top. Their morphology can be simple biconcave ovals, dumbbells, twinned dumbbells or rosettes or spherulite (Saeed R. Khan & Hackett, 1987), as shown in Figure 6.1 bottom. These stones made of COM crystal mostly are frequently hard, dark brown with a dull gray exterior. When sectioned, they present radial growing pattern from nidus with round off wedges that lead to a smooth exterior (Figure 1 bottom b) and f)). COD crystallizes as bipyramids due to its tetragonal crystal point group symmetry, yet its structure can change with additives, as shown in Figure 6.2. Pure COD stones are usually small and spherical with a tan or yellow cluster of platelets, which are sharp with various orientations (Figure 6.2 bottom d) and f)).

The second major class of components of stones is phosphate salts (15~20% of

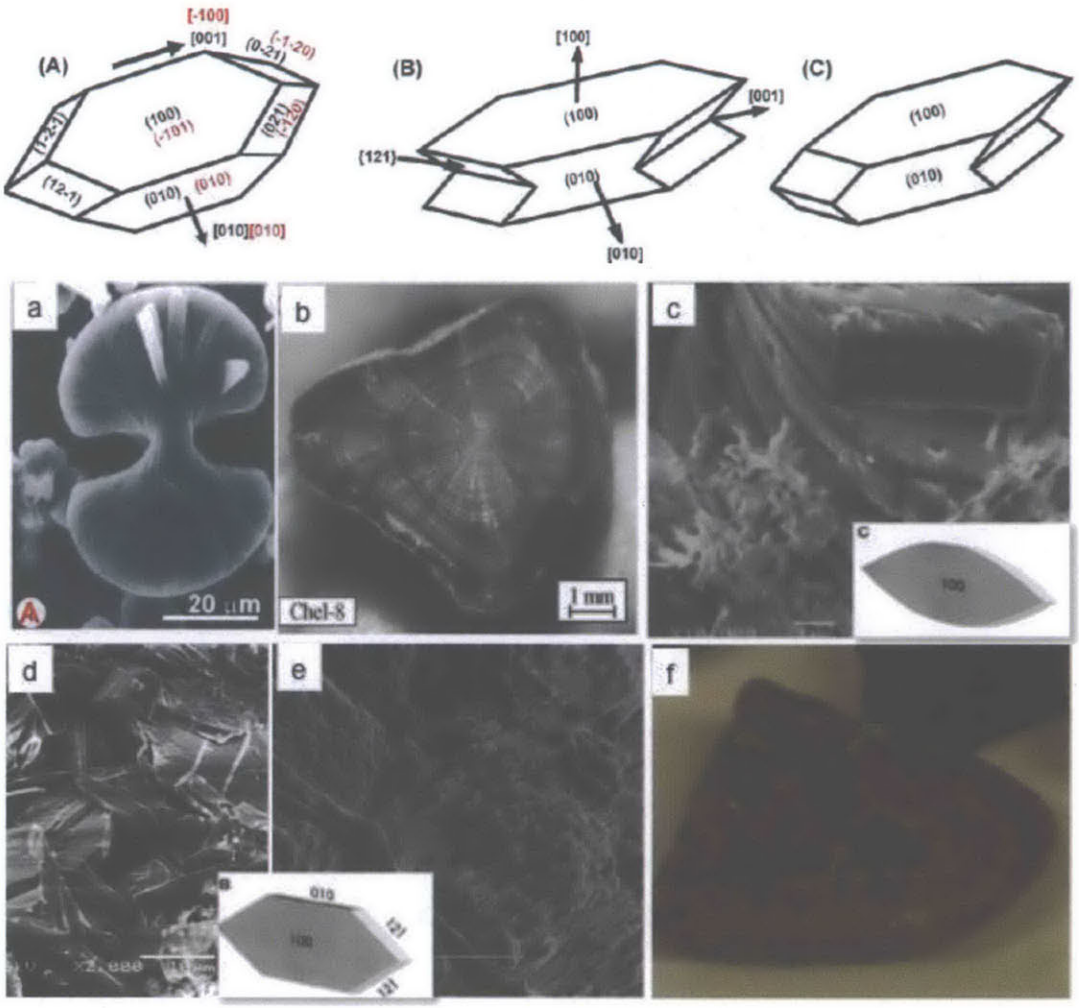

Figure 5.25: Top (A) The crystal faces developed and major crystallographic directions indicated for a COM single crystal of six-sided polyhedral habit. Twinned crystals of COM which are often classified as penetration twin (B) and contact twin (C). Indexing with black letters corresponds to Tazzoli's notation and with red to Deganello's notation(Thomas, 2009).
Bottom: (a) COM stone with dumbbell /fan-like morphology. (b) Polished cross-section of a COM spherulitic stone representing concentric laminations, image from (Sokol et al., 2005) (c) SEM image of fractured surface of COM stone showing modified shape of the crystal habit. (d) SEM image of fractured surface of a COM stone exhibiting the randomly stacked plate, (e) SEM image of fractured surface of COM stone shows edges of closely stacked plate-like crystals. These crystals are stacked by contacts between their (100) faces. (f) Fractured surface showed concentric circles at the edge of the stone.

kidney stones), which includes four different calcium phosphate salts and two magnesium phosphate salts. The calcium phosphate salts have different calcium-to-phosphate ratio, hydroxyl-vs.-hydrogen ion content. One typical example is magnesium ammonium phosphate hexahydrate stone (Struvite), they usually have off-white to light brown color

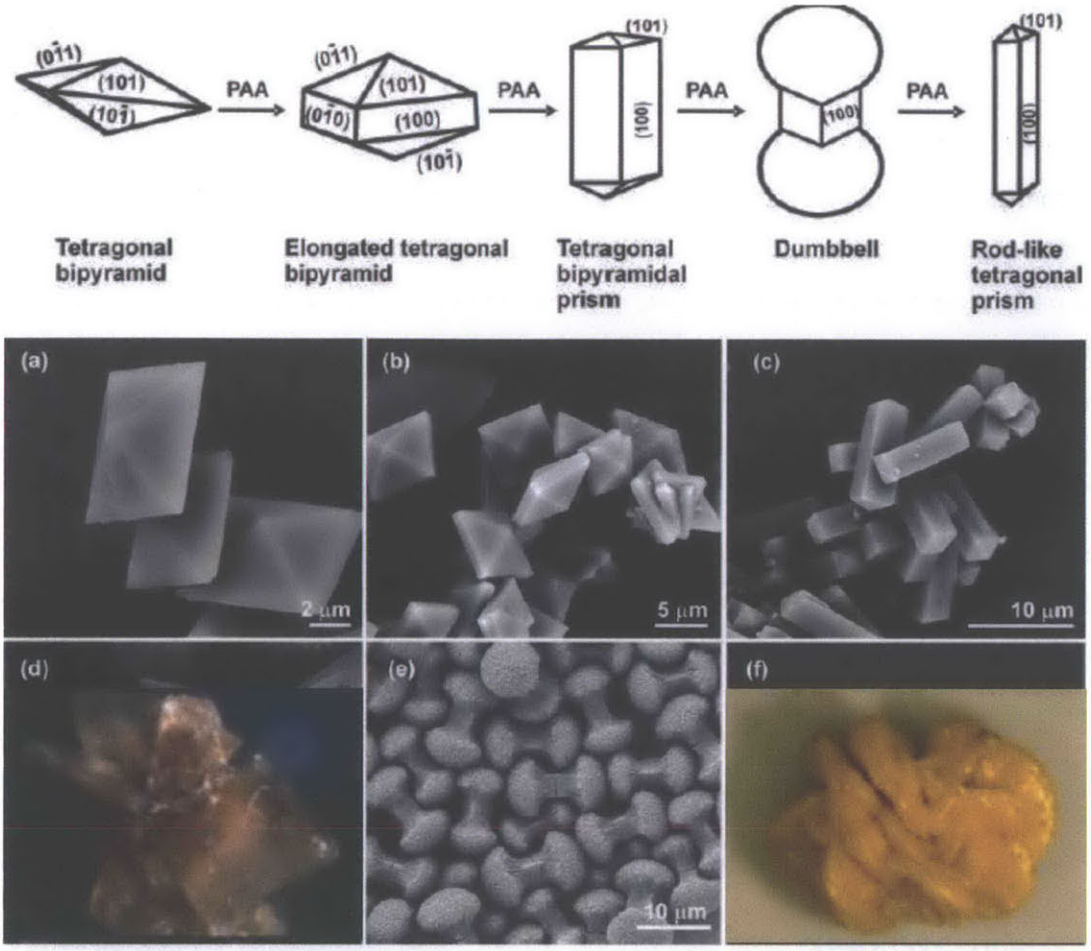

Figure 5.26: Top: Schematic representation of the influence of polyacrylate (PAA) concentration on the morphologies of COD.
Bottom: SEM images of COD crystals produced in the presence of 1.2 mM CaOx and
(a) 16, (b) 48, (c) 64, (e) 96 μg/mL PAA. These images show the morphological development of COD. (a) Tetragonal bipyramids, (b) elongated tetragonal bipyramids, (c) tetragonal bipyramidal prisms, (d) kidney stone mainly composed of COD, (e) dumbbells and (f) kidney stone mainly composed of COD. Image from (Thomas, 2009), except (d) and (f) from Louis C. Herring &Company website.

with a rough textured surface. They frequently grow in a stag horn shape with concentric rings in its interior(Walton, Kavanagh, & Heywood, 2003), as shown in Figure 6.3.

L-cystine crystal has also been found in kidney stone, which affect at least 20,000 individuals in the United States. Compared to calcium oxalate, stones made of L-cystine mostly are larger (Figure 6.3) and can cause chronic kidney disease due to more frequent occurrence. Uric Acid stones (10%) usually have a smooth yellow-orange surface with spherical shape. Orange concentric rings usually appeared as its sectioned interior (Figure 6.3). In contrast, Uric acid dehydrate stone is darker orange with small spherical regions. Its interior usually has a well-defined nidus with thick

concentric rings (Walton et al., 2003).

6.1.2 Crystal - Matrix relationship

Besides the inorganic crystal, kidney stones also contain various organic substances. Various groups have investigated the role of organic substance. In the early studies, it was found that for calcium oxalate crystalluria, the organic material tends to concentrate at the center and selected concentric layers (Saeed R. Khan & Hackett, 1987). For a kidney stone with dumbbell morphology, the matrix were found to be mostly fibrillar, mostly arranged mostly radially in longitudinal cross section and appeared reticulate in transverse cross section, as shown in Figure 6.4.

Several functionality of the organic matrix has been proposed, organic substance can form matrix to bind the crystal nuclei together to facilitate the growth of crystal aggregates. The macromolecules absorbed on top of mineral crystal surface can protect them from dissolving. The matrix may also help regulate the crystal habit and texture of

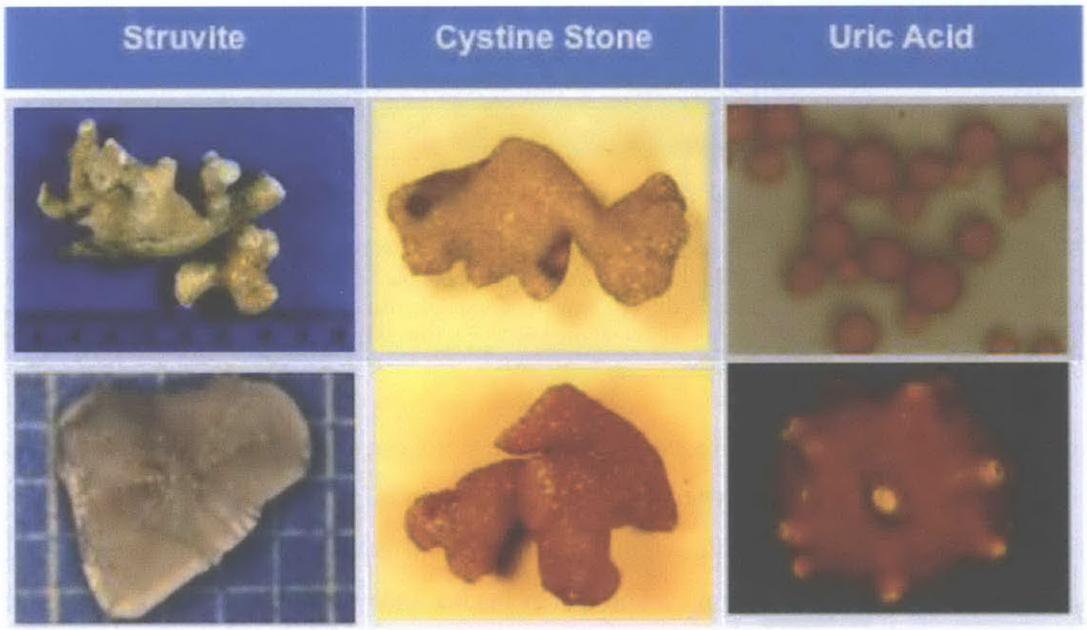

Figure 5.27: Various morphology for several classes of kidney stone, top left image from Lithostat website. All the reset images are retrieved from Louis C. Herring &Company website.

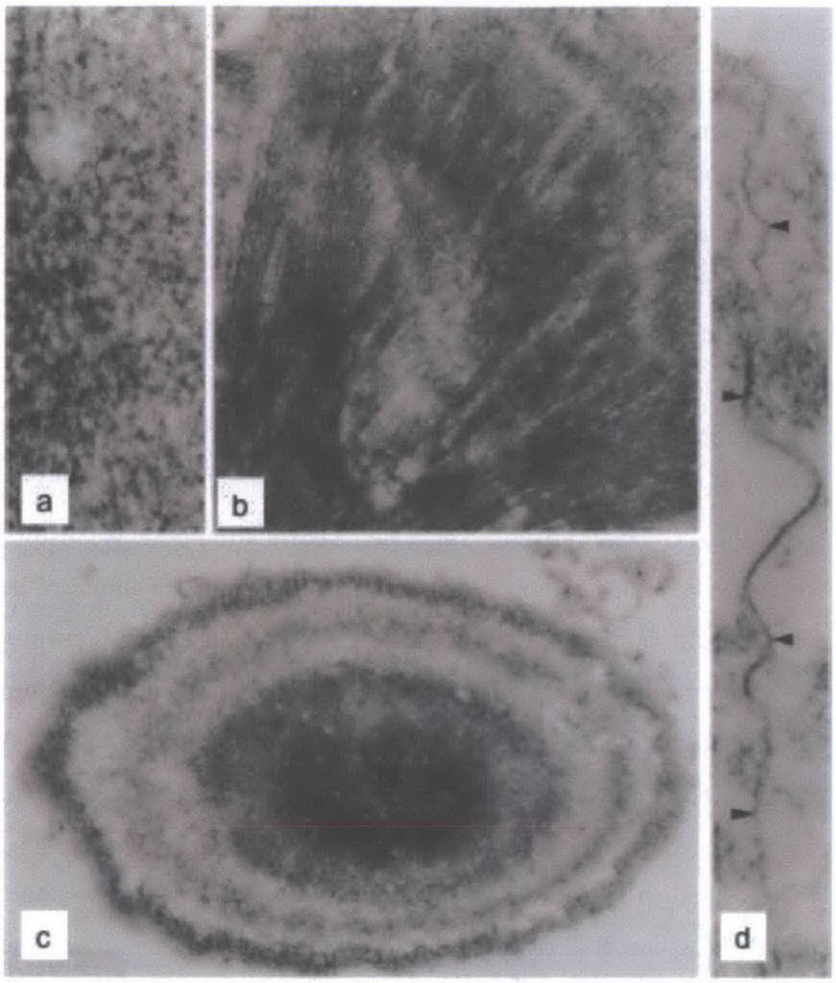

Figure 5.28: a) Higher magnification TEM of a cross-section through the bar of the dumbbell ghost showing compactness of the organic material and its reticulate nature. x262,500. b) Higher magnification of a longitudinal section through the bar of a dumbbell ghost. Most of the organic material is organized radially. x60,000. c) A cross-section through the bar of the dumbbell ghost showing a compact center (N). x55,000. d). Longitudinal section through the periphery of a dumbbell ghost showing internal partition by a radial membrane (arrowheads). x135,375. Image from (Saeed R. Khan & Hackett, 1987)

the stones. (Saeed R. Khan & Hackett, 1987). The discrepancy between volume and weight ratio (around 2%) of organic components leads Sokol to conclude porosity is common in stones. Furthermore, the presence of amorphous caphosphates or globules of biogenic apatite in the center of stone cast doubt (Sokol et al., 2005) on hypothesis that protein contribute to intra-crystalline ultrastructure formation in kidney stones. (Walton et al., 2003)

6.1.3 Pathway of stone formation

Stone formation usually starts with mass heterogeneous nucleation from supersaturated urine, which can be facilitated by fragments of exfoliated epithelium, blood clots, and bacterial colonies. It was also proposed that calcium oxalate might crystallize on the uric acid and its salts due to the high correlation between uric acid excretion and the formation of oxalate kidney stones (Mandel (1996). The crystals formed would move along nephritic tubules with urine flow, some of which might be retained and attached to soft tissue(Sokol et al., 2005) and then form aggregates, as shown in Figure 6.5; the mechanism for this process can be described by Randall – Carr's theory (Randall, 1937; 1940; Carr, 1953; Hess & Kok, 1996). Since COD crystal are likely to be voided, most kidney stone retained mainly consists of COM. Study also suggested a correlation between history of hypertension and attachment of crystal to urothelium. Healthy urothelium has been shown to be able to protect against nucleation and adhesion of calcium oxalate crystals. On contrary, chemically injured urothelium does not have such property and results in the adherence of calcium oxalate crystals. Heparin, a sulfated heteropolysaccharide of glucuronic acid and glucosamine, was shown to be able to restore the anti-crystal-adhesion capacity of injured urothelium (Walton et al., 2003).

Studies have been conducted to investigate how various factors affect the morphology of the stone, especially for calcium oxalate stones. Millan et al (Millan, 2001) conducted both theoretical and experimental studies on other factors that influences crystal shape of the two COM (whewellite) polymorphs. They found that theoretical modals based on basic structure of COM crystal performance better than those based on derivative crystal structures. They hence concluded that the crystal shape is depended on the basic structure instead of the enantiotropic phase transformation between 38 and 45 °C. The spherulites formation of needle crystal might suggest random condensation of linear nuclei, which could be produced by fast mixing of supersaturated reactants solution. They also found that intensive interaction between Ca^{2+}, $C_2O_4^{2-}$ and water molecules leads to wetting effect on crystal formed in water. Since additives can induce crystal habit modification, e.g. flattening of crystal along [100] direction, it was proposed that to eliminate the active

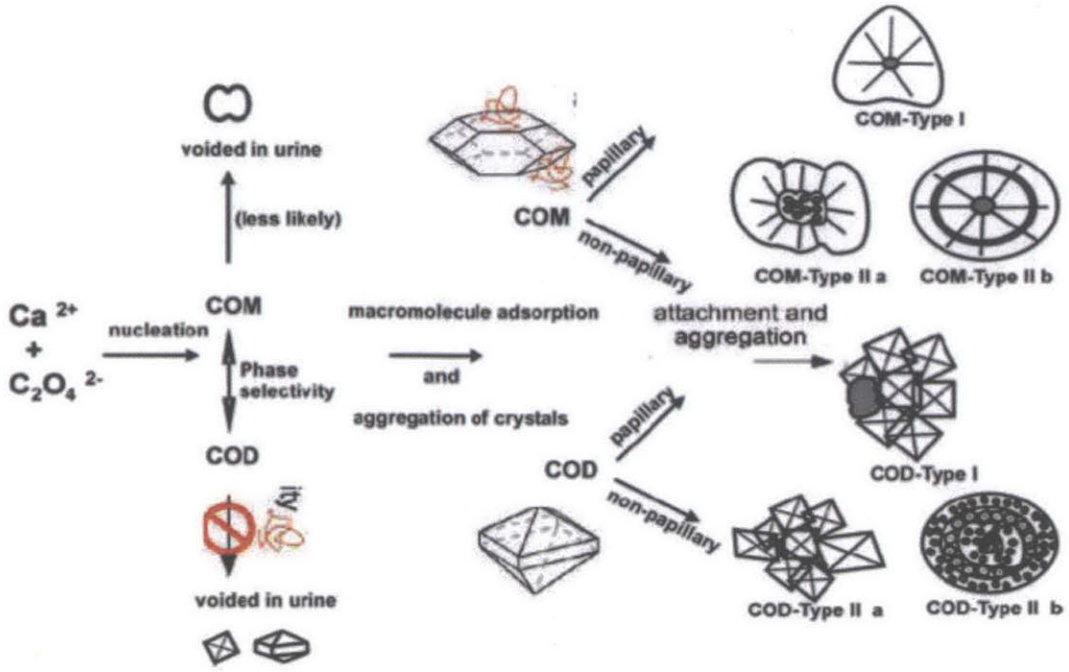

Figure 5.29: Pathway for the formation of COM and COD calculi. The crystals which are not voided through urine are aggregated through the adsorption of macromolecules and grow into larger aggregates. The morphology of COM and COD calculi are generally classified as type I (papillary) and type II (non-papillary). The regions shaded with grey color are either organic matter or hydroxyapatite or a minor fraction of COM. Images reproduced from (Thomas, 2009)

COM (100) surface in urine environment, therapeutic agents that reduce the size of (100) surface or adhesion strength upon adsorption would be effective (Wesson & Ward, 2007).

Thomas also conducted systematic studies on how sodium salt of polyacrylate (PAA) can change structure and habit of calcium oxalates crystals. They found that with a fixed CaOx concentration, the hydration states of calcium oxalates can be determined by pH of the start solutions. The rare COT was found at higher pH value in absence of PAA. The concentration of PAA also affects the morphology of COD crystals. Besides, organic gels, agar, agarose, carrageenan and gelatin were used to generate biomimetic calcium oxalates. It was founded again pH affects the hydration state while the saturation level affects the morphology of the crystal, as shown in Figure 6.6. Not surprisingly, it was also found that temperature affects the morphology of the final crystal morphology as well(Thomas, 2009).

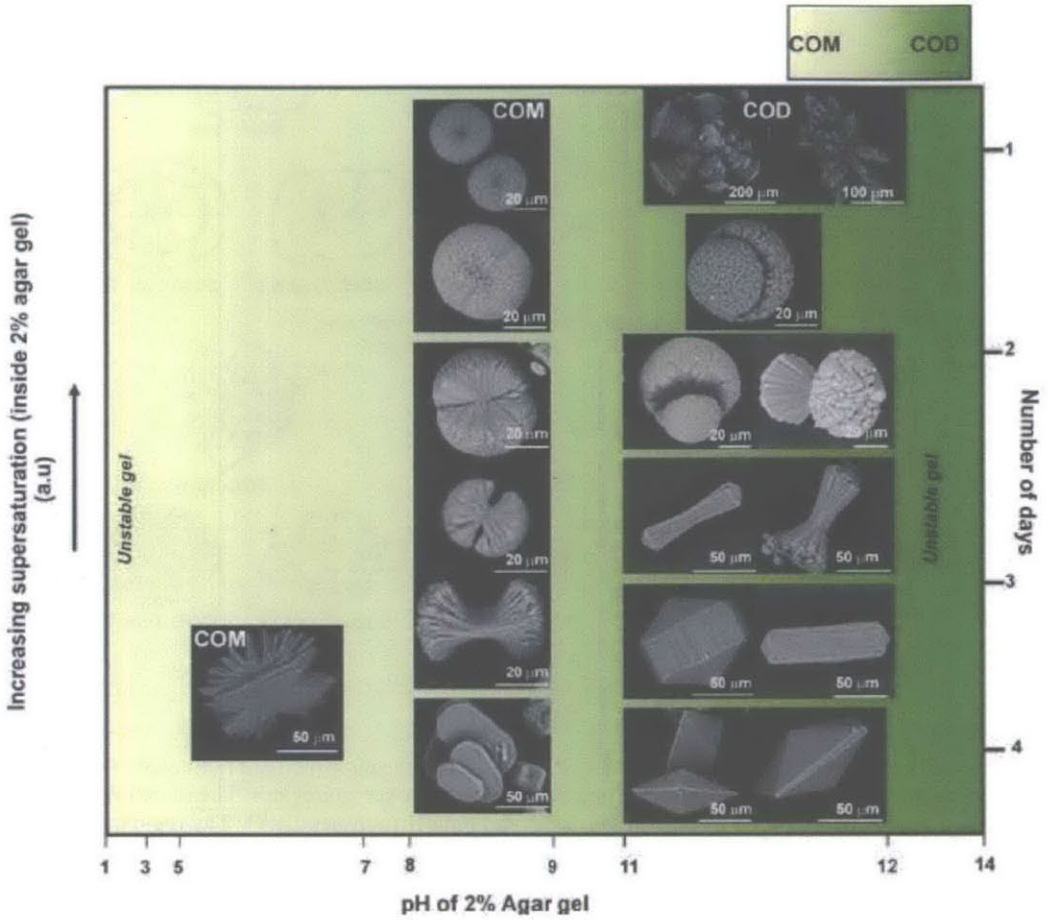

Figure 5.30: Morphology and hydration state map of calcium oxalate aggregates grown in 2wt.-% agar gels at different pH values (Thomas, 2009).

A study conducted by the authors confirmed some of the literature findings. Modified COM crystal habit was found in kidney stone's fractured surface, which resemble the shape in the presence of additives or mucoprotines (Millan, 2001), as shown in Figure 6.1 (c,d,e). Struvite with different crash resistance can have different microscopic structures, stones that are harder to crash tend to have more crystalline phase while the relatively softer ones seem to have amorphous porous network with crystalline phase in between, as shown in Figure 6.7. The struvite stones studied processes core-envelop layer structure, where the relatively smooth interface between them is observed at a fractured envelope piece (Figure 6.7 bottom right).

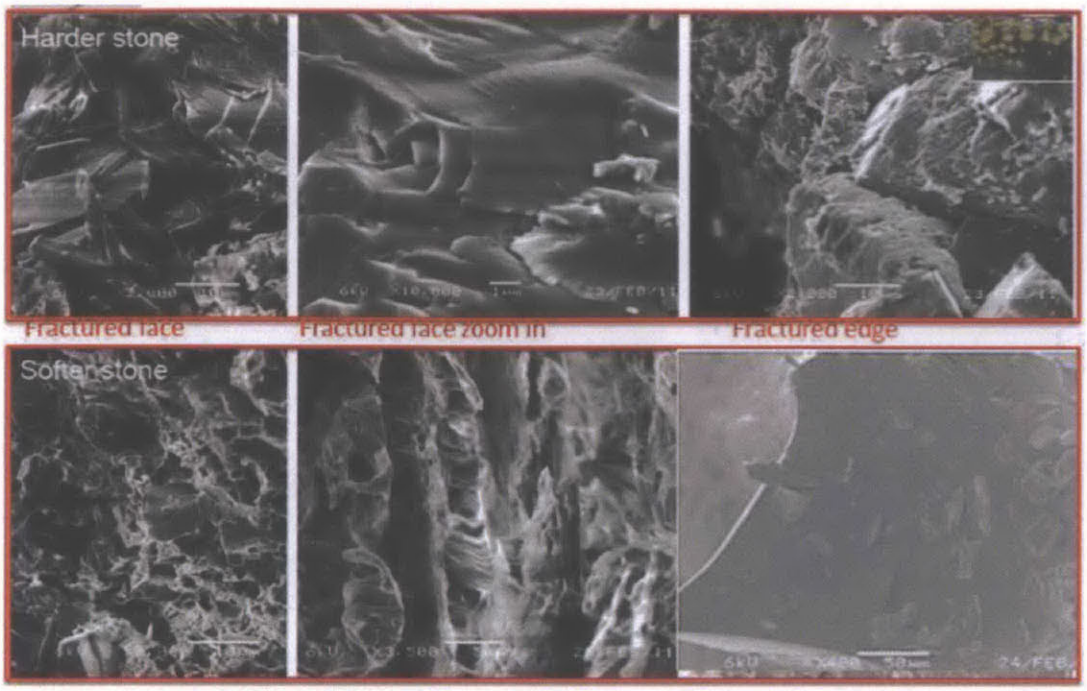

Figure 5.31: SEM images of fractured struvite stones. Top row is for stones that are harder to crash, while the bottom row is for stone that is easier to crash. Bottom right images shows a smooth interface that could be the interface between the core and the envelop layers.

A common structure for large stones with smooth surface seems to be calcium oxalate layer enveloping uric acid stones. The closed packed layered structures was observed in fractured surface with macroscopic laminar structure, due to varying pigment densities at each layer, as shown in Figure 6.8. The fractured images showed layered structure along the radial direction and also periodic serrated surface transversely. Although this closely packed regular structure might contribute to the toughness of the stone, it is hard to identify if the fractured surface corresponds to any crystal surface of calcium oxalate. Microcrack along the transverse direction has also been observed, which might indicates the disruption during the growth or could be caused during crashing of the stones. This are consists with report that uric acid stone might serve as nuclei for calcium oxalate crystal to deposit and grow the densely packed laminar structure.

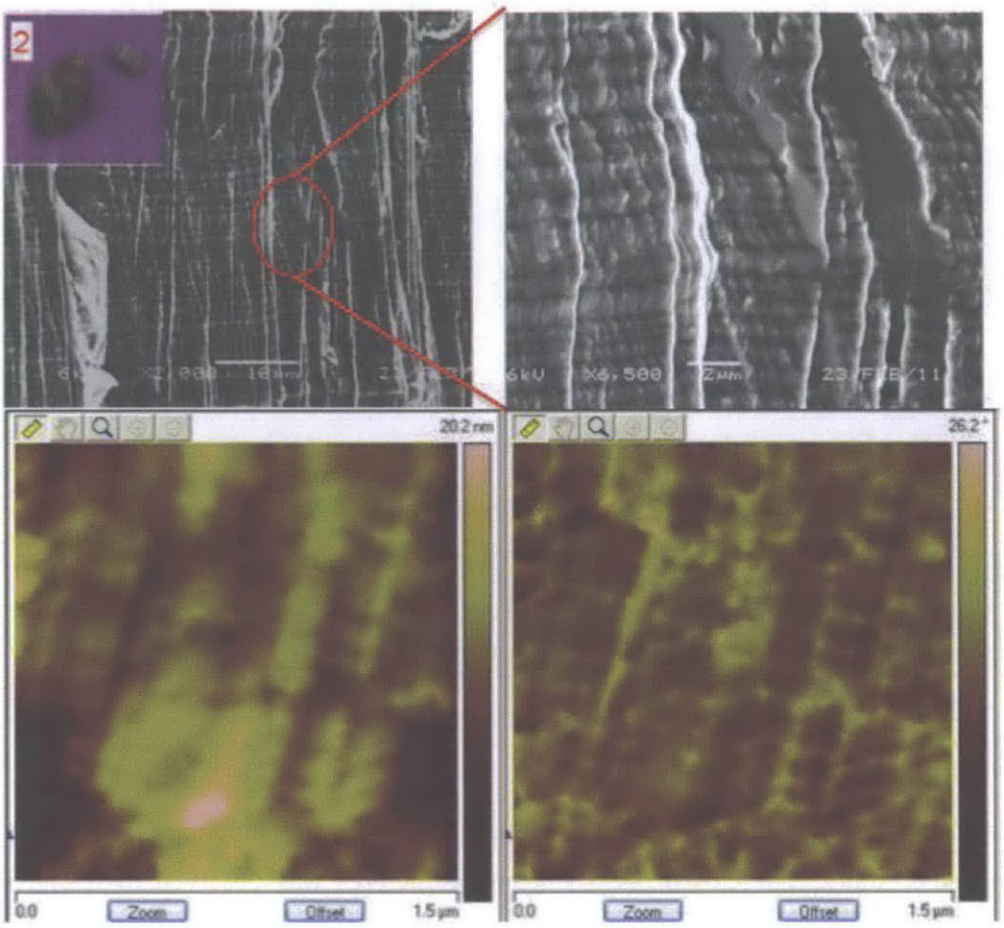

Figure 5.32: The SEM images (zoomed in on the right) shows the laminar structure on the calcium oxalate enveloping layers, AFM height and phase images confirmed the periodic structure in both radial and transverse direction.

For stones with smooth, reflective and scratch resistant surface, they seem to share common macrostructure, where dense amorphous (organic) substance cover the stone with small mineral crystals clusters exposed at times, as shown in Figure 6.9. This difference between the interior layered structure and the amorphous structure at the surface might indicate growth disruption at the surface. Also smaller crystal size seems to lead to higher packing density, hence higher scratch resistance of the stone surface. Whether the disruption of layer growth caused the growth of amorphous structure or the attachment of amorphous substance disrupts the growth could be an interesting question to investigate. A better understanding might help us to develop ways to control the size of the stone size.

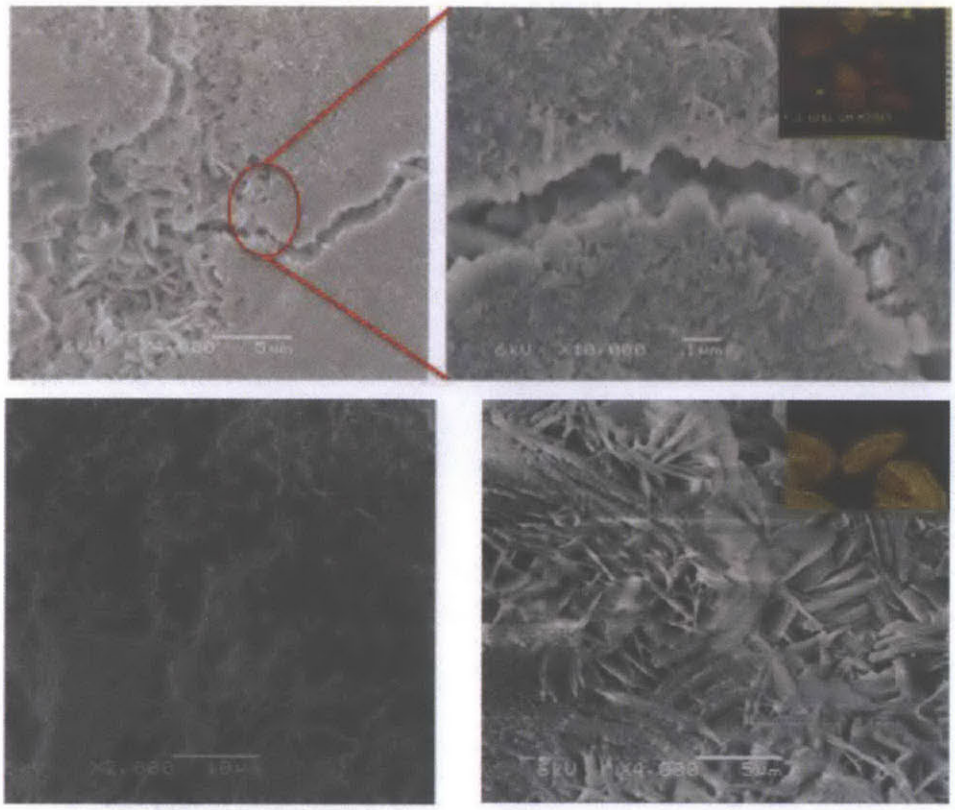

Figure 5.33: The SEM images (zoomed in on the right) for the top row show the surface structure with amorphous substance densely packed and crystal cluster exposed at times.
The bottom row shows the surface structure of another kidney stone sample. The inserts show the macroscopic look of fractured kidney stones.

Moreover, the dumbbell structure common in synthetic COD crystal has also been observed in the natural stone fracture interior surface, although with more pointing tips, as shown in Figure 6.10. The dumbbell structure also appeared at stone surface near a spherulites structure. Although spherulite structure has also been produced in synthetic COD crystal, this structure occurred in natural stone seems to have different building blocks. Since COD crystals are unlikely to form big aggregates, they might have deposited on the surface randomly during or after the growth. Moreover, there are also organic buddle like structure observed on the surface and interior of densely packed crystals, as shown in Figure 6.11. The buddle seems smooth with little texture and it is not clear if it is structurally relevant. Further studies on its chemical composition might help to understand its properties and its role in stone formation.

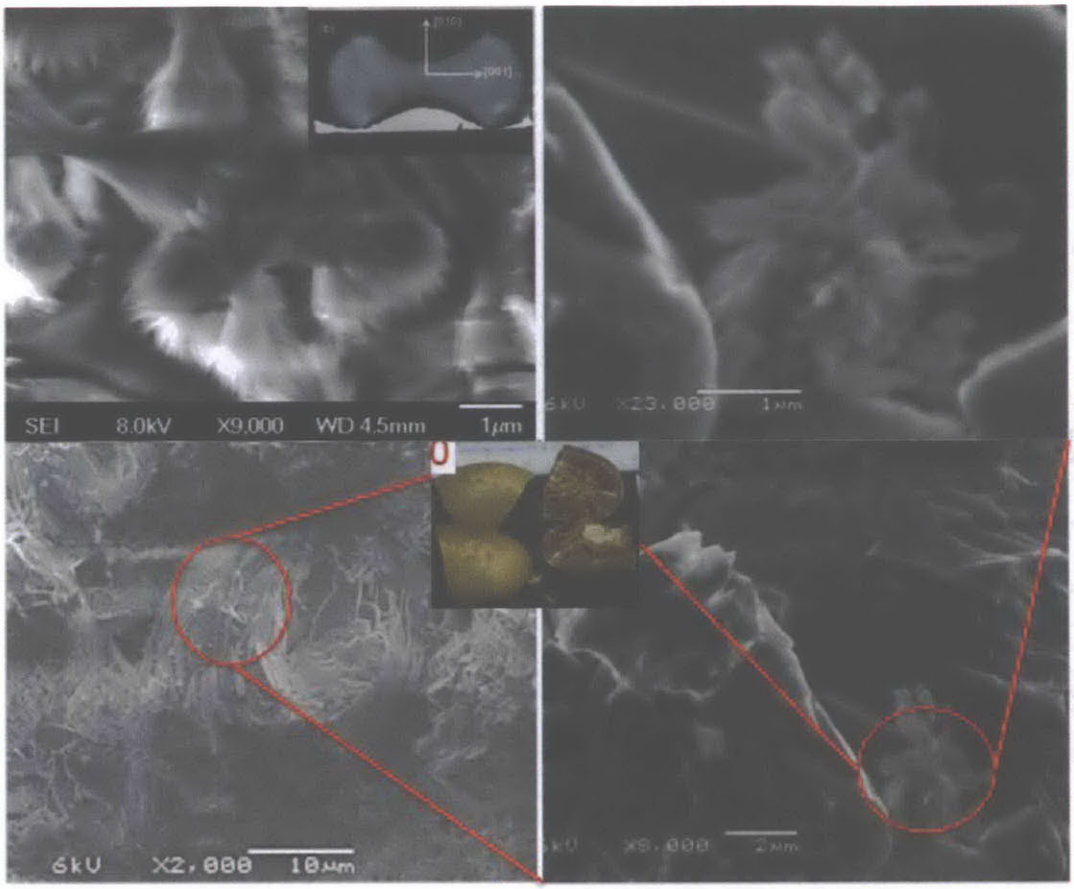

Figure 5.34: The SEM images showed dumbbell structure observed at fracture surface. Spherulite structure has also been showed at the surface of the stone with dumbbell like crystallite despite randomly. The inserts show the macroscopic look of fractured kidney stones

Moreover, enzymes could also play a role in stone formations. Difference in enzyme activity between stone formers and healthy group has been show. The crystallization of calcium oxalate in vitro has shown to be retarded by L-glutamic acid (Azoury, Garti, Perlberg, & Sarig, 1982). A later study conducted by Duncan seems to suggest that O. formigenes might play an important role in oxalate degradation activity. Although its importance cannot be confirmed exclusively, a single oral ingestion of O. formigenes do show recovered oxalate degradation ability for a prolonged time (Duncan et al., 2002). For cystine stones, Rimer et al also use AFM measurement to demonstrate that a potentially benign crystal growth inhibitor (unsymmetrical L-CME) at low concentrations can minimize L-cystine crystallization. Therefore, it might have the potential to replace drugs that contains alkalinizing potassium or sodium salts for L cysteine stone prevention
(Rimer et al., 2010).

6.1.4 Pathological mechanisms for kidney stones formation

Since the stone pathway involves multiple stages, many factors can contribute to stone formation. Supersaturation of urinary CaOx can be affected by cellular defect or dysfunction, which can affect participating urinary ions and macromolecules. Other endogenous processes that produce substances like oxaluria, citrate, pyrophosphate and several other macromolecules can also affect stone formation. Moreover, genes that connected to hypercalciuria, such as CLCN5, CASR, CLDN16, have also been suspected despite the lack of substantial proof (Saeed R Khan, 2011).

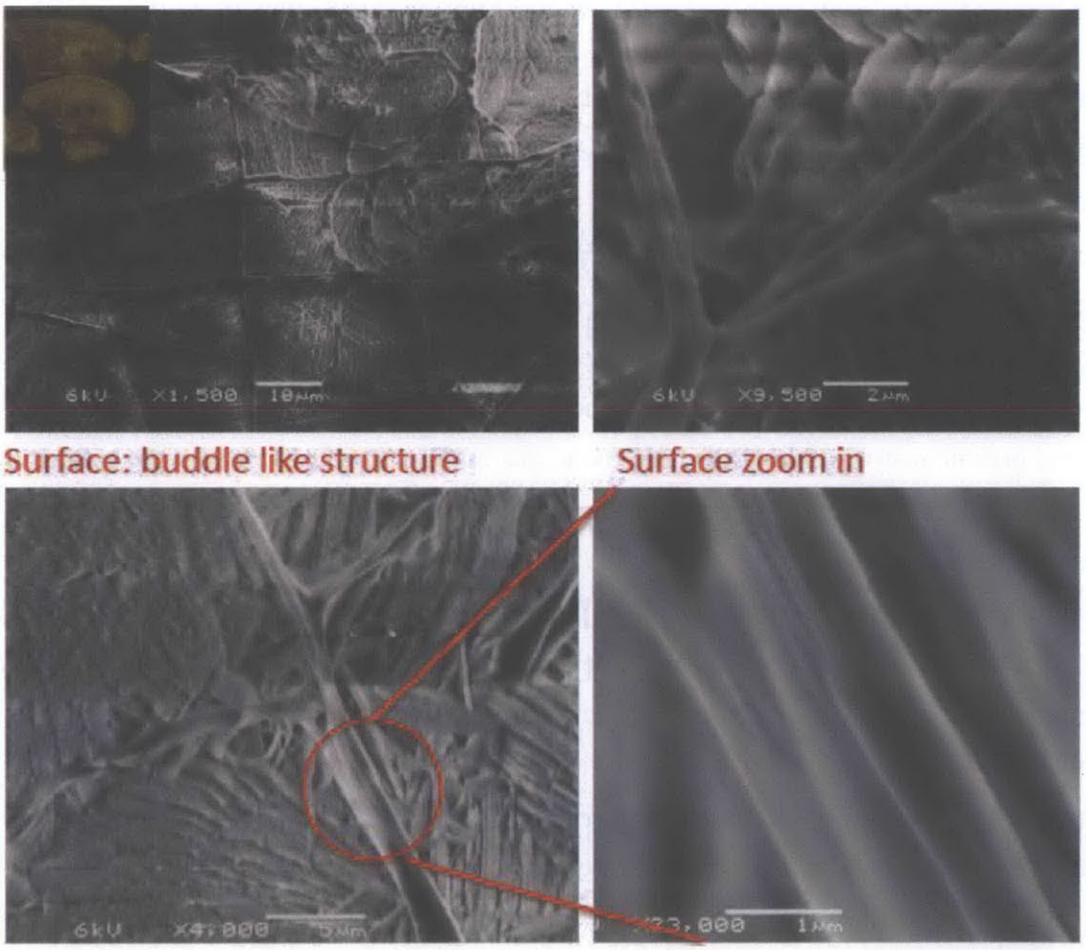

Figure 5.35: The SEM images showed buddle like structure at stone surface. The inserts show the macroscopic look of fractured kidney stones

Renal epithelial injury was showed to promote crystallization of calcific crystals in vivo in animal modals. Large aggregates of calcific crystals were continuously excreted in the urine with the

presence of epithelial injury (Stoller, Meng, Chung, & Abrahams, 2007). It was found that crystal binding became possible on surfaces of mature cells only after injury, which support the hypothesis that renal injury might promote crystal retention by facilitating stone nidus on renal papillary surface(S. R. Khan, 2011). Moreover, the architecture of human kidney might also explain the preferred stone deposit site of stone due to disturbance of the urinary flow and impedance of the crystal movement. Dietary has long been suspected as another trigger for stone formation. Study showed that supersaturation of urinary CaOx depends on the concentration of Ca and Ox, as well as but also occurrence of ions like citrate and magnesium (Stoller et al., 2007).

6.2 Early study on mechanical properties of the stones

Kidney stone has been investigated over several decades and various techniques have been employed to characterize their properties.

Mechanical properties of kidney stones have been studied few decades ago. Knoop micro hardness indentation tests were performed on stones composed of calcium oxalate, calcium phosphate, uric acid, cystine, and magnesium ammonium phosphate (Johrde & Cocks, 1985, 1986). They found that hardness along one layer is higher compared to hardness across layers (due to alternation of crystal and organic matrix phase). They also found that exposure to urine (for pH with a range of 4 to 12) would decrease their hardness compared (up to 55 %) to dry hardness. A Knoop micro-hardness study was also conducted to study the difference between COM and COD stones. The COM stone is harder than COD stone although pure COM crystal has higher hardness value than COM crystal (Girija, 2000). Therefore, the superstructure between pure crystals does play a role in micro-hardness of the stones. During a static loading, working hardening as well as working softening has also been observed.

To study the morphology of various natural and/or synthetic stone, mostly fractured or cross section surfaces have been studied by Scanning electron microscopy (SEM). To study how crystal and organic matrix interact with each other, decalcified stone ghosts (decalcified stone) have also been studied using Transmission electron microscopy

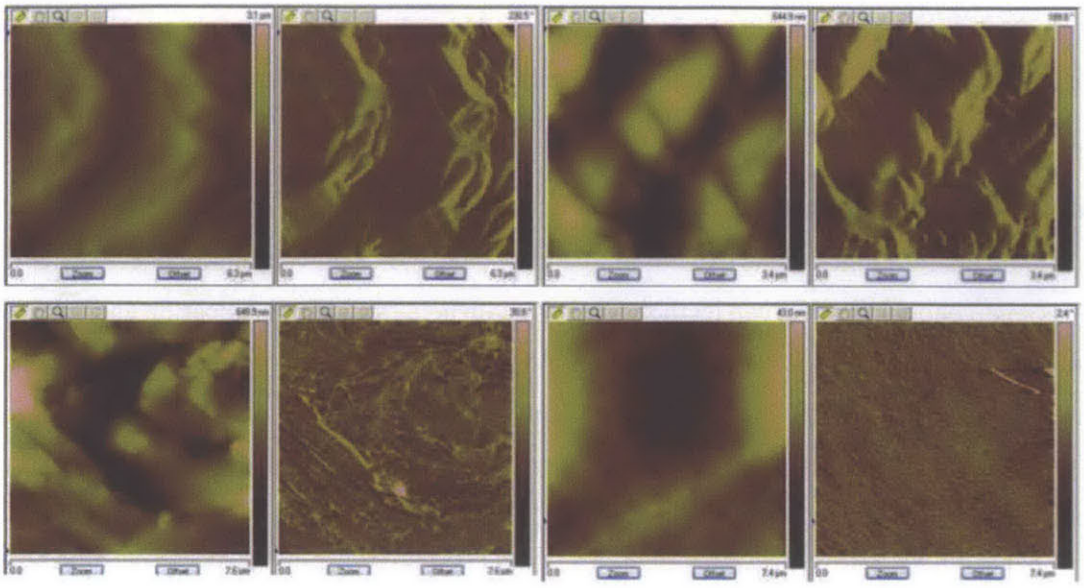

Figure 5.36: The height (left) and phase (right) images obtained from the same flakes of kidney stones, demonstrated the heterogeneous structure of the kidney stone.

(S R. Khan et al, 1987). To study the macroscopic concentric laminar structure of transversal cross section if COM stones, Polarized light microscope could be quite a suitable tool. Moreover, to study the in situ growth of crystal, AFM measurement has also been used(Rimer et al., 2010). AFM has also been used to measure the adhesive force of various surface of COM and COD crystals. They found that COM (100) exhibits the largest adhesion strength among all the faces examined, which might be the main reasons that COM stacking in aggregates and attaching to epithelial cell(Wesson & Ward, 2007).

Since natural kidney stone usually are hybrid crystal aggregates, X-ray diffraction analysis (XRD) has been used to identify crystalline components with more than 5 wt. % in stone powders. However, XRD can be limited by its sensitivity with limited amount of sample and may fail to characterize sample whose crystal structure is unpublished. Accompanied with SEM, Energy-Dispersive X-ray Spectroscopy (EDX) can be used to map chemical composition of fracture surface. To identify individual chemical mineral elements, CAMEBAX electron micro-probe was also used for quantitative analysis with petrographic thin-section samples(Sokol et al., 2004). To identify the chemical bonds inside of the kidney stones, transmission IR-spectra is attractive due to its high sensitivity. Raman Spectroscopy has also been used as a nondestructive analytical tool to study the chemical bonds of cysteine, phosphate and uric acid type stone. (Venkata Venkata R.

K. et al 1990 a) and b);(Venkata R. K. et al, 1991). AFM might also be helpful to look at finer structure and obtain phase information of stone structures, as shown in Figure 6.12.

6.3 Treatments for kidney stones

Various treatments for kidney stone exist to mitigate the pain and/or prevent future occurrence. If the stone is small enough, patient can let the stone pass with help from pain medication and/or take more fluid. The doctor might also prescribe other medication to help pass the stone(s). Various home remedies have also been suggested with herbs and fluidic mixtures. If the stone is large enough to block the urinary tract and/or you are experience severe pain, the doctor might suggest a procedure, such as lithotripsy or surgery. In literature, both medication and lithotripsy optimization have been active research area. It was found oral intake of the bacteria (Oxalobacter formigenes) that breaks down the calcium oxalate crystal might reduce urinary oxalate excretion and recover oxalate degrading activity in adults (Duncan et al., 2002).

Extracorporeal shock wave lithotripsy (ESWL) is a treatment option that use acoustic waves to break the kidney stone into smaller parts to pass out. It is preferred due to the non-invasiveness compared to surgery.

6.3.1The physics of acoustic waves to break the stone

The acoustic wave breaks the stone through several mechanisms: 1) cavitation, which causes pitting on stones surfaces; 2) spalling, a large tensile stress near the back wall of the stone that generate cracks 3) dynamic fatigue, where the micro-crack progressively developed and coalesce into crack that result in disintegration, as illustrated in Figure 6.13.

6.3.1.1 Cavitation

When acoustic wave passes through the fluid near the stone surface, gas cavities (i.e. bubbles) can be generated when the tensile phase is sufficient to rip the fluid apart. The bubble generated can go through inertial cavitation where they expand and collapse subsequently due to the pressure difference the bubble wall experiences. The collapse of

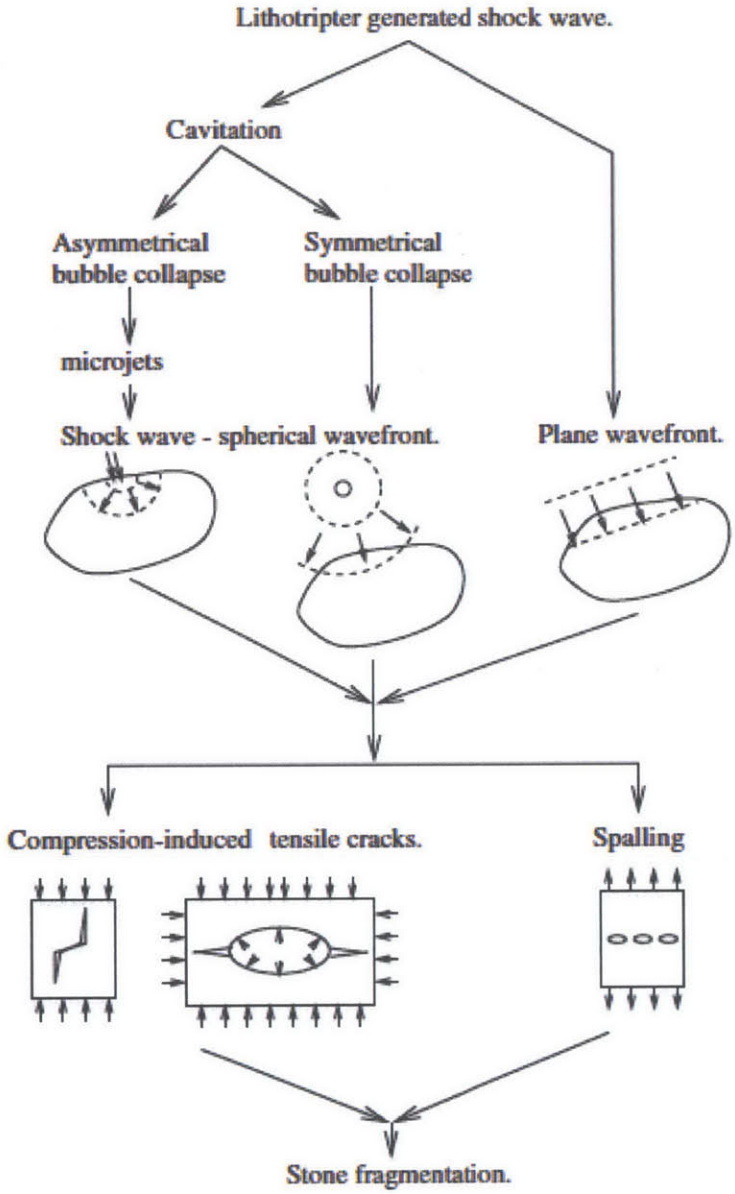

Figure 5.37: Mechanism of stone fracture by Lithotripter generated shock wave (Murtuza Lokhandwalla and Bradford Sturtevant, 2000)

bubble generates high-speed liquid jet, which causes surface pitting on rigid stone surfaces. Various theories have been proposed to describe the cavitation behavior due to the undesirable corrosive effects in machines like propeller and turbines(Neppiras, 1980).

Although theoretical studies on single spherical bubble in acoustic field have made significant progress, multi-bubbles in acoustic fields and condition for its instabilities to form and develop remains an active research fields.

Starting with the laws of conservation of Mass, Momentum and Energy, general relationship can be written and solved by applying appropriate boundary condition and reasonable assumptions. Due to the short time frame, the collapsing of bubble is usually considered as inertial controlled adiabatic process. The pressure and temperature profile near the collapsing bubble wall has been simulated, which depends on the initial radius, driving amplitude and frequency. The collapsing bubble can also emit acoustic waves, which can result in shock waves when they start to crowd each other. Studies showed that the pressure around the bubble wall, however, drops more rapidly than typical geometric law. Experimental studies confirmed that only in the immediate vicinity, the shock pressure of collapsing bubbles can have cavitation effects. On the other hand, the experimental studies have shifted form natural bubble-aggregates to controlled single cavities or bubble fields with high-speed photographic techniques.

Recently, acoustic cavitation has been used in sonochemistry since it can concentrate acoustic energy and heat the gas up to thousands of Kevin at the end of collapse. Its ability to convert acoustic energy into extreme physics can be used for other applications. However, the multidisciplinary nature of the acoustic cavitation also makes it challenging to understand the physics of the process(Louisnard et al., 2011). The nonlinear oscillation, sub-harmonic spectral component f/2 or a broadband spectrum has been correlated to erosive effects experimentally. Early experiments showed that subharmonic and chaotic sound emission is caused by the subharmonic and chaotic bubble oscillation (W. Lauterbornt, 1994).

Although the energy released during collapsing for single bubble might peak at certain frequency, it cannot be generalized to multi-bubbles. Furthermore, the nucleation and spatial distribution of bubbles observed is inhomogeneous and non-stationary. Some common bubble structures are streamers and filaments, jelly fish layers and cluster (Louisnard & González-garcía, 2011). Several conceptual frameworks have been used to explain the bubble distributions and their dynamic behavior. Strange attractors has also been used to study the geometric properties as well as the nonlinear dynamics of the multi-bubble fields (W. Lauterbornt, 1994). To explain the dendritic branch structure of erosion surface by cavitation, diffusion limited aggregation modal has also been used to describe the bubble distribution(Jing & Jian, 2009).

6.3.1.2 Spalling and tensile stress

Spalling is the overlap of reflected acoustic waves from the stone's back wall and the tensile tail of the subsequent propagating waves. The resulted tensile stress causes nucleation and growth of microcracks, which eventually reach critical size to result in stone fragmentation.

Various studies have been conducted to modeling the behaviors of stones under stress loading. To learn how the cracks propagate, a model was built to study how each pre-pulse (δn) and post-pulse ($\delta n+1$) crack opening related to each other, given the values of pulse amplitude and duration (σ_{in}, τ), and stone physical properties. They use springs (or absent of) to modal interlamellar flowed region (or void) the stone materials. To simplify the process, a worst case scenario with linear fragmentation process and a best case scenario with logarithmic fragmentation process is assumed (Murtuza L. and Bradford S., 2000). They found that the number of shocks need to spall stone into two pieces is $N = \frac{t_c}{\tau} \ln \frac{\sigma^{in}}{\sigma^{in} - \sigma_{fr}}$, where σ_{fr} is the fracture stress of the stone, $tc = \rho c \delta_{cr} / 2\sigma_{fr}$ provides a characteristic time scale for the process of crack growth. Although this might be informative of the crack propagation process due to stress, the uniform flaw-free crystalline material assumption might be too simplified given the complex structure of the stones. Moreover, the interlamellar flowed region in between the layers might fill with organic matrix or organic substance, whose viscoelastic properties might not fully represented by spring used in the modal.

A finite difference analysis has also been used to study the propagation of shock waves in kidney stones with spherical and cylindrical geometries. By plotting out the stress and displacement, they found that minimal longitudinal perturbations happened after the shock wave passage from the divergence images of particle velocity (Figure 6.14). However, shear wave is generated at the edges of the stone and an inverted diffracted compression wave is produced. This shear wave is caused by the interaction of the shock

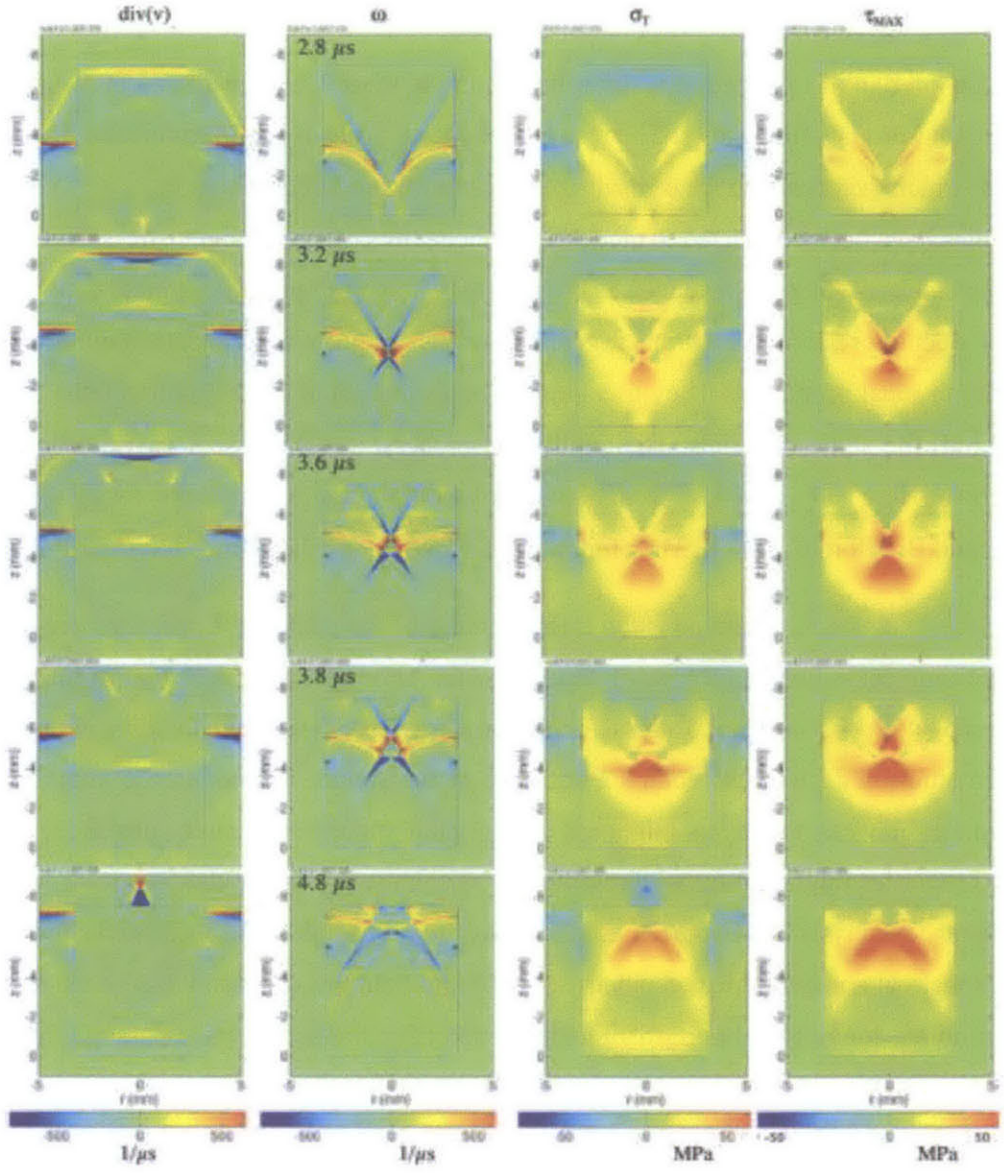

Figure 5.38: (color) Snapshots of the divergence, curl, max tensile stress and maximum shear stress inside a cylindrical stone at 2.6, 3.2, 3.6, 3.8 and 4.8 μs after the SW is incident on the stone. The shock wave is incident from beneath the stone(Cleveland & Sapozhnikov, 2005).

wave in the water passing the outside of the stone, which also intensify the shear stress. They found the peak tensile stress occurs due to an interaction of reflected longitudinal wave with shear wave at 3.8 μs for cylindrical stone. Moreover, the peak tensile strain almost coincides with the peak tensile stress spatially. It was proposed that shear wave interacting with the longitudinal waves caused by passage of pressure waves outside stone results in highest stress and strain.

Moreover, the focal zone diameter also influences all of the peak stresses significantly. The increased shock rise time was found to decrease all the peak stresses (tensile, compressive, and shear) in the stone. However, the generation of high stresses was not strongly related to stone shape. Hence it was proposed that lithotripters with large focal widths and short rise times will result in high peak stresses inside the stone (Cleveland & Sapozhnikov, 2005). Despite the fact that wavelength of acoustic wavelength is usually much larger than the interface of kidney stone, the assumption that stones behave as linear, isotropic, elastic medium might be source of concern since the effective medium methodology might over simplified the process.

It has been largely agreed upon that spalling and cavitation work synergistically to disintegrate kidney stone in ESWL. It is thought that stress wave-induced fracture is important for the initial disintegration of kidney stones while cavitation helps to make finer stone fragments passable (Cleveland & Sapozhnikov, 2005). Since the cracks are usually initiated at junctures of growth increments or structural discontinuity (e.g. border between adjacent spherulites), they are usually vulnerable sites for disintegration.

The high degree of viscoelasticity of kidney stones requires quite a few strong, tissue-injuring ultrasound impulses in ESWL (Sokol et al., 2005). Worse still, the scattering of acoustic wave increase number of shocks from a few hundred to a few thousands to reduce the size of the fragments to below 2 mm clinically (Bierkens et al. 1992), (Zhu, 2002).

Besides the ones mentioned above, others mechanisms have also been proposed to contribute to breaking the stones. Different sounds speed in stones and surrounding fluid can lead to maximum stress at side and back wall of the stone. This can lead to squeezing and splitting along the axial of the stones. Moreover, the geometry of the stone might also contribute to the focus of the reflected wave (from the stone's back wall) by refraction or diffraction.

6.3.2 Mechanism of Tissue damage

Since acoustic impedance mismatch between tissue and water is small, the acoustic or shock wave can pass the water-tissue interface without significant reflection. If the sound wave cannot sense the impedance variation in the tissue, the sound speed in tissue will be almost constant, hence avoiding differential squeezing stress.

However, tissue with size 10 μm to 1 mm could encounter significant stress variation as shock wave passes through them. Moreover, non-uniform shear strain resulted from the short rise time

of shock waves could also result in shearing forces, which could cause damage since tissue structure are sensitive to shear. Besides shear stress, cavitation is another major cause of tissue damage, which is well known to exert significant effects in vitro setting. It was found that blood vessels are more vulnerable to cavitation-induced injury than surrounding tissue. This is because blood pools from vessel rupture provide a fluid filled space for cavitation to happen (Skolarikos, Alivizatos, & de la Rosette, 2006).

There has been biochemical evidence of renal injury right after ESWL treatment. The most common renal trauma is gross haematuria, which usually resolves or heals in a few days. However, transient functional damage of tubular function in children due to shock wave energy has been observed, and small kidneys are more prone to the renal vasoconstriction induced by ESWL. Furthermore, evidence shows that cavitation suppression can reduce lithotripsy damage (Skolarikos et al., 2006).

Moreover, animal modal has also been conducted to study the tissue damage of shock wave. They found a range of damage to renal tubules, such as total tubular destruction, focal cellular fragmentation, necrosis, cell vacuolarization, and membrane blebbing. They also propose cavitation as a major factor for tissue damage due to the tensile stressed induced and free radicals generated. It was found that normal physiology of collecting ducts can be altered as a result of ESWL treatment, which results in increased urinary pH, calcium phosphate supersaturation, and crystallization of calcium phosphate rather than calcium oxalate (Stoller et al., 2007).

6.3.3 Ways to improve the performance

Based on mechanism for stone fragmentation, various ways have been proposed to improve the effectiveness of ESWL. To maximize the impact of cavitation, a dual beam configuration is proposed (Xi, 2000). It was found that stone comminution could be

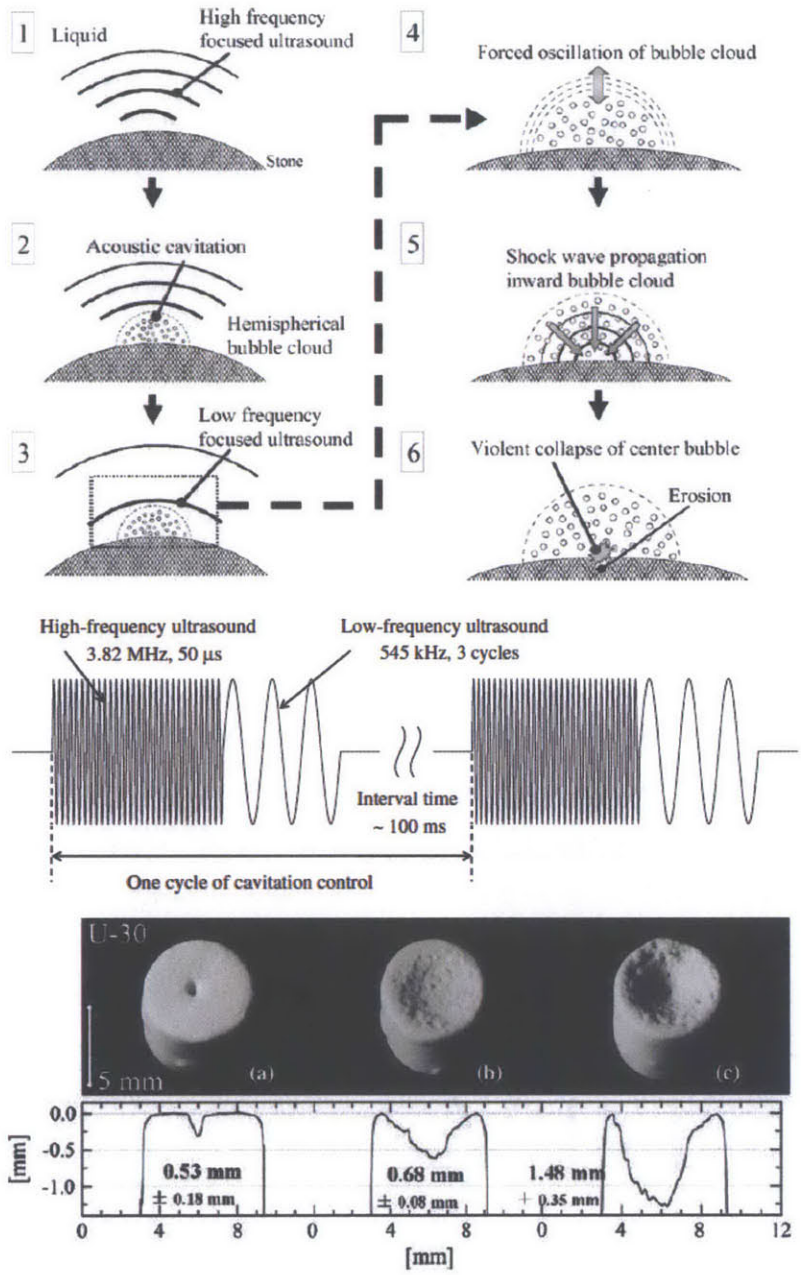

Figure 5.39: Top: Schematic of cloud cavitation control and typical cavitation control waveform. The high-frequency ultrasound is focused at the stone surface to generate cavitation. The bubble cloud is forced to collapse by low frequency focused ultrasound. The interval time between pulses should be long enough to dissolve all of the bubbles into the surrounding liquid

Bottom: Results of model stone crushing tests. Three waves are focused upon the U-30 stones. In figure, case a is high frequency wave (3.82 MHz) alone, b is low-frequency (545 kHz) wave alone and c is the C-C waveform. The PRF of the each ultrasound wave is 25 Hz. Each stone is subjected to 2.0 min ultrasound irradiation

significantly enhanced when the shock wave-bubble interaction occurred during the collapsing phase of the bubbles. Hence, a dual beam setup was proposed using piezoelectric annular array (PEAA) and electrohydraulic sources (EH). Both PEAA and EH sources are powered by two independent high voltage pulse generators, which leads to different shock wave profiles. When the PEAA shock wave arrives near the collapsing phase of the bubbles, the stone fragmentation increase by 60% to 80%, as shown in Figure 6.15. A tandem shock wave setup was proposed by Loske, et al. Using rectangular and spherical stone phantoms, the fragmentation efficiency was significantly enhanced when the second pulse was delayed by 400 μs and 250 μs respectively (Loske, Prieto, Fern ndez, & Cauwelaert, 2002).

As mentioned before, due to scattering and viscoelastic property of the stone, large number of shock waves is needed to reduce the stones size, which also leads to tissue damage around the stones. To minimize the tissue damage, a dual pulse of C-C form has been proposed. Such setup can localize the timing and location of the cavitation collapsing with high reproducibility (Yoshizawa et al., 2009). These studies all contributed to the understanding of maximizing synergies between cavitation and spalling. However, the common concern might be that the modal stones are usually uniformly inorganic, which might be very different from heterogeneous structure natural kidney stones have. On the one hand, the interface might provide vulnerable site for crack initiation; on the other hand, it might also stop/delay the propagation of crack inside the stones.

Moreover, in real clinical situation, the stones might move due to aspiration. Hence feedback loop to compensate for the movement has been proposed. They suggest to adjust for the movement by tracking and following the affected area through stereo ultrasound imaging while simultaneously irradiating the affected area(Norihiro et al. 2008).

6.4 Conclusion

In conclusion, kidney stone have negative impact on people's life, sometimes can be debilitating. Kidney stones can be classified according to the major crystal component. The most crystals are calcium oxalate, phosphate salts and L-cystine, usually mixed with organic substance in various ways. The morphology of inorganic crystals is influenced by several factors, such the ion concentration, macromolecules, pH value of urine etc. Various roles of organic materials have

been proposed and studied, including matrix materials that contribute to the architecture of kidney stones.

The pathway for stone formation includes nucleation, crystal growth, attachment and/or aggregates. The multiple stages involved leads to various risk factors that might contribute to the stone formation. Both intrinsic factors (such genetics, renal cell injury) and extrinsic factors (such as dietary, other ions and urine pH) could influence in stone formation.

To improve and optimize treatment for kidney stones, its properties have been studied using various techniques. The current treatment options include biochemical intervention and physical removal, such as lithotripsy or surgery. Our focus has been on lithotripsy since it is noninvasive compared to surgery and could be further improved. Currently, thousands of shocks needs to be fired to break large stone into passable fragment <2mm. This could be caused by several reasons: a) the shock wave cannot focus accurately on the stone due to respiration movement; b) shock wave's effectiveness is reduced due to scattering by tissue, smaller stone fragment; c) shock wave temporal and spatial profile is not optimized to break the stones. d) Acoustic cavitation mechanism is not fully optimized to break the stone, instead causing damage to tissue, especially to blood vessels.

To address these issues, several methods have been proposed to improve the efficacy of lithotripsy treatment. A dual beam configuration with two beams focuses on same spot to control the size and time of wave's focus has been show to increase the stone fragmentation efficiency. A tandem dual pulse is shown to improve the stone break ability when the second pulse impacts at the collapsing phase of bubbles. Other theoretical and experimental studies have also been conducted to understand acoustic cavitation and stone breaking under shockwave induced stress. However, the multi-disciplinary nature of the cavitation problem and the heterogeneous nature of stones are challenges to be overcame in this active research field. It is also a delicate balance to strike between the inexpensive simulation and expensive clinical trial for better understanding of the process.

In order to improve the impact of cavitation on stone while minimize tissue damage, better model to describe bubble fields interacting with acoustic/shock waves is needed. Theory showed that a large focal zone and fast rise time is desirable to generate maximum stress and strain in stones. However, large focal zone might mean more chances to affect the surrounding tissue and short rise time might mean severe shear stress in tissue. Hence a tradeoff between maximizing effectiveness and minimizing damage need to be achieved. Moreover, it is appreciated that cavitation and

spalling work synergistically to break the stone. More studies are needed to understand and realize the full potential of the synergy from both mechanisms.

6.5 References

Azoury, R., Garti, N., Perlberg, S., & Sarig, S. (1982). May enzyme activity in urine play a role in kidney stone formation? *Urological Research*, *10*(4), 185–189–189.

Cleveland, R. O., & Sapozhnikov, O. A. (2005). Modeling elastic wave propagation in kidney stones with application to shock wave lithotripsy. *The Journal of the Acoustical Society of America*, *118*(4), 2667–76.

Duncan, S. H., Richardson, A. J., Kaul, P., Holmes, R. P., Allison, M. J., & Stewart, C. S. (2002). Oxalobacter formigenes and Its Potential Role in Human Health. *Applied and Environmental Microbiology*, *68*(8), 3841–3847.

Girija, E. (2000). Knoop microhardness studies of urinary calculi and pure calcium oxalate monohydrate crystals. *Materials Chemistry and Physics*, *63*(1), 50–54.

Jing, L., & Jian, L. (2009). Erosion characteristics in ultrasonic cavitation. *Proceedings of the Institution of Mechanical Engineers, Part J: Journal of Engineering Tribology*, *223*(7), 985–991.

JOHRDE, L., & COCKS, F. (1985). Microhardness studies of renal calculi. *Materials Letters*, *3*(3), 111–114.

Khan, S. R. (1995). Calcium oxalate crystal interaction with renal tubular epithelium, mechanism of crystal adhesion and its impact on stone development. *Urological Research*, *23*(2), 71–79.

Khan, Saeed R. (2011). Renal Cellular Dysfunction/Damage and the Formation of Kidney Stones. In N. P. Rao, G. M. Preminger, & J. P. Kavanagh (Eds.), *Urinary Tract Stone Disease* (pp. 61–86). London: Springer London.

Khan, Saeed R., & Hackett, R. L. (1987). Crystal-matrix relationships in experimentally induced urinary calcium oxalate monohydrate crystals, an ultrastructural study. *Calcified Tissue International*, *41*(3), 157–163.

Kodati, V. R., & Tu, A. T. (1990). Raman Spectroscopic Identification of Cystine-Type Kidney Stone. *Applied Spectroscopy*, *44*(5), 837–839.

Kodati, V. R., Tu, A. T., & Turumin, J. L. (1990). Raman Spectroscopic Identification of Uric-Acid-Type Kidney Stone. *Applied Spectroscopy*, *44*(7), 1134–1136.

Kodati, Venkata Ramana Tomasi, Gordon E. Turumin, Jacob L. Tu, A. T. (1991). Raman Spectroscopic Identification of Phosphate-Type Kidney Stones. *Applied Spectroscopy*, *45*(4), 581–583.

Loske, A. M., Prieto, F. E., Fern ndez, F., & Cauwelaert, J. van. (2002). Tandem shock wave cavitation enhancement for extracorporeal lithotripsy. *Physics in Medicine and Biology*, *47*(22), 3945–3957.

Louisnard, O., & González-garcía, J. (2011). Acoustic Cavitation. In H. Feng, G. Barbosa-Canovas, & J. Weiss (Eds.), *Ultrasound Technologies for Food and Bioprocessing* (pp. 13–65). New York, NY: Springer New York.

Millan, A. (2001). Crystal Growth Shape of Whewellite Polymorphs: Influence of Structure Distortions on Crystal Shape. *Crystal Growth & Design*, *1*(3), 245–254.

Murtuza Lokhandwalla and Bradford Sturtevant. (2000). Fracture mechanics model of stone comminution in ESWL and implications for tissue damage. *Physics in Medicine and Biology*.

Neppiras, E. A. (1980). Acoustic cavitation. *Physics Reports*, *61*(3), 159–251.

Norihiro Koizumi, Kohei Ota, D. L., Shin Yoshizawa, Akira Ito, Y. K., Kiyoshi Yoshinaka, Y. M., & Mitsuishi, and M. (2008). Feed-Forward Controller for the Integrated Non-Invasive Ultrasound Diagnosis and Treatment. *Journal of Robotics and Mechatronics*, *20*(1), 89–97.

Rimer, J. D., An, Z., Zhu, Z., Lee, M. H., Goldfarb, D. S., Wesson, J. A., & Ward, M. D. (2010). Crystal growth inhibitors for the prevention of L-cystine kidney stones through molecular design. *Science (New York, N.Y.)*, *330*(6002), 337–41.

Skolarikos, A., Alivizatos, G., & de la Rosette, J. (2006). Extracorporeal shock wave lithotripsy 25 years later: complications and their prevention. *European urology*, *50*(5), 981–90; discussion 990.

Sokol, E., Nigmatulina, E., Maksimova, N., & Chiglintsev, A. (2005). CaC2O4H2O spherulites in human kidney stones: morphology, chemical composition, and growth regime. *European Journal of Mineralogy*, *17*(2), 285–295.

Stoller, M. L., Meng, M. V., Chung, H.-J., & Abrahams, H. M. (2007). *Urinary Stone Disease*. (M. L. Stoller & M. V. Meng, Eds.) (pp. 55–68–68). Totowa, NJ: Humana Press.

Thomas, A. (2009). *Biomimetic Growth and Morphology Control of Calcium Oxalates*. Technischen Universität Dresden.

W. Lauterbornt, J. H. and A. B. (1994). Chaotic behavior in acoustic cavitation. In *Proceedings of IEEE Ultrasonics Symposium ULTSYM-94* (pp. 801–810 vol.2). IEEE.

Walton, R. C., Kavanagh, J. P., & Heywood, B. R. (2003). The density and protein content of calcium oxalate crystals precipitated from human urine: a tool to investigate ultrastructure and the fractional volume occupied by organic matrix. *Journal of Structural Biology*, *143*(1), 14–23.

Wesson, J. A., & Ward, M. D. (2007). Pathological Biomineralization of Kidney Stones. *Elements*, *3*(6), 415–421. doi:10.2113/GSELEMENTS.3.6.415

Xi, X. (2000). Improvement of stone fragmentation during shock-wave lithotripsy using a combined EH/PEAA shock-wave generator—in vitro experiments. *Ultrasound in Medicine & Biology*, *26*(3), 457–467.

Yoshizawa, S., Ikeda, T., Ito, A., Ota, R., Takagi, S., & Matsumoto, Y. (2009). High intensity focused ultrasound lithotripsy with cavitating microbubbles. *Medical & biological engineering & computing*, *47*(8), 851–60.

Zhu, S. (2002). The role of stress waves and cavitation in stone comminution in shock wave lithotripsy. *Ultrasound in Medicine & Biology*, *28*(5), 661–671.

7. Future Work

Our investigation of phononic metamaterial based on fractal geometry (PMFG) shows promising properties, such as broadband response, subwavelength and nonlinear behavior for a wide range of applications. To further our understanding of PMFG, both numerical work and experimental investigation need to be carried out in future. We will discuss future work based on our current work and future outlook.

7.1 Theoretical Work

Although we have conducted extensive study on three PMGF systems, there are still several aspects of their behavior that entail more in-depth study to shine light on this new kind of metamaterial.

7.1.1 Simulation of SAM with moving point source

To understanding the behavior of materials system, there is tension and synergetic interaction between experiments and simulation. When the experimental equipment have constrain, a more sophisticated simulation model is required in order to find the correspondence between experiments and theory. In this case, all our simulation assumes a stationary point source to excite the PMFG system. However, the current SAM has a moving point source moving together with the receiver. Therefore, if we can implement a model in COMSOL with a moving acoustic wave source, we can compare the simulation result and compare them to experiment result to verify the simulation. Furthermore, we can also extract additional information from the simulation result to help us optimize the experimental parameters to gain insight on the behavior of in-plane eigenmodes and out of plane transmission for PMFG.

Once such simulation is implemented, it can have an even wider implication where other type of samples can also be studied. Since simulation is usually a cost effective way of implementing different constrains and varying parameters, it can help design experiments more effectively for specific experiments. For example, the scanning speed, center frequency of the acoustic wave source.

7.1.2 Optimize the parameter for phononic metamaterials based on deterministic fractals

Although the system we studied exhibit broadband response, especially with increased levels of iteration for both fractal scatterer phase or fractal interface between scatterer and matrix phase, the bandgaps has been interrupted or segmented by flat bands isolated in the bandgap. If we can further optimize the design parameters, i.e. t/l of H arm, material impedance contrast, we can obtain a single broad bandgap by merging all the bandgap together. Furthermore, an in-depth study on the symmetry of the eigenmodes might also allow us to identify the polarization specific bandgap, e.g. bandgap for transverse (longitudinal) wave specifically where only longitudinal (transverse wave) can pass the material with that specific frequency(Koh, 2011). We already shown that larger t/l resulted in stronger interaction and localization of eigenmodes, hence it might lead to larger bandgaps with both increased separation and flattened dispersion bands.

To benchmark their performance, we should also survey the status quo of comparable systems and map out their performance space in terms of relevant system parameters. For visualization purpose, usually three parameters can be chosen (where x and y coordinates and color represents each of them respectively) and the performance can be represented in z-axis. However, we can always have built up a database with more than three parameters and give user the flexibility to choose relevant parameters for their applications. Furthermore, once the infrastructure of the database has been setup, we can invite the metamaterials community to contribute by inputting their data to the database system. This does not only setup a systematic way of evaluating performance of such broadband system, but might also help us further improve the guidelines to make it more accessible and applicable for industrial designer and general audience.

7.1.3 Expending the meaning of symmetry

As mentioned in Chapter 4, most of the fractal like geometry in nature, such as terrain, river network, mountain, has a random fractal nature(Mandelbrot, 1977, 1983). Although there is no unified grand theory to explain the cause of such geometry, different theory has been proposed to explain the behavior, with the theme of optimizations with regard to the energy efficiency(Salat et al., 2011) or global access to flow(Bejan 2013, 2000). Since fractal dimensions can be used to characterize natural geometries, we might be able to answer a more fundamental question: can we "hear" the shape of the objects? While the shape is often linked to "sight" (i.e. light), *a phononic signature* might be beneficial for opaque materials, which are not accessible for electromagnetic

wave due to scattering or absorption. Since most of the materials in seismology or exploration geophysics are opaque(Miyashita, 2005; Zosimov et al., 1995), a better understanding for such system would also accelerate the development in seismic science and oil and gas explorations.

If we can establish (or even disapprove) an isomorphic relationship between the phononic spectrum and shape of the fractal geometry, it might help us to better characterize the opaque materials system. Furthermore, in order to apply our general framework to such system from a material scientist point of view, we need to extend the definition of *symmetry*(Greene, 2011). Symmetry itself can have different layers of meaning, from the simplest geometric symmetry to supersymmetry in particle physics(Gross, 1996). While the geometric symmetry we discussed so far are sufficient to describe the crystals and deterministic fractal based PMFG, further extension of symmetry concept are needed to describe the PMFG based random fractal. Given the link between the random matrix, chaos theory and fractal geometry(Edelman et al., 2005), there might be a mathematical tool we can borrow to further generalize our framework to include a large class of natural materials.

To go even one step further, by understanding the behavior of such fractal based system, it might shine light on the cause of fractal geometries and reveal the underlying relation between the second thermodynamics laws and self-organized behavior, hence further our pursue in the boundless journey of understanding nature.

7.2 Experimental Work

Besides the theoretical studies, further experimental studies should also been carried out to verify the extensive simulations we have conducted on the three PMGF systems.

7.2.1Characterization of fractal based material using Scanning Acoustic Microscope

As mentioned in chapter 3, the SAM can be used to measure transmission of acoustic/elastic waves through structures (i.e. extraordinary acoustic transmission)(Christensen, Martin-Moreno, & Garcia-Vidal, 2008; Ghaemi & Thio, 1998; Jean, Strehlow, & Ziebarth, n.d.; Lu et al., 2007; Wang, 2010). For the H tree samples studied, SAM can be used as a detector/receiver to scan the transmitted signals in xy plane by providing a stationary planar or point source. It has been shown that novel electromagnetic wave transmission behavior can be achieved by stacking fishnet like structures. Hence it would be interesting to see whether the experimental transmission behavior

would correspond to the simulation result obtained in Chapter 3. Besides the transmission property, the in-plane (xy plane) eigenmodes of the structure can also be used to investigate the displacement behavior. Since the z position of the transducer can be adjusted, a 3D scan of surface displacement can be obtained to conduct in depth study of surface waves as well as bulk waves.

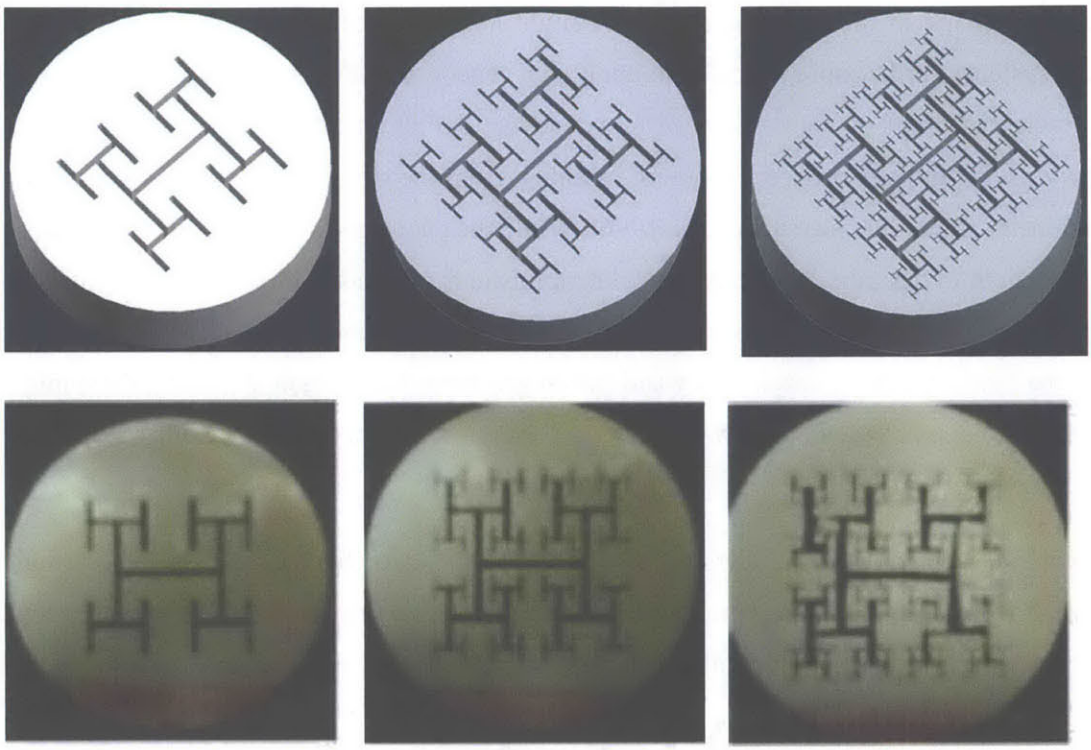

Figure 5.40: 3D drawing of H tree based sample for out of plan transmission measurement with increasing level of iterations from left to right. Fabricated samples using 3D printer (Project 6000) (2nd row)

Supposing the future experimental results correspond well with our numerical studies as well as our hypothesis, other fractal structures can be designed and studied to tailor their behavior for more specific applications. For example, fractal structures for heat management and Nano-phononic engineering, which have profound impact on super computers given the ever increasing need for computation capacity with lower power constrains.

A similar experimental setup can also be used to study samples based on the random fractals studied in Chapter 4. Both out of plane transmission and in plane eigenmodes can be probed using the same setup, the experimental data could further reinforce our understanding this new classes of metamaterials. Furthermore, this setup would allow us to study the "fractal drum" problem (the

fractal bounded membrane) at a much smaller length scale since the relevant wavelengths are reduced to the micrometer scale(Banjai, 2007)(Sapoval et al., 1991).

7.2.2 Characterization of mesoscopic phononic metamaterials

As mentioned in Chapter 5, a mesoscopic scale system can be used to manipulate surface acoustic waves by varying the types of geometries and the strength of the bond between the grating and scatters. It would be interesting to verify the prediction with experimental results to accelerate applications in surface acoustic wave devices. Brillion light scattering (BLS) can be used to investigate the phononic behavior of the metamaterials, since it allows direct measurement of the complete phononic dispersion relation (Gorishnyy, 2005)(Still, 2009)(Kuzmany, 2009). A Brillion light scattering apparatus has been built for our group. For highly transparent samples, the transmission setup is used with angle resolved capability, i.e. the incident angle can be varied to access a larger range (almost 0 to 180 degree) of the q vector. The sample holder has a separate rotation stage to allow adjustment of sample orientation, such that the sample plane is normal to the scattering plane. For opaque samples, the samples are measured in the backscattered setup. Some of my prelimilary experiments indicate that one of the major challenges is to increase singal to noise ratio for thin samples.

Furthermore, to study temperature-dependent acoustic phonon spectra in our sample, we can also setup micro-BLS by adding focusing optics and sample micropositioning to our current BLS. In micro-BLS, laser light is focused onto the sample by microscope objective. For example, a focal spot as small as about 250 nanometers can be realized for the probing light with the wavelength of 514 nanometers. The micro-focus BLS setup has been used to study eigenmodes of submicrometer magnetic squares with Landau domain structure and spin caloritronic and thermal transport phenomena.

Besides the BLS technique, Near-Field Scanning Optical Microscopy (NSOM) is another technique to probe the surface acoustic wave behavior of a fabricated system. NSOM is a versatile technique that allows flexibility for designing the experiments(Bhushan & Othmar Marti, 1985), i.e., NSOM is a type of modified optical scanning acoustic microscope. For an all-optical scanning acoustic microscope, the acoustic wave is usually generated by a pulsed laser with high intensity; while the probing wave is usually a continuous wave with lower intensity(Sharples, 2003).

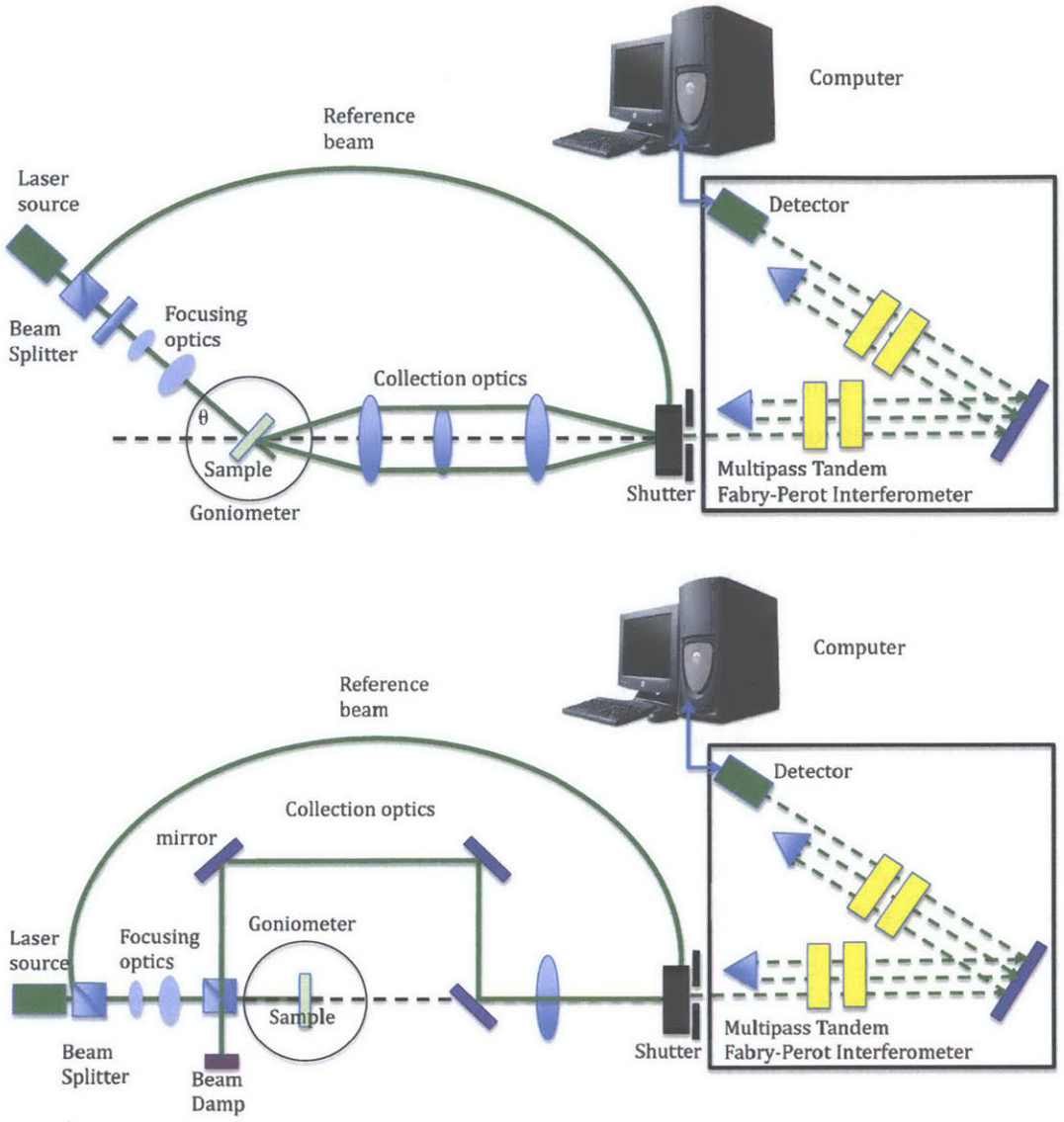

Figure 5.41: Schematics for experimental setup of Brillion light scattering with forward scattering (transmission) mode (top) and backscattering (reflection) geometry (bottom).

The optical energy transferring to the sample as thermal energy will cause a thermoelastic response or ablation, depending on the intensity of the laser as well as the absorptivity of the materials. To minimize the damage to the sample, the surface acoustic wave can also generated by patterning a piezoelectric materials on one side of the feature. Various optical detection techniques for surface acoustic waves have been proposed and used: knife-edge techniques, interferometry techniques,

holographic techniques, diffraction techniques, photo-emf detection etc(Dhar 2000; D. Hurley, Morkoç, 1987a, 1987b; J.P. Wolfe; S. Tamura 1995; Tachizaki, 2006; Vines 1995)(Profunser, 2006). Among them, knife-edge techniques and interferometric techniques are preferred for probing a general broadband wave disturbance. Some techniques provide spatial-amplitude or time-angle scanning, which elucidates the regions of energy localization and features of the band structure. Recently, Dieter et. al. used Sagnac interferometer"(Tachizaki et al., 2006) that can map surface phonon in real time in two dimensions up to 1GHz using a 1D phononic crystal. The direct measure of the amplitude and phase of the field over space and time would infer the full 2D band structure and Bloch Harmonics. Given the current setup of the MIT NSOM, a modified knife-edge technique could be employed.

7.2.3 Where art meets science: Jackson Pollock's painting in 3D

Jackson Pollock received tremendous acclaim as a leading "Abstract Expressionism" artist. The complexity of his painting does not only fuel the imagination of artist and its viewers, but also attracted attention from the scientific community. Taylor et al. found that the pattern of Jackson Pollock's painting is fractal using box counting methods(Taylor et al., 1999). Colors were filtered using the physical model based on red-green-blue primaries and a perceptual model on L*a*b color space. They found that the fractal dimension of Jackson's painting has evolved from a lower D value (e.g. D = 1.1) to a higher D = 1.7 from his classical period.

On the other hand, eye-tracking techniques have been used to study gaze behavior in artworks with fractal patterns having different D values. Surprisingly, the eye movement of the search pattern traces exhibit a value of around D = 1.5 regardless of the D values of the fractal pattern observed. The link between the fractal pattern's D value and visual esthetic preference is also intriguing. It

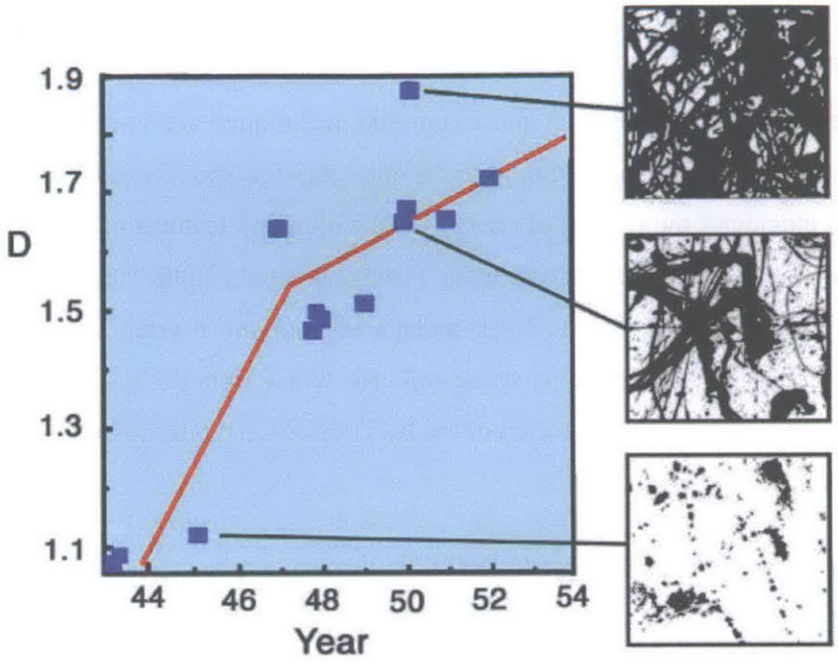

Figure 5.42: The fractal dimension D of Pollock paintings plotted against the year in which they were painted (1943–1953). The right hand images show computer constructions of three of Pollock's paintings. Source:(Taylor et al., 2011)

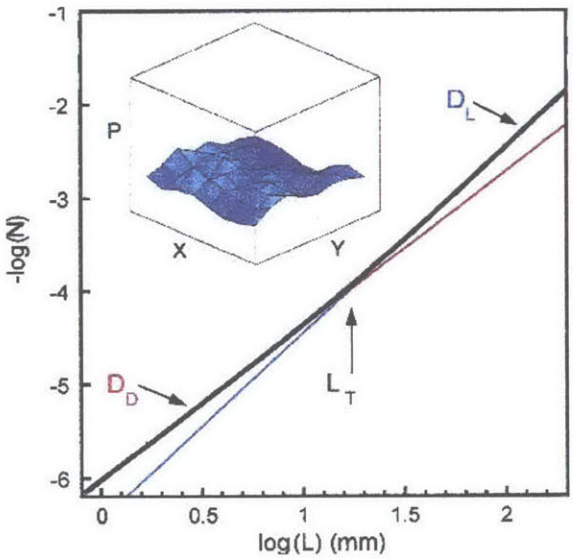

Figure 5.43: The plot of log N (L) versus log L for the aluminum trajectories of the painting 'Blue Poles'. The black line is the data (composed of 1523 data points within the first decade). The red and blue lines indicate the two gradients. Note that the graph remains linear beyond the range shown. The upper inset shows a plot of pattern density P versus the X and Y positions across the painting 'Number 14' (0.57m by 0.78m). P is defined as the percentage of the canvas surface area filled by the pattern within a square of side length L= 0.05m. The plotted ranges are $0 < P < 100\%$ and $0< X, Y < 0.43$m. Source:(Taylor et al., 2011)

was found that highest average visual preference is observed for fractal dimension in 1.3-1.5 range for simple fractals (e.g. natural fractal, mathematical fractals and manmade fractals) with little variance based on gender and cultural background. It is proposed that we prefer patterns with D = 1.3-1.5 because nature's fractals cluster around D = 1.3 and the exposure to them establishes familiarity. It is conjectured that Jackson Pollock's high D value paintings esthetically challenging to engaging the viewer's eyes in constant search through the dense structure.

Furthermore, another study has shown that Jackson's painting showed different D values originated from two different processes, chaotic dripping of painting and his lateral movement across the canvas. The analysis reveals two distinct D values over the ranges 1mm<L<5cm and 5cm<L<2.5m, as shown in Figure 7.4. Hence fractal paintings show scale dependent behavior due to different mechanisms in their creation (Taylor et al., 2011).

Despite the significant progress in understanding the mathematical nature of art work and our aesthetic perceptions, there is still great potential to be further explored in mimicking the fractal geometry to design novel materials for advance applications.

7.3 Future Applications

Given its unique properties, PMFG can be implemented for several applications depending on their frequency (wavelength), as shown in Figure 7.5. As mentioned in last section, Jackson Pollock's painting exhibit fractal dimension, if we can extract the 2D pattern and add in the third dimension parameter by either argument the thickness of the paint) or convert the color into numerical height value, we might be able to create a Jackson Pollock's sculpture. Therefore, not only the visually impaired people can enjoy Jackson Pollock's painting, we might also enjoy it from a different "sense". Furthermore, given its broadband response and well-known damping properties(Jusserand et al., 2012; Russ et al., 2002; Felix, et al.), we can also use PMFG to design and fabricate shielding devices for various applications. One interesting applications related to Chapter 6 would be to design biocompatible shielding "membrane" to cover the tissue surrounding the kidney stone so it can minimize the impact of shockwave. Obviously, this structure can also be used for blast resist vest for soldiers and equipment in battlefields.

Given its long range correlation and sparse spatial distribution, we can design new generation of stealth smart skin (i.e. sensor network) to be embedded in structural components, e.g. aircraft shaft,

bridges, buildings, to provide real-time structural data to centralized or distributed headquarter for monitoring. Hence it might be able to prevent catastrophic failure of structural and better understanding the mechanical behavior of system. Furthermore, a fractal gene has also been proposed to explain to encode the fractal geometry reoccurring at different length scale in human body. If we can utilize the scalable features of fractal geometry, we might be able to implement such smart skin to various structural components using similar governing rule. Hence we achieve the most efficient way of information processing using scale invariant algorithm. Besides, the vascular systems in human are within the reach of every five cells while only occupy a small portion of human body(Guidolin et al., 2011; Seuront, 2010). Therefore it is a very efficient geometry for distribution and circulation, where a constructal law has been proposed to describe

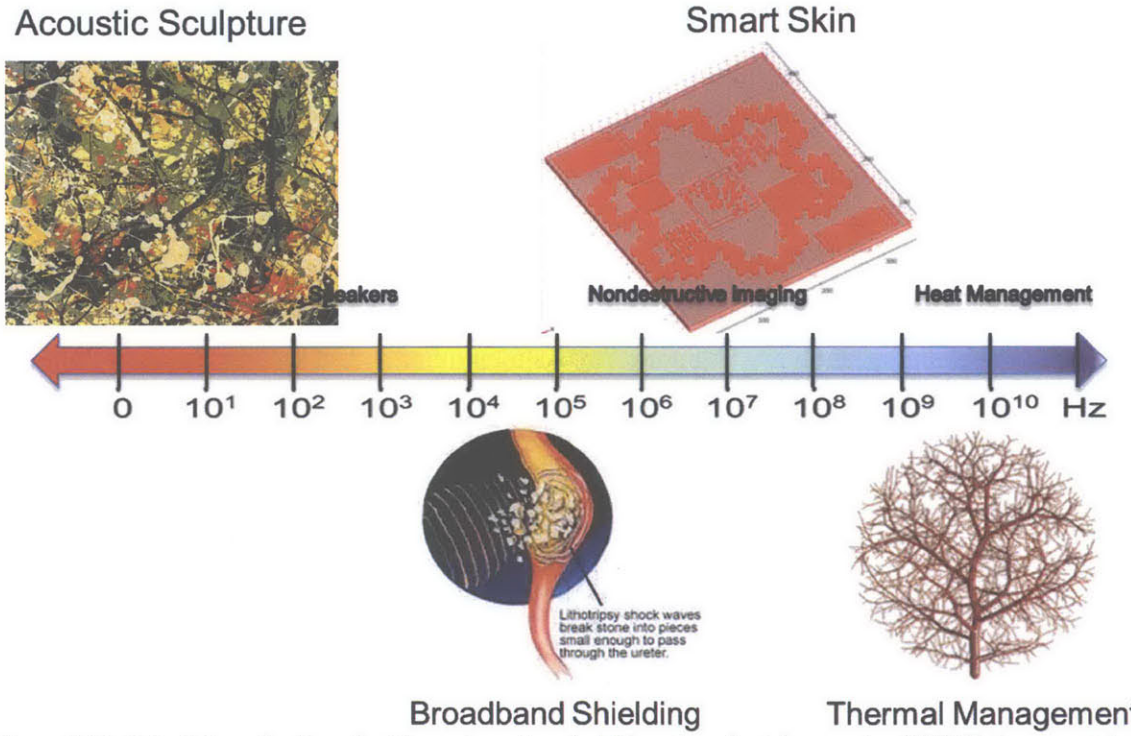

Figure 5.44: Potential applications for Phononic metamaterial based on fractal geometry (PMFG) Images retrieved from Google for acoustic sculpture, broadband shielding and thermal management. Image courtesy to Google: (Acoustic Sculpture) http://www.ibiblio.org/wm/paint/auth/pollock/ (broadband shielding) http://health.ucsd.edu/specialties/surgery/urology/areas-expertise/kidney-stone-center/treatments/Pages/shock-wave-lithotripsy.aspx (thermal management) http://news.sciencemag.org/sciencenow/1997/04/04-01.html

it as a geometry "provides easier access to the imposed current that flow through it" in order to persist in time(Bejan, 2000). Since the tree-like geometry has been proposed to achieving flow

access between one point and a volume, it might be in interesting geometry to be implemented for thermal management where the heat need to be dissipated a point to surrounding volume.

7.4 Reference

Banjai, L. (2007). Eigenfrequencies of fractal drums. *Journal of Computational and Applied Mathematics*, *198*(1), 1–18. doi:10.1016/j.cam.2005.11.015

Bejan, A. (2000). *Shape and Structure, from Engineering to Nature* (p. 324). Cambridge University Press.

Bejan, A., & Zane, J. P. (2013). *Design in Nature: How the Constructal Law Governs Evolution in Biology, Physics, Technology, and Social Organizations* (p. 296). Knopf Doubleday Publishing Group.

Bhushan, B., & Othmar Marti. (1985). Scanning Probe Microscopy - Principle of Operation, Instrumentation and Probes. In B. Bhushan (Ed.), *Handbook of Nanotechnologies* (pp. 591–635). 2004 Springer - Verlag.

Christensen, J., Martin-Moreno, L., & Garcia-Vidal, F. (2008). Theory of Resonant Acoustic Transmission through Subwavelength Apertures. *Physical Review Letters*, *101*(1), 2–5.

Dhar, L., & Rogers, J. A. (2000). High Frequency One-Dimensional Phononic Crystal Characterized with a Picosecond Transient Grating Photoacoustic technique. *Applied Physics Letters*, *77*(9), 1402. Edelman, A., & Rao, N. R. (2005). Random matrix theory. *Acta Numerica*, *14*, 233–297.

Ghaemi, H. F., & Thio, T. (1998). Extraordinary Optical Transmission Through Sub-wavelength Hole Arrays. *Nature*.

Gorishnyy, T., Ullal, C., Maldovan, M., Fytas, G., & Thomas, E. (2005). Hypersonic Phononic Crystals. *Physical Review Letters*, *94*(11), 1–4.

Greene, : Brian. (2011). *The Hidden Reality: Parallel Universes and the Deep Laws of the Cosmos* (p. 384). Alfred A. Knopf.

Gross, D. J. (1996). The Role of Symmetry in Fundamental Physics. *Proceedings of the National Academy of Sciences*, *93*(25), 14256–14259.

Guidolin D, Crivellato E, R. D. (2011). The "Self-similarity Logic" Applied to the Development of the Vascular System. *Development Biology*, *351*(1), 156–62.

Hurley, D., Tamura, S., Wolfe, J., & Morkoç, H. (1987). Imaging of Acoustic Phonon Stop Bands in Superlattices. *Physical Review Letters*, *58*(23), 2446–2449.

J.P. Wolfe;Shin-Ichiro Tamura; R.E Vines. (1995). Surface Acoustic Wave Focusing and Induced Rayleigh Waves. *Physical Review Letters*, *74*(14), 2729–2732.

Jean, R., Strehlow, E., & Ziebarth, J. (n.d.). Extraordinary Transmission Through Small Apertures.

Jusserand, B., Fainstein, A., Ferreira, R., Majrab, S., & Lemaitre, A. (2012). Dispersion and Damping of Multiple Quantum-well Polaritons from Resonant Brillouin Scattering by Folded Acoustic Modes. *Physical Review B*, *85*(4), 041302.

Koh, C. Y. (Henry). (2011). *Generalized Phononic Networks: Of Length Scales, Symmetry Breaking and (Non) locality "Controlling Complexity through Simplicity."* Massachusetts Institute of Technology.

Kuzmany, H. (2009). 9 Light Scattering Spectroscopy. In H. Kuzmany (Ed.), *Solid-State Spectroscopy,* (pp. 183–215). Springer Berlin / Heidelberg.

Lu, M.-H., Liu, X.-K., Feng, L., Li, J., Huang, C.-P., Chen, Y.-F.,Ming, N.-B. (2007). Extraordinary Acoustic Transmission through a 1D Grating with Very Narrow Apertures. *Physical Review Letters*, *99*(17), 1–4.

Mandelbrot, B. B. (1977). *Fractals : Form, Chance, and Dimension* (p. 365). San Francisco : W. H. Freeman, c1977.

Mandelbrot, B. B. (1983). *The Fractal Geometry of Nature* (p. 468). San Francisco : W.H. Freeman, c1983.
Miyashita, T. (2005). Sonic Crystals and Sonic Wave-Guides. *Z. Kristallogr*, *16*(5), R47–R63.
Profunser, D., Wright, O., & Matsuda, O. (2006). Imaging Ripples on Phononic Crystals Reveals Acoustic Band Structure and Bloch Harmonics. *Physical Review Letters*, *97*(5), 1–4.
Russ, S., & Sapoval, B. (2002). Increased Damping of Irregular Resonators. *Physical Review E*, *65*(3), 036614.
S. Felix, M. Asch, M. F. and B. S. (n.d.). *Localization and Increased Damping in Irregular Acoustic Cavities S. F′ elix* (pp. 1–30).
Salat, S., & Bourdic, L. (2011). Power Laws for Energy Efficient and Resilient Cities. *Procedia Engineering*, *21*, 1193–1198.
Sapoval, B., Gobron, T., & Margolina, A. (1991). Vibrations of Fractal Drums. *Physical Review Letters*, *67*(21), 2974–2977.
Seuront, L. (2010). Self-Similar Fractals. In *Fractals and Multifractals in Ecology and Aquatic Science* (pp. 25–98). CRC press Taylor & Francis Group.
Sharples, S. D. (2003). *All-Optical Scanning Acoustic Microscope. Scanning*. The University of Nottingham.
Still, T. (2009). *High Frequency Acoustics in Colloid-based Meso- and Nanostructures by Dpontaneous Brillouin Light Scattering*. Johannes Gutenberg–Universit¨ at Mainz.
Tachizaki, T., Muroya, T., Matsuda, O., Sugawara, Y., Hurley, D. H., & Wright, O. B. (2006). Scanning Ultrafast Sagnac Interferometry for Imaging Two-Dimensional Surface Wave Propagation. *Review of Scientific Instruments*, *77*(4), 043713.
Taylor, R. P., Micolich, A. P., & Jonas, D. (1999). Fractal Analysis of Pollock's Drip Paintings, *399*(6735), 422.
Taylor, R. P., Spehar, B., Van Donkelaar, P., & Hagerhall, C. M. (2011). Perceptual and Physiological Responses to Jackson Pollock's Fractals. *Frontiers in Human Neuroscience*, *5*, 60.
Thomas, A. (2009). *Biomimetic Growth and Morphology Control of Calcium Oxalates*. Technischen Universität Dresden.
Vines, R. E., Hauser, M. R., & Wolfe, J. P. (1995). Imaging of Surface Acoustic Waves. *Zeitschrift for Physik B Condensed Matter*, *98*(2), 255–271.
Wang, X. (2010). Acoustical Mechanism for the Extraordinary Sound Transmission through Subwavelength Apertures. *APPLIED PHYSICS LETTERS*, *96*, 134104.
Zosimov V, V, Lyamshev, L. M. (1995). Fractals in Wave Processes. *Physics-*, *38*(4), 347–385.

8. Conclusion

Facing the growing challenges of energy, environment, security and disease treatment, the demand for novel materials remains strong. Meanwhile, the advancement of science and technology has expanded the horizon for material research, e.g. increasing computation power and higher resolution imaging instruments. Facing the growing challenges and opportunities, material scientists and engineers continues to innovate through both gradual and breakthrough discoveries. While the material centric approach has resulted in development of new materials for advanced applications, we introduced a geometric-centric approach as a complementary point of view for further innovation in this ever expanding and growing field.

The potential of the geometric approach can be illustrated in metamaterials, artificial materials designed to exhibit novel properties. Since metamaterials enable us to design "atoms" or "molecules" and their arrangement relatively with greater freedom (i.e. not limited by the chemical bond or ionic bond in classical material systems), the geometric feature of building blocks and their arrangement can be greatly exploited to develop new materials. To fully leverage on this perspective, we aim to develop a design framework that would enable engineers to develop a physical intuition on design of material systems for specific applications. Using the symmetry group concept and representation theory, Koh's design framework highlighted the underlying physical principles that govern the wave dispersion behavior in metamaterials, especially phononic metamaterials (C. Y. Koh, 2011). To expand the framework on more complex geometries, a more generalized framework can be developed leveraging on the new theories developed in theoretical physics.

Inspired by the ubiquitous fractals-like geometry in natures, *scale transformation* (i.e. dilation or contraction) is included in the framework since a fractal geometry shows structures at all scales (but of course discrete and finite in the physical world). To describe the roughness of fractal system/process, scale relativity gives up the differentiability of geometries and processes and adds scale transformation (e.g. resolution variables) in addition to other conventional transformations, such as translation, rotation etc. Although this framework employed fractal as a more abstract concept, some of the concepts and tools can be helpful in understanding fractal material system given the analogy between medium-scatterer and space (or space-time)-object. Based on this

foundation, we developed a generalized framework that could expand the horizon for designer materials, e.g. based on complex geometries.

To capture both scale dependent and scale independent behavior of the materials observed, the relationship$X(s,\varepsilon) = x(s)\{1 + \zeta_x(s)\left(\frac{\lambda}{\varepsilon}\right)^{\tau}\}$, which relates the properties of the material with a fractal-like geometry undergoing a fractal-nonfatal transition, is employed. Therefore, for materials that still retain translational symmetry yet with fractal-motifs (in their unit cell), Koh's framework would still be applicable when the wavelength is comparable to the unit cell.

We aim to further our understanding of phononic metamaterials and our framework using prefractals from both exact-self similar fractal and random fractal samples. For exact-self similar fractals, we choose the H tree based prefractals and Hilbert Curve prefractals bounded system. The H tree is chosen since it allows the scatterer phase to be highly connected (i.e. you can travel between any two point in the scatterer phase without ever leaving the scatter phase within the unit cell), hence one phase exhibit fractal like geometry. On the other hand, the Hilbert Curve, a spacing filling curve (i.e. filling the 2D plane after an infinite number of iterations), defines a fractal like interface between the scatterer and matrix phase.

For H tree based metamaterials, we studied both in–plane eigenmodes and out-of-plane transmission behavior for 2D and 2D plate with finite thickness systems. For 2D system, several factors have been studied systematically on how they would impact the behavior of the systems. It was found that the length/thickness ratio, level of iteration and materials properties can all be used to control the wave propagation behavior in the system through different mechanism. By increasing the level of iteration, multiple bandgaps can be achieved across different length scale. For 2D fractal resonator with finite thickness, the lowest eigenmodes exhibit subwavelength frequencies from full wave simulation, which is ~ 1/75 of the frequency comparable to the Euclidean dimension of the plate. A simple equivalent electric circuit is developed to describe the Helmholtz resonator tree, which in turn can be used to explain in-plane eigenmodes of the 2D plate with finite thickness slab with H tree prefractal. The resonance frequency obtained are consistent with the full wave simulation. 2D fractal resonators with finite thickness have been fabricated using high resolution 3D printer, where the scaffolding and other parameters have to be optimized to achieve the precision and robust mechanical properties of the final sample. To study their

mechanical behavior, SAM has also been used for imaging the surface and subsurface of sample (in reflection mode) as well as the transmission characteristic of such samples (in transmission mode). The reflection images revealed topographic features informative of the surface finish of the sample.

For Hilbert Curve prefractal bounded sample, their in-plane eigenmodes have been studied for 2D system. Again multiple spectral band gaps have been observed for the samples studied. It was found that higher impedance contrast between scatterers and matrix are preferred for band opening since high strain region are more localized in softer phase, hence flatten the dispersion curves. Furthermore, the bandgap size increases and decrease with increasing level of iteration (as well as filling ratio of scatterer phase), which might indicate an optimal fill fraction. Furthermore, the eigenmodes are less confined with increasing level of iterations although they still obey the symmetry of the relevant k vector. Besides the level of iterations, arrangement of the building blocks also influence the behavior, although the symmetries of the unit cell is retained, their variation in local dynamics also changed the dispersion behavior system. The bandgap size of modified system can be larger or smaller than the pure prefractal system depending on the level of iteration. Furthermore, it was found the bandgap size of the fractal interface is larger than that of a fractal phase (although the interface of H tree prefractal also exhibit certain fractal like properties).

While the prefractals of exact self-similar fractals retain certain degrees of familiarity (i.e. symmetry elements) of a traditional material, they add in the new element of *scale variance*. To move into a space where symmetry element exhibit a more statistical nature, e.g. fractional Brownian Surface., we studied a binary system based on random fractals generated from projection of a fractional Brownian surface. We choose the Hurst constant as a key factor to define the behavior of random fractal based system with moderate impedance contrast since it defines the geometric correlation relations among scatterers in the binary phase. Despite the loss of information on detailed distribution of displacement eigenmodes due to the statistical nature, it was found that the Hurst constant can be used to characterize the dispersion behavior of metamaterials based on random fractals. Furthermore, the filling fraction also affects the behavior

of the system through both effective mechanical properties at long wavelength and at the scale of the largest cluster size of scatterers.

Furthermore, it was also found that the dispersion behavior varies little with different grid number/cell (i.e. relative scale) for system with small impedance contrast. This is desirable for studying pseudo-random fractal systems with reduced computation time and resource consumption. Since the arrangement of the local cells also affects the geometric properties of the supercell, we found that a given the super cells with a homogenous H value or mixed H value have different behavior.

By taking a systematic approach to the study of fractal based metamaterials, the factors that could influence the dispersion behavior have been identified and discussed. This opens up a new field for further investigation in light of both better understanding of nature, but also developing novel materials for ever more demanding applications. It can also serve as a model system for simulating microcrack propagation for wave propagating medium, if the scatters are assumed as initiation site of microcrack.

Besides understanding the fundamental physics of wave propagation in metamaterials, we are also interested in applying them into device design and integration. One potential application area is surface acoustic wave device, which has grown substantially for a wide range of applications.

We employed a 2D simplified system to probe the behavior of a mesoscopic system consisting of a 1D continuous grating and circular scatterers. The system shine light on how the 1D grating would interact with circular scatterers in different ways through different arrangement of the 1D gratings and scatterers.

Moving into 3D full wave simulation, we first studied a system with a 1D grating and spherical scatterers. We found several parameters that enable us to manipulate dispersion behavior of the surface wave or pseudo-surface wave, e.g. the period of 1D grating, the size of spherical scatterers, arrangement of the scatterers and the materials properties of the scatterers. For applications where wide spectral gap is desirable, spherical scatters should be in contact with 1D grating to perturb their behavior along the longer axis of 1D grating (i.e. direction with continuous 1D grating phase).

For a system with 1D grating and cylindrical scatterers, artificial mechanical bonding between scatters and/or 1D grating are introduced and varied using soft rubber connecting blocks. Similarly, without the bound, cylindrical scatterers and 1D grating are almost independent with each other. However, by bonding the scatters with 1D grating, localized eigenmodes and flattened dispersion behavior can be achieved. The bonding through a cap block on top of both scatters and 1D gratings are shown to be particularly effective. Furthermore, introducing defects in the 1D grating can eliminate the extended modes along the XM direction. The diversity of bonding between scatterers and/or 1D grating would enable it to generate multiple spectral gaps or fewer large gaps for surface waves.

Besides the full wave simulations, experimental samples with 1D grating and spherical scatterers (i.e. nanoparticles) have also been fabricated using a vertical deposition technique, where the density and fill ratio can be controlled by the deposition parameters.

Another interesting application is understanding the shock wave induced fracture of kidney stone as a non-invasive treatment of kidney stones. Kidney stones can have debilitating effects in people's life, causing much pain and discomfort. Kidney stones have a wide range of chemical composition and morphology due to their dynamic growth environment in the human body. The multiple stages in stone formation allows several risk factors in stone formation, both internal and external factors.

Depending on the size and location of the stone, different options can be used to treat kidney stone. Extracorporeal lithotripsy is non-invasive compared to surgery by launching shockwave through the abdomen or the back to breakdown the stone. There are two main mechanism involved in breaking up the stone: 1) spalling: stressed-induced expansion of stone 2) cavitation: microject cause induced pitting on the surface, hence initiate crack/defects sites. Studies suggest that cavitation and spalling work synergistically to break the stone. More studies are needed to understand and realize the full potential of the synergy from both mechanisms. This treatment can be further improved to increase the effectiveness of stone breaking and minimizing the tissue damage. Several methods have been proposed to improve the efficacy of lithotripsy treatment: 1) A dual beam configuration with two beams focused on same spot to control the size and time of

wave's focus 2) tandem dual pulse where the second pulse impacts at the collapsing phase of bubbles(Loske, Prieto, Fern ndez, & Cauwelaert, 2002) (Yoshizawa et al., 2009).

Despite the advancement, the multi-disciplinary nature of the cavitation problem and the heterogeneous nature of kidney stones are challenges to be overcame in this active research field. For the multibubble cavitation field, the distribution of bubbles and the emission of sound waves showed fractal characteristics. Given that we are more interested in the collective (or statistical) properties of the impact of cavitation field, a fractal model might be appropriate to capture the spatial attributes and the collective wave produced to better understand its interaction with the kidney stone.

Therefore, the general design framework put forth in this thesis provides an intuitive yet insightful way for materials scientists to design new materials for advanced application, such as acoustic sculpture, broadband shielding devices, smart skin and fractal thermal devices. By introducing the complex geometry into metamaterial, it does not only expands the repertoire for novel materials system; but also provides us a way to understand nature better since fractal geometry is so ubiquitous. Compared to natural systems, most manmade systems adopt a regular geometry in Euclidean space, e.g. continuous smooth lines, surfaces, volume (although strictly speaking all volume consuming object are 3 dimensional) since their deterministic nature makes them easy to standardize, mass produce and be stable. They serve their functions well most of the time since they are used in relatively well controlled environments for limited time (e.g. life time of manmade object). However, systems in nature usually adopt a less regular geometry (i.e. fractal) since they have nonlinear and deterministic interaction within a dynamic system.

As material scientists, we are constantly humbled by the material systems in nature and trying to learn from them through mimicking. On the other hand, we are constantly trying to exceed nature by designing metamaterials that behave differently than natural materials. With understanding of materials based on fractal geometries, we can fully utilize their potential in applications requiring adaptive and dynamic properties. On the hand, our mimicking effort should not lose sight of the importance of simplifying and abstracting from nature, which might enable superior performance.

Appendix A: Theoretical Studies on Local Resonance-like systems in more details

To verify the general framework, we carried out studies on several metamaterials system with different symmetry and other local properties. As mentioned in the introduction, avoided crossing is the general mechanism to form spectral gap and is applicable to both Bragg scattering and local resonance. Since the avoided crossing will only happens to eigenmodes with the same symmetry (i.e. irreducible representation for the relevant wave vector), material system with different symmetry will be studied. Moreover, since the material choice will perturb the degree of non-locality, the material properties, e.g. impedance, will be varied to tune the degree of impedance contrast. It will be demonstrated that by tuning the material parameters, the "weakness" of the non-locality becomes clear.

A.1How does the symmetry of the lattice affect the spectral gap opening?

As mentioned before, the irreps of the wave vector determines of the eigenmode of the polarization field. Avoided crossing only happens between/among eigenmodes with the same symmetry (irreducible representation with respect to the relevant wave vectors). To prove the first point, track the polarization field along the boundary $\Gamma \rightarrow M \rightarrow K \rightarrow \Gamma$ for a three phases system (with scatter, rubber and matrix, adopted from the sonic crystal used by Liu et al). The band diagrams from three different lattice types demonstrate that the symmetry of the unit cell irreps would determine which two bands would encounter avoided crossing, as shown in Figure A.1.

Γ point as shown in Figure 3.2 bottom:

For p6mm, the symmetry is C6, m and E. the symmetry at the center of the scatter is C2, mx, y and E, since the two mirror plane is equivalent, the two mode are degenerate. For p4mm, the symmetry is C4, mx, y and E, since the two mirror plane is equivalent, the two mode are degenerate. p2mm at the Γ point lower the symmetry (only C2, m and E) and the perturbation lifted the degeneracy as shown in the dispersion curve and correspond eigenmodes.

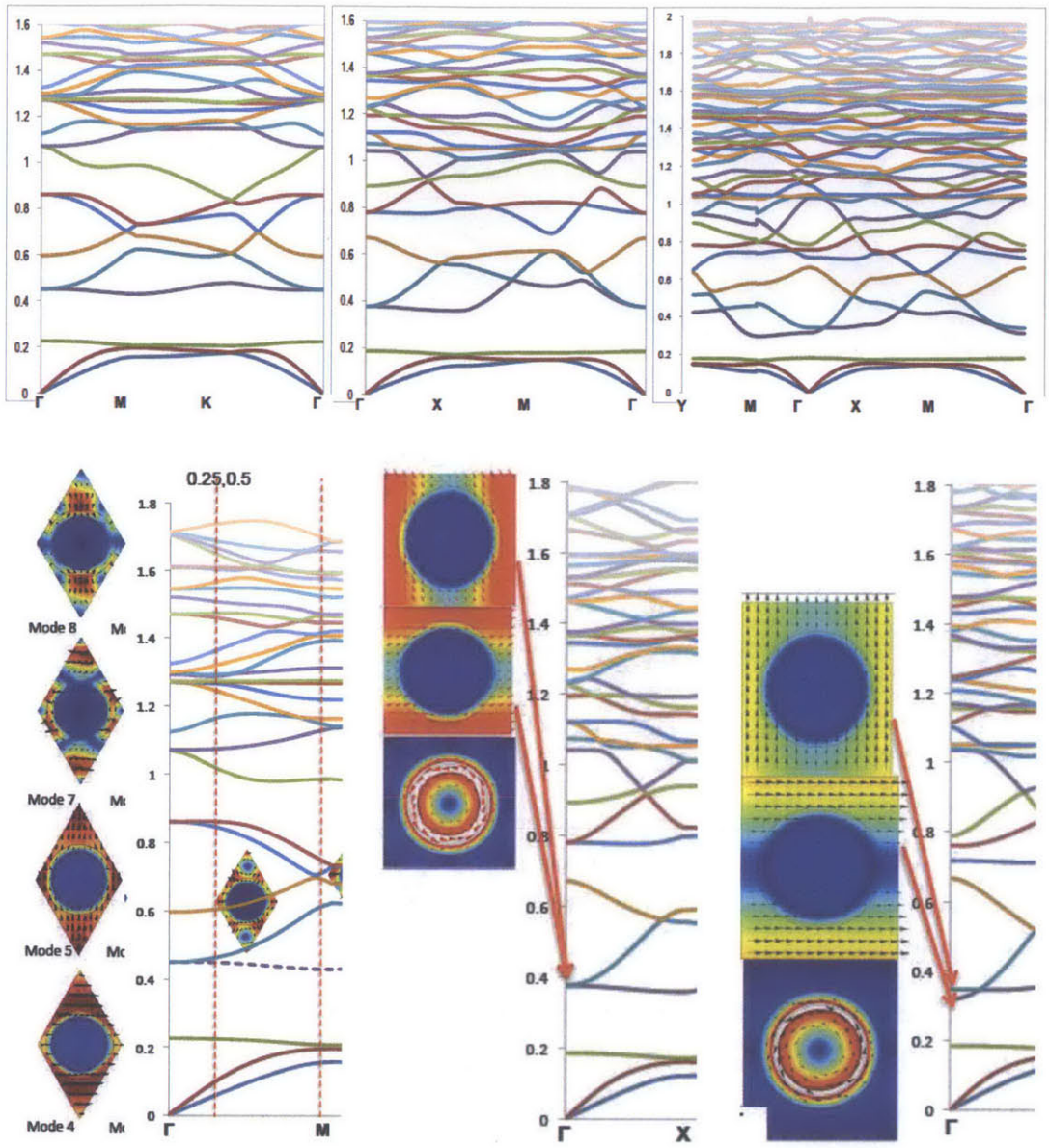

Figure A.1: Top: dispersion curves calculated for three structures with unit cell possessing different symmetry. From left to right, the symmetry at Γ point is hex (p6mm isotropic in 2D), p4mm and p2mm. Bottom, the corresponding eigenmodes at Γ point for the three system with different symmetry.

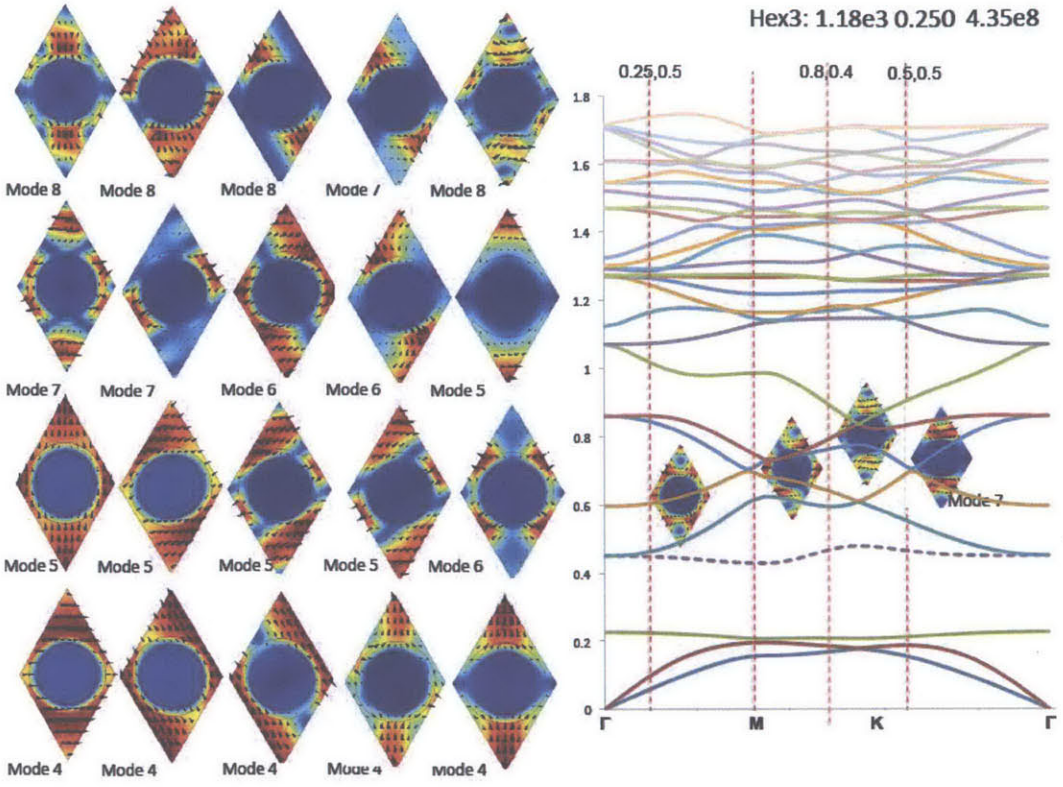

Figure A.2: Displacement plot for selected eigenmodes and the dispersion curves calculated from COMSOL for the selected three phase system. Γ point has C3v symmetry. Along ΓM direction, the symmetry is entity E; along MK it has the mirror plane; along KΓ, it has mirror plan (mx). The eigenmodes on the left corresponds to Γ and four dashed lines on the diagram on the right.

For the eigenmodes along the BZ boundary, as shown in Figure A2, the symmetry of the displacement filed for certain eigenmode is determined by the irreps of the relevant wave vector. To further investigate the necessary condition for avoided crossing to happen, the unit cell with p4mm and p2mm are chosen. For both p4mm and p2mm, along the ΓX direction, the k vector has mx, E symmetry; hence the eigenmode would conform to the

Table A.1 Materials constant used in the simulation

	Scatter	Rubber	Matrix
Young's Modulus Pa	400e8	4.35e8	43.5e8
Poisson Ratio	0.25	0.25	0.25
Density kg/m3	11600	1180	1180

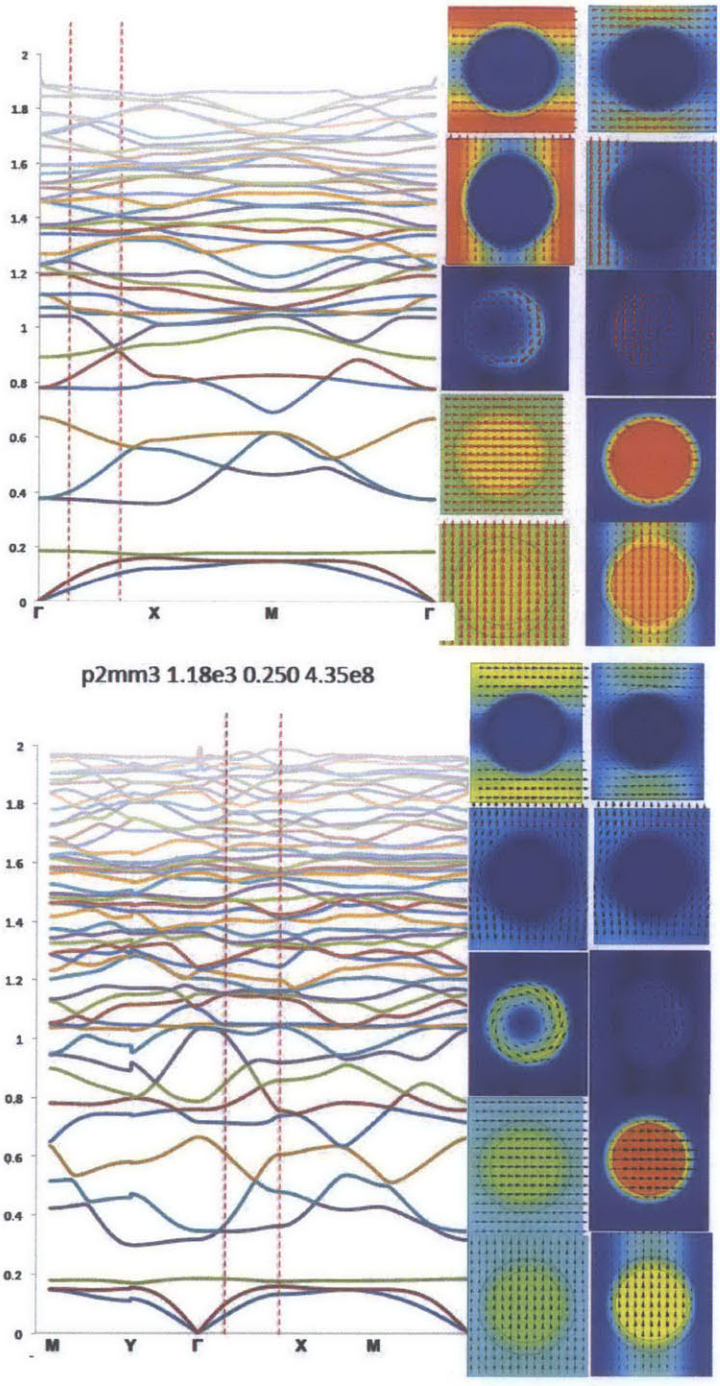

Figure A.3: Displacement plot for selected eigenmodes and the dispersion curve calculated using the COMSOL for p4mm (left) and p2mm (right) system

symmetry of the wave vector along this direction. Avoid crossings occur between modes 2 and 5 as well as between modes 1 and 4 since they are symmetric and antisymmetric with respect to mx plane.

Even if we reduce the elastic constant to 0.435e8 Pa holding the other parameters constant, the band diagram starts to resemble the local resonance system. However, if the eigenmode is investigated further, the general principles still apply to this system: the symmetry of the polarization still conforms to the irreps of the relevant wave vector. Moreover, avoided crossing happens only between the bands with the same symmetry regardless of the position where the spectral gaps happens, i.e. Bragg like or subwavelength resonant like. Therefore, the position and width of spectral gaps are not always determined by the bands that bound the gap. Furthermore, the fact that the avoided crossing happens not at Γ point for the second case indicates the non-locality of the mechanism. Therefore, the system studied further verified the hypothesis proposed by Koh. While the symmetry of the structure bound the possibilities of interaction through global invariants, the local properties, i.e. group velocity, strength of interaction can be manipulated with other parameters.

A.2 Fine tune the materials properties to manipulate the dispersion curve

As mentioned before, the local phononic behavior can be tuned by several parameters, e.g. geometry and material constants. Therefore, the material property for the rubber interlayer is varied (as listed in Table A2) to study its effect on local dispersion behavior of the system.

For the p4mm case, as we tune rubber from constants of Lead scatter to matrix and then to soft rubber, the system evolves from crystal case to local resonant like system, as shown in Figure A1 and Figure A4. As the rubber become softer, the eigenmodes are more localized. For example, by inspecting modes 4, 5 from the top left to the right

Table A2: The materials constants used in the simulation

	Rubber 1	Rubber2	Rubber3	Rubber4	Rubber 5
Young's Modulus Pa	400e8	43.5e8	13.5e8	4.35e8	0.435e8
Poisson Ratio	0.25	0.25	0.25	0.25	0.25
Density kg/m3	11600	1180	1180	1180	1180

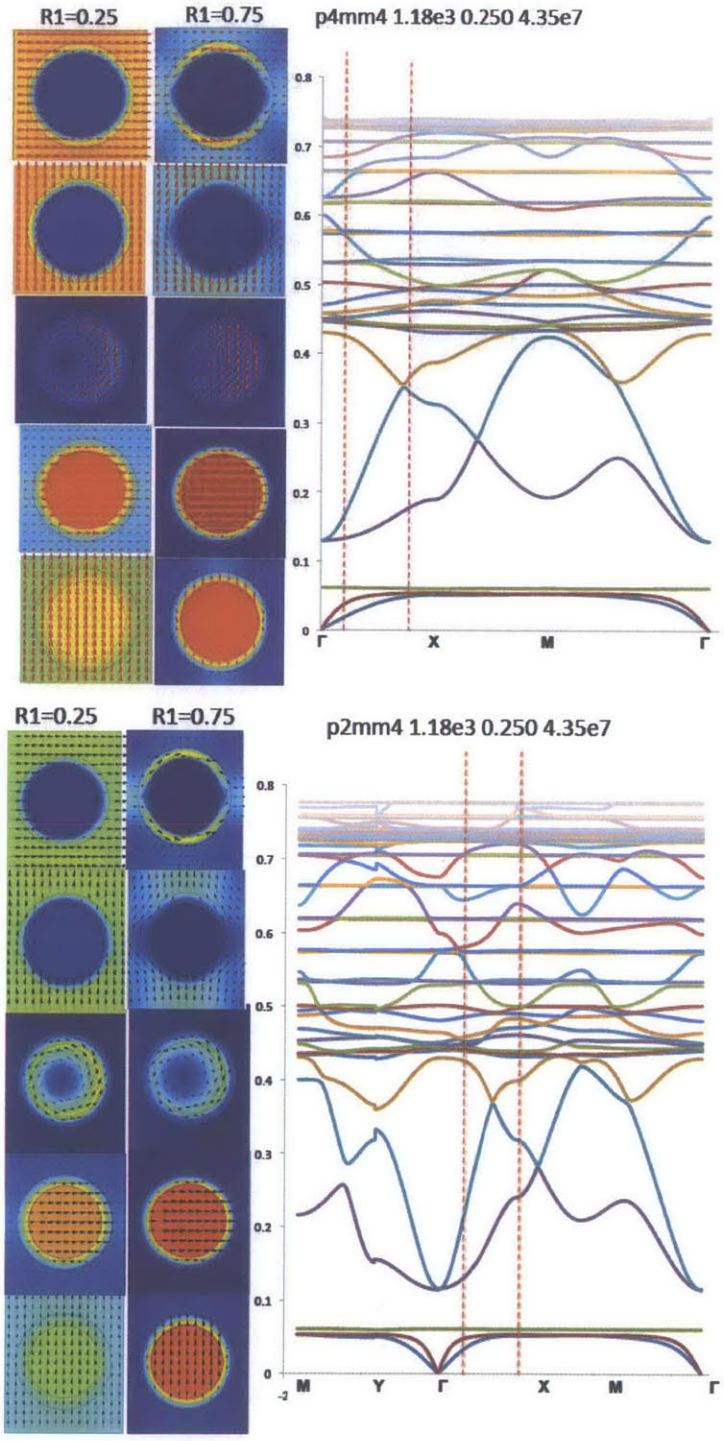

Figure A4: Displacement plots for selected eigenmodes and the dispersion curve for p4mm (left) and p2mm (right) system with case for rubber with modulus 4.35e8 Pa.

bottom dispersion curve, as shown in Figure A4. The frequency where the avoided crossing happens also decrease with decreasing elastic constant of the rubber. It is also noted that the modes at the long wavelength limit is relatively less affected, since the wavelength can hardly probe/resolve the change in rubber properties. Comparing Figure A4 and Figure A3, indicates that avoided crossing between mode 2 and 5 happen closer at smaller k value as the elastic constant of the rubber is decreased keeping other materials properties constant. Since the avoided crossing for mode 1 and 4 occurs near the BZ edge, the k value are less affected by the varying of the material properties.

Similar trends are found for the p2mm case as demonstrated Figures A3 and A4. Similar trends are also observed in the p6mm system. Therefore, by varying the material property, the dispersion curve can evolve dramatically, i.e. from crystal-like to local resonance-like. Note that the general framework remains valid throughout all the case studied so far.

The first one is a binary system with the "rubber phase" has the same material constant as the scatter, as shown in Figure A5. The binary systems exhibit properties similar to phononic crystal with a spectral gap occurring at a length scale comparable to the lattice period, i.e. Bragg-like scattering at the BZ boundary.

If the scatter take the property of rubber, i.e. Es = 0.0435e8 Pa. The dispersion curves demonstrate local resonance-like behavior, as shown in Figure A6. The softer scatter introduces a resonance state at subwavelength scale, when its symmetry is the same as the extended state in the matrix, avoided crossing will happen and generate the subwavelength spectral gap.

A.3 Symmetry of the scatter motif

Besides the material property, the symmetry of the scattering motif also affects the dispersion behavior, as shown in figure A7. When the scatter varies from single circle to paired triangle to connected paired triangle, the dispersion curve varied accordingly. When changing from circular to triangular pair, the 2nd spectral gap shifted upwards. Comparing the middle and the right dispersion curves, the connecting channel between two triangular pair lowered the symmetry of the scatter motif from p6mm to p2mm at the

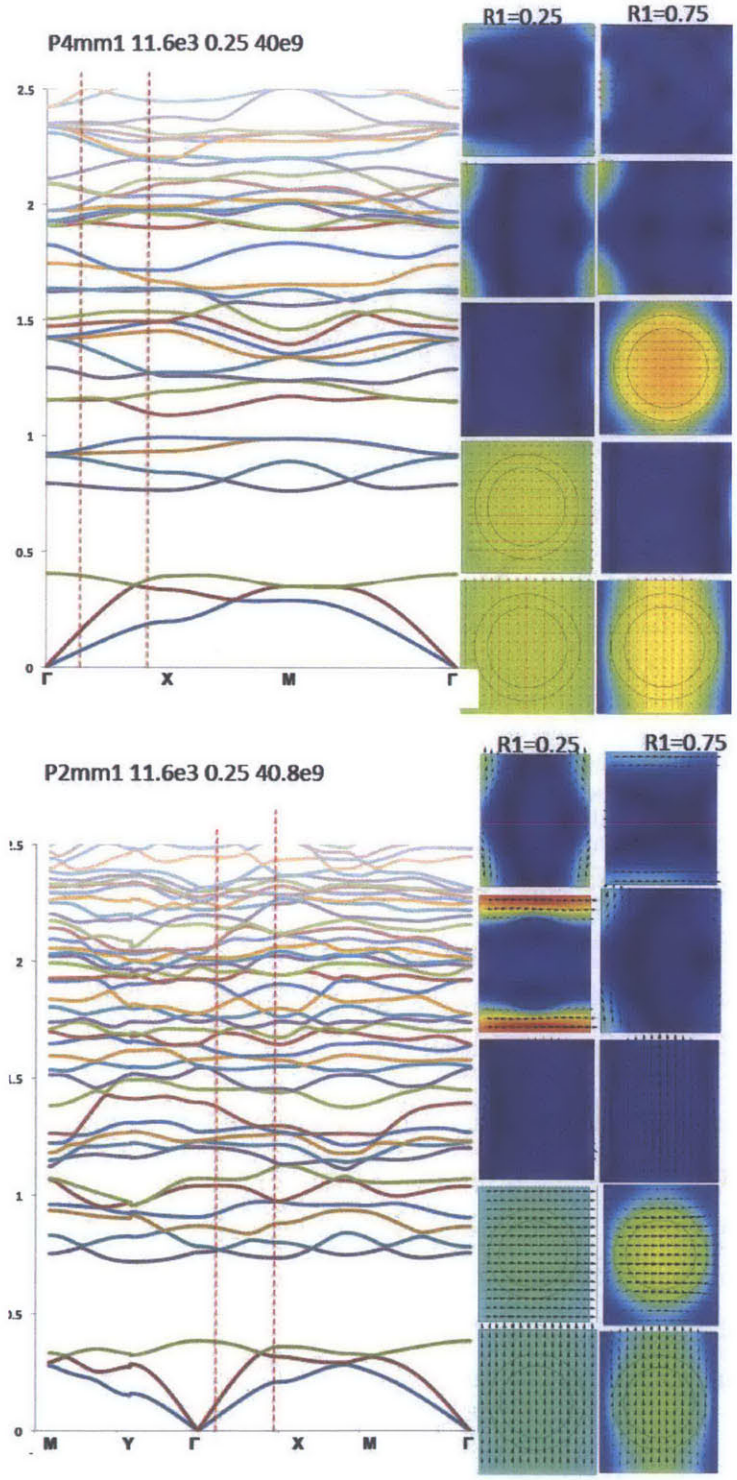

Figure A5: Displacement plots for selected eigenmodes and the dispersion curve calculated for both p4mm (left) and p2mm (right) system with case for rubber with E = 400e8 Pa

center of the unit cell. It induces an avoided crossing between band 2 and 3 along ΓM direction (mode 3 shown in the band diagram).

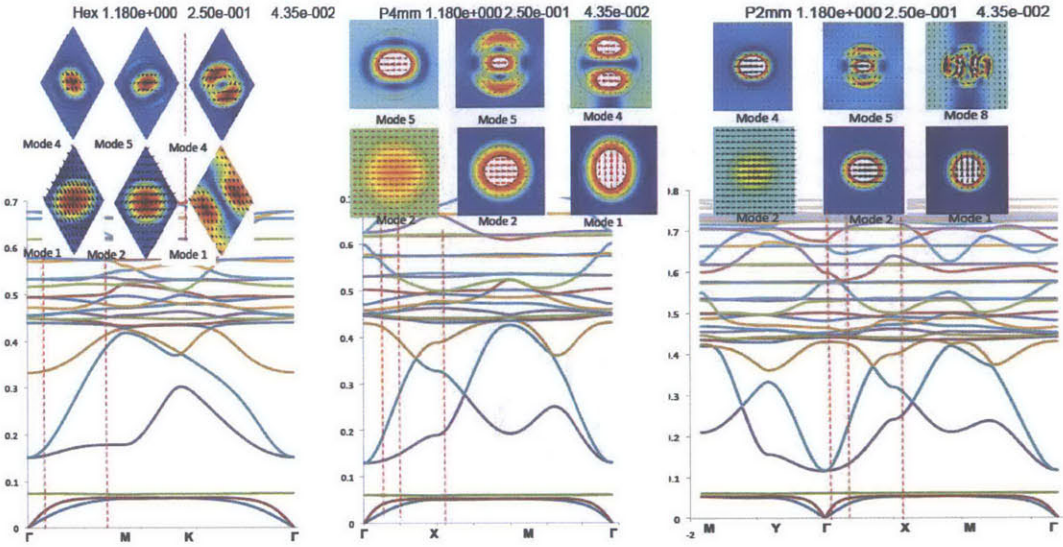

Figure A6: Displacement plots for selected eigenmodes and the dispersion curve calculated from the COMSOL the for hex (left), p4mm (middle) and p2mm (right) system with case for soft scatter

The symmetry of the scatter also affects the polarization field, i.e. mode 3 at $r_1 = 1$ on the middle and right dispersion curve. At M point, mode 1 and 7, mode 3 and 8, and mode 4 and 11 are interacting with each other since they share the same symmetry with respect to the mirror plane. At K point, mode 1 and 7, mode 2 and 10, and mode 4 and 8 are interacting with each other since they share the same symmetry with respect to the mirror plane.

Relatively little effect occurs across at the long wavelength limit ($k \rightarrow 0$) along ΓK. As the wave vector goes closer to the BZ boundary, the connecting channel slightly modify the polarization direction in the middle section where channel sits, (see mode 2). The presence of the cut also reduces the group velocity of eigenmode and the displacement field concentrate along the channel with a polarization perpendicular to the channel, i.e. mode 7. It also affect the polarization field, i.e. mode 11 at $r_1 = 1$ on the middle and right dispersion curve.

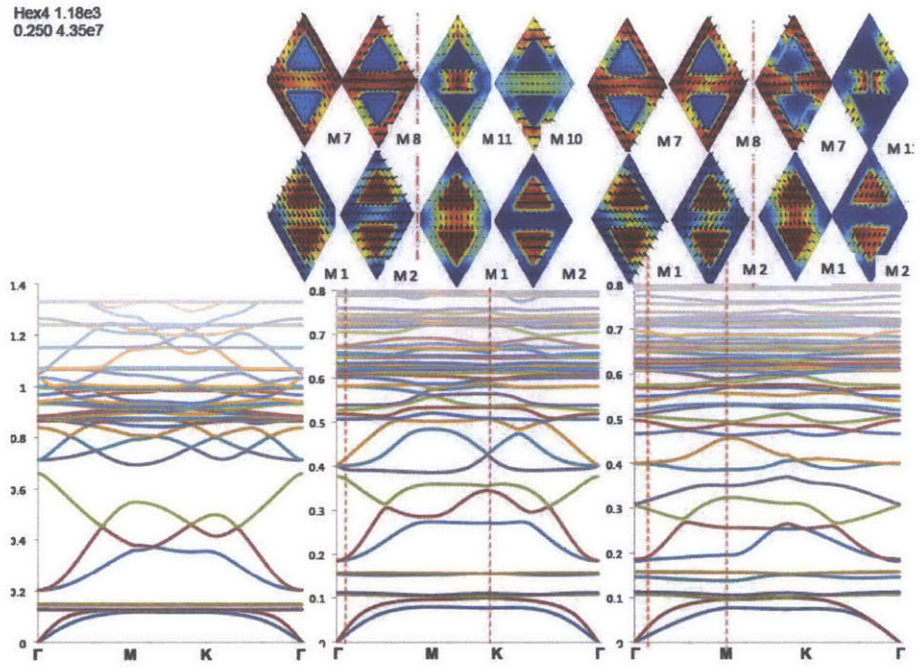

Figure A7: The dispersion curves from left to right are for the circular scatter pair, triangular scatter pair and the triangular scatter pairs with the middle connected respectively. The rubber are relatively soft with Er = 4.35e7 Pa.

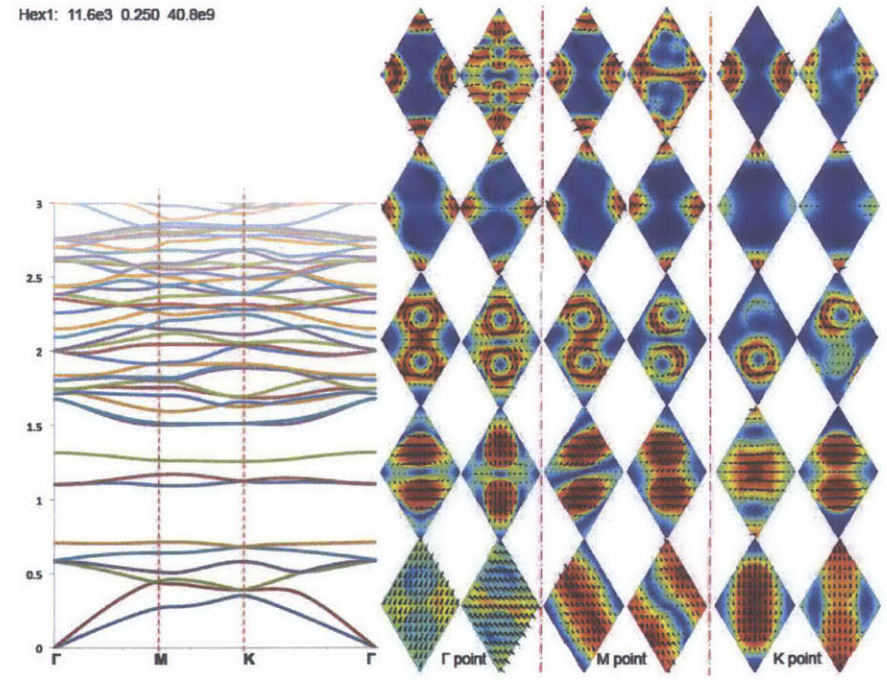

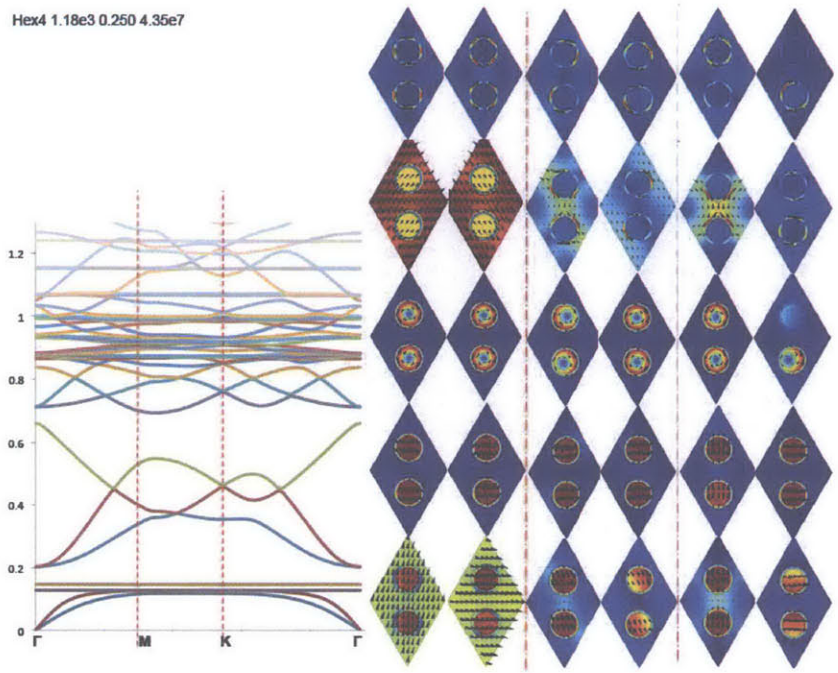

Figure A8: The dispersion curves and displacement field of the eigenmodes from mode 1 to mode 10 at the F, M and K point in the unit cell, with the mode 1 at bottom left and mode 10 at top right corner. Top for rubber 1 and bottom for rubber 4

Appendix B: Scale Relativity

As the physical approaches moving from descriptive modeling to predictive theory founded on basic principles, we evolved from Ptolemy's model to Newton's theory to Einstein's general relativity and quantum theory. Scale relativity aims to pave the way to unifying the quantum and relativity concept on the basis of first principles. In the framework of scale relativity, quantum field become manifestation of geometry of space-time, which now included a scale parameter.

Since the scale relativity naturally follows the general relativity, we will review the important concepts in relativity theory.

Starting from the foundation of theoretical physics-principle of least action and conservation laws, basic equations can be constructed relating energy, momentum and angular momentum. The action is defined as the integral of Lagrange function $S = \int_{t_1}^{t_2} \mathcal{L}(x, v, t)\, dt$, which exists given a generalized coordinates x_i and generalized velocity $v_i = dx_i/dt$. The *principle of least action* states that the motion of the system between x (t_1) and x (t_2) is such that it optimizes the value of this action to a constant, minimum value (i.e.$\delta S = 0$). The principle of least *action* become the geodesic principle in relativity theory, where geodesic is generalized notion of "straight line" to "curved space".

From the principle of least action, a generalized form of motion equation can be derived

$$\frac{d}{dt}\left(\frac{\partial \mathcal{L}}{\partial v}\right) - \frac{\partial \mathcal{L}}{\partial x} = 0$$

Which is the known as Euler-Lagrange equation, which become Newton's fundamental equation of dynamics if we write $\mathcal{L}(x, v, t) = \sum \frac{1}{2} m v^2 - \phi(x)$.

Linked to this principle, the existence of physical quantities and the conservation laws can be proved (Noether's theorem). Due to the symmetries of the underlying basic variables that describe the system, their characters are conserved. Hence, energy is conserved due to the uniformity of time; momentum is conserved due to the uniformity of space.

Given the tools to describe laws of physics using mathematical equation, the *principle of relativity* states that the laws of physics should apply for any state of reference system (origin, orientation, motion, scale etc.). To implement this principle, three related principles have to be developed.

First, the principle of covariance requires "equations of physics keep their form under change of the state of reference system". Secondly, principle of equivalence states "a gravitational field is locally equivalent to an acceleration field". In the framework of scale relativity, quantum behavior is locally equivalent to nondifferential and fractal motion. Third, geodesic principle defines free trajectories as the geodesics of space-time. This principle means the fundamental equation of dynamics is completely determined by the geometry of space-time. Hence, the action dS can be identified with the fundamental metric invariant ds - the proper time - as $dS = -mcds$. To go even further, instead of thinking geodesic as trajectories of particles, they can be viewed as pure geometrical path, from which the various properties of wave-particle emerge.

By giving up the differentiability of space-time, scale relativity redefine derivatives in order to not give up the partial differential equation. For system where nondifferentiability can be neglected, the standard differentiable physics would be sufficient. However, when nondifferentiability cannot be ignored with small and large length scale, as well as mesoscopic complex system. Scale relativity suggests that all scales are connected together via scale differential equations and various physical quantities now also dependent on the space-time scale/resolution. Therefore, fundamental equation of physics will also depends on scale, constrained by the requirement to be covariant under scale transformation of resolutions, where resolution con be considered as the measuring sticks in simplest case (although its nature is tensorial).

To construct the scale relativity theory, the laws of scale at a given point and instant, was first found constrained by principle of scale relativity. Then the laws of motion in standard space-time are found, including the effects of nondifferentiability and fractality in the differentiation. After that, the law of coupling between scale and motion are developed.

From a continuous and nondifferentiable manifold with scale divergence in the limit resolution $\varepsilon \rightarrow 0$, fractal can be derived as secondary property. As mentioned in chapter 1, the length of the fractal curve can be estimated using $\mathcal{L}(s,\varepsilon) = s(\frac{\lambda}{\varepsilon})^{\tau}$, where s is a renormalized curvilinear

coordinate along the fractal curve and the exponent is defined as $\tau = D_F - D_T$, where D_F and D_T are the fractional and topological dimension respectively.

To carry out for the scale transformation, an infinitesimal dilation operator is derived as $\widetilde{D} = \varepsilon \frac{\partial}{\partial ln\varepsilon}$, which shows lnε as the natural variable for the resolution. The simplest equation for $\mathcal{L}$ under scale transformation is achieved when it is a function of $\mathcal{L}$ only, that is $\frac{\partial \mathcal{L}(s,\varepsilon)}{\partial ln\varepsilon} = \beta(\mathcal{L})$, Defining β($\mathcal{L}$) =a+b$\mathcal{L}$+…, we have

$\mathcal{L}(s,\varepsilon) = \mathcal{L}_0(s)\{1 + \zeta(s)\left(\frac{\lambda}{\varepsilon}\right)^{\tau}\}$, Therefore the projection of $\mathcal{L}$ on any direction can be written as $X(s,\varepsilon) = x(s)\{1 + \zeta_x(s)\left(\frac{\lambda}{\varepsilon}\right)^{\tau}\}$. The differential of the projection can be written as $dX = dx + d\xi$, where dx is a classical differential element and $d\xi \propto \mathrm{dx}^{1/D_F}$. It is obvious that the dx corresponds to the differentiable element while $d\xi$ captures the

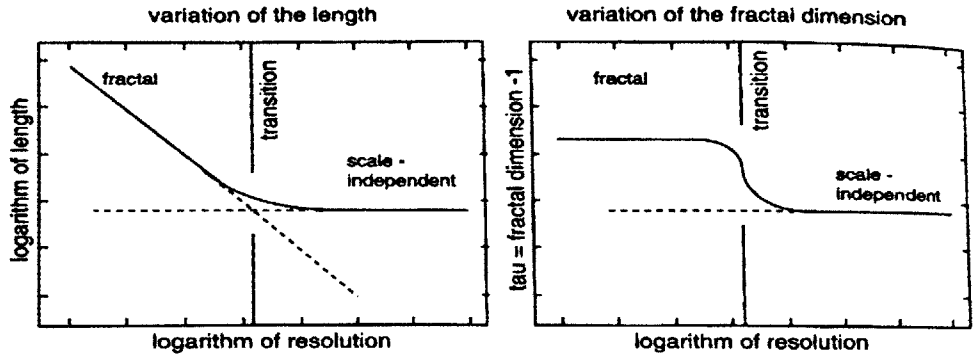

Figure 2.2 Fractal length and fractal dimension for self-similar fractals. The two figures show the scale dependence of a length of a fractal and the fractal dimension in the case of inertial scale laws, which are solutions of simple first order scale differential equations. It transforms from scale dependent at small scale to scale-invariant large scale.

nondifferentiability. It is easy to see that when (i) $\varepsilon \ll \lambda$, $\mathcal{L}(s,\varepsilon) \approx \mathcal{L}_0(s)\{\zeta(s)\left(\frac{\lambda}{\varepsilon}\right)^{\tau}\}$, $\mathcal{L}$ follows a power law observed fractal curve, when (ii)$\varepsilon \gg \lambda$ $\mathcal{L}(s,\varepsilon) \approx \mathcal{L}_0(s)$ is given by a scale invariant, as shown in the plot. This transition can be clearly seen in Figure 2.2.

The scale symmetry is spontaneous broken by the very existence of standard (e.g. translation, rotation). The symmetry breaking is achieved by domination of one law over the other when

moving to extreme scale. And this transition is identified with the Einstein-De Broglie scale. This would reveal that quantum classical transition as being fractal-nonfractal transition in scale space.

To further generalize the relationship, we can include even higher order term by writing $\frac{\partial \mathcal{L}(s,\varepsilon)}{\partial ln\varepsilon} = a + b\mathcal{L} + c\mathcal{L}^2$ ..., which would leads to two transitions to scale independence (both large and small scales) as shown below.

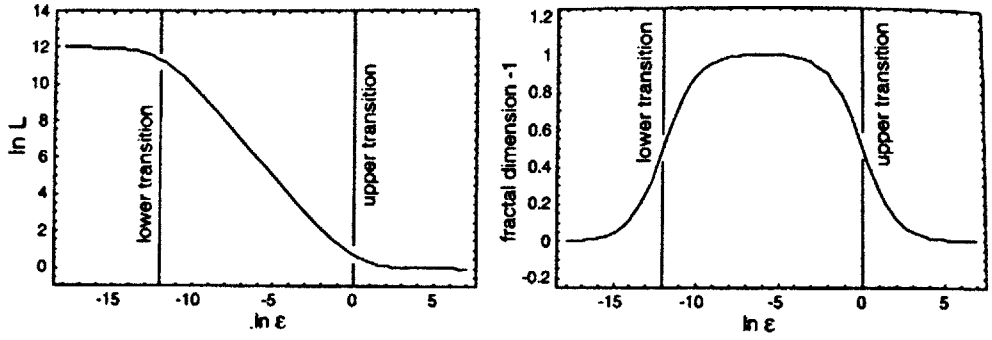

Figure 2.3 Fractal length and fractal dimension for self-similar fractals: two transitions. The two figures show the scale dependence of a length of a fractal and the fractal dimension in the case of inertial scale laws, which are solutions of simple first order scale differential equations. It transforms from scale dependent at small scale to scale-invariant large scale.

One the hand, by introducing a complex value of b (or fractal dimension) such that

$\frac{\partial \mathcal{L}(s,\varepsilon)}{\partial ln\varepsilon} - v\mathcal{L} = \chi$, set $v' = v + \eta$, the solution is $\mathcal{L}(\varepsilon) = a\varepsilon^v[1 + b\varepsilon^\eta]$, by defining $\eta = i\omega$

$\mathcal{L}(\varepsilon) = a\varepsilon^v[1 + bcos(\omega ln\varepsilon)]$,

To make it more realistic by adding in term $\mathcal{L}_0$, we have

$$\mathcal{L}(\varepsilon) = \mathcal{L}_0\{1 + \left(\frac{\lambda}{\varepsilon}\right)^\tau [1 + bcos(\omega ln\varepsilon)]\}.$$

We will obtain a log-periodic behavior, which can be viewed as a stationary wave in scale-space.

With the scale transformation ($\varepsilon \rightarrow \varepsilon'$) defined, we need to find the form of physical equations under such transformations. To obey the principle of covariance for fractal length $\mathcal{L}$ under scale transformation, we need to find four functions $a(\mathbb{V}), b(\mathbb{V}), c(\mathbb{V})$ *and* $d(\mathbb{V})$ such that

$$ln\frac{\mathcal{L}'}{\mathcal{L}_0} = a(\mathbb{V})ln\frac{\mathcal{L}}{\mathcal{L}_0} + b(\mathbb{V})\tau,$$

$$\tau' = c(\mathbb{V})ln\frac{\mathcal{L}}{\mathcal{L}_0} + d(\mathbb{V})\tau,$$

where $\tau' and\ \tau$ are scale time or "djinn". The general solution to this problem is the Lorentz group. To solve this problem, we impose the physical constrain: composed transformation keep the same form as the initial ones; reflection invariance where the choice of x axis orientation should not alter the relation. Hence, the Lorentz scale transformation can be derived as $\mathbb{W} = \frac{\mathbb{U}+\mathbb{V}}{1+\mathbb{U}\times\mathbb{V}/\mathbb{C}^2}$ in terms of scale,

where μ, v, ϱ are scale ratios, $\mathbb{W} = ln\mu, \mathbb{U} = lnv, \mathbb{V} = ln\varrho$, $\mathbb{C} = ln\mathbb{K}$ is a fundamental dimensionless scale constant that related to the universal length. Define $\Lambda = \mathbb{K} \times \lambda_0$, the composition law now takes the form

$$\mathbb{W} = \frac{\mathbb{U}+\mathbb{V}}{1+\mathbb{U}\times\mathbb{V}/\mathbb{C}^2} = ln\mu = \frac{lnv + ln\varrho}{1 + lnvln\varrho/ln^2\mathbb{K}} = ln\frac{\lambda_2}{\lambda_0} = \frac{\ln(\frac{\lambda_1}{\lambda_0}) + ln\varrho}{1 + \ln(\frac{\lambda_1}{\lambda_0})ln\varrho/ln^2(\frac{\Lambda}{\lambda_0})}$$

it can be shown that we cannot find any scale $\lambda < \Lambda$ if we start from any scale $\lambda > \Lambda$. Hence Λ is invariant under dilations and contractions, which resulted from principle of scale relativity and existence of fractal to non-fractal transition.

With the foundation laid out, the special relativity can be constructed under the scale relativity framework. The nondifferentiability of the space have three main consequences:

1) *Infinite number of geodesics* demands defining a fractal velocity fields V = V(x(t, dt), t, dt) for the flow of the geodesics. This loss of information (purely geometric origin) meaning at the level of particle paths, probabilistic description will replace the deterministic description.
2) *Fractal geodesics* requires a fractal velocity field, which can be defined as $V[x,t,dt] = v[x,t] + w[x,t,dt] = v[x,t]\{1 + \zeta\left(\frac{\tau_0}{dt}\right)^{1-\frac{1}{D_F}}\}$, where τ_0 is a transition time-scale. This equation shows that scale dependent persists for all scale although it is dominated by

different parts at different scale. Fractal part dominates at small scale while the differentiable classical part dominates at large scale. The transition is identified as *the de Broglie scale* of quantum to classical transition. Moreover, it might also predict the classical behavior in quantum regime and vice visa.

3) *Symmetry breaking under the reflection (dt → -dt)* implies two valuedness of the velocity,

$$V_+[x(t,dt),t,dt] = v_+[x(t),t] + \omega_+[x(t,dt),t,dt],$$
$$V_-[x(t,dt),t,dt] = v_-[x(t),t] + \omega_-[x(t,dt),t,dt],$$

which is shown to be the origin of the complex nature of the quantum tool.

Again to obey constrain of internal composition law and recovering classical limit, the velocity field is defined as

$$\tilde{V} = \left(\frac{v_+ + v_-}{2} - \alpha\frac{v_+ - v_-}{2}\right) + \left(\frac{\omega_+ + \omega_-}{2} - \alpha\frac{\omega_+ - \omega_-}{2}\right)$$

A complex operator $\frac{\hat{d}}{dt} = \frac{\partial}{\partial t} + \mathcal{V}\cdot\nabla - i\mathcal{D}\Delta$is introduced to deal with the nondifferentiability by replacing the d/dt. Here $\mathcal{V}$ is differentiable part of the complex velocity field and $\mathcal{D}$ characterizes the amplitude of fractal fluctuation since $\mathcal{D} = \frac{\langle d\xi_{\pm i} d\xi_{\pm j}\rangle}{\pm 2\delta_{ij}dt}$ where i ,j = x, y, z

This operator enables us to recover the form of physics laws as their differentiable counterpart. Starting from Newton's equation of dynamics $\mathrm{m}\frac{\hat{d}}{dt}\mathcal{V} = -\nabla\phi$ and defining $\varphi = e^{iS/2m\mathcal{D}}$, we obtain

$$\mathcal{D}^2\Delta\varphi + \mathrm{i}\mathcal{D}\frac{\partial}{\partial t}\varphi - \frac{\phi}{2m}\varphi = 0, \qquad (1)$$

When $\hbar = S_0 = 2m\mathcal{D}$ standard Schrödinger equation can be recovered. Hence there is natural link between the Compton relation and the Schrödinger equation, where $\mathcal{D}$ can be defined by the fractal-nonfractal transaction. Since $m = S_0/2\mathcal{D}$, it can be perceived as a large-scale geometric property of fractal geodesics, which emerged from the geometry itself.

Similarly, new form of Langrage in terms of complex action is defined as $Ł = \frac{\hat{d}S}{dt} = \frac{\partial S}{\partial t} + \hat{\mathcal{V}}\cdot\nabla S$, and the covariant Hamiltonian function is defined as

$$\mathcal{H} = \hat{\mathcal{V}}\cdot\mathcal{P} - Ł = \mathcal{V}\cdot\mathcal{P} - \mathrm{i}\mathcal{D}\nabla\cdot\mathcal{P} - Ł. \qquad (2)$$

By redefining the Hamiltonian operator as $\widehat{\mathcal{H}} = -2m\mathcal{D}^2\Delta + \phi$, again the Schrodinger equation can be written as

$$\widehat{\mathcal{H}}\varphi = (-2m\mathcal{D}^2\Delta + \phi)\varphi = 2\mathrm{im}\mathcal{D}\frac{\partial\varphi}{\partial t} \quad (3)$$

Further generalization can be obtained b introduce full wave function $\tilde{V} = -2\mathrm{i}\mathcal{D}\nabla ln\tilde{\varphi}$ and accounting for doubling of the partial time derivative

$$\frac{\tilde{\partial}}{\partial t} = \frac{1}{2}\left(\frac{\partial_+}{\partial t} + \frac{\partial_-}{\partial t}\right) - \frac{1}{2}i\left(\frac{\partial_+}{\partial t} - \frac{\partial_-}{\partial t}\right). \quad (4)$$

Hence the more general Schrodinger Equation would present as

$$\mathcal{D}^2\Delta\tilde{\varphi} + \mathrm{i}\mathcal{D}\frac{\tilde{\partial}}{\partial t}\tilde{\varphi} - \frac{\phi}{2m}\tilde{\varphi} = 0 \quad (5)$$

Given that the derivation only needing parameter $\mathcal{D}$ to be conservative, this model is applicable for macrophysics. The general method can be applied to macrophysics, where a new constant instead of $\hbar = 2m\mathcal{D}$ (particular case applicable for microphysics) could be introduced. While all the derivation above assumes the fractal dimension D_F =2, the theory can be further expand by considering the fractal dimension $1<D_F<2$, which however lead to degenerate and unphysical Schrodinger equation.

The fractal space-time can also be introduced in framework for relativistic quantum mechanics. Since the energy is now expressed as $E^2 = p^2c^2 + m^2c^4$, the transition from fractal to nonfractal is now given by the four-dimensional de Broglie scale $\lambda_\mu = \hbar/p^\mu$. Since its corresponding time $\tau_{dB} = \frac{\hbar}{E} = \hbar/\sqrt{p^2c^2 + m^2c^4}$ is always smaller than the $\tau_E = \frac{\hbar}{E} = \hbar/mc^2$, then fractal space will happen first and then fractal space and time when going down the scale. The time differential element has to be replaced by proper time differential element ds. To account for the three discrete symmetry breaking from the nondifferentiability of space, i.e. $ds \leftrightarrow -ds\ dx^\mu \leftrightarrow -dx^\mu\ x^\mu \leftrightarrow -x^\mu$, biquanternionic velocity is introduced. The two valuedness properties originated from reflection in s and dx and standard effect of Parity (P) and time reversal (T).

Hence the quantum-type mechanics (regard to laws of motion) in space-time can be derived from the simplest possible scale laws constrained by scale relativity principle and stand law of motion.

Another field of application for the scale relativity framework is the gauge field, by considering resolution variables as function of the space-time coordinates. It is proposed that gauge fields can be constructed as the manifestation of the dilations of the scale variable. By introducing the new scale symmetry, the charge can be constructed as the conservative quantities, hence as the generator of the scale transformation group. Furthermore, the links between electromagnetism and scale variation is made. This leads to correspondence between local expansion/contraction or staticity of the fractal space-time to a charged or an uncharged particle. Therefore, gauge field is conceptualized as locally equivalent to expansions or contractions of the internal resolution variables for describing a nondifferentiable manifold.

Besides the quantum type law of motion derived above, a quantum scale-law can also be constructed under the scale relativity framework. One approaches propose a "scale law function the $\psi[ln\varepsilon(x,t),x,t]$. If it only depends on time variables, a Schrödinger equation can be written as

$$\mathcal{D}^2\frac{\partial^2\psi}{(\partial \ln\varepsilon)^2}+\mathrm{i}\mathcal{D}_\varepsilon\frac{\partial\psi}{\partial t}-\frac{1}{2}\phi_\varepsilon\psi=0 \qquad (6)$$

It gives rise to a log-periodic behavior, equivalent to classical stationary wave equation. The probability of a structure present at some relative scale can be described by the solution. The propagation of quantum wave can then be described by the time dependent solutions in scale space. A more generalized Schrodinger equation can be obtained by introducing wave function $\psi(\varepsilon_{\mu\upsilon})$ to account for the tensorial nature of the scale variables:

$$\mathcal{D}_\varepsilon{}^2\partial_{\mu\upsilon}\,\partial^{\mu\upsilon}\psi+\mathrm{i}\mathcal{D}_\varepsilon\frac{\partial\psi}{\partial t}-\frac{1}{2}\phi_\varepsilon\psi=0 \qquad (6)$$

Another approach for quantum scale law can be arrived by considering djinn or "scale time" as the main new variable. The Schrodinger equation can be constructed starting from the Euler-Lagrange form:

$$\mathcal{D}_s{}^2\frac{\partial^2\Psi_s}{(\partial \ln\mathcal{L})^2}+\mathrm{i}\mathcal{D}_s\frac{\partial\Psi_s}{\partial t}-\frac{1}{2}\phi_s\Psi_s=0 \qquad (7)$$

Starting from fractal objects in nature, the concept of fractal abstracts into a geometric description through several stages. Starting from Mandelbrot's fractal objects, scale relativistic fractals are

proposed by suggesting only scale ratio has physical meaning. Furthermore, if the scale ratios between structures become the variable of the coordinates (with non-static fractal structure), the gauge transformations can be interpreted with a scale relativistic interpretation. And the Fourier transform of solution $\Psi_s(ln\varrho)$ from equation (7) will provide probability amplitude for the possible values of $ln\varrho$. Hence the probability density will be given by $|\Psi_s|^2(ln\varrho)$, which describe a given probability for two structures to be related by a given ratio. Hence an infinite family of possible behavior will self-organize since some value of $ln\mathcal{L}$ become more probable than others. Furthermore, a conserved quantity will emerge from the uniformity of the new time scale variable if the equation is invariant with respect to djinn (or scale time). This quantity is defined as $\mathbb{E} = \mathbb{V}\frac{\partial \tilde{\mathcal{L}}}{\partial \mathbb{V}} - \tilde{\mathcal{L}}$, defined as a scale energy "Complexergy", equivalent of energy for motion. The complexergy is universally quantized (i.e. discrete level of hierarchy of organization in nature) due to the universal minimal value of djinn (τ>0). Hence the system would jump from one organization to a more complicated one if the system is to increase its energy with time.

Besides the satisfaction derived from funding the underlying link between geometry (in a broad space-time-scale sense), the theory also have interesting applications. As mentioned before, quantum behavior might be observed in macroscopic (in traditional sense) for irreversible reflection process. Hence in the framework of scale relativity, a system might meet the condition and described by quantum like tool. For mesoscopic and macroscopic fractal systems, it would be interested to know the necessary condition for the possible existence of a macroscopic Schrodinger regime. Numerical studies carried out showed the prerequisite to be a large enough scale range (scale ratio of 1e5 between the upper and lower transition) exhibiting fractal behavior. A scale ratio is applicable to time-scale as well as length-scales, which could be hard to achieve in laboratory scale. However, the demonstration of applying such framework has already been achieved (e.g. the Higgs mechanism and super conductivity). The analogy between medium-scatter and space (or space-time) object holds potential for studying material physics to understand fundamental physics. The propagation of waves in geological media has already attracted huge amount of interest, other fractal medium also present potential system for studying quantum like behavior.

The other interesting application is to understand the relation between quantum laws and diffusions, given their formal similarity between their governing equations

$D\Delta P - \frac{\partial P}{\partial t} = 0$ for classical diffusion equation

$\mathcal{D}\Delta\psi + \mathrm{i}\frac{\partial \psi}{\partial t} = 0$ for free Schrodinger-type equation

Despite the similarity of the format in their equation, their difference is quite striking: the diffusion is dissipative, non stationary, non isentropic with an tendency to become disorganization; on the other hand, the Schrodinger equation exhibits stationary and quantized solution for a given boundary condition, hence tendency toward self-organization. To reconcile the differences, it was proposed to conceptualize Quantum laws as anti-diffusion. Starting from the complex velocity field, by expressing force as probability density at each point and instant, a diffusion potential - $\phi_{diff} = 2D^2\Delta\sqrt{P}/\sqrt{P}$ - exactly opposite to quantum potential can be derived. By varying the value of $\mathcal{D}$, three regimes can be identified: self-organizing quantum-type process $\mathcal{D}^2$; weakly organized classical process $(\mathcal{D}^2 = 0)$; disorganizing entropy increasing diffusion process $(-\mathcal{D}^2)$.

Since dimension $\mathcal{D}$ is not tied to the $\hbar$, the transition among the three stages might be observed by fine-tuning the quantum potential. Hence an experimental setup to simulate the quantum potential has been proposed. It involves three steps retroactive loop with detector, computer and actuators. The detector measures the quantity as the density, the computer will compute the quantum potential $Q = 2D^2\Delta\sqrt{\rho_n}/\sqrt{\rho_n}$, the actuator will apply the new value of potential to the system at each time t_n. Hence the continuous loop might stimulate quantum like behaviors.

Appendix C: MATLAB Code to generalize random fractal

```
function field1=Brownian_field(H,n)
% generates Fractional Gaussian field projected binary system with a given Hurst parameter 'H';
% the covariance function is isotropic and the method used is

% inputs:
% 'H' is the Hurst parameter
% 'n' is the number of grid points on a square lattice that includes the circular region of interest

% output:
% plot, which is also plotted as shown below

clear all

R=2; % [0,R]^2 grid, may have to extract only [0,R/2]^2
n=150; m=n; % size of grid is m*n; covariance matrix is m^2*n^2
tx=[1:n]/n*R; ty=[1:m]/m*R; % create grid for field
Rows=zeros(m,n);
H = 0.5;

for i=1:n
   for j=1:m % rows of blocks of cov matrix
      Rows(j,i)=rho([tx(i),ty(j)],[tx(1),ty(1)],R,2*H);
   end
end
BlkCirc_row=[Rows, Rows(:,end-1:-1:2);
   Rows(end-1:-1:2,:), Rows(end-1:-1:2,end-1:-1:2)];

% compute eigen-values
lam=real(fft2(BlkCirc_row))/(4*(m-1)*(n-1));
lam=sqrt(lam);
% generate field with covariance given by block circular matrix
Z=complex(randn(2*(m-1),2*(n-1)),randn(2*(m-1),2*(n-1)));
F=fft2(lam.*Z);
F=F(1:m,1:n); % extract sub-block with desired covariance
[out,c0,c2]=rho([0,0],[0,0],R,2*H);
field1=real(F); field2=imag(F); % two independent fields

% make correction for embedding with a term c2*r^2
field1=field1 + kron(ty'*randn,tx*randn)*sqrt(2*c2);
[X,Y]=meshgrid(tx,ty);

%renormalize field 1
field1((X >1)|(Y>1))=nan;
field1=field1(1:n/2,1:m/2);
```

```
field1=field1-median(median(field1))

%find the threshold value of h
B = reshape (field1,[],1);
Bsort = sort(B);
p = 0.9;
cap = Bsort(floor(numel(Bsort)*p));
fprintf ('the cap value is %f,', cap);

%surf(tx(1:n/2),ty(1:m/2),field1,'EdgeColor','none')
%colormap pink
[row1,col1]=find(field1>cap);

% draw the circles

for jj = 1:1:numel(row1)

r= R/n;
x(jj)=row1(jj)*R/n;
y(jj)=col1(jj)*R/n;

rectangle('Position',[x(jj),y(jj),r,r],'Curvature',[1,1]);
hold on;
axis equal;

end

axis([0 R/2 0 R/2]);

%define function rho

function [out,c0,c2]=rho(x,y,R,alpha)
% embedding of covariance function on a [0,R]^2 grid
if alpha<=1.5 % alpha=2*H, where H is the Hurst parameter
   beta=0;c2=alpha/2;c0=1-alpha/2;
else % parameters ensure piecewise function twice differentiable
   beta=alpha*(2-alpha)/(3*R*(R^2-1)); c2=(alpha-beta*(R-1)^2*(R+2))/2;
   c0=beta*(R-1)^3+1-c2;
end
% create continuous isotropic function
r=sqrt((x(1)-y(1))^2+(x(2)-y(2))^2);
if r<=1
   out=c0-r^alpha+c2*r^2;
elseif r<=R
   out=beta*(R-r)^3/r;
else
```

```
    out=0;
end
```

Appendix D: MATLAB Code to generate dispersion curve

```
import com.comsol.model.*
import com.comsol.model.util.*

model = ModelUtil.create('Model');

model.modelPath('C:\Users\Snowocean\Desktop\environmentalcomplex');

model.name('CS43_2n100_H3H7mixCap9.mph');

model.param.set('ax', '325');
model.param.set('gx', 'pi/ax');
model.param.set('k1x', 'r1*gx');
model.param.set('k1y', '0*gy');
model.param.set('k2x', '0*gx');
model.param.set('k2y', 'r2*gy');
model.param.set('r1', '0');
model.param.set('r2', '0');
model.param.set('eM', '3e9');
model.param.set('vrM', '0.375');
model.param.set('rhoM', '2500');
model.param.set('vrSc', '0.329');
model.param.set('rhoSc', '972');
model.param.set('d', '1e6');
model.param.set('eR', '4.35e8');
model.param.set('vrR', '0.25');
model.param.set('rhoR', '1180');
model.param.set('eSc', '4.35e7');
model.param.set('ay', '325');
model.param.set('gy', 'pi/ay');

model.modelNode.create('mod1');

model.geom.create('geom1', 2);
model.geom('geom1').feature.create('imp1', 'Import');
model.geom('geom1').feature.create('r1', 'Rectangle');
model.geom('geom1').feature.create('r2', 'Rectangle');
model.geom('geom1').feature.create('spl1', 'Split');
model.geom('geom1').feature.create('dif1', 'Difference');
model.geom('geom1').feature.create('copy1', 'Copy');
model.geom('geom1').feature.create('dif2', 'Difference');
model.geom('geom1').feature.create('mov1', 'Move');
model.geom('geom1').feature('imp1').set('type', 'dxf');
model.geom('geom1').feature('imp1').set('filename',
'C:\Users\Snowocean\Desktop\n100_H3H7.dxf');
```

```
model.geom('geom1').feature('r1').set('pos', {'118' '47'});
model.geom('geom1').feature('r1').set('size', {'343' '341'});
model.geom('geom1').feature('r2').set('pos', {'518' '47'});
model.geom('geom1').feature('r2').set('size', {'343' '341'});
model.geom('geom1').feature('spl1').selection('input').set({'imp1'});
model.geom('geom1').feature('dif1').selection('input').set({'r1'});
model.geom('geom1').feature('dif1').selection('input2').set({'spl1(1)' 'spl1(100)' 'spl1(101)'
'spl1(106)' 'spl1(11)' 'spl1(13)' 'spl1(145)' 'spl1(146)' 'spl1(147)' 'spl1(15)' ...
'spl1(17)' 'spl1(177)' 'spl1(18)' 'spl1(182)' 'spl1(19)' 'spl1(20)' 'spl1(202)' 'spl1(209)' 'spl1(21)'
'spl1(222)' ...
'spl1(223)' 'spl1(224)' 'spl1(238)' 'spl1(249)' 'spl1(250)' 'spl1(265)' 'spl1(266)' 'spl1(273)'
'spl1(274)' 'spl1(282)' ...
'spl1(283)' 'spl1(288)' 'spl1(289)' 'spl1(297)' 'spl1(298)' 'spl1(299)' 'spl1(3)' 'spl1(300)' 'spl1(301)'
'spl1(311)' ...
'spl1(312)' 'spl1(313)' 'spl1(314)' 'spl1(315)' 'spl1(316)' 'spl1(317)' 'spl1(327)' 'spl1(328)'
'spl1(329)' 'spl1(33)' ...
'spl1(330)' 'spl1(331)' 'spl1(34)' 'spl1(35)' 'spl1(36)' 'spl1(37)' 'spl1(38)' 'spl1(39)' 'spl1(54)'
'spl1(55)' ...
'spl1(56)' 'spl1(57)' 'spl1(58)' 'spl1(59)' 'spl1(7)' 'spl1(71)' 'spl1(72)' 'spl1(73)' 'spl1(74)'
'spl1(86)' ...
'spl1(87)' 'spl1(88)' 'spl1(89)' 'spl1(9)'});
model.geom('geom1').feature('copy1').set('displx', '400');
model.geom('geom1').feature('copy1').selection('input').set({'dif1'});
model.geom('geom1').feature('dif2').selection('input').set({'r2'});
model.geom('geom1').feature('dif2').selection('input2').set({'copy1'});
model.geom('geom1').feature('mov1').set('displx', '-400');
model.geom('geom1').feature('mov1').selection('input').set({'dif2'});
model.geom('geom1').run;


model = mphload('CS43_2n100_H3H7mixCap9.mph');

% (Default values are not included)
matfile = ['C:\Users\Snowocean\Desktop\environmentalcomplex\list.txt'];
A = load(matfile);
rhoA= A(:,1).*1e3;
vA= A(:,2);
eA=A(:,3).*1e9;
ss=31;
xx=max(size(A));% number of iterations
fprintf('starting the sweep CS43_2n150_H5Cap9 now!\n')


r1=0;
r2=0;
neig = 23;
```

```
EigFreqGX= zeros(21,neig);
nEigFreqGX= zeros(21,neig);
%--------------------------------------------------------------------------

for mm=1:xx
   update=['\n we are running entry' num2str(mm) 'now\n'];
   fprintf(update)
   material=['the E is' num2str(eA(mm)) 'the rho is' num2str(rhoA(mm)) 'the vr is'
num2str(vA(mm)) '\n'];
   fprintf(material)


for jj=0:20
    ind=jj/20;
r2=ind;
r1=1;
fprintf('r1=')
fprintf(num2str(r1));
fprintf('r2=')
fprintf(num2str(r2));

model.param.set('r1', num2str(r1));
model.param.set('r2', num2str(r2));
model.param.set('vrSc', num2str(vA(mm)));
model.param.set('rhoSc', num2str(rhoA(mm)));
model.param.set('eSc',num2str(eA(mm)));

ModelUtil.showProgress(true) % display the progress bar?
model.sol('sol1').runAll; % solve

Freq_Imag = mphglobal(model,'imag(freq)')';
Freq_Real = mphglobal(model,'real(freq)')';

EigFreqGX(jj+1,1:length(Freq_Real))= Freq_Real;
nEigFreqGX(jj+1,1:length(Freq_Real))= EigFreqGX(jj+1,1:length(Freq_Real))*2.58621e-10;

end

filesave=['C:\Users\Snowocean\Desktop\environmentalcomplex\dispersion\n100H3H7cap9'
num2str(mm) 'XM.txt'];
save(filesave, 'EigFreqGX', '-ascii', '-tabs');

nfilesave=['C:\Users\Snowocean\Desktop\environmentalcomplex\dispersion\Nn100H3H7cap9'
num2str(mm) 'XM.txt'];
save(nfilesave, 'nEigFreqGX', '-ascii', '-tabs');
```

```
fprintf('finished XM\n');

clear Freq_Real Freq_Imag EigFreqGX nEigFreqGX

for jj=0:20
    ind=jj/20;
r2=1;
r1=1-ind;% we pin r2 as zero
fprintf('r1=')
fprintf(num2str(r1));
fprintf('r2=')
fprintf(num2str(r2));% Constants

model.param.set('r1', num2str(r1));
model.param.set('r2', num2str(r2));
model.param.set('vrSc', num2str(vA(mm)));
model.param.set('rhoSc', num2str(rhoA(mm)));
model.param.set('eSc',num2str(eA(mm)));

ModelUtil.showProgress(true) % display the progress bar?
model.sol('sol1').runAll; % solve

Freq_Imag = mphglobal(model,'imag(freq)')';
Freq_Real = mphglobal(model,'real(freq)')';

EigFreqGX(jj+1,1:length(Freq_Real))= Freq_Real;
nEigFreqGX(jj+1,1:length(Freq_Real))= EigFreqGX(jj+1,1:length(Freq_Real))*2.58621e-10;

end

filesave=['C:\Users\Snowocean\Desktop\environmentalcomplex\dispersion\n100H3H7cap9'
num2str(mm) 'MY.txt'];
save(filesave, 'EigFreqGX', '-ascii', '-tabs');

nfilesave=['C:\Users\Snowocean\Desktop\environmentalcomplex\dispersion\Nn100H3H7cap9'
num2str(mm) 'MY.txt'];
save(nfilesave, 'nEigFreqGX', '-ascii', '-tabs');

fprintf('finished YG\n');

clear Freq_Real Freq_Imag EigFreqGX nEigFreqGX

for jj=0:20
    ind=jj/20;
r1=0;
```

```
r2=1-ind;% we pin r2 as zero
fprintf('r1=')
fprintf(num2str(r1));
fprintf('r2=')
fprintf(num2str(r2));% Constants

model.param.set('r1', num2str(r1));
model.param.set('r2', num2str(r2));
model.param.set('vrSc', num2str(vA(mm)));
model.param.set('rhoSc', num2str(rhoA(mm)));
model.param.set('eSc',num2str(eA(mm)));

ModelUtil.showProgress(true) % display the progress bar?
model.sol('sol1').runAll; % solve

Freq_Imag = mphglobal(model,'imag(freq)')';
Freq_Real = mphglobal(model,'real(freq)')';

EigFreqGX(jj+1,1:length(Freq_Real))= Freq_Real;
nEigFreqGX(jj+1,1:length(Freq_Real))= EigFreqGX(jj+1,1:length(Freq_Real))*2.58621e-10;

end

filesave=['C:\Users\Snowocean\Desktop\environmentalcomplex\dispersion\n100H3H7cap9'
num2str(mm)  'YG.txt'];
save(filesave, 'EigFreqGX', '-ascii', '-tabs');

nfilesave=['C:\Users\Snowocean\Desktop\environmentalcomplex\dispersion\Nn100H3H7cap9'
num2str(mm) 'YG.txt'];
save(nfilesave, 'nEigFreqGX', '-ascii', '-tabs');

fprintf('finished YG\n');

clear Freq_Real Freq_Imag EigFreqGX nEigFreqGX


for jj=0:20
    ind=jj/20;
r1=ind;
r2=0;% we pin r2 as zero
fprintf('r1=')
fprintf(num2str(r1));
fprintf('r2=')
fprintf(num2str(r2));% Constants

model.param.set('r1', num2str(r1));
```

```
model.param.set('r2', num2str(r2));
model.param.set('vrSc', num2str(vA(mm)));
model.param.set('rhoSc', num2str(rhoA(mm)));
model.param.set('eSc',num2str(eA(mm)));

ModelUtil.showProgress(true) % display the progress bar?
model.sol('sol1').runAll; % solve

Freq_Imag = mphglobal(model,'imag(freq)')';
Freq_Real = mphglobal(model,'real(freq)')';

EigFreqGX(jj+1,1:length(Freq_Real))= Freq_Real;
nEigFreqGX(jj+1,1:length(Freq_Real))= EigFreqGX(jj+1,1:length(Freq_Real))*2.58621e-10;

end

filesave=['C:\Users\Snowocean\Desktop\environmentalcomplex\dispersion\n100H3H7cap9'
num2str(mm) 'GX.txt'];
save(filesave, 'EigFreqGX', '-ascii', '-tabs');

nfilesave=['C:\Users\Snowocean\Desktop\environmentalcomplex\dispersion\Nn100H3H7cap9'
num2str(mm) 'GX.txt'];
save(nfilesave, 'nEigFreqGX', '-ascii', '-tabs');

fprintf('finished GX\n');

clear Freq_Real Freq_Imag EigFreqGX nEigFreqGX


for jj=0:20
    ind=jj/20;
r2=1-ind;
r1=r2;% we pin r2 as zero

model.param.set('r1', num2str(r1));
model.param.set('r2', num2str(r2));
model.param.set('vrSc', num2str(vA(mm)));
model.param.set('rhoSc', num2str(rhoA(mm)));
model.param.set('eSc',num2str(eA(mm)));

fprintf('r1=')
fprintf(num2str(r1));
fprintf('r2=')
fprintf(num2str(r2));

ModelUtil.showProgress(true) % display the progress bar?
```

```
model.sol('sol1').runAll; % solve

Freq_Imag = mphglobal(model,'imag(freq)')';
Freq_Real = mphglobal(model,'real(freq)')';

EigFreqGX(jj+1,1:length(Freq_Real))= Freq_Real;
nEigFreqGX(jj+1,1:length(Freq_Real))= EigFreqGX(jj+1,1:length(Freq_Real))*2.58621e-10;

end

filesave=['C:\Users\Snowocean\Desktop\environmentalcomplex\dispersion\n100H3H7cap9'
num2str(mm) 'MG.txt'];
save(filesave, 'EigFreqGX', '-ascii', '-tabs');

nfilesave=['C:\Users\Snowocean\Desktop\environmentalcomplex\dispersion\Nn100H3H7cap9'
num2str(mm) 'MG.txt'];
save(nfilesave, 'nEigFreqGX', '-ascii', '-tabs');

fprintf('finished MG\n');

clear Freq_Real Freq_Imag EigFreqGX nEigFreqGX

end
fprintf('finished run here of the contact SAW_n100H1cap9\n')
```